Abstract

Preventive action by early detection of disease has been identified as one of the best means of improving health care. This has created a demand for high-sensitivity biosensors. By detecting low levels of disease specific molecules in human samples of blood, saliva, urine or spinal fluids, biosensors can be used to discover illnesses at a stage where they are still harmless and treatable. There is also demand for automated desktop appliances or hand held devices, as these can replace labor intensive analysis, lower costs and improve efficiency.

This thesis covers the development of a novel type of single particle detector that potentially fulfills all of the above demands. Through simulations, fabrication, and optical characterization, I have shown how free-standing dielectric membranes with a well-designed pattern of holes can be used to detect single particles trapped in the holes. The particles are detected with the help of narrowband illumination. In combination with chemical surface functionalization, the detector can potentially arrange for specific capture and detection of particles in the form of proteins, deoxyribonucleic acid (DNA), ribonucleic acid (RNA) or viruses. I estimate the detection limit of the present detector to be particles with a radius of 26 nm, corresponding to the size of a single virus.

The pattern is etched in the dielectric membrane, forming a square lattice of through holes. The permittivity hence varies periodically in two dimensions in the plane of the membrane. Such structures are called 2D photonic crystals (PCs). In general, they possess a number of useful optical properties. The structures that I have designed and fabricated, operate as narrowband filters in the visible range, while supporting resonantly enhanced fields in the vicinity of the membrane. This is achieved by coupling to so-called guided-resonance modes, which are optical modes that concentrate their power in the vicinity of the membrane, similar to fully guided modes. They are different from fully guided modes in the way that they can be coupled to by plane waves, incident on the membrane plane. Fabricated PCs are made in a three layered thin film stack of $Si_3N_4/SiO_2/Si_3N_4$, with a total thickness of 150 nm. Lattice periods are in the order of 500 nm, and the holes have a radius in the order of 100 nm.

I have also designed an imaging system based on a standard optical microscope,

where particles in the membrane appear as bright spots in the microscope image. Supported by simulation and experimental results, I have developed a model that explains this effect: Particles trapped in my crystals, are detected as a result of enhanced Rayleigh scattering. The intensity of the signal they produce is proportional to the square of their volume, and to the square of the amplitude of the field where they are located. This has motivated a study on how the resonantly enhanced field can be maximized, i.e. a study on high-Q guided-resonance modes.

In theory, high-Q modes can be achieved by decreasing the scattering strength of the PC lattice, for example, by decreasing the hole radius. However, in general this only holds for infinite structures. In my research collaboration, an experiment has been designed and carried out to verify this fact. The experimental results, supported by my simulations, show how the Q-factor of guided resonance modes is fundamentally limited by lattice size. Edge related losses may entail a need for an impractically large number of periods in the lattice, in order for high-Q optical modes to be observable.

I have designed methods that suppress these edge losses, resulting in a PC bound by in-plane Bragg mirrors. I show, both in simulations and experiments, how Bragg mirrors can be exploited to reduce edge related loss. In addition to presenting a way around the fundamental limitation on Q-factors for guided resonances in finite PCs, the new design gives an intuitive demonstration of the physical nature of guided resonance modes.

Throughout the following text, publications resulting from the thesis work are referenced in bold (i.e. [**23**]).

Preface

This dissertation is submitted in partial fulfillment of the requirements for the degree of Philosophiae Doctor (PhD) at the Norwegian University of Science and Technology (NTNU). The work has been a carried out at the Department of Electronics and Telecommunications at NTNU, SINTEF ICT MiNaLab, the Nano laboratory at the Department of Physics and Technology at the University in Bergen (UiB), the University Graduate Center at Kjeller (UNIK) and at Stanford University. Professor *Johannes Skaar*, Chief Scientist *Ib-Rune Johansen*, Professor *Aasmund Sudbø*, and Professor *Olav Solgaard* have acted as thesis supervisors.

The research has been funded by a scholarship from NTNU. Additional funding for publication, fabrication and optical characterization has been provided by SINTEF ICT MiNaLab, UNIK, Professor *Bodil Holst* at UiB, and Professor *Solgaard* at Stanford University. Funding has also been received from the Research Council of Norway (NFR), through the Norwegian Nano-Network and the ISBILAT program.

Acknowledgments

It seems most common among PhD students writing their dissertation to start this section by thanking their supervisors. However, my impression is that there are no clear guidelines concerning the form of the Acknowledgements section that force me to follow this trend. I have therefore chosen to deviate from this standard, and will instead begin by acknowledging my wife. Without going into detail, this seems to me the strategically smart thing to do. If this is disturbing to some of you supervisors, I can assure you that you will receive considerable gratitude if you continue reading the rest of this section.

So, first of all, I thank my wife, *Lise*. Prior to the start of my studies, you were a little skeptical to me embarking on the PhD-adventure. I could not really give an account of what I would gain by acquiring a Dr.-title. To me, it simply seemed like a nice thing to do, and I think you found this strange. Despite these initial doubts, you have been a great support throughout these four years. Especially, I want to thank you for coming with me to Stanford University, where you took a leave of absence from your job in Norway, and with the help of a cleaning lady tended to all my non-professional needs. My final, and maybe most substantial, conclusion after six months at Stanford University (with a stay-at-home wife), is that the men of the 50's were truly fortunate.

That said, I think it is time to focus on the acknowledgment of my supervisors. I have been fortunate enough to acquire a relatively large number of you, four in total: Professor *Aasmund Sudbø*, Chief Scientist *Ib-Rune Johansen*, Professor *Johannes Skaar*, and Professor *Olav Solgaard*. With this many (strong) personalities, it seems likely the result can be summarized by a direct translation of a Norwegian saying: *The more cooks, the greater the mess*. However, this is not the case. To the contrary, I would say that I have been very lucky with my supervisors. The cooperation among us has been excellent. I would like to thank all of you for that.

On a personal level, I thank *Aasmund* for always taking the time to answer my questions and giving my written work detailed reviews (even my notes). Especially, I have enjoyed your feedback, pinpointing where I'm wrong, when I think I have understood what is going on. Your fantastic ability to see the physical explanation of observations made in simulations and experiments has been a key driving force

in my research. Going further, I would like to thank *Ib-Rune*. Your perpetual optimism has been a great motivation to me. I have you to thank for a large part of my technical funding, allowing me to fabricate devices and build our optical setups. In my recollection, I find that the initial idea for the nano-particle sensor was born in your mind. Our series of profound scientific discussions have been highly enjoyable, and important for my general understanding of photonic crystals.

To *Olav*, thank you for letting me come and visit your group at Stanford. My time in California was professionally fruitful. At least one paper was a direct result of the visit. You were an excellent supervisor during my stay in the states. I hope that I contributed to your group, if not completely, then close to the level of what your letter of recommendation prescribed. I also wish to thank my friends and colleagues at Stanford for making me feel like a true Solgaard Guardian, and helping me out in the lab. To *Antonio* in particular, you were a great sparring partner.

To *Johannes*, you have been both a great friend and a great supervisor. Thanks to you, I have rediscovered why I like cross-country skiing and am now a proud owner of a pair of cross-country racing skis. If it had not been for your clear guidance, I could have gone for the touring model. Needless to say, that would have been a huge mistake. Although our scientific cooperation has been somewhat limited in the last years, you gave me a rocketing start. During my first year as a PhD student, you helped me acquire my first journal paper, and sent me as your replacement to my first international conference. I also have to thank you for giving me the opportunity to gain experience as a teacher, by letting me teach at the Master's level at the University in Trondheim.

Continuing to my collaborators: I am sure I would not be where I am today, had it not been for the help of Dr. *Peter Kaspar* at ETZH, and the group and fabrication facilities of Professor *Bodil Holst* at Bergen University. Thank you *Peter* for making fantastic photonic crystals for me. A special thanks for the one that happened to have a close to ideal test-particle accidentally made in it. *Bodil*, thank you for letting me be a part of your group and for supporting my ideas. Finally, Dr. *Martin* (M. Greve), you are the man! Spending time with you has been extremely rewarding, both professionally and out on the rock.

During my four years as a PhD-student, I have spent most of my time at SINTEF MiNaLab in Oslo. I therefore thank SINTEF for allocating an office for me, and for letting me use their lab facilities. I must also say that I have found the parking facilities quite luxurious, enabling me to park my car inside at work during winter. To all my colleagues at MiNaLab, thank you for your professional support and for forcing me to eat lunch.

To my dad, I know that you were worried for a while. It seemed like I would not choose to take a PhD. I was, of course, just pulling your leg. Hopefully you will

be able to relax now. Joking aside, I feel fortunate to have a dad that understands what I have been doing over the last few years. To my whole family, including my in-laws, thank you for showing interest in my work and for your moral support. Spending time with you guys is usually great! To my sister in particular, thank you for reading the thesis and correcting my terribel spelling.

Finally, to all my friends, the world is boring without you! I tried to make a list of you all, but it turned out too long.

Contents

Chapter 1

Introduction

Going back a 150 years in time, the science of medicine was at a premature state. Little was known of how the body functioned, what caused disease and how diseases could be treated. There were men that called themselves doctors, and a number of memorable medicines and treatments, but in many cases both the doctors and their healing remedies did more harm than good. Bloodletting, for example, which consisted of withdrawal of "smaller" quantities of blood from a patient, was up until the end of the 18th century regarded as a treatment that could cure virtually any illness. It did, however, not do *George Washington* much good. In 1799, doctors proposed to bleed him healthy of a throat infection, but instead, after draining a total of 3.75 liters, had to declare the former president dead [1].

Luckily, the science of medicine has evolved since then. We currently gain progressive knowledge on human physiology, enabling us to live longer and healthier lives. In part, this is thanks to the development of biosensing techniques [2]. Biosensing has allowed us to identify the source of diseases, and now plays an important role in medical diagnostics [3]. Tools that can analyze biological samples for contents of bacteria, virus, proteins, DNA and RNA, are currently used as an aid to help doctors expose the cause of their patient's medical illnesses, and determine which treatment to apply.

The duration of convalescence, and chance of full recovery, is generally improved by early exposure of an illness. Early detection of diseases is therefore identified as one of the best and most cost efficient means of improving health care, and creates a demand for high-sensitivity biosensors [4, 5]. Moreover, the sensors should be made small and cheap, allowing them to be applied by physicians at point-of-care or as a personal appliance, affordable to the general population [6–8]. A need for small and cheap high sensitivity biosensors can also be found in environmental control [9, 10], where they can monitor the quality of air, water and food.

In this thesis, I present an optical transducer that can be used to realize a biosensor that is both cheap, compact and sensitive. My aim has been to create

a tool that will fit on a desktop, and can be used to detect molecules like protein, DNA and RNA, label-free, in samples of human blood. We will return to why detection of such molecules is useful, and what label-free biosensing is.

Although the motivation for my work is clearly anchored in biosensing, the work has in essence been limited to the development of a transducer that can detect single nano-particles. These nano-particles will in a final device be relevant biological molecules that label specific diseases. My transducer design accommodates chemical methods that are needed in order to trap such relevant targets, but these accommodations have not been explored in published work. A brief general summary of biosensing and biosensors is therefore given in the introduction, but the main body of the thesis reviews the optical properties of the developed transducer and its potential application in nano-particle detection.

1.1 Protein detection in human blood

Biological molecule is a collective term, used for all molecules produced by living organisms. It includes a range of subcategories, such as proteins, DNA, RNA, lipids, etc. [11]. We will be focusing on proteins, and more specifically on protein concentrations in human blood. This is because the presence or concentration of specific proteins in human blood, provides continuously updated information on a person's health [12].

Proteins are produced in our cells, and can be considered as the workhorses in living organisms. They have a wide range of functions, both within their mother cell and outside [3,13]. When proteins in the human body are transported from the cell where they are made, to the area where they are applied, they travel through the blood stream. The human body contains roughly 5 liters of blood, which is continuously pumped through the body at a rate of about 5 liters per minute. Thus, within a minute, the blood has visited virtually all cells in the human body. In this way, the protein content of human blood, mediates cellular activity in the whole body and is continuously updated.

There are two major challenges with detection of proteins in blood [11]. One is that proteins are small, with a typical diameter of 2-10 nm. It is difficult to detect them directly through their mass, size, electrical impedance or dielectric permittivity. The second is that targeted proteins are often present in concentrations of fg/ml and pg/ml, in solutions where the concentration of other proteins exceeds that of the target by many orders of magnitude. This makes it difficult to selectively detect the targeted protein, without interference from non-targeted molecules. A third challenge is related to red and white blood cells, and platelets. These are larger particles that can easily lead to clogging, and passivation or saturation of the sensor, unless properly filtered out. The latter issue is especially

relevant in compact devices, where sample preparation, cleaning and reactant delivery, require lab-on-chip technology [14, 15].

We will discuss solutions to the former of these three challenges, and to some degree review how design considerations can be made to accommodate specificity and sample preparation. Details on the chemical methods used to capture specific targets in solutions with millions of other proteins, and lab-on-chip technology used for micro scale sample preparation, falls outside the main scope of this thesis.

1.1.1 Tag assisted biosensing

The difficulty of detecting proteins directly, can been solved by attaching a label to the biomolecule that is under investigation [11]. This tag can be fluorescent, luminescent, radiometric, or colorimetric, allowing the biomolecule to be detected indirectly by exposing the sample to an excitation source, and detecting the emitted signal from the tag.

An analysis typically starts by drawing a sample of human blood and extracting the plasma with the help of a centrifuge or filtering device. This step filters out all red and white blood cells, and platelets. The sample is thereafter transferred onto a surface that has been furnished with capture molecules, specific to the targeted molecules in the sample. We will refer to the targeted molecule as the analyte, and the capture molecule as the receptor ligand. When a surface is made to capture an analyte, we say that it is functionalized. In practice, it involves furnishing the surface with receptor ligands designed to bond specifically to the analyte.

The surface furnished with receptor ligands can, for example, be the inside of wells in a micro-titer plate. If analytes are present in the sample, they will bond to the receptor ligands residing on the walls of the wells. Next, a solution of molecules with tags is added to each well. The tag-molecules are designed to bind to a second binding site on the analyte. We will use a fluorescent tag as an example, which is used in the common enzyme-linked immunosorbent assay (ELISA) [3, 13]. After washing away unbound molecules and tags, you are left with a surface of receptor ligands, where analytes have been immobilized and are connected to a fluorescent tag-molecule. When illuminating the wells with an excitation source, the fluorescent tags will emit light at specific wavelengths. The concentration of analytes in each well is proportional to the emitted light at these wavelengths, which can be measured using a spectrometer.

Although tag assisted biosensing can be both sensitive and selective, and is widely used today, it has some limitations and unattractive aspects [11]. Biosensing using radioactive tags can provide excellent sensitivity, but is in general expensive. It must be performed in labs specially fitted to handle radioactive materials, and generates contaminated waste that has to be disposed of properly. Moreover, tag assisted assays involve at least two, and sometimes several, separate chemical

reactions. This limits the efficiency, and entails more steps that potentially can go wrong. Over the last decades, there has therefore been a drive towards developing label-free biosensors.

1.1.2 Label-free biosensors

In contrast to tag assisted biosensing, label-free biosensing aims to detect biomolecules directly through their intrinsic properties [11]. In essence, they can all be considered to consist of two parts: A chemistry that enables functionalization of a surface, and a transducer that holds this surface and converts molecular changes on the surface to a measurable signal. The transducer is in general non-specific, and will respond to all molecular changes on the sensing surface. Thus, the chemistry provides selectivity and the transducer provides sensitivity.

Three main classes of label-free biosensors can be defined. These are mechanical [16], electric [17, 18] and optical sensors [11, 19–21]. Mechanical sensors are commonly made using cantilevers with micro- and nano-meter dimensions, with vibration modes that show a change in center frequency for a mass change of just a few molecules. By functionalizing the surface of a cantilever, analytes can settle on the cantilever when it is exposed to a sample. This causes a change in the mass of the cantilever, resulting in a measurable shift in center frequency related to the concentration of analytes in the sample. Alternatively, the concentration can be monitored as a function of static deflection of the cantilever, induced by a change in surface-stress from analytes binding on the surface.

Electric sensors, measure the electric properties of molecular layers. Typically, a functionalized surface is equipped with electrodes that enable the resistance or impedance in the surface to be monitored. The change in resistance or impedance, caused by analytes in a sample settling on the functionalized surface, can be used to deduce the initial concentration of analytes in the sample.

Both mechanical and electric biosensors can potentially be used to realize the next generation of label-free biosensors. Electric biosensors in particular, have advantages in regards to making compact and cheap devices [17, 18], which is essential for realizing sensors for point-of-care. However, currently it seems that the most sensitive class of label-free biosensors is optical [8,19,20]. Multiple optical label-free biosensors claim to have the potential of reaching the "Holy-grail" of biosensing [22, 23]**[24, 25]**, namely single molecule detection. Recently, this has reportedly also been achieved [26–28].

Optical biosensors detect biomolecules through their dielectric permittivity [1] [11]. As for mechanical and electric sensors, a surface is functionalized and exposed

[1] The square root of the relative dielectric constant is the more commonly known refractive index.

to a sample under investigation. Thereafter or simultaneously, a source of light is focused onto the detector through free space or guided to it through a waveguide. The surface is generally designed to concentrate the field where analytes are made to settle. Changes in permittivity on the surface can be detected as a shift in center frequency of an anomaly in the reflected or transmitted spectrum, a change in reflected or transmitted amplitude, or as scattering. The size of the change is used to deduce the concentration of analytes in the sample.

A number of different sensors exist that can be categorized as label-free optical biosensors. It is useful to divide them into two groups, based on the type of transducer they exploit. One group utilizes in-plane coupled transducers. These are designed to couple incident light to the sensing surface, and detect the response, through waveguides. In-plane coupled transducers exploit Mach-Zehnder interferometers [29, 30], ring resonators [31, 32], photonic cavity resonators [22, 23, 33], and whispering gallery mode-nanoshells [26]. They can potentially be used to demonstrate single molecule sensitivity, and some also have [26]. The negative aspect of these schemes is, however, that they often require elaborate alignment procedures to couple light in and out of the waveguides that lead to and from the transducer. Moreover, complex designs are often needed in order to achieve high dynamic range.

The other group, utilizes out-of-plane coupled transducers. These are designed to couple incident light to the sensing surface, and detect the response, through free-space. Out-of-plane coupled transducers, e.g. exploit coupling to surface-plasmon resonance (SPR) modes in metallic structures [4,34,35], or guided-resonance modes in dielectric photonic crystals (PCs) **[24, 25]**[36, 37]. As of today, they have not been used to demonstrate true single molecule sensitivity, but can be made with high dynamic range and do not require elaborate alignment procedures. An exception to this statement are certain transducers exploiting local surface-plasmon-resonance modes in nano-particles. These have been used to detect single molecules [27, 28]. They do not require elaborate alignment procedures, but to obtain high dynamic range, complex designs are still needed. Consequently, these schemes seem more applicable as laboratory tools, and less suitable for cheap and compact point-of-care devices.

The functionalized surface in SPR based transducers is usually made of gold. This gives SPR sensors an advantage over PC sensors, because one can utilize established chemical methods compared to the relatively new methods used to functionalize dielectrics [21, 38]. Furthermore, SPR based sensing exploits surface bound optical modes that are supported at metal-dielectric interfaces. The large contrast in permittivity, found at a metal-dielectric interface, is a better starting point for creating confined areas with high electric fields than the smaller contrast found at dielectric-dielectric interfaces, available in dielectric PC based sensors.

The ability to concentrate the electromagnetic field is of fundamental importance in label-free optical biosensing. This can be deduced from perturbation theory [39]. Intuitively, we can understand why by considering the response induced by a change in permittivity in an area with zero fields. This corresponds to looking for something in complete darkness, and the resulting response is hence zero. To detect a change in permittivity, the change has to be in an area where the field is non-zero, and the field should be maximized to induce the strongest response [8, 40].

The unit that provides these high fields, in label-free optical sensors, is the transducer. We will focus on transducers designed to function as optical resonators. The ability of an optical resonator to concentrate the field can be described by its Q-factor, which is the ratio of the energy stored in a resonator divided by the energy that exits the resonator per cycle. The sensitivity of the transducer is hence strongly related to the Q-factor of the optical mode that it supports, and we want the Q-factor to be as high as possible [19].

Since metals are intrinsically lossy in the optical range, the Q-factor of resonant modes in SPR structures is fundamentally limited by material properties. Dielectric materials, like Si_3N_4 and SiO_2, can on the other hand be manufactures with virtually zero loss. The Q-factor of optical resonators made in dielectric materials is therefore mainly limited by design and fabrication accuracy. Hence, with the ongoing improvement of nano-fabrication techniques, dielectric PC transducers can potentially give higher sensitivities.

1.2 Sample preparation and target binding affinity

If procedures currently done in laboratories are to be performed within minutes using table-top or hand-held devices, sample preparation and delivery of the analytes to and from the transducer has to be done within a very limited volume. This can be achieved using lab-on-chip technology, where filtering, mixing and pumping of fluids is all done on a platform measuring just a few square centimeters in size. Lab-on-chips are typically made in polymers, structured on the micron scale by embossing or injection molding, and driven by exterior pumps [3, 41, 42].

A prepared blood sample generally consists of extracted plasma, and it is exposed to the sensor by simply flushing it over the functionalized surface. This must be done at a rate that allows analytes to bind to the receptor ligands. If the flow is too high, relative to the size of the zone where receptor ligands reside, the probability of analytes interacting with receptor ligands diminishes. Analytes simply flow right past the receptor ligands without binding to them. In compact and

efficient sensors that also need to be sensitive, this leads to conflicting demands: You want the sample to be processed as fast as possible, flushing it at a high rate across the functionalized surface, but need a low flow rate to ensure that analytes bind with high probability [8, 43, 44].

Certain transducers are reported to incorporate these flow and binding related issues [**24**][45]. Free-standing perforated membranes, composed of a periodic lattice of holes, can support optical modes that concentrate an incident field in the vicinity of the membrane. The membrane surface is functionalized and produces a response that is sensitive to changes in permittivity in the vicinity of the membrane. Instead of flushing a sample over the surface of the membrane, the sample is pumped through. This forces analytes closer to the membrane surface, increasing the chance that they interact with receptor ligands residing on the surface. Further increase of the binding probability can be induced by arranging for functionalization limited to the inside of the holes in the membrane [**24**]. By tuning the membrane thickness and radius of holes relative to the mean-free path of analytes, one can ensure that analytes and receptor ligands must interact many times during the time it takes for analytes to flow through each hole.

1.3 Organization of thesis

In this thesis, I present the manufacture and working principle of a transducer that can be categorized as an out-of-plane coupled transducer. High sensitivity is achieved by field confinement in dielectric PCs that support so-called guided-resonance modes in the visible range. Fabricated devices are composed of a 150 nm thick free-standing membrane, with a lattice of through holes. The dielectric materials used in the current fabricated structures are Si_3N_4 and SiO_2. A center layer of SiO_2, 50 nm in thickness, is covered on both sides by 50 nm of Si_3N_4. This creates a ring of SiO_2 inside every hole that is chemically distinguishable from the outer surface of the membrane, and enables functionalization of the inside of the holes only. Limiting the functionalization to the inside of every hole is motivated by both optical and fluidic aspects: The optical modes that we exploit in our design concentrates the electric field at the center of the membrane and peaks at the hole walls. Capture events are hence optically most significant if they take place at the hole wall. In a final application, we aim for samples to be pumped through the holes in the membrane. The probability of analytes settling on the surface inside the holes can hence be optimized, as discussed, in section 1.2.

In addition to presenting a novel transducer, I review some of the fundamental limitations of field confinement induced by guided-resonance modes, and present a novel structure that can overcome these fundamental limitations.

I have chosen to organize the thesis as follows: Chapter 2 is dedicated to

explaining what PCs are, why they support guided-resonance modes, and how they can be simulated and fabricated. Chapter 3 reviews how 2D PC membranes can be exploited as transducers for single particle detection. In order for the transducer to be applied, it must be incorporated in a optical setup. Two possible setups are presented in chapter 4, namely the setups used in this thesis. The purpose of the first four chapters is to prepare the reader for the seven scientific reports found in the appendix. A summary of the main results and conclusions of these reports is given in chapter 5. The reports are listed in chapter 6. A detailed description of my contributions to each report is found in chapter 7.

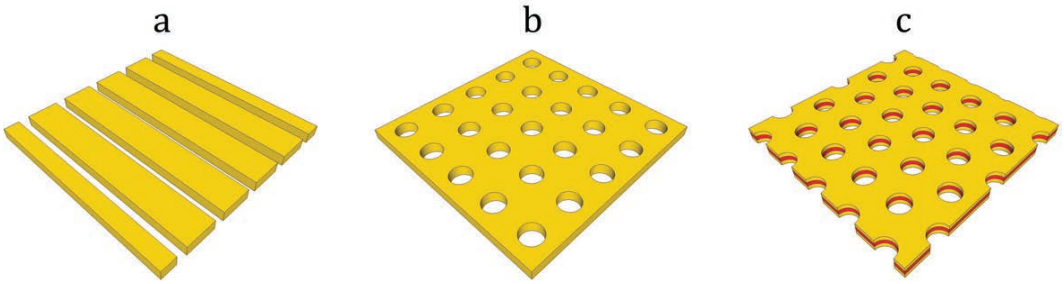

Figure 2.1: Slab structures with infinite in-plane extent, having (a) one-dimensional and (b and c) two-dimensional periodic permittivity in the plane. The colors label different materials with different permittivity.

Chapter 2

Photonic crystal slabs

Photonic crystals (PCs) are materials or fabricated structures with a periodic permittivity. The name comes from their similarity to crystalline solids. As electrons are affected by a periodic potential in crystalline materials, photons are affected by a periodic permittivity in PCs. The Schrödinger equation describes the behavior of electrons in crystalline solids, while Maxwell's equations describe the behavior of photons in PCs. Solutions to these equations have similar properties. Specifically, they both show that certain electron and photon energies are not allowed to propagate in a given crystal. For PCs this translates into bands of frequencies where no optical modes exist, so-called photonic band gaps [39]. This property of PCs is exploited in a number of different applications, e.g. PC fibers [46], beam splitters, multiplexers and waveguides [47].

Another property of PCs is that they can support guided-resonance modes [48, 49]. These modes are not related to photonic band gaps, where no modes exist, but rather the frequencies where there are solutions to Maxwell's equations. In this chapter, we study guided-resonance modes in dielectric PC slabs with 1D-

and 2D-periodic permittivity in the plane. Figure 2.1 holds illustrations of such structures. It shows three infinite slabs with periodic permittivity in the plane, imposed by a lattice of slits (a) or holes (b and c).

The structures in Fig. 2.1 are called PC slabs, PC membranes, or simply 1D and 2D PCs. We will use the latter names. Talking of PCs, 1D or 2D PCs in the following text, we mean a structure that is composed of a slab with a given thickness and infinite extent in the plane, that has a 1D- or 2D-periodic permittivity in the plane of the slab, and that is surrounded by a lower permittivity material. As seen in Fig. 2.1 (c), the terms may refer to slabs that are composed of multiple thin films as well.

In this chapter, we first introduce Maxwell's equations, and find general solutions for dielectric materials and homogeneous dielectric slabs. Secondly, we present Bloch's theorem, and explain how Bloch's theorem, in combination with the general solution describing the modes of a homogeneous slab, can be used to understand what guided-resonance modes are, and what structures support these modes. Next, we will introduce Temporal Coupled Mode Theory, which models the resonant behavior of 1D and 2D PCs. Finally, we describe methods used in this thesis to simulate and fabricate PCs.

2.1 Maxwell's equations

Maxwell's equations describe the behavior of electromagnetic fields in general. We will restrict our study to dielectric structures and visible light. This is a good approximation for all the materials and structures investigated in this thesis. Furthermore, it allows us to solve Maxwell's equations for time-harmonic fields, assuming that no free charges or currents are present, and that all materials are linear, isotropic, non-magnetic and lossless. Under these restrictions, Maxwell's curl equations can be reduced to the following [39]:

$$\nabla \times \mathbf{E}(\mathbf{r}) = i\omega\mu_0 \mathbf{H}(\mathbf{r}) \tag{2.1}$$

$$\nabla \times \mathbf{H}(\mathbf{r}) = -i\omega\epsilon_0 \epsilon(\mathbf{r},\omega)\mathbf{E}(\mathbf{r}) \tag{2.2}$$

The complex amplitudes $\mathbf{E}(\mathbf{r})$ and $\mathbf{H}(\mathbf{r})$, represent the electric and magnetic field. These relate to the real electric and magnetic field, $\mathbf{E}(t,\mathbf{r})$ and $\mathbf{H}(t,\mathbf{r})$, through

$$\mathbf{E}(t,\mathbf{r}) = \Re\left(\mathbf{E}(\mathbf{r})e^{-i\omega t}\right) \text{ and } \mathbf{H}(t,\mathbf{r}) = \Re\left(\mathbf{H}(\mathbf{r})e^{-i\omega t}\right),$$

where t is the time, ω is the angular frequency, and $\mathbf{r}$ is the position vector. Parameters μ_0 and ϵ_0 are the permeability and permittivity of vacuum, and $\epsilon(\mathbf{r},\omega)$ is the position and frequency dependent relative permittivity.

Solutions to Eqs. (2.1) and (2.2) provide all field configurations allowed to propagate in a structure defined by $\epsilon(\mathbf{r},\omega)$. By taking the divergence on both sides in these equations, we are left with Maxwell's equations of divergence:

$$\nabla \cdot [\epsilon_0 \epsilon(\mathbf{r}) \mathbf{E}(\mathbf{r},\omega)] = 0 \tag{2.3}$$

$$\nabla \cdot \mathbf{H}(\mathbf{r}) = 0 \tag{2.4}$$

In further derivations, we will assume that the relative permittivity, $\epsilon(\mathbf{r},\omega)$, is independent of frequency. This is generally a good approximation for dielectric materials, as long as we investigate a limited range of frequencies at a time. Throughout the text, the relative permittivity will thus be denoted by ϵ or $\epsilon(\mathbf{r})$.

2.1.1 Hermitian operator

By combining Eqs. (2.1) and (2.2), we can further formulate an eigenvalue problem:

$$\hat{\Theta}\mathbf{H}(\mathbf{r}) = \left(\frac{\omega}{c}\right)^2 \mathbf{H}(\mathbf{r}), \tag{2.5}$$

where $c = 1/\sqrt{\mu_0\epsilon_0}$ is the speed of light in vacuum, and $\hat{\Theta}$ is an operator. A solution $\mathbf{H}(\mathbf{r})$ to this equation is called an eigenfunction, and the corresponding (ω/c)-value is called the eigenvalue. We will refer to ω in this fraction as the eigenfrequency, and to the eigenfunctions as modes. Furthermore, we refer to Eq. (2.5) as the **master equation**, since it in combination with Eqs. (2.3) and (2.4), fully describes our system: By solving it, we find the magnetic field amplitude of all modes allowed to propagate in our system. The electric field amplitude can thereafter be found from Eq. (2.2)[1].

The operator, $\hat{\Theta}$, takes the curl, then divides by $\epsilon(\mathbf{r})$, and then takes the curl again:

$$\hat{\Theta}\mathbf{H}(\mathbf{r}) \triangleq \nabla \times \left(\frac{1}{\epsilon(\mathbf{r})}\nabla \times \mathbf{H}(\mathbf{r})\right).$$

It is Hermitian, meaning that it is linear and fulfills the inner product equality $(\hat{\Theta}\mathbf{G}, \mathbf{F}) = (\mathbf{G}, \hat{\Theta}\mathbf{F})$ for arbitrary vector fields $\mathbf{G} = \mathbf{G}(\mathbf{r})$ and $\mathbf{F} = \mathbf{F}(\mathbf{r})$ [39]. The inner product is defined as

$$(\mathbf{G}, \mathbf{F}) \triangleq \int \mathbf{G}^* \mathbf{F} d^3\mathbf{r},$$

[1] A master equation can also be formulated in terms of the electric field: $(1/\epsilon(\mathbf{r}))\nabla\times\nabla\times\mathbf{E}(\mathbf{r}) = (\omega/c)^2\mathbf{E}(\mathbf{r})$. Combined with Eqs. (2.3) and (2.4), this master equation also gives a full description of the system. However, it is somewhat more complicated mathematically, as the operator on the left side is not Hermitian.

where the asterisk denotes complex conjugation.

The linearity of an operator is defined by

$$\hat{\Theta}(\mathbf{G} + \mathbf{F}) = \hat{\Theta}\mathbf{G} + \hat{\Theta}\mathbf{F}$$

and

$$\hat{\Theta}\beta\mathbf{G} = \beta\mathbf{G},$$

where β is a constant. Consequently, if both modes $\mathbf{H}_1(\mathbf{r})$ and $\mathbf{H}_2(\mathbf{r})$ are solutions of the master equation, and these have the same eigenfrequency, then $\alpha\mathbf{H}_1(\mathbf{r}) + \beta\mathbf{H}_2(\mathbf{r})$ is also a solution with the same eigenfrequency. In relation to formal arguments, it can therefore be useful to define the normalized mode $\mathbf{H}(\mathbf{r})$:

$$\mathbf{H}(\mathbf{r}) = \frac{\mathbf{H}'(\mathbf{r})}{\sqrt{\mathbf{H}', \mathbf{H}'}},$$

where $\mathbf{H}'(\mathbf{r})$ and $\mathbf{H}(\mathbf{r})$ only differ by an overall multiplier, and the inner product $(\mathbf{H}, \mathbf{H}) = 1$.

The second requirement on the Hermitian operator, $(\hat{\Theta}\mathbf{G}, \mathbf{F}) = (\mathbf{G}, \hat{\Theta}\mathbf{F})$, implies a set of rules. Derivation of these rules can be found in [47]. A summary of the rules used in this thesis is given here.

- For $\epsilon(\mathbf{r}) > 0$, the eigenfrequency ω is real and nonnegative.
- Orthogonal modes: Given two modes $\mathbf{H}_1(\mathbf{r})$ and $\mathbf{H}_2(\mathbf{r})$ whose eigenfrequencies are ω_1 and ω_2, where $\omega_1 \neq \omega_2$, the two modes are orthogonal, meaning that their inner product is zero, $(\mathbf{H}_1, \mathbf{H}_2) = 0$.
- Degenerate modes: Given two linearly independent modes $\mathbf{H}_1(\mathbf{r})$ and $\mathbf{H}_2(\mathbf{r})$ whose eigenfrequencies are ω_1 and ω_2, where $\omega_1 = \omega_2$, they are said to be degenerate modes.

2.1.2 Symmetry operators

We are now in principle ready to start searching for solutions of the master equation. However, before we do so, we will discuss symmetry. Symmetry is an important topic when dealing with crystals. The reason is that symmetries of a system provide a set of restrictions that reduce the number of modes allowed to propagate in the system. By categorizing a system, based on its symmetries, we can determine the modes of the crystal without having to solve the master equation for each and every one of them.

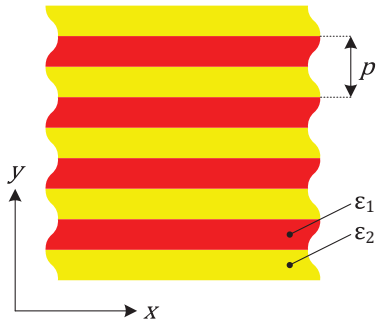

Figure 2.2: One-dimensional photonic crystal, periodic in the y-direction and continuous in the x-direction, composed of two materials with permittivities ϵ_1 and ϵ_2, where $\epsilon_1 \neq \epsilon_2$.

The symmetries of a system can be defined by under which operations a crystal is left invariant. For example, a 1D lattice, as illustrated in Fig. 2.2, has continuous translation symmetry parallel to the material boundaries, and discrete translation perpendicular to the boundaries. Thus, if we displace the crystal by an arbitrary distance in the x-direction, defined by a translation vector $\mathbf{d}$, the crystal looks exactly the same. Similarly, if we displace the crystal by an arbitrary number of periods in the y-direction, defined by a translation vector $\mathbf{R} = Np\mathbf{u}_y$, where N is an integer, the crystal looks exactly the same.

In mathematical terms, these displacement operations can be expressed by operators $\hat{T}_\mathbf{d}$ and $\hat{T}_\mathbf{R}$. When these operate on a function, such as $\epsilon(\mathbf{r})$, they shift the argument by $\mathbf{d}$ and $\mathbf{R}$, respectively: $\hat{T}_\mathbf{d}\epsilon(\mathbf{r}) = \epsilon(\mathbf{r}-\mathbf{d}) = \epsilon(\mathbf{r})$ and $\hat{T}_\mathbf{R}\epsilon(\mathbf{r}) = \epsilon(\mathbf{r}-\mathbf{R}) = \epsilon(\mathbf{r})$. A number of other symmetries can be defined and expressed by their own separate operator, $\hat{S}$. Examples are rotational, inversion, mirror and time-reversal symmetry.

In order to see how symmetries restrict the modes of a given system, we have to relate $\hat{S}$ to solutions of the master equation. We begin by noticing that if a crystal is left invariant under a symmetry operation, then so is the Hermitian operator. In this case, it does not matter if we apply $\hat{\Theta}$, or if we first apply $\hat{S}$, then $\hat{\Theta}$, and finally $\hat{S}^{-1}$:

$$\hat{\Theta} = \hat{S}^{-1}\hat{\Theta}\hat{S} \tag{2.6}$$

A rearrangement of Eq. (2.6) yields $\hat{S}\hat{\Theta} - \hat{\Theta}\hat{S} = 0$. The left hand side of this equation defines the commutator of two operators $\hat{S}$ and $\hat{\Theta}$, denoted $[\hat{S}, \hat{\Theta}]$. The commutator is itself an operator that can be applied to the mode of a system $\mathbf{H}(\mathbf{r})$:

$$[\hat{S}, \hat{\Theta}]\mathbf{H} = \hat{S}(\hat{\Theta}\mathbf{H}) - \hat{\Theta}(\hat{S}\mathbf{H}) = 0 \tag{2.7}$$

This tells us that $\hat{S}(\hat{\Theta}\mathbf{H}) = \hat{\Theta}(\hat{S}\mathbf{H})$. Combining the master equation and Eq.

(2.7), we obtain

$$\hat{\Theta}(\hat{S}\mathbf{H}) = \left(\frac{\omega}{c}\right)^2 (\hat{S}\mathbf{H}),$$

which states that if $\mathbf{H}(\mathbf{r})$ is a mode allowed in the system, then so is the mode $\hat{S}\mathbf{H}(\mathbf{r})$, and these have the same eigenfrequency. Unless the two modes are degenerate, they can only differ by an overall multiplier:

$$\hat{S}\mathbf{H}(\mathbf{r}) = \alpha\mathbf{H}(\mathbf{r}), \tag{2.8}$$

where α is a constant. Hence, provided our system has a certain symmetry, non-degenerate modes not only satisfy the master equation, but also Eq. (2.8) for the corresponding symmetry operator $\hat{S}$.

Since most symmetry operators $\hat{S}$ are less complex than $\hat{\Theta}$, Eq. (2.8) is a useful result. Starting with $\hat{S}$, limiting the possible solutions to those that satisfy Eq. (2.8), and then finding the subset that satisfies the master equation, is usually easier than starting with $\hat{\Theta}$ directly.

2.2 Solving Maxwell's equations

We now have two equations that $\mathbf{H}(\mathbf{r})$ must satisfy before it can be called a mode of our system: $\nabla \cdot \mathbf{H}(\mathbf{r}) = 0$ and $\hat{\Theta}\mathbf{H}(\mathbf{r}) = \left(\frac{\omega}{c}\right)^2 \mathbf{H}(\mathbf{r})$. In addition, we have $\hat{S}\mathbf{H}(\mathbf{r}) = \alpha\mathbf{H}(\mathbf{r})$, which might be useful for determining the form of possible solutions, and for deciding which solutions are unique.

The equation $\nabla \cdot \mathbf{H}(\mathbf{r}) = 0$ suggests that one solution $\mathbf{H}(\mathbf{r})$ takes the form of a sum of plane transverse waves:

$$\mathbf{H}(\mathbf{r}) = \sum_m \mathbf{h}_m e^{i\mathbf{k}_m\mathbf{r}}, \tag{2.9}$$

where $\mathbf{h}_m$ is an amplitude vector and $\mathbf{k}_m$ is a wave vector, and $\mathbf{h}_m \cdot \mathbf{k}_m = 0$. The latter condition is what makes the waves transverse. Since each term $\nabla \cdot \mathbf{h}_m e^{i\mathbf{k}_m\mathbf{r}}$ is equal to zero for any choice of $\mathbf{h}_m$ and $\mathbf{k}_m$ satisfying $\mathbf{h}_m \cdot \mathbf{k}_m = 0$, $\nabla \cdot \mathbf{H}(\mathbf{r})$ must also be zero.

Given a finite space with periodic boundary conditions, the sum in Eq. (2.9) is a general description of $\mathbf{H}(\mathbf{r})$. We can further apply Eq. (2.2) to calculate the electric fields $\mathbf{e}_m e^{i\mathbf{k}_m\mathbf{r}}$, resulting from each of the components $\mathbf{h}_m e^{i\mathbf{k}_m\mathbf{r}}$, and use Eq. (2.3) to show that also $\mathbf{e}_m \cdot \mathbf{k}_m = 0$.

Consequently, we should try to find solutions $\mathbf{H}(\mathbf{r})$ that can be expressed as plane transverse waves, or as a sum of plane transverse waves. As illustrated in Fig. 2.3, for a plane transverse wave with a wave vector $\mathbf{k}_m$, the magnetic field is perpendicular to the electric field, and both fields are perpendicular to the direction of propagation.

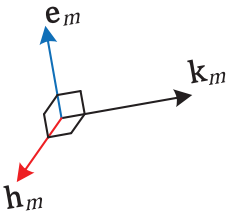

Figure 2.3: Illustration of a plane transverse wave, showing how the orientation of the electric field vector, $\mathbf{e}_m$, is perpendicular to the magnetic field vector, $\mathbf{h}_m$, and both vectors are perpendicular to the propagation vector, $\mathbf{k}_m$

2.2.1 Homogeneous media

The simplest form of a system composed of a dielectric material is homogeneous. The relative permittivity is constant, $\epsilon(\mathbf{r}) = \epsilon$, and it can be shown that all $\mathbf{H}(\mathbf{r}) = \mathbf{h}_m e^{i\mathbf{k}_m \mathbf{r}}$, where $\mathbf{k}_m \cdot \mathbf{h}_m = 0$, are modes of the system. We will derive this for waves with the form

$$\mathbf{H}(z) = he^{ikz}\mathbf{u}_y,$$

i.e. plane waves traveling in the z-direction with a magnetic field of amplitude h oriented in the y-direction. Since a homogeneous medium has continuous rotational symmetry, this is the same as doing the derivation for an arbitrary orientation of $\mathbf{k}_m$ and $\mathbf{h}_m$. Thus, it holds for all $\mathbf{H}(\mathbf{r}) = \mathbf{h}_m e^{i\mathbf{k}_m \mathbf{r}}$. We further note that the system has continuous translation symmetry in all direction, and that the chosen test-function also satisfies the eigenvalue equation defined by the symmetry operator $\hat{T}_\mathbf{d}$:

$$\hat{T}_\mathbf{d} he^{ikz}\mathbf{u}_y = he^{ik(z+d)}\mathbf{u}_y = e^{ikd} he^{ikz}\mathbf{u}_y.$$

The factor e^{ikd} is indeed a constant, and hence $\hat{T}_\mathbf{d}\mathbf{H}(z) = \alpha\mathbf{H}(z)$.

We begin by inserting $\mathbf{H}(z)$ into the master equation:

$$\begin{aligned}
\hat{\Theta}\mathbf{H}(z) &= \left(\frac{\omega}{c}\right)^2 \mathbf{H}(z) \\
\nabla \times \frac{1}{\epsilon}\nabla \times he^{ikz}\mathbf{u}_y &= \left(\frac{\omega}{c}\right)^2 he^{ikz}\mathbf{u}_y \\
\frac{1}{\epsilon}\nabla \times -ikhe^{ikz}\mathbf{u}_x &= \left(\frac{\omega}{c}\right)^2 he^{ikz}\mathbf{u}_y \\
\frac{1}{\epsilon}k^2 he^{ikz}\mathbf{u}_y &= \left(\frac{\omega}{c}\right)^2 he^{ikz}\mathbf{u}_y
\end{aligned} \tag{2.10}$$

Equation (2.10) is only satisfied for certain values of k, namely

$$k = \frac{\omega\sqrt{\epsilon}}{c} = \frac{\omega n}{c} \Rightarrow \omega = k\frac{c}{n} = kc_n, \tag{2.11}$$

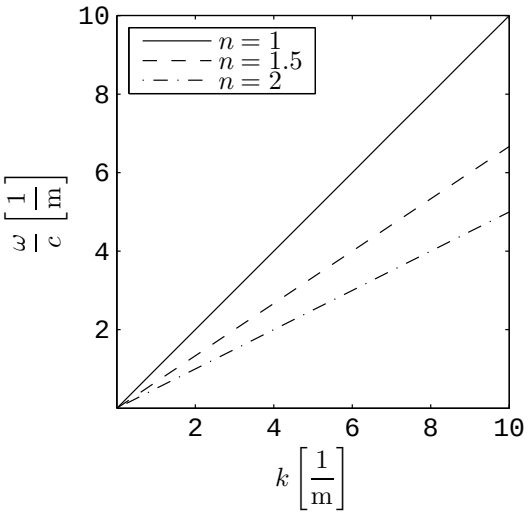

Figure 2.4: Band diagrams, representing the relation between eigenfrequencies ω and the absolute value of the wave vectors k, for three systems composed of a homogeneous material with refractive index $n = 1$, $n = 1.5$ and $n = 2$.

where $n = \sqrt{\epsilon}$ is called the refractive index of the material, and c_n is defined as the speed of light in a material with refractive index n.

In conclusion, in a system with homogeneous permittivity, $\epsilon(\mathrm{r}) = \epsilon$, all modes $\mathbf{H}(\mathrm{r}) = \mathbf{h}_m e^{i\mathbf{k}_m \mathbf{r}}$ are allowed, and have eigenfrequencies determined by the amplitude of the wave vector $k = |\mathbf{k}_m|$. All solutions can be represented in a $\omega(k)$-plot, which is commonly referred to as the band diagram or dispersion relation. Figure 2.4 shows the band diagram for three different homogeneous media, each line representing the relation between k and ω for a given refractive index n. We also notice that since the real fields can be found by

$$\mathbf{H}(z,t) = \Re\left(\mathbf{H}(z)e^{-i\omega t}\right) = h\cos(kz - \omega t)\mathbf{u}_y,$$

k relates to the wavelength through

$$k = \frac{2\pi}{\lambda},$$

where λ is the distance between two consecutive maxima in $\mathbf{H}(z,t)$ at a fixed time t.

2.2.2 Homogeneous slabs

A modification of our system is now made by introducing a second material, as illustrated in Fig. 2.5(a and b). The permittivity in this system, $\epsilon(\mathbf{r})$, can be

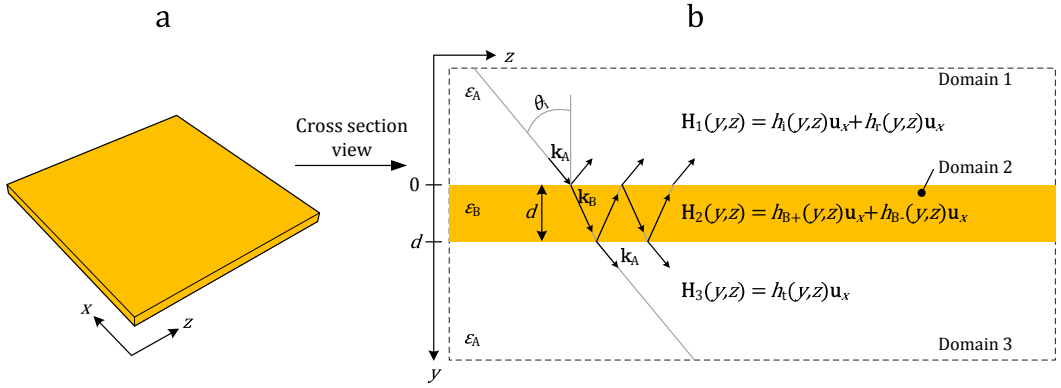

Figure 2.5: (a) Three dimensional illustration of a slab with permittivity ϵ_B and infinite extent in the plane, surrounded by a material with permittivity ϵ_A. (b) Cross section view of the yz-plane, indicating how a plane wave incident from the top with wave vector $\mathbf{k}_\mathrm{A}$ is reflected, transmitted and diffracted at the boundary between the three domains, and couples through the slab by a wave vector $\mathbf{k}_\mathrm{B}$.

expressed as

$$\epsilon(\mathbf{r}) = \epsilon(y) = \begin{cases} \epsilon_\mathrm{B}, & \text{for } -\frac{d}{2} < y < \frac{d}{2} \\ \epsilon_\mathrm{A}, & \text{for } |y| > \frac{d}{2} \end{cases}.$$

Two half infinite domains, domain 1 and 3, composed of material A, with permittivity ϵ_A, are separated by domain 2, composed of material B, with thickness d and permittivity ϵ_B. In other words, the system is composed of a homogeneous slab with thickness d, free-standing in material A. We will assume that $\epsilon_\mathrm{A} < \epsilon_\mathrm{B}$.

Solutions, $\mathbf{H}(\mathbf{r})$, within each domain, still take the same form as in the previous section. They are plane transverse waves, $\mathbf{H}(\mathrm{r}) = \mathbf{h}_m e^{i\mathbf{k}_m \mathbf{r}}$, where $|\mathbf{k}_m| = \omega\sqrt{\epsilon}/c$. The difference is now that in material A, $|\mathbf{k}_m| = |\mathbf{k}_\mathrm{A}| = \omega\sqrt{\epsilon_\mathrm{A}}/c$, whereas in the slab we have $|\mathbf{k}_m| = |\mathbf{k}_\mathrm{B}| = \omega\sqrt{\epsilon_\mathrm{B}}/c$. This means that only a selected set of $\mathbf{k}_\mathrm{A}$ are allowed, given a particular set of $\mathbf{k}_\mathrm{B}$, and vice versa. We must require that the tangential components of the magnetic and electric field are continuous at all boundaries [50]. This is only satisfied if the tangential component of the wave vector for fields propagating in material A equals those propagating in B.

In order to see what this statement implies, we define a magnetic field $\mathbf{H}_\mathrm{i}(y, z)$ incident from domain 1, as illustrated in Fig. 2.5(b):

$$\mathbf{H}_\mathrm{i}(y, z) = h_\mathrm{i} e^{i(k_{\mathrm{A}y} y + k_z z)} \mathbf{u}_x,$$

i.e. a plane wave traveling in the yz-plane with a magnetic field of amplitude h_i oriented in the x-direction, and a wave vector

$$|\mathbf{k}_\mathrm{A}| = |k_{\mathrm{A}y}\mathbf{u}_y + k_z \mathbf{u}_z| = \sqrt{k_{\mathrm{A}y}^2 + k_z^2}.$$

We do not denote the z component of the wave vector by A or B, since it must be equal in all domains.

The incident field is reflected and transmitted at the boundary between domains 1 and 2, resulting in a field propagating upwards in domain 1 and a field propagating downwards in domain 2. The transmitted field reaches the lower boundary between domains 2 and 3, and is again reflected and transmitted, resulting in fields propagating upwards in domain 2 and downwards in domain 3. Denoting the fields in domain 1, 2 and 3 by $\mathbf{H}_1(x,z)$, $\mathbf{H}_2(x,z)$ and $\mathbf{H}_3(x,z)$, we can express them as follows:

$$\begin{aligned}\mathbf{H}_1(y,z) =& h_\mathrm{i} e^{i(k_{\mathrm{A}y}y+k_z z)}\mathbf{u}_x + h_\mathrm{r} e^{i(-k_{\mathrm{A}y}y+k_{\mathrm{A}z}z)}\mathbf{u}_x \\ \mathbf{H}_2(y,z) =& h_\mathrm{B}^+ e^{i(k_{\mathrm{B}y}y+k_z z)}\mathbf{u}_x + h_\mathrm{B}^- e^{i(-k_{\mathrm{B}y}y+k_z z)}\mathbf{u}_x \\ \mathbf{H}_3(y,z) =& h_\mathrm{t} e^{i(k_{\mathrm{A}y}y+k_z z)}\mathbf{u}_x\end{aligned}$$

Referring to Fig. 2.5, we further use that the magnetic and the electric field are continuous at all domain boundaries. The latter condition forces the y-derivative of the magnetic field, multiplied by the inverse relative permittivity, to be continuous:

$$\mathbf{H}_1(0,z) = \mathbf{H}_2(0,z) \Rightarrow h_\mathrm{i} + h_\mathrm{r} = h_\mathrm{B}^+ + h_\mathrm{B}^- \tag{2.12}$$

$$\mathbf{H}_2(d,z) = \mathbf{H}_3(d,z) \Rightarrow h_\mathrm{B}^+ e^{ik_{\mathrm{B}y}d} + h_\mathrm{B}^- e^{-ik_{\mathrm{B}y}d} = h_\mathrm{t} e^{ik_{\mathrm{A}y}d} \tag{2.13}$$

$$\begin{gathered}\frac{1}{\epsilon_\mathrm{A}}\frac{\partial|\mathbf{H}_1(0,z)|}{\partial y} = \frac{1}{\epsilon_\mathrm{B}}\frac{\partial|\mathbf{H}_2(0,z)|}{\partial y} \\ \Downarrow \\ \frac{1}{\epsilon_\mathrm{A}}\left(k_\mathrm{A}h_\mathrm{i} - k_\mathrm{A}h_\mathrm{r}\right) = \frac{1}{\epsilon_\mathrm{B}}\left(k_\mathrm{B}h_\mathrm{B}^+ - k_\mathrm{B}h_\mathrm{B}^-\right)\end{gathered} \tag{2.14}$$

$$\begin{gathered}\frac{1}{\epsilon_\mathrm{B}}\frac{\partial|\mathbf{H}_2(d,z)|}{\partial y} = \frac{1}{\epsilon_\mathrm{A}}\frac{\partial|\mathbf{H}_3(d,z)|}{\partial y} \\ \Downarrow \\ \frac{1}{\epsilon_\mathrm{B}}\left(k_\mathrm{B}h_\mathrm{B}^+ e^{ik_{\mathrm{B}y}d} - k_\mathrm{B}h_\mathrm{B}^- e^{-ik_{\mathrm{B}y}d}\right) = \frac{1}{\epsilon_\mathrm{A}}k_\mathrm{A}h_\mathrm{t}e^{ik_{\mathrm{A}y}d}\end{gathered} \tag{2.15}$$

For a frequency, ω, we can calculate both $|\mathbf{k}_\mathrm{A}|$ and $|\mathbf{k}_\mathrm{B}|$, which equal $\sqrt{k_{\mathrm{A}y}^2 + k_z^2}$ and $\sqrt{k_{\mathrm{B}y}^2 + k_z^2}$, respectively. Chosing a k_z, we can hence also calculate $k_{\mathrm{A}y}$ and $k_{\mathrm{B}y}$. This leaves only four unknows in Eqs. (2.12–2.15), namely h_i, h_r, h_B^+, and h_B^-. Thus, there must exist a unique solution to this system of equations. This means that for a fixed value of ω, modes exist for all k_z from zero to $\omega\sqrt{\epsilon_\mathrm{A}}/c$. Referring to Fig. 2.5, these are waves incident from domain 1, with θ_i from 0 to 90 degrees. They occupy an area in the $\omega(k_z)$-diagram defined by $k_z < \omega\sqrt{\epsilon_\mathrm{A}}/c$, and have been labeled by "Continuum of modes" in Fig. 2.6.

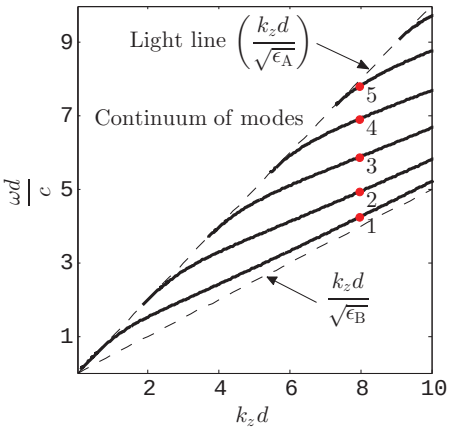

Figure 2.6: Band diagram, black lines representing the traverse magnetic modes of a homogeneous slab. Referring to the model in Fig. 2.5, this example uses $\epsilon_A = 1$ and $\epsilon_B = 4$.

Because a slab has continuous rotational symmetry about an axis normal to the slab surface, and mirror symmetry about the center plane of the slab, the derivation above applies to all plane transverse waves incident on the slab from domain 1 or 3, as long as the field is transverse magnetic (TM). By TM we mean that the magnetic field is normal to the axis of highest symmetry. The axis of highest symmetry is in this case normal to the slab surface, which means that for TM-fields, the magnetic field vector lies in the xz-plane. The other option is transverse electric (TE) fields, where the electric field vector lies in the xz-plane. It is possible to show that also then, a continuum of modes exists for $k_z < \omega\sqrt{\epsilon_\mathrm{A}}/c$ given a particular frequency, ω.

As pointed out in Fig. 2.6, the limit defined by $k_z = \omega\sqrt{\epsilon_\mathrm{A}}/c$ is called the light line. What happens in the case $k_z > \omega\sqrt{\epsilon_\mathrm{A}}/c$? Are there any modes fulfilling this inequality? The answer is yes, and these are so-called fully guided modes. In order to understand what a fully guided mode is, we will use that the component of the wave vector parallel to the domain boundaries must be equal in materials A and B. Mathematically speaking,

$$k_{\mathrm{A}z} = k_{\mathrm{B}z}. \tag{2.16}$$

This is Snell's law. We know that the absolute value of the wave vector in material A, $|\mathbf{k}_\mathrm{A}| = \omega\sqrt{\epsilon_\mathrm{A}}/c$, can be expressed as a function of the absolute value of its components, $k_{\mathrm{A}y}$ and $k_{\mathrm{A}z}$:

$$\frac{\omega\sqrt{\epsilon_\mathrm{A}}}{c} = \sqrt{k_{\mathrm{A}y}^2 + k_{\mathrm{A}z}^2} \Rightarrow k_{\mathrm{A}z}^2 = \frac{\omega^2\epsilon_\mathrm{A}}{c} - k_{\mathrm{A}y}^2 \tag{2.17}$$

From Eq. (2.17), it appears that $k_{\mathrm{A}z}$ is maximized when $k_{\mathrm{A}y} = 0$, and in this case

$k_{\mathrm{A}z} = \omega\sqrt{\epsilon_{\mathrm{A}}}/c$. Since $\epsilon_{\mathrm{A}} < \epsilon_{\mathrm{B}}$, this suggests that Eq. (2.16) can never be satisfied, implying that there are no modes below the light line. However, if we let $k_{\mathrm{A}y}$ be purely imaginary, $k_{\mathrm{A}z}$ can exceed $\omega\sqrt{\epsilon_{\mathrm{A}}}/c$ and still satisfy Snell's law. We can further note that if $k_{\mathrm{A}y} = i\alpha$ is a valid wave vector, where α is a constant, the sign of α can be determined from what is physically possible. The right sign entails that the amplitude of the field decreases exponentially as we move away from the slab in the y-direction. The opposite sign leads to unphysical fields with infinite amplitude far away from the slab.

Defining our coordinate system as shown in Fig. 2.5, and letting α be a positive constant, we can now express all transverse magnetic modes as follows:

$$\begin{aligned}
\mathbf{H}_1(y,z) =& h_1 e^{\alpha y + ik_z z}\mathbf{u}_x, && y < 0 \\
\mathbf{H}_2(y,z) =& h_{\mathrm{B}}^{+} e^{i(k_{\mathrm{B}y} y + k_z z)}\mathbf{u}_x + h_{\mathrm{B}}^{-} e^{i(-k_{\mathrm{B}y} y + k_z z)}\mathbf{u}_x, && 0 < y < d \\
\mathbf{H}_3(y,z) =& h_3 e^{-\alpha y + ik_z z}\mathbf{u}_x, && y > d
\end{aligned}$$

The fields are denominated by numbers 1, 2, and 3, referring to which of the three domains in Fig. 2.5 they inhibit. Examining these equations, we see that these modes propagate in the z-direction, and that the field amplitude decreases exponentially as we move away from the slab in the positive and negative y-direction. In other words, a fully guided mode is bound to the slab. It cannot be coupled to by a plane wave source located in domain 1 or 3, and it will not radiate out into domains 1 and 3.

We further compose a set of boundary conditions, given by the continuity of the tangential component of the magnetic and the electric field. This derivation can be found in numerous textbooks [51, 52], and the resulting conclusion is that modes must obey

$$\left(\cot\left(d\sqrt{\frac{\omega^2\epsilon_{\mathrm{B}}}{c^2} - k_z^2}\right) - \frac{\epsilon_{\mathrm{A}}}{\epsilon_{\mathrm{B}}}\frac{\sqrt{\frac{\omega^2\epsilon_{\mathrm{B}}}{c^2} - k_z^2}}{\sqrt{k_z^2 - \frac{\omega^2\epsilon_{\mathrm{A}}}{c^2}}}\right)^2 - \frac{1}{\sin^2\left(d\sqrt{\frac{\omega^2\epsilon_{\mathrm{B}}}{c^2} - k_z^2}\right)} = 0. \quad (2.18)$$

Solutions of Eq. (2.18) have been found numerically and are plotted in Fig. 2.6 for an example where $\epsilon_{\mathrm{A}} = 1$ and $\epsilon_{\mathrm{B}} = 4$. As seen in the figure, for each value of the z component of the wave vector, k_z, there can be a number of solutions. Solutions along the line with the lowest frequency is called the fundamental mode, the one above is the second order mode, solution along the line with the third lowest frequency, is called the third order mode, and so on. All solutions lie between a line defined by the material in domains 1 and 3, $k_z d/\sqrt{\epsilon_{\mathrm{A}}}$, and a line defined by the slab material, $k_z d/\sqrt{\epsilon_{\mathrm{B}}}$.

Five specific solutions have been marked by numbered red dots in Fig. 2.6. For these five solutions, the absolute value of the magnetic field is plotted as a function

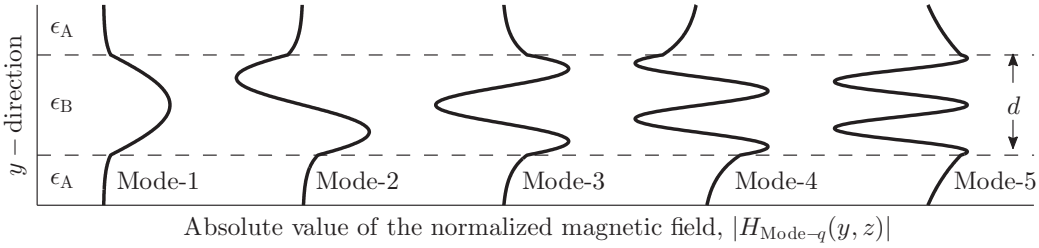

Figure 2.7: Absolute value of the magnetic field, as a function of y, for the five transverse magnetic guided modes with a fixed wave vector k_z, marked by red numbered dots in Fig. 2.6, for $\epsilon_A = 1$ and $\epsilon_B = 4$.

of y in Fig. 2.7. The figure shows how the fundamental mode is symmetric about the center plane of the slab, the second order mode is anti-symmetric, the third is again symmetric, and so forth.

The same derivation can also be carried out for TE-modes. Equation (2.18) then takes a slightly different form, replacing the fraction ϵ_A/ϵ_B by 1. Also, both the electric field and its derivative will be continuous across the boundaries, as oppose to the TM-modes, where the derivative of the magnetic field across boundaries is discontinuous (see Eqs. (2.14) and (2.15)).

Finally, we recall that a slab has continuous rotational symmetry about an axis normal to the slab surface. The derivations above, will hence be identical for any orientation of our axes-system, as long as we keep the y-axis normal to the slab plane. Instead of expressing the guided modes of a slab as a function of k_z, as done in Eq. (2.18), we can use the same equation substituting k_z by β, where $\beta = \sqrt{k_x^2 + k_z^2}$.

2.2.3 Photonic crystal slabs

We now make a second modification of our system, inducing a periodic permittivity in the plane of the slab, as illustrated in Fig. 2.8(a and b). The permittivity in the system, $\epsilon(\mathbf{r})$, can then be expressed as

$$\epsilon(\mathbf{r}) = \epsilon(z) = \epsilon(z + p).$$

From Bloch's theorem [39, 53], we know that possible solutions to the master equation take the form

$$\mathbf{H}_{k_x,k_z}(\mathbf{r}) = e^{ik_x x} e^{ik_z z} \mathbf{u}_{k_z}(y,z), \tag{2.19}$$

where

$$\mathbf{u}_{k_z}(y,z) = \mathbf{u}_{k_z}(y,z+p).$$

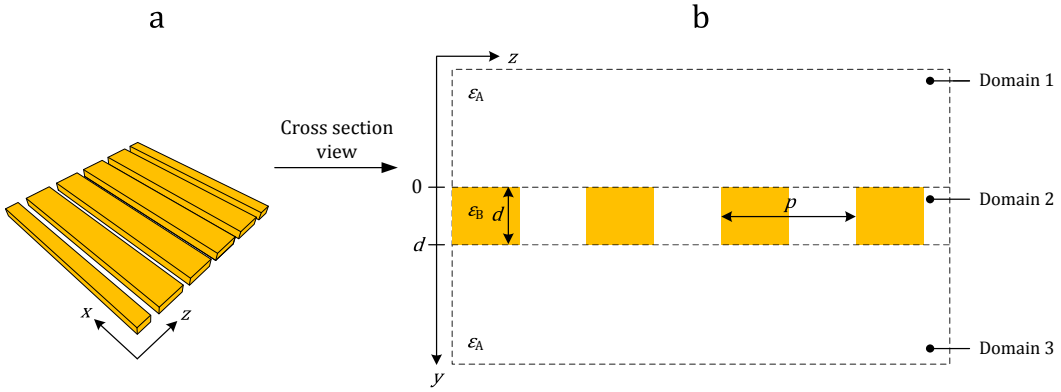

Figure 2.8: (a) Three dimensional illustration of a slab with infinite extent in the plane, and periodic permittivity in the z-direction, $\epsilon(\mathbf{r}) = \epsilon(z) = \epsilon(z+p)$. (b) Cross section view of the yz-plane, pointing out the thickness d, lattice period p, and permittivity of the slab material and its surroundings.

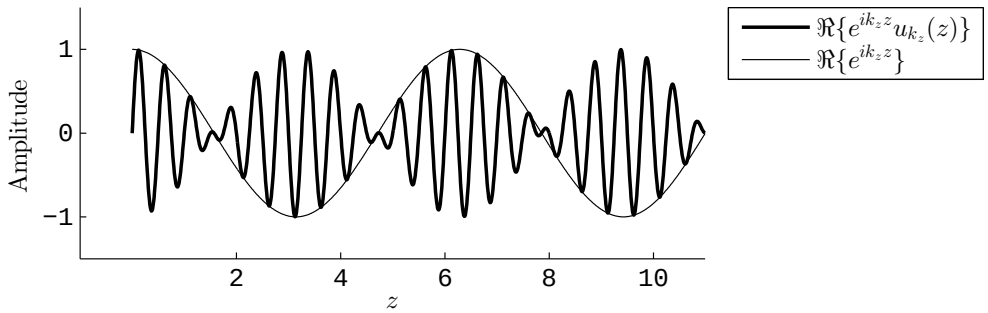

Figure 2.9: The real amplitude of the Bloch function $e^{ik_z z}u_{k_z}(z)$, where $u_{k_z}(z) = \sin(k_p z)$, and $k_p = 4\pi$ and $k_z = 1$.

The physical interpretation of this function is most easily seen when $k_x = 0$. In this case,

$$\mathbf{H}_{k_z}(\mathbf{r}) = e^{ik_z z}\mathbf{u}_{k_z}(y,z) = e^{ik_z z}\mathbf{u}_{k_z}(y,z+p),$$

and the mode can be considered as a wave with wavelength $2\pi/k_z$ in the z-direction, that modulates the amplitude of a field with period p. An example of such a function is illustrated in Fig. 2.9.

Bloch's theorem can be generalized to include systems that have periodic permittivity in both two and three dimensions:

$$\mathbf{H}_{\mathbf{k}}(\mathbf{r}) = e^{i\mathbf{kr}}\mathbf{u}_{\mathbf{k}}(\mathbf{r}) = e^{i\mathbf{kr}}\mathbf{u}_{\mathbf{k}}(\mathbf{r}+\mathbf{R}),$$

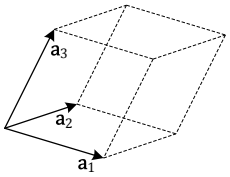

Figure 2.10: Arbitrarily shaped 3D unit cell, defined by the primitive lattice vectors $\mathbf{a}_1$, $\mathbf{a}_2$ and $\mathbf{a}_3$.

for a system with permittivity

$$\epsilon(\mathbf{r}) = \epsilon(\mathbf{r} + \mathbf{R}).$$

Solutions $\mathbf{H}_\mathbf{k}(\mathbf{r})$ satisfying the master equation are usually called Bloch modes or Bloch states.

One useful property of Bloch modes, is that a Bloch mode $\mathbf{H}_\mathbf{k}(\mathbf{r})$ can always be expressed as $\mathbf{H}_{\mathbf{k}+\mathbf{G}}(\mathbf{r})$. The vector $\mathbf{G}$ is a reciprocal lattice vector, defined by

$$\mathbf{G} = l\mathbf{b}_1 + m\mathbf{b}_2 + n\mathbf{b}_3, \tag{2.20}$$

where

$$\mathbf{b}_1 = \frac{2\pi\mathbf{a}_2 \times \mathbf{a}_3}{\mathbf{a}_1 \cdot (\mathbf{a}_2 \times \mathbf{a}_3)}, \quad \mathbf{b}_2 = \frac{2\pi\mathbf{a}_3 \times \mathbf{a}_1}{\mathbf{a}_1 \cdot (\mathbf{a}_2 \times \mathbf{a}_3)}, \quad \text{and } \mathbf{b}_3 = \frac{2\pi\mathbf{a}_1 \times \mathbf{a}_2}{\mathbf{a}_1 \cdot (\mathbf{a}_2 \times \mathbf{a}_3)},$$

the parameters l, m, and n are integers, and the vectors $\mathbf{a}_1$, $\mathbf{a}_2$, and $\mathbf{a}_3$ are the primitive lattice vectors that define the unit cell of the real lattice, illustrated in Fig. 2.10.

By letting $\mathbf{u}_{\mathbf{k}+\mathbf{G}}(\mathbf{r}) = \mathbf{u}_\mathbf{k}(\mathbf{r})e^{-i\mathbf{G}\mathbf{r}}$, we ensure that $\mathbf{H}_\mathbf{k}(\mathbf{r}) = \mathbf{H}_{\mathbf{k}+\mathbf{G}}(\mathbf{r})$. Then, if the modes of a system with permittivity $\epsilon(\mathbf{r}) = \epsilon(\mathbf{r} + \mathbf{R})$ are plotted in a $\omega(\mathbf{k})$-diagram, $\omega(\mathbf{k})$ must be periodic:

$$\omega(\mathbf{k}) = \omega(\mathbf{k} + \mathbf{G}). \tag{2.21}$$

Time reversal symmetry can further be used [39] to show that also

$$\omega(\mathbf{k}) = \omega(-\mathbf{k}).$$

2.3 Guided-resonance modes

With Bloch's theorem in mind, we go back to our homogeneous slab, and the $\omega(\mathbf{k})$-diagram in Fig. 2.6, where the modes of the slab have been plotted for a vector $\mathbf{k} = k_z\mathbf{u}_z$. For simplicity, we consider values of k_z where only the fundamental

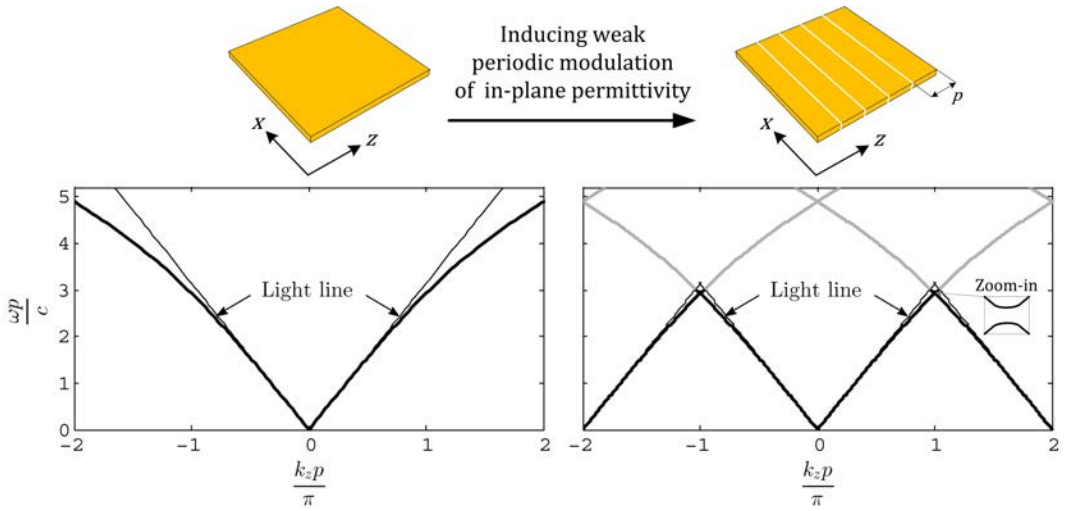

Figure 2.11: (Left) Band diagram of a homogeneous slab with thickness d, composed of a material with permittivity $\epsilon_B = 4$ surrounded by permittivity $\epsilon_A = 1$. Fully guided modes are represented by the thick black lines. The thin black line is the light line. Inducing a weak periodic modulation of the in-plane permittivity with period equal to $p = 10d/3$, we get $\omega(k_z) = \omega(k_z + \frac{2\pi n}{p})$, for an integer n. As long as the modulation is very weak, the resulting band diagram must then resemble a $\frac{2\pi n}{p}$-periodic repetition of the band diagram of the homogeneous slab (right), with small band gaps opening (in-cut right) for $k_z = N\pi/p$, where N is an integer. Modes located above the light line, represented by gray thick lines, are guided-resonance modes.

mode is guided, i.e. small k_z. Next, we construct a 1D PC by introducing a very weak modulation of the permittivity in the plane of the slab in the z-direction, in the form of a p-periodic lattice of slits. Bloch's theorem, then tells us that modes can take the form of Eq. (2.19). Consequently, from Eq. (2.21), it follows that

$$\omega(k_z) = \omega(k_z + \frac{2\pi n}{p}),$$

where n is an integer.

At the same time, since the grating is imposed by a very weak modulation of the in-plane permittivity, the band diagram of the grating should be similar to a homogeneous slab. It turns out that the approximate representation of the band diagram of the 1D PC, can be found by imposing $2\pi/p$-periodicity on the band diagram of a homogeneous slab [48, 49, 54]. This process is shown in Fig. 2.11.

In the right plot in Fig. 2.11, we can observe how the 1D PC still supports fully guided modes, represented by the thick black line below the light line. However,

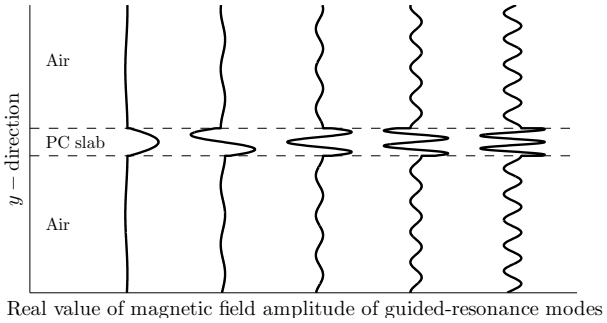

Figure 2.12: Qualitative illustration of the real amplitude of the magnetic field as a function of y in the PC slab illustrated in Fig. 2.8. The field inside the slab resembles a fully guided mode. The field amplitude in domains 1 and 3 is small compared to the field amplitude inside the slab, but does not decrease exponentially as we move away from the slab.

fully guided modes also seem to end up above the light line, represented by the gray thick lines. Modes that are located above the light line cannot be fully guided; it is possible to couple to all modes above the light line from a source placed outside the slab, and vice versa. At the same time, modes represented by the gray thick lines should in some way resemble guided modes. They are a pure mathematical result, induced by a periodic modulation of the permittivity with infinitely small amplitude, and result from folding of fully guided modes.

In conclusion, a new type of modes arises. These are called guided-resonance modes[2] [48, 49], and can intuitively be understood as semi-guided modes: Their power is concentrated in the vicinity of the slab, similar to fully guided modes, but they can also radiate out to the medium surrounding the slab. Referring to Fig. 2.8, the field amplitude in domains 1 and 3 will generally be small compared to the field in the vicinity of the PC slab, but it does not decrease exponentially for $y < 0$ and $y > d$. Qualitative examples of how the real amplitude of the magnetic field of a guided-resonance mode can vary as a function of distance from the slab are given in Fig. 2.12.

As illustrated by the in-cut in the right plot in Fig. 2.11, periodic modulation of the in-plane permittivity leads to small band gaps appearing for every $k_z = N\pi/p$, where N is an integer. This can be explained qualitatively by comparing the two lowest order modes (those with the smallest eigenfrequencies) for $k_z = \pi/p$. These modes have a field profile with period $2p$ in the z-direction. Due to inverse symmetry about the center of a unit cell in the lattice, one of the two modes must

[2]The phenomenon is also described as guided-mode resonance (GMR) in the scientific literature [54]. Communities working with 1D photonic crystal slabs tend to use GMR, while communities working with 2D photonic crystal slabs speak of guided-resonance modes.

have its zero-nodes centered in the unit cell in the slab material, while the other has its zero-nodes centered in the hole material. Consequently, the two modes will see two different effective permittivities, and hence have different eigenfrequencies [39].

Introducing 2D periodic variation of the permittivity, complicates the discussion above slightly, but in general the same line of arguments apply [48, 49]. For a modulation of the in-plane permittivity defined by in-plane lattice vectors $\mathbf{a}_1$ and $\mathbf{a}_3$, the band diagram must be periodic in two dimensions:

$$\omega(\mathbf{k}_1, \mathbf{k}_3) = \omega(\mathbf{k}_1 + l\mathbf{b}_1, \mathbf{k}_3 + n\mathbf{b}_3),$$

where $\mathbf{k}_1$ and $\mathbf{k}_3$ are the wave vector components parallel to unit vectors $\mathbf{a}_1$ and $\mathbf{a}_3$, l and n are integers, and $\mathbf{b}_1$ and $\mathbf{b}_3$ are defined in Eq. (2.20). In the limit where the amplitude of the modulation goes to zero, the band diagram must, as in the 1D case, merge to that of a homogeneous slab. The approximate band diagram of a 2D PC, with very weak modulation of the in-plane permittivity, can be found by performing a 2D folding of the band diagram of a homogeneous slab.

When the modulation amplitude of the permittivity is increased, the band diagram of a homogeneous slab can no longer be used to approximate the band diagram of a 1D or 2D PC. However, guided-resonance modes will still resemble fully guided modes, and the homogeneous slab analog can be used to understand how changes in design parameters will affect eigenfrequencies in general. For example, reducing the permittivity of a homogeneous slab will result in an increase of all eigenfrequencies. This can be seen in Fig. 2.6: The line $k_z d/\sqrt{\epsilon_\mathrm{B}}$, is set by the permittivity of the slab. All guided modes lie between $k_z d/\sqrt{\epsilon_\mathrm{B}}$ and $k_z d/\sqrt{\epsilon_\mathrm{A}}$. If ϵ_B is reduced, $k_z d/\sqrt{\epsilon_\mathrm{B}}$ is increased, and all modes must move towards higher frequencies. Decreasing the permittivity ϵ_B in a homogeneous slab, corresponds to increasing the ratio slit width divided by the lattice period in a 1D PC. We can hence expect a shift of guided-resonance modes towards higher frequencies if we fix the period and increase the slit width. Increasing the permittivity of the material surrounding the PC will generally lead to the opposite effect. Increasing the period in a PC slab will generally cause a shift of modes towards lower frequencies, as the folding of fully guided modes is then done about a smaller in-plane wave vector.

2.4 Photonic crystal slabs modeled as optical resonators

We have now established that a set of semi-guided modes must appear when we impose a periodic modulation of the in-plane permittivity of a slab. These modes lie above the light line, and can therefore be coupled to by a plane wave source

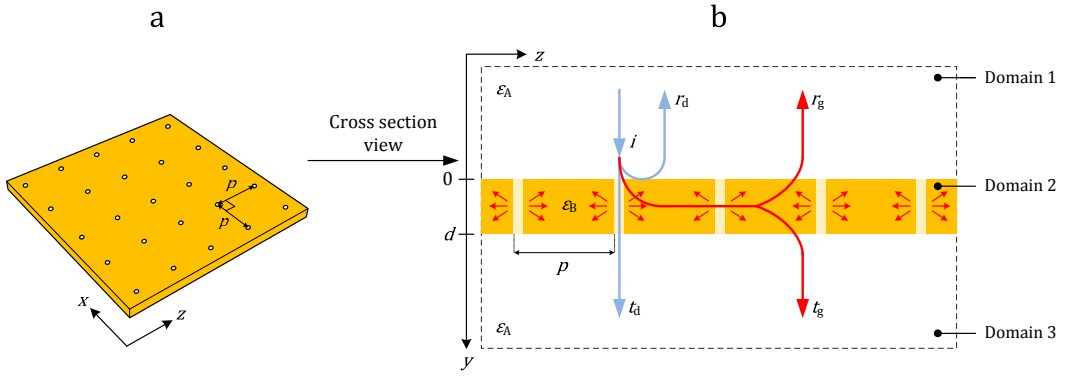

Figure 2.13: (a) Three dimensional illustration of a 2D photonic crystal slab, composed of a square lattice of small holes. (b) A cross section view shows how the holes are imposed on a homogeneous slab with permittivity ϵ_B, surrounded by a lower permittivity, ϵ_A. An incident field with amplitude $i = 1$ is reflected and transmitted, producing a reflected and transmitted amplitude. The illustration shows how the light can take two paths; one similar to that of light in a homogeneous slab, denoted by subscript d, and one resulting from the light coupling into guided-resonance modes, denoted by subscript g.

placed outside the PC. The coupling is in principle an effect of scattering. To understand why, we return to the example where the modulation of the permittivity in the plane of the slab is weak, imposed by a 2D lattice of very small holes.

An incident wave with amplitude $i = 1$ falls onto the PC, as illustrated in Fig. 2.13. Since the holes are small, the light sees a structure that is very similar to a homogeneous slab. The reflected and transmitted amplitude, r and t, can therefore be estimated by deriving r and t as if the slab were homogeneous. We mark these reflection and transmission coefficients by subscript d, indicating that r_d and t_d are the result of a direct path. For most frequencies, the only contribution to the reflected and transmitted amplitude is approximately limited to r_d and t_d. However, the holes in the slab will scatter a small part of the incoming light out in the plane, illustrated by small red arrows on each side of the holes in Fig. 2.13(b). The scattering process represents a second path for the light through the slab, referred to as the indirect path. At selected frequencies, this scattered light can couple to guided-resonance modes. If this happens, a second contribution to the reflected and transmitted amplitude will appear as a result of the radiating field of the guided-resonance mode. This is denoted by r_g and t_g in Fig. 2.13(b).

Figure 2.14 (a) gives an example of what the total reflectance and transmittance might be. The figure shows how the transmittance and reflectance of a PC slab can be viewed as a resonant term, superimposed on an underlying spectrum equal to that of a homogeneous slab with a fitted permittivity. In this example, a

plane wave source with amplitude 1, incident on a PC slab with infinite in-plane periodicity, is scanned across a spectrum of frequencies, while the transmitted and reflected light is recorded. Referring to the band diagram in Fig. 2.11, we are then located above the light line, where multiple guided-resonance modes must be located along a line defined by the k_z-vector of our incident field. To simplify the analysis, we therefore limit the spectrum of frequencies to only overlap with one single guided-resonance mode. We call this mode A, and assume that all other guided-resonance modes do not interfere with mode A. We also assume that the period of the lattice is smaller than the wavelength of the incident light in the material surrounding the PC slab. The latter assumption ensures that we do not have any higher orders of diffraction in the far-field of the slab: All fields far away from the slab propagate in a direction parallel to the incident light.

The equations that form this model are as follows, and are derived from Temporal Coupled Mode Theory [20, 55, 56]:

$$r = r_\mathrm{d} \pm r_\mathrm{g} = r_\mathrm{d}(\omega) \pm f\frac{\gamma_\mathrm{A}}{i(\omega - \omega_\mathrm{A}) + \gamma_\mathrm{A}}, \tag{2.22}$$

and

$$t = t_\mathrm{d} + t_\mathrm{g} = t_\mathrm{d}(\omega) + f\frac{\gamma_\mathrm{A}}{i(\omega - \omega_\mathrm{A}) + \gamma_\mathrm{A}}, \tag{2.23}$$

where ω is the frequency of the incident light, ω_A is the eigenfrequency of mode A, and γ_A is the bandwidth of the mode. The coefficients r_d and t_d are the reflection and transmission coefficients of a homogeneous slab with a permittivity ϵ_fit surrounded by a material with permittivity ϵ_A.

Examining Eqs. (2.22) and (2.23), it is evident that they describe a harmonic oscillator that form anti-symmetric peaks and dips in the reflected and transmitted spectrum of the incident field. These spectral features are called Fano resonances or Fano lines. If the oscillator is lossless, then $f = -(t_d \pm r_d)$: The peaks and dips always go all the way up to one and down to zero, respectively. For a lossy oscillator, $f = -\alpha(t_\mathrm{d} \pm r_\mathrm{d})$, where α is a scalar smaller than one. In this case, the peak and dip amplitude is reduced. The $(\pm)$-sign is determined by the symmetry of the mode providing the terms r_g and t_g. For 1D and 2D PCs supporting guided-resonance modes, the $(+)$ sign applies for modes symmetric about the center plane of the slab, and the $(-)$ sign applies for anti-symmetric modes. Looking at Fig. 2.12, we can see the physical interpretation of the sign. The fields of a symmetric mode, radiating out to the surroundings, are in phase. The radiating fields of an anti-symmetric modes are π out of phase.

In Fig. 2.14 (b), the relation between the form of the dip and the bandwidth, γ_A, and center frequency, ω_A, are pointed out. From the figure, it is clear that the anti-symmetric shape of Fano lines makes it challenging to calculate the Q-factor of a guided-resonance mode directly from the reflected and transmitted spectrum

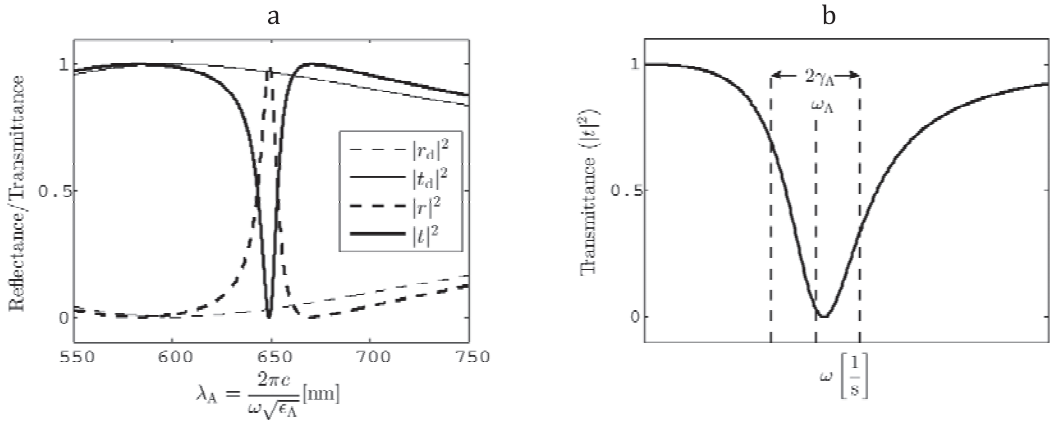

Figure 2.14: (a) Reflectance and transmittance of a PC slab as a function of wavelength, resulting from coupling to a guided-resonance mode, using the model described by Eqs. (2.22) and (2.23). The direct path for normal incidence light, represented by coefficients r_d and t_d, is calculated for a slab of thickness 150 nm with permittivity $\epsilon_\mathrm{B} = 4$, surrounded by permittivity $\epsilon_\mathrm{A} = 1$. Coefficients r and t result from $\gamma = 7.43 \cdot 10^{-5}$ 1/s ($\Delta\lambda = 5$ nm), and center wavelength of $\omega_0 = 650$ nm. (b) The transmittance, t, as a function of frequency, showing how γ and ω_0 relate to the shape of the dip in the transmitted spectrum.

of incident light. However, based on equations (2.22) and (2.23), it is possible to calculate a Q-factor after a fitting procedure:

$$Q = \frac{\omega_\mathrm{A}}{2\gamma_\mathrm{A}}. \tag{2.24}$$

Equation (2.24) is found from the definition of the Q-factor for a harmonic oscillator, which is the ratio of energy stored in the oscillator divided by the energy lost per cycle. This means that high Q-factor guided-resonance modes lead to high field confinement. Moreover, it is evident that high Q-factor guided-resonance modes are supported in PCs that are modeled with a small γ, e.g. where the coupling to the guided-resonance mode from an incident field is weak.

In conclusion, a PC supporting guided-resonance modes can be considered as an optical resonator. Since coupling to guided-resonance modes is fundamentally a scattering effect, the Q-factor can be tuned by adjusting the scattering strength of the PC lattice. For example, for a 2D PC composed of holes imposed on a homogeneous slab, smaller holes lead to larger Q-factors. In theory, the Q-factor of guided-resonance modes can hence be made arbitrarily large by reducing the scattering strength of the PC lattice [48]. In practice, this method of increasing the Q-factor is limited by what is possible to fabricate. Fabrication defects and

limited lattice extent are both factors that introduce loss and limit the achievable Q-factor in real structures [57][**58**].

2.5 Simulation of optical properties of photonic crystals

We have now established a qualitative understanding of what guided-resonance modes are in PCs composed of a weak periodic modulation of the permittivity in the plane of the slab. When the modulation amplitude is increased, the periodic permittivity in the plane of the slab must still produce a periodic band diagram, and as a result guided-resonance modes should appear above the light line. The eigenfrequencies and field profiles of these modes may, however, differ substantially from those of fully guided modes of a homogeneous slab. For 1D PCs, existing analytical models can be utilized [59, 60]. For 2D PCs, as is relevant in this thesis, analytical models are yet to be developed. As of today, the modes of 2D PCs can only be found with the help of simulation tools. Two methods for simulating 2D PCs have been used extensively in this thesis: Rigorous coupled-wave analysis (RCWA) and finite-difference time-domain analysis (FDTD). We will review the basics of the two techniques.

2.5.1 Rigorous coupled-wave analysis (RCWA)

RCWA is applied to find the scattering of an incident plane wave from structures with periodic permittivity, giving an approximate solution by limiting the number of diffraction orders used to represent the field. We will later return to what diffraction orders are. The theory of RCWA was largely established in the 1980's, by M. G. Moharam and T. K. Gaylord [61–63]. Since then, multiple improvements have been made to the technique [64, 65], which now also includes the scattering of incident Gaussian beams [66].

In this thesis, we have only utilized RCWA of plane incident waves, implemented in the commercially available software GD-calc [67]. The software is based on RWCA as presented in [68], and runs on a MatLab platform. The user can define a diffraction grating with a unit cell having arbitrary shape and permittivity, only limited by discretisation of the simulation domain. The first step in performing a simulation is designing the diffraction grating. This is done, as illustrated in Fig 2.15 (a) and (b), by defining a superstrate and substrate with a chosen permittivity, and a set of blocks, with a given permittivity, that define the grating. The incident wave is defined with an arbitrary angle of incidence, and the user sets the number of diffraction orders needed to guarantee a converging result. The computation is thereafter carried out, and the scattered field of an arbitrary

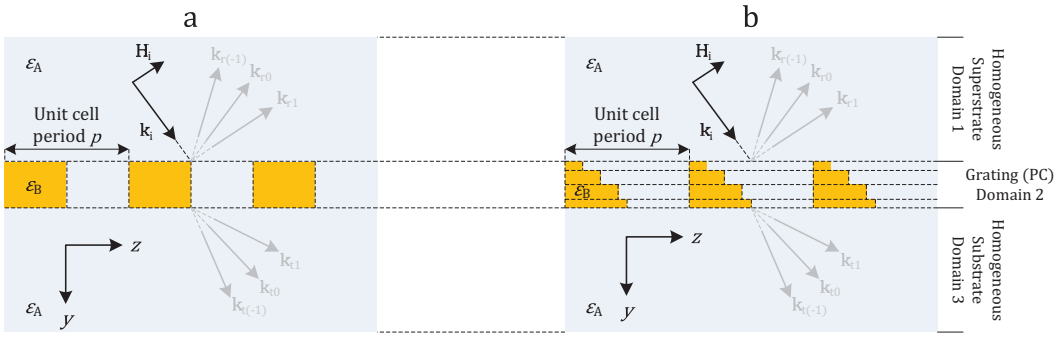

Figure 2.15: (a) Illustration of a 1D-periodic grating. The structure is composed of three domains with parallel boundaries, two domains with homogeneous permittivity above and below a domain with p-periodic permittivity. The field is incident from the superstrate with a defined wave vector $\mathbf{k}_\mathrm{i}$, scattering into three orders of diffraction, $\mathbf{k}_{\mathrm{r}(-1)}$, $\mathbf{k}_{\mathrm{r}0}$, and $\mathbf{k}_{\mathrm{r}1}$. (b) A more complex structure. The top and bottom domains are still homogeneous, and the center domain is composed of 5 sub-domains forming a grating with slanted walls.

polarization of the incident field can be deduced. Fig. 2.15 only illustrates a possible 1D periodic geometry, but the software also allows for 2D periodic gratings.

To review RWCA in detail, we will use the structure in Fig. 2.15 (a) as an example. The incident field is assumed to be TE, having its electric field oriented in the x-direction, and the wave vector oriented as shown in the figure. The incident field can thus be expressed as $\mathbf{E}_\mathrm{i}(y,z) = e_\mathrm{i} e^{i(k_{y1}y+k_z z)}\mathbf{u}_x$. We further denote the field in the superstrate, grating, and substrate, by $\mathbf{E}_1$, $\mathbf{E}_2$, and $\mathbf{E}_3$, and know that solutions in the grating can have the form $\mathbf{E}_2(y,z) = e^{ik_z z}u_{2,k_z}(y,z)\mathbf{u}_x$, where $u_{2,k_z}(y,z) = u_{2,k_z}(y,z+p)$.

Since $u_{2,k_z}(y,z)$ is p-periodic in the z-direction, we can rewrite $\mathbf{E}_2(y,z)$ using Bloch's theorem:

$$\mathbf{E}_2(y,z) = \sum_{n=-\infty}^{\infty} u_{2,k_z,n}(y) e^{i(k_z+\frac{2\pi n}{p})z}\mathbf{u}_x. \tag{2.25}$$

In order for the tangential component of the electric and magnetic field to be continuous at all domain boundaries, the k_z component of all wave vectors in the system must be the same in all regions. Hence, we can express the total field in the superstrate (the medium above the grating, see Fig. 2.15) and substrate as

$$\mathbf{E}_1(y,z) = \sum_{n=-\infty}^{\infty} u_{1,k_z,n}(y) e^{i(k_z+\frac{2\pi n}{p})z}\mathbf{u}_x, \tag{2.26}$$

and

$$\mathbf{E}_3(y,z) = \sum_{n=-\infty}^{\infty} u_{3,k_z,n}(y) e^{i(k_z+\frac{2\pi n}{p})z}\mathbf{u}_x. \tag{2.27}$$

Equations (2.26) and (2.27) can further be substituted into the master equation. We first investigate insertion of Eq. (2.26), and for mathematical convenience we choose to utilize the master equation expressed in terms of the electric field:

$$\nabla^2\mathbf{E}(y,z) = \left(\frac{\omega}{c}\right)^2 \epsilon(\mathbf{r})\mathbf{E}(y,z)$$
$$\Downarrow$$
$$\sum_{n=-\infty}^{\infty}\left(\frac{\partial^2 u_{1,k_z,n}(y)}{\partial y^2} + k_{y1,n}^2 u_{1,k_z,n}(y)\right) e^{i(k_z+\frac{2\pi n}{p})z} = 0, \tag{2.28}$$

where

$$k_{y1,n}^2 = \frac{\omega^2\epsilon_{\mathrm{A}}}{c^2} - \left(k_z + \frac{2\pi n}{p}\right)^2.$$

Equation (2.28) has solutions when

$$\frac{\partial^2 u_{1,k_z,n}(y)}{\partial y^2} + k_{y1,n}^2 u_{1,k_z,n}(y) = 0,$$

concluding that

$$u_{1,k_z,n}(y) = r_{k_z,n} e^{\pm i k_{y1,n} y},$$

where

$$k_{y1,n} = \sqrt{\frac{\omega^2\epsilon_{\mathrm{A}}}{c^2} - \left(k_z + \frac{2\pi n}{p}\right)^2}, \tag{2.29}$$

and $r_{k_z,n}$ are constants.

The only wave traveling with a positive $k_{y1,n}$, is the incident field, with $k_{y1,n} = k_{y1,0}$ and $r_{1,k_z,n} = e_{\mathrm{i}}$. The total field in domain 1, can therefore be expressed as

$$\mathbf{E}_1(y,z) = \left[e_{\mathrm{i}} e^{i(k_{y1,0}y + k_z z)} + \sum_{n=-\infty}^{\infty} r_{k_z,n} e^{-ik_{y1,n}y} e^{i(k_z+\frac{2\pi n}{p})z}\right]\mathbf{u}_x. \tag{2.30}$$

By a similar derivation, the field in domain 3 can be expressed as

$$\mathbf{E}_3(y,z) = \sum_{n=-\infty}^{\infty} t_{k_z,n} e^{ik_{y3,n}y} e^{i(k_z+\frac{2\pi n}{p})z}\mathbf{u}_x, \tag{2.31}$$

where

$$k_{y3,n} = \sqrt{\frac{\omega^2 \epsilon_{\mathrm{A}}}{c^2} - \left(k_z + \frac{2\pi n}{p}\right)^2},$$

and $t_{k_z,n}$ are constants.

The terms in the sums in Eqs. (2.30) and (2.31) are what we refer to as diffraction orders. The 0^{th} order of diffraction in reflection travels in a direction defined by $\mathbf{k}_{1,0} = -k_{y1,0}\mathbf{u}_y + k_z\mathbf{u}_z$, the 1^{st} order of diffraction in a direction defined by $\mathbf{k}_{1,1} = -k_{y1,1}\mathbf{u}_y + k_z\mathbf{u}_z$, the negative 1^{st} order in a direction defined by $\mathbf{k}_{1,-1} = -k_{y1,-1}\mathbf{u}_y + k_z\mathbf{u}_z$, etc. The orders of diffraction in transmission are similarly defined, with a wave vector defined by $\mathbf{k}_{3,n} = k_{y3,n}\mathbf{u}_y + k_z\mathbf{u}_z$.

At this point, we can understand why scattering by a grating with period smaller than the wavelength of the incident field in domains 1 and 3, only yields non evanescent effect in the 0^{th} order of diffraction in reflection and transmission. This is seen by inserting the result in Eq. (2.11) into Eq. (2.29), which yields

$$k_{y1,n} = \sqrt{\frac{\omega^2 \epsilon_{\mathrm{A}}}{c^2} - \left(k_z + \frac{2\pi n}{p}\right)^2} = \sqrt{\left(\frac{2\pi}{\lambda_{\mathrm{A}}}\right)^2 - \left(k_z + \frac{2\pi n}{p}\right)^2}.$$

The parameter λ_{A} is the wavelength of the incident field in domains 1 and 3. Hence, as long as $\lambda_{\mathrm{A}} > p$ and k_z is real, $k_{y1,n}$ will be purely imaginary for any integer $n \neq 0$.

We are left with an infinite set of unknown constants, $r_{k_z,n}$ and $t_{k_z,n}$, defining the amplitudes of the different orders of diffraction in reflection and transmission. For details on how $r_{k_z,n}$ and $t_{k_z,n}$ are found, we refer to the work of M. G. Moharam and T. K. Gaylord [61]. In short, it involves inserting a series expansion of the field in the grating, $\mathbf{E}_2(y, z)$, into the master equation, which results in an infinite set of differential equations that can be formulated as an eigenvalue problem. One further chooses a limited number of equations, bounding the number of diffraction orders retained in the calculation, which allows the eigenvalue problem to be solved by a computer. The number of equations that need to be retained in order to find physically correct approximate solution is grating dependent. In relation to PCs and guided-resonance modes, the number of diffraction orders needed typically increases with the Q-factor of the modes.

Solutions to the eigenvalue problem give a set of eigenvalues that can be used to express the field in the grating in general terms. Boundary conditions further impose that the tangential component of the electric and the magnetic field is continuous at the boundary between domains 1 and 2, and domains 2 and 3. These conditions are used in the final step, solving for constants $r_{k_z,n}$ and $t_{k_z,n}$, and the field inside the grating.

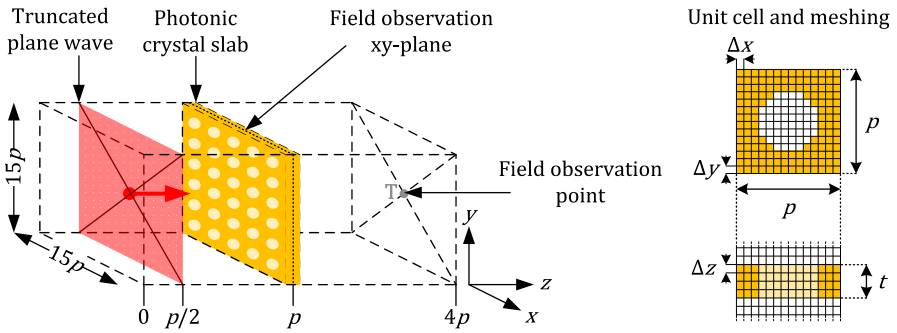

Figure 2.16: Illustration showing an example of a FDTD simulation domain with size $15p \times 15p \times 4p$. A plane wave source and a photonic crystal can be seen inside the domain, as well as observation points and planes, where the field can be recorded as a function of time. A unit cell of the photonic crystal is included to the right, showing how the simulation domain is divided into discrete blocks in space.

2.5.2 Finite-difference time-domain (FDTD) analysis

Where RCWA solves Maxwell's equations in the frequency domain, FDTD takes place in the time domain [69]. All FDTD simulations presented in this thesis have been performed using the commercially available software Optiwave [70]. Using this software, each simulation involves the following steps: First, a simulation domain is composed by defining the outer boundaries of the domain, and choosing a mesh resolution inside the domain. The boundaries can be programmed to be of the perfectly match type (PML). It is also possible to assign periodic boundary conditions, for simulation of infinite structures. A permittivity is thereafter specified at each mesh point, defining what structure is to be simulated. A source is introduced in the system, producing a wave with a chosen form in space and time evolution. In addition, an arbitrary number of observation points and planes can be inserted in the domain. When a simulation is running, the user can record the field in all observation points and planes as a function of time. An example of a typical simulation domain is illustrated in Fig. 2.16.

During a simulation, the electric field at a node at time t_n, where n denotes an arbitrary discrete time step, is calculated based on the electric field in that node at time t_{n-1}, and the magnetic field in neighboring nodes at time t_n. This makes FDTD computationally intensive, especially for large simulation domains with high mesh resolution, where we want to follow the evolution of the field over a long period of time. For smaller simulation domains it is, however, ideal, and produces highly intuitive results. The result of a FDTD simulation allows us to see how the electric and magnetic fields evolve in real time and space. Moreover,

since it is possible to simulate how a pulse propagates through a structure, the frequency response of a structure can be found by taking the Fourier transform of the field as a function of time. In other words, we can investigate many different frequencies in one single simulation run.

Mathematically speaking, FDTD involves a discretisation in time and space, down to a level where the differentials in Maxwell's equations can be replaced by finite differences. We will examine what this means for a structure that is homogenous in the x- and y-direction, $\epsilon(x, y, z) = \epsilon(z)$, for a wave traveling in the z-direction. Maxwell's time-dependent curl equations can then be reduced to

$$\nabla \times E(t,z)\mathbf{u}_x = \mu_0 \frac{\partial H(t,z)\mathbf{u}_y}{\partial t} \Rightarrow \frac{\partial E(t,z)}{\partial z} = \mu_0 \frac{\partial H(t,z)}{\partial t} \tag{2.32}$$

and

$$\nabla \times H(t,z)\mathbf{u}_y = -\epsilon_0 \epsilon(z) \frac{\partial E(t,z)\mathbf{u}_x}{\partial t} \Rightarrow \frac{\partial H(t,z)}{\partial z} = \epsilon_0 \epsilon(z) \frac{\partial E(t,z)}{\partial t}, \tag{2.33}$$

where $E(t,z)$ and $H(t,z)$ are the amplitudes of the electric and magnetic field, respectively, and the differentials can be approximated using the Taylor series [71]

$$f\left(x_0 + \frac{\delta}{2}\right) = f(x_0) + \frac{\delta}{2} \left.\frac{\partial f(x)}{\partial x}\right|_{x=x_0} + \frac{1}{2!}\left(\frac{\delta}{2}\right)^2 \left.\frac{\partial^2 f(x)}{\partial x^2}\right|_{x=x_0} + \cdots \tag{2.34}$$

and

$$f\left(x_0 - \frac{\delta}{2}\right) = f(x_0) - \frac{\delta}{2} \left.\frac{\partial f(x)}{\partial x}\right|_{x=x_0} + \frac{1}{2!}\left(\frac{\delta}{2}\right)^2 \left.\frac{\partial^2 f(x)}{\partial x^2}\right|_{x=x_0} - \cdots . \tag{2.35}$$

Combining Eqs. (2.34) and (2.35), we get

$$\left.\frac{\partial f(x)}{\partial x}\right|_{x=x_0} \approx \frac{f\left(x_0 + \frac{\delta}{2}\right) - f\left(x_0 - \frac{\delta}{2}\right)}{\delta}, \tag{2.36}$$

for small values of δ.

Introducing a discrete z-axis and time line, composed of elements with length Δz and Δt, Eqs. (2.32) and (2.33) can hence be approximated by

$$\frac{E\left(j\Delta t, q\Delta z + \frac{\Delta z}{2}\right) - E\left(j\Delta t, q\Delta z - \frac{\Delta z}{2}\right)}{\Delta z} = \mu_0 \frac{H\left(j\Delta t + \frac{\Delta t}{2}, q\Delta z\right) - H\left(j\Delta t - \frac{\Delta t}{2}, q\Delta z\right)}{\Delta t}$$

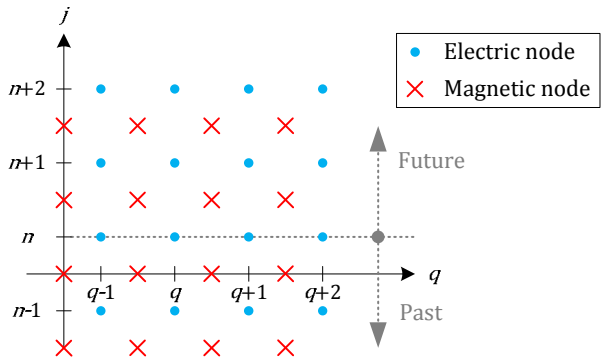

Figure 2.17: Illustration of the Yee mesh [72] in a 1D Finite-Difference Time-Domain simulation. A set of electric and magnetic nodes are defined at discrete points in time and space. The distance between points are Δt and Δz, respectively, and the two sets of nodes are shifted by $\Delta t/2$ and $\Delta z/2$ relative to each other.

and

$$\frac{H\left(j\Delta t, q\Delta z + \frac{\Delta z}{2}\right) - H\left(j\Delta t, q\Delta z - \frac{\Delta z}{2}\right)}{\Delta z} = \epsilon_0\epsilon(q\Delta z)\frac{E\left(j\Delta t + \frac{\Delta t}{2}, q\Delta z\right) - E\left(j\Delta t - \frac{\Delta t}{2}, q\Delta z\right)}{\Delta t},$$

where j and q are integers. We simplify these equations to

$$\frac{E\left(j, q+\frac{1}{2}\right) - E\left(j, q-\frac{1}{2}\right)}{\Delta z} = \mu_0\frac{H\left(j+\frac{1}{2}, q\right) - H\left(j-\frac{t}{2}, q\right)}{\Delta t} \tag{2.37}$$

and

$$\frac{H\left(j, q+\frac{1}{2}\right) - H\left(j, q-\frac{1}{2}\right)}{\Delta z} = \epsilon_0\epsilon(q)\frac{E\left(j+\frac{1}{2}, q\right) - E\left(j-\frac{1}{2}, q\right)}{\Delta t}.$$

A grid of points is further constructed in the zt-plane, where the electric field is evaluated at times $j\Delta t$ and positions $q\Delta z$, and the magnetic field is evaluated at times $j\Delta t + \Delta t/2$ and positions $q\Delta z + \Delta z/2$. This mesh has been named the Yee mesh, after Kane S. Yee and his publication on numerical solutions of Maxwell's equations in isotropic media [72]. The mesh is illustrated in Fig. 2.17, and can be used to express Eq. (2.37) as follows:

$$\frac{E\left(j, (q+1)\right) - E\left(j, q\right)}{\Delta z} = \mu_0\frac{H\left(j+\frac{1}{2}, q+\frac{1}{2}\right) - H\left(j-\frac{1}{2}, q+\frac{1}{2}\right)}{\Delta t},$$

which rearranged says that

$$H\left(j+\frac{1}{2},q+\frac{1}{2}\right)=H\left(j-\frac{1}{2},q+\frac{1}{2}\right)+\frac{\Delta t}{\mu_0\Delta z}\left[E\left(j,(q+1)\right)-E\left(j,q\right)\right].$$

This is the update equation for the magnetic field. It can be applied to any magnetic node, and shows that the magnetic field at a future time $(j+\frac{1}{2})\Delta t$, in position $(q+\frac{1}{2})\Delta z$, only depends on its previous value and the electric field at the neighboring electric nodes. A similar equation can be derived for the electric field, providing the electric field at all electric nodes as a function of its previous value and the magnetic field at the neighboring magnetic nodes. Starting with a fixed set of nodes in the zt-space, and enforcing a field on a subset of the nodes, one can hence track the development of the field in all nodes as function of time. This is easily implemented in a computer, and can also be done in two- or three-dimensional space.

Approximating a differential by a finite difference, as in Eq. (2.36), requires that δ is sufficiently small. The accuracy and stability of the FDTD method depends on the the mesh resolution in time and space. As a rule of thumb, meshing of the space should produce 10 points per wavelength: For a vacuum wavelength, λ_0, corresponding to the highest frequency in the simulation, and ϵ_s being the highest permittivity represented in the simulation domain, the meshing should satisfy

$$\Delta x,\Delta y,\Delta z\leq\frac{\lambda_0}{10\sqrt{\epsilon_\mathrm{s}}}.$$

The Courant-Friedrichs-Levy (CFL) condition [73, 74] can thereafter be used to set an appropriate resolution in time:

$$\Delta t\leq\frac{1}{c_\mathrm{s}\sqrt{\frac{1}{(\Delta x)^2}+\frac{1}{(\Delta y)^2}+\frac{1}{(\Delta z)^2}}},$$

where c_s is the speed of light in the region with permittivity ϵ_s.

The remaining question is how to determine the wavelength λ_0. A harmonic field with vacuum wavelength λ_0 is enforced on a grid of nodes by ramping up the field amplitude, starting from zero field at time $t=0$, until one reaches the desired field amplitude at time $t=t_1$. In theory, all frequencies are then represented, and a small t_1 leads to a broad banded signal. The influence of components corresponding to vacuum wavelengths smaller than λ_0, will typically die out with time. However, if the field is ramped up too fast, this time can be impractically long, and even lead to instabilities causing unphysical results. A second rule of thumb is therefore to restrict the rate at which the field is ramped up. Figure 2.18 illustrates suggested ramping times for a continuous source and a Gaussian pulse simulation.

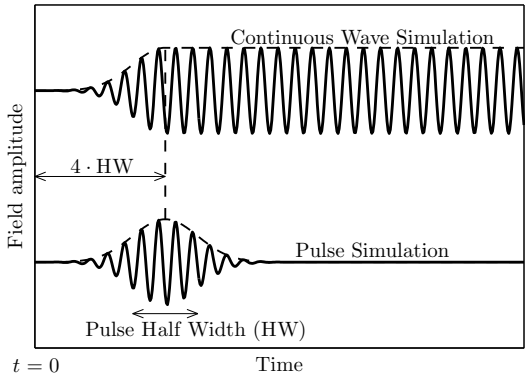

Figure 2.18: The induced field as a function time at nodes in a FDTD simulation, illustrating suggested ramping times for a continuous source and Gaussian pulse simulation.

2.6 Fabrication of photonic crystal slabs

The PCs made in this thesis were fabricated using standard micro-fabrication techniques, which have been reviewed in detail in several textbooks [75–77]. The following techniques were used extensively: Low pressure chemical vapor deposition (LPCVD), optical lithography, electron-beam (E-beam) lithography, reactive ion etching (RIE) and wet etching by Tetra Methyl Ammonium Hydroxide (TMAH).

All PCs have been made using one of two different process flows, named P1 and P2. Process P1 is summarized in Fig. 2.19, while P2 is described in detail in [**58**]. In this section, we give a short overview of the above mentioned fabrication techniques, and relate them to the two different process flows.

2.6.1 Thin film deposition

Both processes P1 and P2 start with a double-side-polished Si wafer, with a $\langle 100 \rangle$ crystal oriented surface, as shown in step 1 in Fig. 2.19. The second step is LPCVD of Si_3N_4, followed by LPCVD of poly-Si and thermal oxidation, and finally LPCVD of Si_3N_4. This forms a three layered stack of Si_3N_4 and SiO_2 on both sides of the wafer, as shown in step 2 in Fig. 2.19. Double-side-polished wafers are used because lithography is performed on both sides of the wafer.

LPCVD is carried out in a furnace, where wafers are exposed to volatile precursors that react on the wafer surface and form solid thin films. For dielectrics like Si_3N_4 and SiO_2, LPCVD in combination with thermal oxidation yields high quality thin films with stoichiometric composition, virtually zero loss, and predictable permittivity. Low roughness can also be achieved, especially for Si_3N_4. For SiO_2, which starts with deposition of poly-Si and is followed by thermal oxidation, the

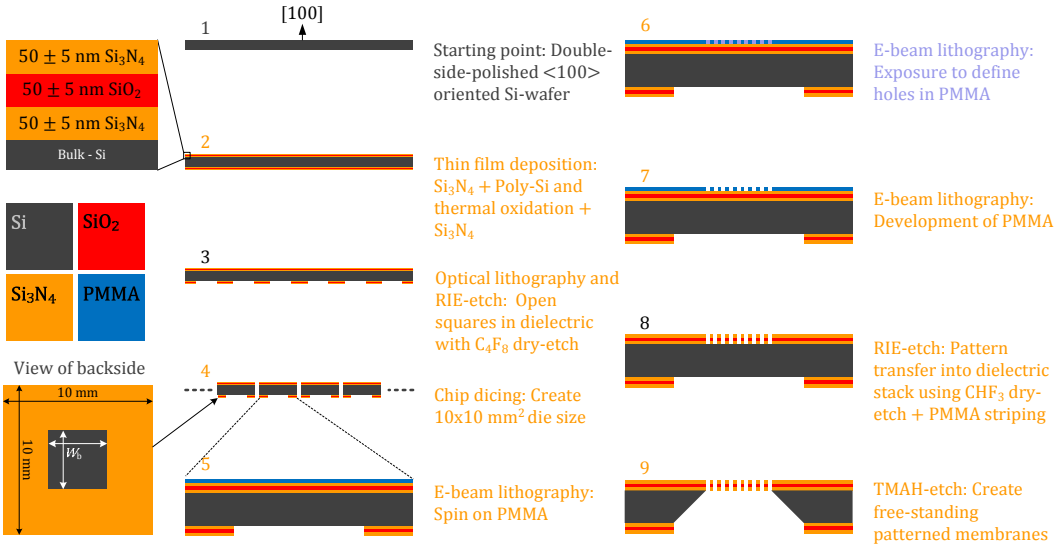

Figure 2.19: Steps involved in the fabrication of a free-standing photonic crystal membrane.

roughness is limited by the grain size of the poly-Si. The roughness of our final thin film stack has not been accurately measured, but based on optical measurements and fabrication experience, the thickness is estimated to vary with less than 5 nm over a 100 mm diameter wafer.

A number of choices for volatile precursors are available. In our process we have used the following reactions to create Si_3N_4 and poly-Si, respectively:

$$3\ SiCl_2H_2(s) + 4\ NH_3(g) \rightarrow Si_3N_4(s) + 6\ HCl(g) + 6\ H_2(g)$$

and

$$SiH_4(g) \rightarrow Si(s) + 2\ H_2(g),$$

where g and s indicates whether the compound is in a solid or gas state. Si_3N_4 was deposited at a temperature of 770 °C, the poly-Si at 620 °C, and the thermal oxidation was performed at 900 °C.

Thin films of LPCVD Si_3N_4 and SiO_2 have tensile and compressive residual stress, respectively. The resulting stress in our thin film stack has not been measured, but it is evident from the properties of our final devices that the total stress is dominantly tensile. The finished, free etched chips, show no signs of curving of membrane if the membrane area does not exceed[3] 700×700 μm^2. Moreover, the membranes are structurally strong. Membranes with areas up to 300×300 μm^2

[3]This is largest membranes that we have made.

have been proven to withstand pressures of 0.5 bar, and have survived accidental drops to the ground from a height of up to 100 cm.

2.6.2 Optical lithography

Following the thin film deposition step, a 2D square grid of openings with period 10 mm is made in the thin film stack on one side of the double-side-polished wafers (step 3, Fig. 2.19). We will refer to this side of the wafer as the backside, as indicated in step 4 in Fig. 2.19. Depending on the desired membrane area resulting from a following TMAH-etch, the openings measure from 500-2000 μm along their sides.

Openings of this size are easily made using standard optical lithography: A resist sensitive to visible light is spun on one side of the wafer. The resist is baked, in order to cure, and thereafter exposed to light through a mask defining the pattern in the resist. The parts of the resist that have been exposed to light are removed in a solution of developer[4], and we are left with openings in the resist that frame the desired openings in the three thin films (see Fig. 2.19, step 4).

2.6.3 Reactive ion etching (RIE)

The resist functions as mask in the following RIE-step, where the square pattern is transferred into the three thin films of Si_3N_4 and SiO_2. Finally, the resist is removed, and the wafer is diced into chips of 10×10 mm^2, leaving us with chips with a cross section as shown in step 5 in Fig. 2.19.

In contrast to wet etches, like TMAH, which will be discussed later on, RIE is done dry. Various forms of plasma can be generated in vacuum by an electromagnetic field, creating charged particles that can attack the surface of the wafer or chip, producing volatile etch products that are carried away from the surface.

RIE can be both chemical and physical. In chemical RIE, the removal of surface material is induced by a chemical reaction between the surface material and the plasma. In physical RIE, the plasma is accelerated towards the surface, bombarding the surface with particles that sputter away material. Chemically controlled RIE can give isotropic etches and be highly selective, while physical etches are typically anisotropic and less selective.

In process P1 and P2, reactive ion etching has been done using a plasma made of either C_4F_8, CF_4 or CHF_3. All of these plasma are dominantly physical when etching Si_3N_4 and SiO_2, and create anisotropic etch profiles. An example of the

[4]Applies to so-called positive resists. For negative resists, areas that are not exposed to light will be removed in a solution of developer.

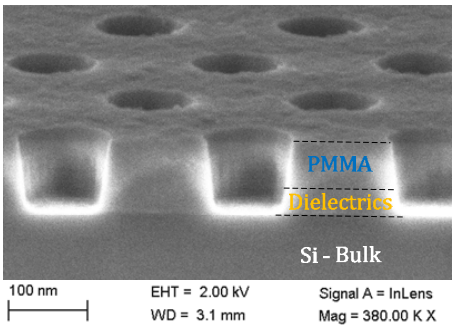

Figure 2.20: Image of holes etched in a thin film stack of 50nm Si_3N_4/50nm SiO_2/50nm Si_3N_4, using reactive ion etching with CHF_3-plasma and a PMMA resist. The image is taken with a scanning electron microscope, and shows that the etch is anisotropic.

etch profile of small holes etch through our dielectric stack, resulting from RIE using CHF_3-plasma, is shown in Fig. 2.20.

2.6.4 Electron-beam (E-beam) lithography

This is the stage in the process flow at which P1 and P2 separate. In P1, E-beam lithography is done on the front side of the individual chips to form the PCs, while the three thin films are still supported by an underlying substrate of silicon. In P2, E-beam lithography is done on the three thin films after they have been etched to a free-standing membrane. We will explain how the membranes are etched to become free-standing in section 2.6.5.

The PC is composed of a square lattice of holes with radius and period in the order 100 nm and 500 nm, respectively. These dimensions can typically not be attained using optical lithography. Thus, alternative methods such as UV or deep UV lithography, E-beam lithography, nano-imprint lithography or scanning probe lithography [**58**], must be applied. In our proof of principle study, the choice has been E-beam lithography. In a final product other techniques should be applied due to the relatively high cost and low efficiency of E-beam lithography.

Standard E-beam lithography was performed in process P1, as summarized by steps 5–8 in Fig. 2.19: The method starts, as for optical lithography, by spinning on a layer of resist. Rather than being sensitive to light, E-beam resist is sensitive to electrons. We have used a common resist made of Poly Methyl Methacrylate (PMMA), which is popular due to its high patterning resolution, reaching down to ∼10 nm [78]. After the resist is cured by a bake, a focused electron beam writes a computer defined pattern directly on the resist. Areas of the resist exposed to electrons are resolved in a developer solution, and the pattern is finally transferred

into the thin film stack by RIE. This makes E-beam lithography a mask less technique, ideal for defining multiple variations of a design in a highly effective manner.

The same property is also a disadvantage with respect to the time of manufacture per pattern feature. Writing-times are proportional to the size of the pattern. Moreover, the write field of an E-beam tool is limited by how much the electron beam can be deflected. For high resolution writing, typical write fields are in order of 100×100 μm^2. Structures larger than the write field are obtained by moving the substrate. The alignment of adjacent write fields is, however, not always accurate enough for the manufacturing of PCs. Structural inaccuracies will be present at the boundaries of adjacent write fields. These inaccuracies are called stitching errors, and can give unwanted optical properties.

An example of the optical effect of a stitching error is shown in Fig. 2.21. An image of a 2D PC has been recorded with an optical microscope, using a light source that is tuned to a wavelength where the PC is highly reflective due to coupling to a guided-resonance mode. The source is incident on the backside of the PC, while the transmitted light is magnified and projected onto a 2D CCD detector. Hence, the image represents the transmittance of the PC with spatial resolution. The stitching error is seen as a low transmission line crossing the membrane in the horizontal direction.

A second disadvantage of E-beam lithography, especially present when exposing dielectric materials, is charging effects. Since dielectrics in general are poor conductors, electrons cannot be transported away from the substrate efficiently. This results in charging of the sample surface during exposure, which can deflect the electron beam and reduce the patterning accuracy. Charging effects can be reduced by coating the sample with a conductive layer, as described in [**58**]. Moreover, when accelerated electrons hit the sample surface, they will scatter and produce secondary electrons. Electrons that travel all the way through the resist can also back-scatter from the substrate. Especially for thick resists and exposure of holes, this will result in a hole radius that increases as a function of distance from the top surface of the resist. For an accurate definition of nominal hole radius, the resist is therefore required to be thin. A thin resist is not necessarily a problem. However, since RIE recipes used for etching dielectrics like Si_3N_4 and SiO_2, also etch PMMA quite aggressively, the achievable aspect ratio in final structures can be limited. Higher aspects ratios can be achieved by using a more complex E-beam lithography procedure, utilizing multi-layered etch masks [**58**][79, 80].

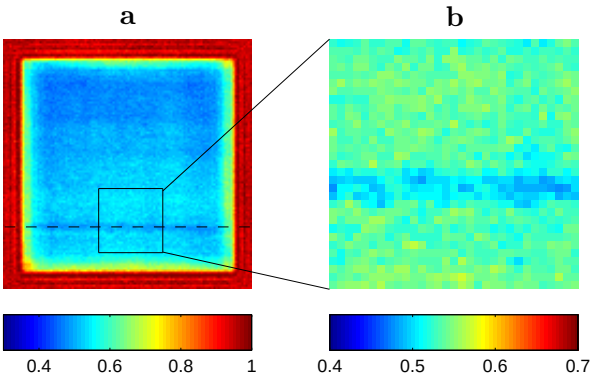

Figure 2.21: (a) False-color image of the transmittance of a 2D PC, composed of a square lattice of 100×100 holes with a period of 500±5 nm and radius 150±10 nm, etched in a thin film stack of 50±5 nm Si_3N_4/50±5 nm SiO_2/50±5 nm Si_3N_4. The image is a recording of the front side of the crystal using a standard optical microscope. The source is a normal incidence collimated beam illuminating the backside of the PC at 644 nm, tuned to a frequency where the incident light can couple into a guided-resonance mode. (b) A distinct line of low transmission, crossing the image in the horizontal direction, can be observed. This is caused by misalignment of adjacent write fields during exposure in E-beam lithography, and is referred to as a stitching error or stitching effect.

2.6.5 Wet etching by Tetra Methyl Ammonium Hydroxide (TMAH)

In both processes P1 and P2, the thin film stack is etched to become a free-standing membrane by a 10 second dip in 2.5% HF, followed by a longer exposure to 25% TMAH. At 70-80 °C, TMAH etches Si in the ⟨100⟩-direction at rate a of ∼100-200 µm/h, while having a high selectivity to the ⟨111⟩-direction (∼100-200 nm/h), and a very high selectivity to Si_3N_4 and SiO_2 (∼1-5 Å/h). The selectivity to the ⟨111⟩-orientation is what produces the characteristic plane surfaces in a TMAH etch. This can be recognized on our chips. A detailed view of the cavity cross section after step 9 in Fig. 2.19, is given in Fig. 2.22. The illustration shows how the resulting size of the free-standing membranes, denoted W_m, is determined by the size of the opening in the dielectric stack on the backside of the wafer, W_b, the thickness of the wafer, t_w, and the ratio of etch rates in crystal directions ⟨100⟩ and ⟨111⟩.

To reduce the risk of contamination, the PC is not covered by an etch resistant protective layer in process P1. Both sides of the chip are exposed during the TMAH-etch. Although the selectivity to Si_3N_4 is very high, this results in the PC being altered from the nominal design. All wafers used in this thesis have been of

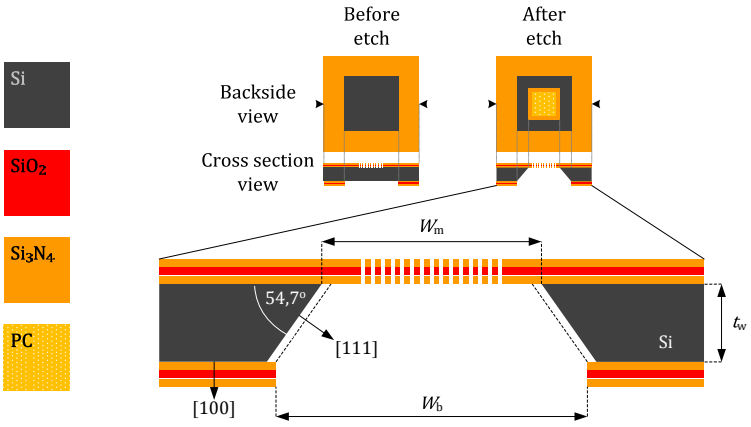

Figure 2.22: Illustration showing the result of the wet TMAH-etch in step 7 in Fig. 2.19. The size, W_{m}, of the free-standing membranes, is determined by the size of the opening on the backside etch mask, W_{b}, the thickness of the wafer, t_{w}, and the ratio of etch rates in crystal directions $\langle 100 \rangle$ and $\langle 111 \rangle$.

thickness 200-300 µm, and the etch times in TMAH have been in the order of 10 hours. The top silicon nitride thin film is consequently reduced by a thickness of about 1-5 nm in the TMAH etch, and we also expect the holes to have rounded edges. These unwanted side-effects of process P1 have not been investigated in detail, but based on a comparison between simulations and optical measurements, it is evident that they are optically significant. Initially, this is why the alternative approach presented in [**58**] was developed, where the TMAH etch is done prior to the definition of the PC. A comparison of the optical properties of PCs resulting from the two different fabrication processes has, however, not shown any significant difference in terms of PC quality. We believe that this is due to limitations in our optical setups. These limitations will be discussed in chapter 4, where we describe how our PCs have been optically characterized.

Chapter 3

Particle detection using photonic crystals

The transducer developed in this thesis can detect small changes in permittivity. It is a 2D photonic crystal (PC), and specifically detects small permittivity changes in the form of particles. In essence, our detection method utilizes PCs supporting guided-resonance modes to amplify the scattered irradiance from particles trapped in the lattice. In this chapter, we review what makes this possible. We will also discuss the difference between detecting an overall change in permittivity on the surface of a PC, and detecting a change that is locally bound. The chapter further covers an introduction to small particle Rayleigh scattering theory, including a basic review of techniques used to minimize the background noise in systems used to detect scattered irradiance from small particles.

3.1 Detecting overall changes in permittivity with photonic crystals

Consider a PC with infinite in-plane 2D-periodicity, composed of holes etched through a homogeneous slab, as shown in Fig. 3.1(a). Assume that the PC lies in a domain with homogeneous permittivity, ϵ_{A}, and that the PC supports a guided-resonance mode at a frequency ω_{A}. This mode is coupled to by a plane wave with normal incidence, yielding a dip in the transmitted spectrum, as shown by the solid black line in Fig. 3.1(c). We further imagine that a small particle is inserted into every hole in the PC lattice, as shown in Fig. 3.1(b), and ask the question: What happens to the transmitted spectrum?

Assuming that the permittivity of the particle is different from ϵ_{A}, the effective permittivity of the PC slab will change. Thus, using the homogeneous slab analog, the eigenfrequencies of the slab modes must change. Consequently, the guided-

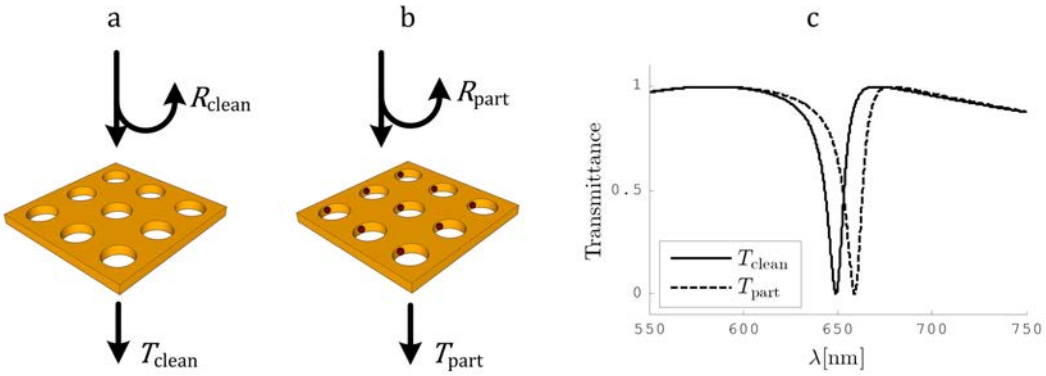

Figure 3.1: Qualitative example showing how the transmittance is affected by placing particles in every hole of a 2D-photonic crystal with different permittivity than the material surrounding the crystal. (a) 3×3 unit cells of a pristine 2D-photonic crystal, with an incident field being reflected and transmitted. (b) The same photonic crystal with a small particle trapped in every hole. (c) Plots, showing the difference in transmittance between the two crystals, as a function of wavelength.

resonance mode frequency, ω_{A}, will also change, and induces a shift in dip position in the transmitted spectrum, as shown in Fig. 3.1(c).

Using perturbation theory, it can be shown that the relative change $\Delta\omega_{\text{A}}/\omega_{\text{A}}$, caused by a small change in permittivity, $\Delta\epsilon(\mathbf{r})$, is dependent on the relative change in permittivity, $\Delta\epsilon(\mathbf{r})/\epsilon(\mathbf{r})$, and is most significant when $\epsilon(\mathbf{r})$ changes in volumes with strong electric fields [39]:

$$\frac{\Delta\omega_{\text{A}}}{\omega_{\text{A}}} \approx -\frac{1}{2}\frac{\int \Delta\epsilon(\mathbf{r})|\mathbf{E}(\mathbf{r})|^2 d^3\mathbf{r}}{\int \epsilon(\mathbf{r})|\mathbf{E}(\mathbf{r})|^2 d^3\mathbf{r}} \tag{3.1}$$

From Eq. (3.1), we see that $\Delta\omega_{\text{A}}/\omega_{\text{A}}$ is insensitive to changes in permittivity in volumes where the electric field is weak. Intuitively, this is reasonable. Such volumes are dark. In order to see changes in permittivity in a volume, the volume must be illuminated.

The optical spectra of PCs can be measured. This can be done in a number of different ways. If the incident light is broad band, interferometers can be used to plot the transmitted light as a function of wavelength. Alternatively, the source can be a laser tuned to the dip position of the pristine PC. Introducing a different permittivity in the system will then increase the transmittance of the PC, which can be detected by a charge-coupled device (CCD). Angle sensitive measurement setups can also be applied. In this way, PCs allow for permittivity sensing, which is more commonly referred to as refractive index sensing. Eq. (3.1) tells us that

these sensors can be optimized by concentrating the field where the change in permittivity will occur.

The property that PCs support guided-resonance modes is popularly exploited in photonic crystal biosensors [9, 36, 37, 81]: A PC is designed to be sensitive to changes in permittivity at its surface, and have an optical spectra with characteristic features that can be monitored by a detector. One example of a feature can be a narrow banded dip in transmittance, similar to the ones shown in Fig. 3.1(c). The PC can be used as a biosensor if the surface is functionalized to capture specific targeted molecules. When the PC is exposed to a sample containing target molecules, a mono-layer of target molecules will settle on the PC surface. If the permittivity of the mono-layer differs from that of the surrounding material, a shift of the center wavelength of the dip can be detected.

3.2 Detecting local changes in permittivity with photonic crystals

Using a scheme similar to the one described above, the PC sensor developed in this thesis can be used to detect overall changes in permittivity on the PC surface. However, our aim has been to reach sensitivities on the order of single molecules. Naturally, single molecules cannot be considered to be a continuous layer covering the entire surface of the crystal. Captured target molecules should rather be considered as locally bound defects that break the symmetry of the lattice. Defects induce local shifts in the frequency of resonant modes, and provide new exit channels for light semi-bound in the guided-resonance mode **[24, 25]**.

Rather than monitoring the overall transmittance of a membrane, we have chosen to design an optical setup that measures the transmittance with spatial resolution. For an incident source tuned to a wavelength where the light couples into a guided-resonance mode, the pristine PC functions as a mirror. Defects in the lattice appear as bright spots, centered at the origin of the defect, on a dark background.

As reported in our published works **[24, 25, 82, 83]**, the behavior of single particles trapped in photonic crystals can be understood as amplified small particle Rayleigh scattering theory. An illustration explaining this model is given in Fig. 3.2: As long as the particle is small enough, the guided-resonance modes will not be affected by the particle, and nearly 100% of the light will be reflected. Simultaneously, the particle will be located in a strong electromagnetic field. The particle will scatter this high field, creating spherical waves that escape and propagate away from the slab. The scattered irradiance can be focused onto a CCD detector by a lens system, and will appear on the screen as a bright spot on a dark surface.

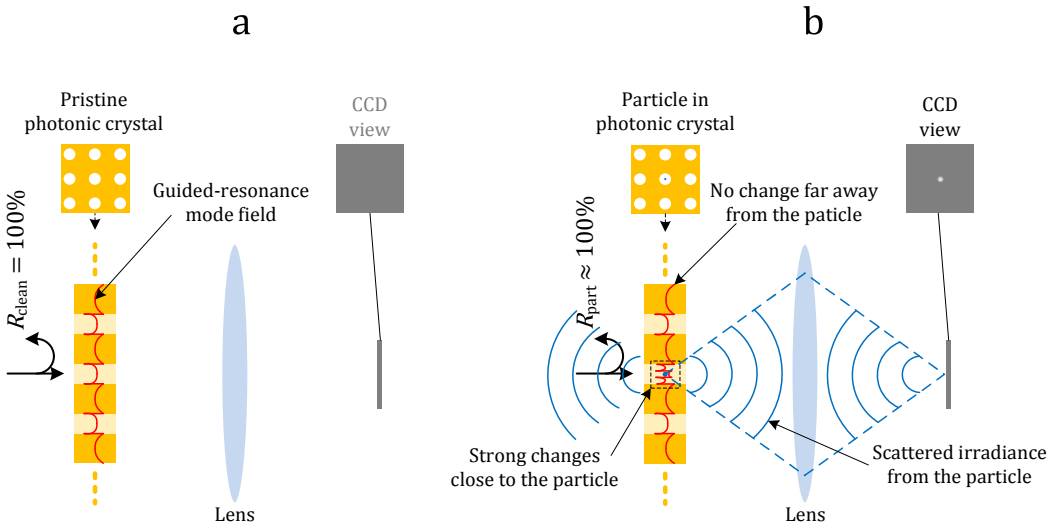

Figure 3.2: (a) Pristine 2D-photonic crystal functioning as a mirror due to coupling of incident light into a guided-resonance mode. (b) A particle is inserted into the crystal lattice. The particle scatters the field supported by the guided-resonance mode. The scattered irradiance is focus onto a CCD screen, causing the particle to appear as a bright spot on the screen.

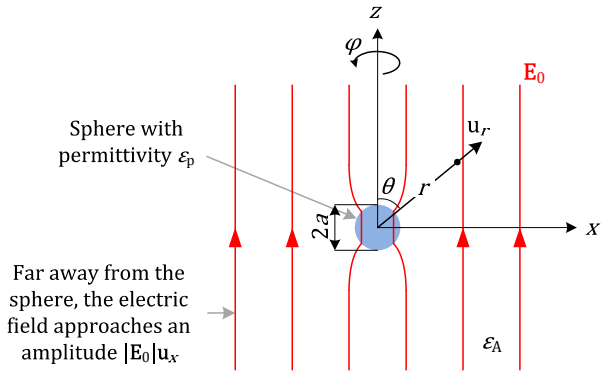

Figure 3.3: Dielectric sphere in uniform static electric field.

3.2.1 Dielectric sphere in static electric field

Small particle Rayleigh scattering is best understood by starting with the example of a homogeneous sphere placed in a uniform static electric field. This system is illustrated in Fig. 3.3. The sphere has permittivity ϵ_p and is surrounded by a homogeneous medium with permittivity ϵ_A.

We first note that the symmetry of the problem ensures that the fields must be

independent of φ. The electric field, $\mathbf{E}(r,\theta)$, can hence be defined by the electric field inside, $\mathbf{E}_\mathrm{p}(r,\theta)$, and outside the sphere, $\mathbf{E}_\mathrm{A}(r,\theta)$, and expressed as a function of the scalar potentials $\Phi_\mathrm{p}(r,\theta)$ and $\Phi_\mathrm{A}(r,\theta)$:

$$\mathbf{E}(r,\theta) = \begin{cases} -\nabla\Phi_\mathrm{p}(r,\theta), & \text{for } r < a \\ -\nabla\Phi_\mathrm{A}(r,\theta), & \text{for } r > a \end{cases} \tag{3.2}$$

Given that there are no free charges present, Laplace's equation further requires that

$$\nabla^2\Phi_\mathrm{p}(r,\theta) = \nabla^2\Phi_\mathrm{A}(r,\theta) = 0, \tag{3.3}$$

and the boundary conditions at $r = a$ are

$$\Phi_\mathrm{p}(a,\theta) = \Phi_\mathrm{A}(a,\theta), \tag{3.4}$$

and

$$\epsilon_\mathrm{p}\frac{\partial\Phi_\mathrm{p}(a,\theta)}{\partial r} = \epsilon_\mathrm{A}\frac{\partial\Phi_\mathrm{A}(a,\theta)}{\partial r}. \tag{3.5}$$

Since the sphere is a passive element, we can assume that as we approach the limit $r \to \infty$, the electric field points in the z-direction and has amplitude $E_0 = |\mathbf{E}_0|$:

$$\lim_{r\to\infty} \Phi_\mathrm{A}(r,\theta) = -E_0 r\cos\theta = -E_0 x \tag{3.6}$$

A possible solution satisfying Eqs. (3.2–3.6) is given by the following two expressions for $\Phi_\mathrm{p}(r,\theta)$ and $\Phi_\mathrm{A}(r,\theta)$:

$$\begin{aligned} \Phi_\mathrm{p}(r,\theta) &= -\frac{3\epsilon_\mathrm{A}}{\epsilon_\mathrm{p}+2\epsilon_\mathrm{A}}E_0 r\cos\theta \\ \Phi_\mathrm{A}(r,\theta) &= -E_0 r\cos\theta + a^3 E_0\frac{\epsilon_\mathrm{p}-\epsilon_\mathrm{A}}{\epsilon_\mathrm{p}+2\epsilon_\mathrm{A}}\frac{\cos\theta}{r^2} \end{aligned}$$

Evidently, the field outside the sphere is a superposition of the potential of the static electric field and the potential induced by the sphere:

$$\Phi_\mathrm{A}(r,\theta) = \Phi_\mathrm{static}(r,\theta) + a^3 E_0\frac{\epsilon_\mathrm{p}-\epsilon_\mathrm{A}}{\epsilon_\mathrm{p}+2\epsilon_\mathrm{A}}\frac{\cos\theta}{r^2},$$

which can be rearranged to read

$$\Phi_\mathrm{A}(r,\theta) = \Phi_\mathrm{static}(r,\theta) + \frac{\mathbf{p}\cdot\mathbf{r}}{4\pi\epsilon_\mathrm{A} r^3}, \tag{3.7}$$

where $|\mathbf{r}| = r$ and

$$\mathbf{p} = 4\pi\epsilon_\mathrm{A} a^3\frac{\epsilon_\mathrm{p}-\epsilon_\mathrm{A}}{\epsilon_\mathrm{p}+2\epsilon_\mathrm{A}}\mathbf{E}_0. \tag{3.8}$$

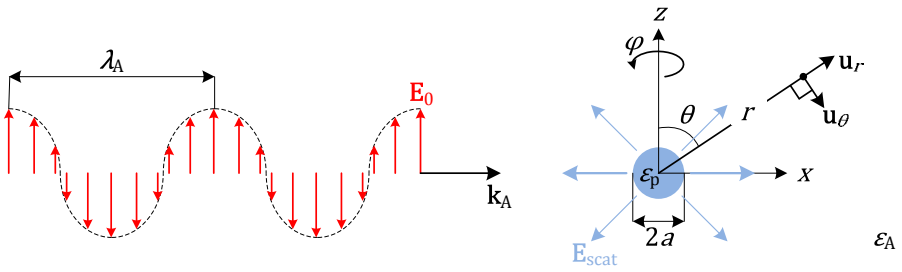

Figure 3.4: Dielectric sphere in plane wave electric field.

The second term on the right side in Eq. (3.7) can be recognized as the potential of an ideal dipole [50, 84], for $r \gg d$, where d is the distance between the two opposite sign charges of the dipole. The only difference is that the dipole moment of an ideal dipole equals qd, while in this case, the dipole moment is given by Eq. (3.8).

We can hence conclude that the resulting field outside the sphere is a superposition of the uniform static electric field, $\mathbf{E}_0$, and the field of an ideal dipole with dipole moment

$$\mathbf{p} = \epsilon_\mathrm{A} \alpha \mathbf{E}_0,$$

where

$$\alpha = 4\pi a^3 \frac{\epsilon_\mathrm{p} - \epsilon_\mathrm{A}}{\epsilon_\mathrm{p} + 2\epsilon_\mathrm{A}}. \tag{3.9}$$

The parameter α is called the polarizability of the dielectric sphere, and determines the amplitude of the dipole moment.

3.2.2 Dielectric sphere in harmonic electric field

The uniform static electric field is now replaced by a plane wave, $\mathbf{E}_0 e^{i(k_\mathrm{A} x - \omega_0 t)}$, polarized in the z-direction and with amplitude $E_0 = |\mathbf{E}_0|$, as shown in Fig. 3.4. The particle will scatter the field. We ask the question: Can the scattered field be expressed simply as a Hertzian dipole [85] with a dipole moment $\mathbf{p} = \epsilon_\mathrm{A}(\omega_0)\alpha(\omega_0)E_0 e^{-i\omega_0 t}\mathbf{u}_x$, where $\alpha(\omega_0)$ is given by Eq. (3.9) and the permittivities ϵ_p and ϵ_A are frequency dependent?

For large spheres, this is clearly not true. Such a model requires that the field across the volume of the sphere is approximately constant at any given point in time. This is not the case if the sphere radius, a, is comparable to, or larger than, the wavelength of the incident plane wave. The field across the sphere is, however, approximately constant if the radius of the sphere is sufficiently small. In fact, it can be shown that for $2\pi\sqrt{\epsilon_\mathrm{p}}a/\lambda_0 \ll 1$, where λ_0 is the vacuum wavelength

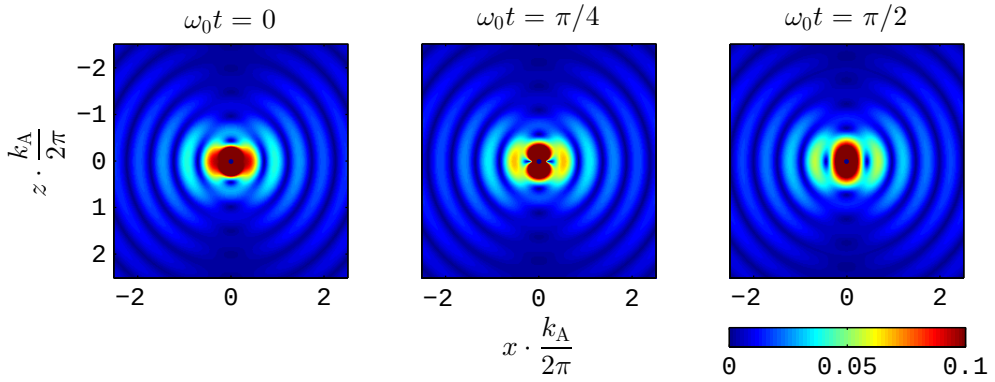

Figure 3.5: Color image representation of the absolute value of the scattered electric field, $|\mathbf{E}_{\text{scat}}|$, as a function of positions x and z, calculated from Eq. (3.10). In this example $|\mathbf{p}| = 4\pi\epsilon_{\text{A}}$ Cm, and the color scale is given in units of Volts.

corresponding to a frequency ω_0, the answer to the question above is yes. The time-dependent scattered field can hence be expressed as

$$\mathbf{E}_{\text{scat}} = \frac{e^{i(k_{\text{A}}r-\omega_0 t)}}{4\pi\epsilon_{\text{A}}}\left[k_{\text{A}}^2 p(\mathbf{u}_r \times \mathbf{u}_z) \times \mathbf{u}_r \frac{1}{r} + p[3\mathbf{u}_r(\mathbf{u}_z \cdot \mathbf{u}_r) - \mathbf{u}_z]\left(\frac{1}{r^3} - \frac{ik_{\text{A}}}{r^2}\right)\right], \tag{3.10}$$

where $k_{\text{A}} = \omega_0\sqrt{\epsilon_{\text{A}}}/c$, and $p = |\mathbf{p}|$ [84–87]. Figure 3.5 shows plots of the absolute value of $\mathbf{E}_{\text{scat}}$ in the xz-plane at times $\omega_0 t = 0$, $\omega_0 t = \pi/4$, and $\omega_0 t = \pi/4$. The figure shows how the scattered field, at some distance from the origin, is a spherical wave propagating outwards, with a zero-field axis parallel to the incident polarization. This is a correct description roughly half a wavelength away from the dipole center, $r > \pi/k_{\text{A}}$, where the $(1/r)$ term in Eq. (3.10) dominates by a factor of 10 or more. For smaller r, the $(1/r^2)$ and $(1/r^3)$ terms are dominant. Also note that due to the symmetry of the system, the scattered field is independent of rotation about the z-axis.

The area where the $(1/r)$-term dominates is called the far field. Omitting the time dependence, we can expression the electric field in the far field as

$$\mathbf{E}_{\text{scat}} = |\mathbf{E}_{\text{scat}}|e^{ik_{\text{A}}r}\mathbf{u}_\theta,$$

where $\mathbf{u}_\theta$ is defined in Fig. 3.4, and

$$|\mathbf{E}_{\text{scat}}| = \frac{1}{4\pi\epsilon_{\text{A}}}\frac{k_{\text{A}}^2 p}{r}\sin\theta = \left(\frac{2\pi}{\lambda_0}\right)^2\left(\frac{\epsilon_{\text{p}} - \epsilon_{\text{A}}}{\epsilon_{\text{p}} + 2\epsilon_{\text{A}}}\right)\epsilon_{\text{A}} a^3 \frac{E_0}{r}\sin\theta.$$

We further construct a sphere of radius R, enclosing the dipole, where we let $R \gg \pi/k_{\text{A}}$. We denote the sphere surface by S_R, and know that the electric dipole

field will always be perpendicular to the surface normal, $\mathbf{n}$. Since the magnetic dipole field is oriented perpendicular to both $\mathbf{u}_r$ and $\mathbf{u}_\theta$, the same is true for the magnetic field. This enables us to calculate the power irradiated from the dipole: Pointing's vector is found as

$$\mathbf{S} = \frac{1}{2}\Re\left(\mathbf{E}_{\text{scat}} \times \mathbf{H}^*_{\text{scat}}\right) = \frac{1}{2}\frac{k_{\text{A}}}{\omega\mu_0}|\mathbf{E}_{\text{scat}}(r=R)|^2\mathbf{u}_r = \frac{\sqrt{\epsilon_{\text{A}}}}{2}\sqrt{\frac{\epsilon_0}{\mu_0}}|\mathbf{E}_{\text{scat}}(r=R)|^2\mathbf{u}_r.$$

The power flowing out of the surface S_R, is found by integrating $\mathbf{S}\cdot\mathbf{n}$ over S_R:

$$P = \int_{S_R}\mathbf{S}\cdot\mathbf{n}dS = \int_{S_R}|\mathbf{S}|dS = \int_{S_R}\frac{\sqrt{\epsilon_{\text{A}}}}{2}\sqrt{\frac{\epsilon_0}{\mu_0}}|\mathbf{E}_{\text{scat}}(r=R)|^2dS.$$

This gives the irradiated power as

$$P_{\text{scat}} = \frac{8\pi}{3}\sqrt{\frac{\epsilon_0}{\mu_0}}\left(\frac{2\pi}{\lambda_0}\right)^4\left|\frac{\epsilon_{\text{p}}-\epsilon_{\text{A}}}{\epsilon_{\text{p}}+2\epsilon_{\text{A}}}\right|^2\epsilon_{\text{A}}^{\frac{5}{2}}a^6E_0^2. \tag{3.11}$$

From Eq. (3.11) one can further derive a parameter called the scattering cross section, which is the scattered irradiance, P_{scat}, divided by the absolute value of the Poynting vector, $\mathbf{S}_{\text{inc}}$, of the incident field:

$$\sigma = \frac{P_{\text{scat}}}{|\mathbf{S}_{\text{inc}}|} = \frac{8}{3}\left|\frac{\epsilon_{\text{p}}-\epsilon_{\text{A}}}{\epsilon_{\text{p}}+2\epsilon_{\text{A}}}\right|^2(k_{\text{A}}a)^4\pi a^2,$$

where $k_{\text{A}} = 2\pi\sqrt{\epsilon_{\text{A}}}/\lambda_0$.

3.2.3 Detecting scattering from small particles

When detecting the scattered irradiance from a particle, for example by using an optical microscope and CCD screen, the intensity of the light observed is proportional to the power that the particle irradiates. Equation (3.11) is therefore useful. It tells us what parameters that need to be tuned to increase the visibility of the particle, and what the limiting factors are.

Examining Eq. (3.11), the main limiting factor is the radius of the particle. The irradiance is proportional to the radius, a, to the power of six. We further see that the irradiance is proportional to the inverse vacuum wavelength to the power of four, λ_0^{-4}, and the squared amplitude of the excitation field, E_0^2. The equation also holds a number of terms containing the permittivities of the system. The permittivities of a given system are typically fixed, and may be regarded as constants. In conclusion, in a sensor where small particles are detected by the scattered light they irradiate, we can optimize the sensitivity of the sensor by using the smallest possible wavelength and a strong excitation field.

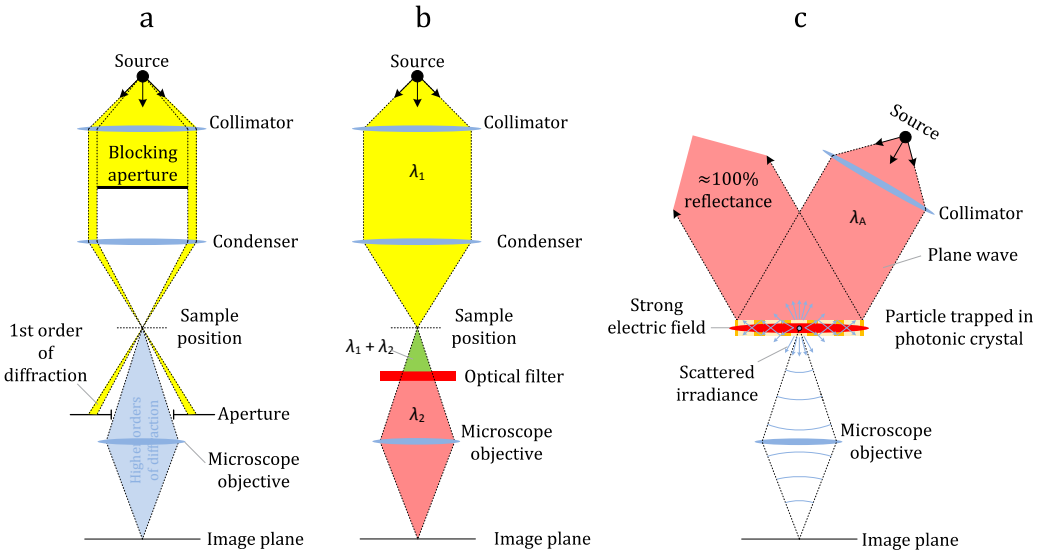

Figure 3.6: Illustration of three techniques, designed to keep the background signal independent of the amplitude of the excitation field: (a) Dark field microscopy, (b) fluorescent microscopy, and (c) particle detection by the use of a 2D photonic crystal supporting a guided-resonance mode.

Since strong excitation fields are easily attained, for example by the use of lasers, the solution seems easy. In theory, a decrease in particle size can always be counteracted by increasing the amplitude of the excitation field. However, increasing the amplitude of the excitation field is generally also followed by an increase in the background noise level. The signal-to-noise ratio, which is what determines the detection limit in practice, is thus not necessarily improved. Consequently, the sensor must be designed in a way that keeps the background signal independent of the amplitude of the excitation field. This can be achieved in a number of ways. In dark field microscopy, the excitation field is blocked from the imaging plane by only imaging higher orders of diffraction, as shown in Fig. 3.6 (a). In fluorescent techniques, a source excites fluorescent samples, causing the samples to emit light at a different wavelength. The excitation wavelength can then be prevented from reaching the imaging plane by using an optical filter. This technique is illustrated in Fig. 3.6 (b). Figure 3.6 (c) shows a setup specially made to detect particles trapped in PCs. A PC supporting a guided-resonance mode reflects incident light while providing high fields inside the membrane. The only light reaching the imaging plane is then scattered irradiance from the particle.

Chapter 4

Optical characterization of photonic crystals

Two optical setups have been built in order to characterize the PCs fabricated in this thesis. These have been named setups A and B, as indicated in Fig. 4.1, and are composed of standard optical components.

In setup A, a diode laser is redirected via a plane aluminum mirror, to provide normal incidence backside illumination on a 2D PC. An optical microscope equipped with a CCD camera views the PC from the top, and provides a magnified image of the transmitted light. If needed, the incident light and the detected light can independently be linearly polarized. In setup B, the source is a halogen bulb, routed through a monochromator, a set of concentrators, a multi-mode fiber and a collimator. Apart from this, the two setups are identical.

In this section, we explain the working principle of each part of the two systems. This includes a basic review of the optical concentrator and collimator, the mirror, the linear polarizer, single-mode and multi-mode optical fibers, the monochromator, the laser, and the CCD detector. Finally, we review optical microscopy, focusing on detection of small particles and the optical diffraction limit. The use of setups A and B is described in our publications [**24, 25, 58, 82**].

4.1 Concentrator and collimator

A collimator is essentially a device that limits the path of a beam, either by physically blocking part of the beam or by reshaping it. In optics, it refers to a lens system that redirects the rays radiating out from a point source with zero wavelength, creating a beam of parallel rays. This situation is illustrated by the black rays in Fig. 4.2 (a), giving an example of perfect collimation. With an extended source and nonzero wavelength, imperfect collimation is obtained, as illustrated by

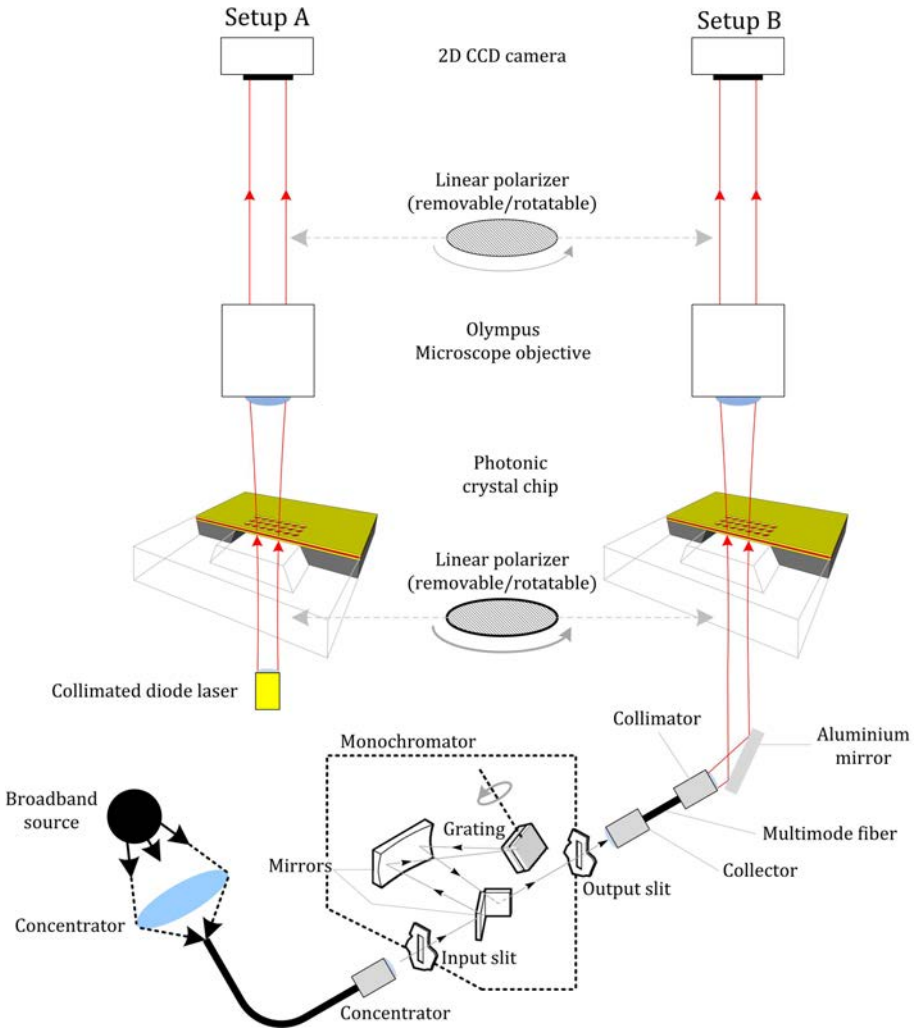

Figure 4.1: Two optical setups. Both are composed of a collimated normal incidence light source illuminating a photonic crystal. The transmitted light is magnified by a BX51 Olympus optical microscope and recorded using a F-view II CCD camera. If needed, the incident light and the detected light can independently be linearly polarized. In setup A, the source is a diode laser with a built in collimator, while in setup B the source is a halogen bulb, routed through a monochromator, a set of concentrators, a multi-mode fiber and a collimator.

the blue beam in Fig. 4.2 (a). Real beams can hence not be perfectly collimated. In setup B, the beam was in fact required not to be optimally collimated, as this increases the field intensity at the sample surface. The beam illuminating the PC in setup B has a shape similar to the dotted blue lines in Fig. 4.2 (a). The PC is placed at the minimum beam waist, marked by w_{min}. Using ray optics, a beam

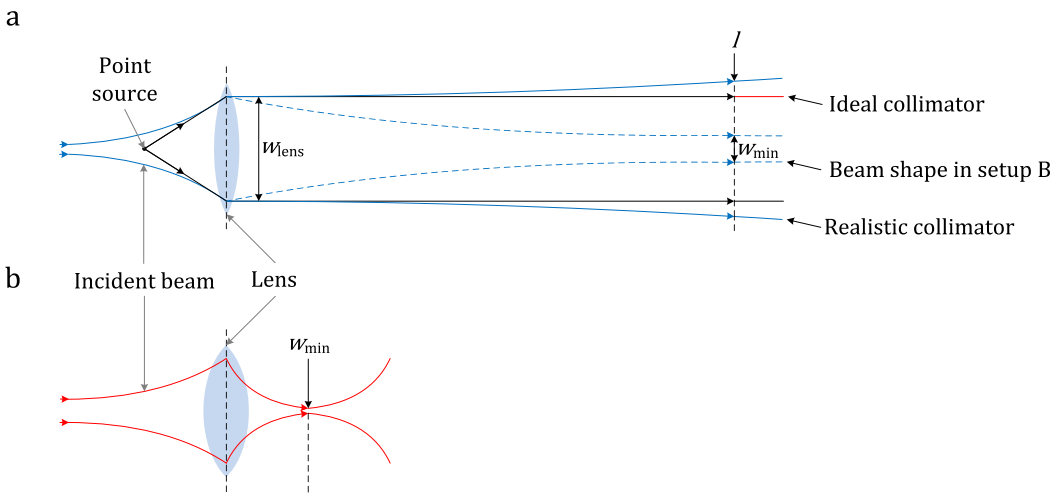

Figure 4.2: Lenses used to (a) collimate and (b) concentrate an incident beam.

waist at the lens of $w_{\text{lens}} = 4$ mm, and a distance between the lens and the PC of $l = 100$ mm, it is estimated that the beam illuminating the PC has a divergence of approximately $(w_{\text{lens}}/2)/l = 20$ mrad.

An optical concentrator is also composed of a lens system, only in this case the system collects the light from a diverging beam, producing a beam that diverges even more. This situation is shown in Fig. 4.2 (b). As can be seen in the figure, a concentrator focuses a beam with wide beam waist down to a narrower beam waist.

For more details on collimators and concentrators, and an explanation of what lenses are and how they work, see the textbooks [51, 52, 88, 89].

4.2 Mirror

A plane mirror with infinite extent in the xy-plane is illustrated in Fig. 4.3(a). It is used to reflect a plane wave with wave vector $\mathbf{k}_{\text{i}}$ and amplitude $\mathbf{E}_{\text{i}}$, producing a plane wave with wave vector $\mathbf{k}_{\text{r}}$ and amplitude $\mathbf{E}_{\text{r}}$. An ideal mirror will produce a reflected wave where $|\mathbf{E}_{\text{i}}| = |\mathbf{E}_{\text{r}}|$, $|\mathbf{k}_{\text{i}}| = |\mathbf{k}_{\text{r}}|$, and $\theta_{\text{i}} = \theta_{\text{r}}$. However, in real life there are no ideal mirrors. What does this imply?

Using Snell's law of reflection, we know that the tangential components of the wave vectors are equal on both sides of the boundary between materials 0 and 1:

$$k_{y1} = k_{y0}, \tag{4.1}$$

where $|\mathbf{k}_{\text{i}}|^2 = \epsilon_0(\omega/c)^2 = k_{z0}^2 + k_{y0}^2$ and $|\mathbf{k}_{\text{t}}|^2 = \epsilon_1(\omega/c)^2 = k_{z1}^2 + k_{y1}^2$.

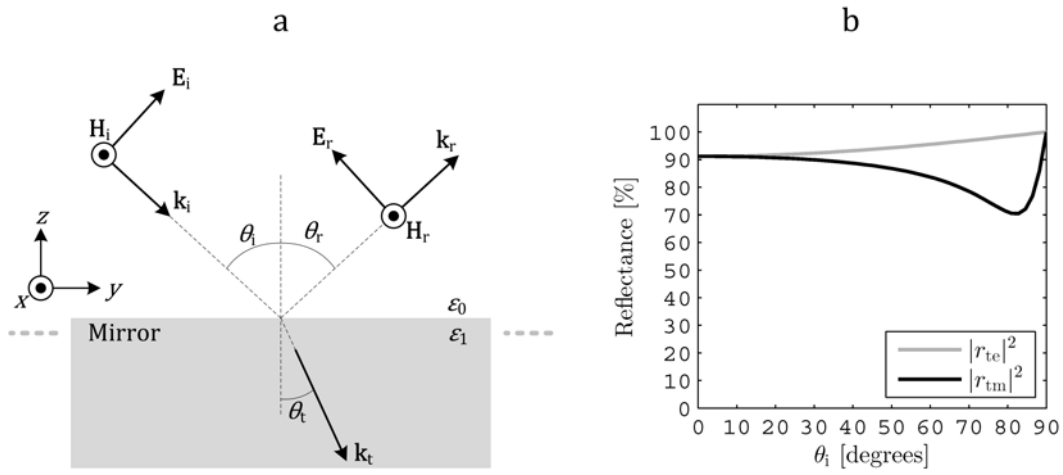

Figure 4.3: Illustration of mirror with infinite extent in the xy-plane. A plane TM wave, with wave vector $\mathbf{k}_\mathrm{i}$, is reflected of the surface of the mirror, producing a reflected plane wave with wave vector $\mathbf{k}_\mathrm{r}$. (b) The reflectance of TM- and TE-polarized plane waves with wavelength 600 nm, as a function of incidence angle, incident on a mirror made of aluminum ($\epsilon_1 = -50.28 + i18$ [90]), represented by the absolute value squared of reflection coefficients r_tm and r_te.

Combining Eq. (4.1) with Fresnel's law of reflection, one can calculate that the coefficients of reflectance for TM- and TE-polarized waves are:

$$r_\mathrm{tm} = \frac{\left|\frac{\mathbf{k}_\mathrm{i}}{\mathbf{k}_\mathrm{r}}\right|^2 k_{z1} - k_{z0}}{\left|\frac{\mathbf{k}_\mathrm{i}}{\mathbf{k}_\mathrm{r}}\right|^2 k_{z1} + k_{z0}} = \frac{\left|\frac{\epsilon_0}{\epsilon_1}\right| \sqrt{\epsilon_1 - \epsilon_0 + \epsilon_0 \cos^2\theta_\mathrm{i}} - \sqrt{\epsilon_0}\cos\theta_\mathrm{i}}{\left|\frac{\epsilon_0}{\epsilon_1}\right| \sqrt{\epsilon_1 - \epsilon_0 + \epsilon_0 \cos^2\theta_\mathrm{i}} + \sqrt{\epsilon_0}\cos\theta_\mathrm{i}}, \tag{4.2}$$

and

$$r_\mathrm{te} = \frac{k_{z0} - k_{z1}}{k_{z0} + k_{z1}} = \frac{\sqrt{\epsilon_0}\cos\theta_\mathrm{i} - \sqrt{\epsilon_1 - \epsilon_0 + \epsilon_0 \cos^2\theta\mathrm{i}}}{\sqrt{\epsilon_0}\cos\theta_\mathrm{i} + \sqrt{\epsilon_1 - \epsilon_0 + \epsilon_0 \cos^2\theta\mathrm{i}}}. \tag{4.3}$$

Analyzing Eqs. (4.2) and (4.3), we see that high reflectance is present when $|\epsilon_0| \ll |\epsilon_1|$. Since the absolute value of the permittivity of metals in general is high in the visible spectrum, metals are great optical reflectors. However, it is also clear that a metallic mirror does not reflect all the light. This is shown in Fig. 4.3(b), where the reflectance off an aluminum mirror is plotted as a function of incidence angle θ_i, for both TM- and TE-polarized plane waves, for a vacuum wavelength of 600 nm. Aluminum mirrors have been used in both setup A and B, and as the figure displays, the reflectance lies between 90 and 100 % in the visible spectrum [90]. Note also, that an aluminum mirror will depolarize the light for $\theta_\mathrm{i} \neq 0°$ and $\theta_\mathrm{i} \neq 90°$, as in this case $|r_\mathrm{tm}|^2 \neq |r_\mathrm{te}|^2$. Aluminum mirrors should hence not be used to steer polarized beams.

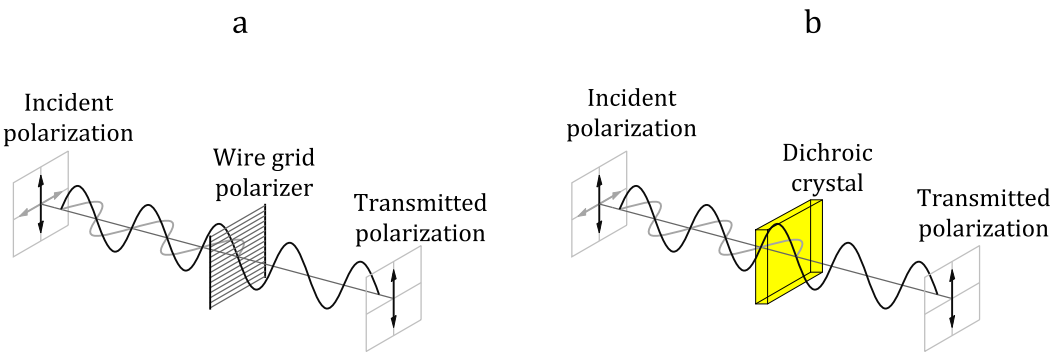

Figure 4.4: (a) Wire-grid-polarizer and (b) dichroic crystal used to linearly polarize an incident electric field.

To obtain mirrors less sensitive to polarization, and with higher reflectance, other metals, or broad band reflectors made of PCs, can be used [91]. Aluminum mirrors were, however, sufficient for the optical experiments in this thesis.

4.3 Linear polarizer

A polarizer is an optical filter that turns an incident field with arbitrary polarization into a field of defined polarization. The defined polarization for a linear polarizer is linear. As illustrated in Fig. 4.4, it blocks the field for all but one orientation.

Linear polarizers are made in a number of ways, and are characterized by their extinction ratio, which is a measure of how well they perform. The extinction ratio can be defined as $R = P_0/P_{90}$, where P_0 is the power transmitted of a field with polarization parallel to the transmitting orientation of the polarizer, and P_{90} is the power transmitted for the same incident field with the polarizer rotated 90 degrees.

Figure 4.4(a) illustrates one of the simpler polarizers, made of a grid of parallel metallic wires. This polarizer works as follows: Fields oscillating with a vector parallel to the wire lines, will induce movement of electrons in a direction parallel to the wires. Since electrons are free to move along the lines, an electrical current is generated, similar to that of currents produced in a mirror. Thus, a strong reflection of this particular polarization is obtained. Electron movement is also induced for the perpendicular polarization, but since electrons cannot jump from wire to wire, they are inhibited from moving. Consequently, this polarization is transmitted. In order for such polarizers to work, the period of the wire lattice is tuned to operate at a specific wavelength region. Extinction ratios in the order of

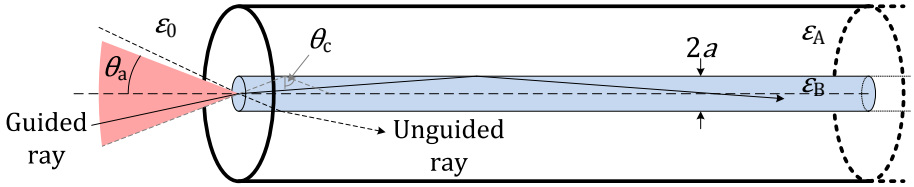

Figure 4.5: (a) Optical fiber, composed of a cylindrical dielectric core with permittivity ϵ_B, surrounded by a coating with permittivity $\epsilon_A < \epsilon_B$. Rays with an incident angles $\theta < \theta_a$, are guided by the fiber by total internal reflection.

100 are typical [92].

Figure 4.4(b) illustrates a linear polarizer made of a dichroic material. Rather than having polarization dependent reflection, this type of polarizer utilizes polarization dependent absorption [51]. Dichroic materials can show very strong absorption of light for one polarization, while a different polarization is virtually not absorbed at all. A number of materials have dichroic properties. The polarizers used in this thesis are made using the dichroic material cellulose triacetate [93], and have extinction ratios in the visible spectrum between 1000 and 5000.

4.4 Optical fibers

Optical fibers are cylindrical waveguides that support fully guided modes. In everyday life, optical fibers allow us to transport the enormous amount of information our society has acquired the need for. In relation to this thesis, they are a practical way of transporting light, from one part of the system to another in setup B. More specifically, light from the output of the monochromator is focused onto the core of a fiber, and the fiber guides the light to the collimator, which in turn focuses the light onto the back of our PCs.

The fully guided modes of a cylindrical waveguide are found by solving Maxwell's equations in a cylindrical coordinate system. This is done in a number of textbooks [51,88]. The results are discrete solutions for a given wave vector component aligned with the fiber core. The amplitude of the modes is a function of distance from the fiber core and rotation about the fiber center axis, and is expressed by Bessel functions.

Optical fibers can be designed to support a single fully guided mode, so-called single-mode fibers, or multiple fully guided modes, so-called multi-mode fibers. A number of different fiber types exist: Step index fibers, graded index fibers [51], hollow-core fibers and PC fibers [39]. We will limit our discussion to step index fibers, as this is what we use in setup B.

An illustration of a step index fiber is given in Fig. 4.5. It is composed of

a cylindrical dielectric core with permittivity ϵ_{B}, surrounded by a coating with permittivity ϵ_{A}. In order for fully guided modes to be supported by the core, we must have $\epsilon_{\mathrm{A}} < \epsilon_{\mathrm{B}}$. In this case, there is a critical angle, labeled θ_{c} in Fig. 4.5, where rays in the core incident on the coating with an angle larger than θ_{c} are totally reflected. This enables us to define the numerical aperture (n_{NA}) of the fiber: If the largest angle at which a ray can enter the core and still be guided is θ_{a} (see Fig. 4.5), then

$$\theta_{\mathrm{a}} = \frac{\sin^{-1} n_{\mathrm{NA}}}{\sqrt{\epsilon_0}} = \sin^{-1} n_{\mathrm{NA}},$$

where the outside of the fiber is assumed to be air, $\epsilon_0 \approx 1$. Using Snell's law at the ϵ_0-ϵ_{B} boundary at the left end of the fiber, and at the ϵ_{B}-ϵ_{A} boundary inside the fiber, n_{NA} can be redefined as

$$n_{\mathrm{NA}} = \sqrt{\epsilon_{\mathrm{B}} - \epsilon_{\mathrm{A}}},$$

and the numerical aperture can further be used to define a parameter V, given a specified fiber core radius, labeled a in Fig. 4.5, and working vacuum wavelength λ_0:

$$V = 2\pi \frac{a}{\lambda_0} n_{\mathrm{NA}}$$

The V-parameter tells us how many fully guided modes the fiber supports. For $V < 2.405$, the fiber only carries one fully guided mode. The number of supported modes M, as a function of larger V, is an integer-valued step function, but M can be approximated for $V \gg 1$ by

$$\mathrm{M} \approx \frac{4}{\pi^2} V^2 = 16 \left(\frac{a}{\lambda_0} \right)^2 n_{\mathrm{NA}}^2 \tag{4.4}$$

The amount of light coupled into a fiber by an incident source, depends on how well the phase front of the light focused onto the fiber core matches the phase front of a superposition of all the modes available. Consequently, if the wavefront extends over a core with a radius that is very small, efficient coupling can require elaborate alignment procedures. This is the case for single modes fibers, which typically have a core radius on the order of the wavelength of the incident light.

In contrast, multi-mode fibers typically have a core radius exceeding the wavelength of the incident light, by an order of magnitude or more. Moreover, the fiber supports a large number of fully guided modes. Compared to a single mode fiber, this makes it easy to couple light into a multi-mode fiber.

The fiber used in setup B is a M27L01 made by ThorLabs. It has a core radius of 100 µm and a numerical aperture of 0.39. For an operating vacuum wavelength

of 600±100 nm, this is a multi-mode fiber. Using Eq. (4.4), the number of fully guided modes supported by the fiber is more than 50000. These modes are coupled to with varying efficiency. The light exiting the multi-mode fiber will naturally be a superposition of many modes, and will result in modal noise, also referred to as speckle [51, 88]. This was, however, not observed, possibly due to the light being too broadband. Alternatively, the exposure times we used might have caused the modal noise to disappear as a result of averaging.

4.5 Monochromator

A 2D illustration of the monochromator in Fig. 4.1, viewed from the top, is shown in Fig. 4.6(a). It works as follows: A broad banded light source is focused in through the input port of a box whose inside is coated with a light absorbing layer, e.g. BlackVelvet [94]. The box is typically filled with air with permittivity $\epsilon_A \sim 1$. After entering the box, the light is reflected off a plane mirror, redirecting the light onto a curved mirror. The curved mirror collimates the incoming light, and produces a plane incident wave on a grating composed of a series of periodic line reflectors, as shown in Fig. 4.6(b). The reflection of the grating is wavelength dependent, resulting in only a subset of the frequencies in the source reflecting back towards the curved mirror, and finally exiting the monochromator out through the output port by reflecting off a second plane mirror. The output port slit width is tuned to adjust the band width of the output light. All other frequencies are absorbed in the inside coating.

To explain why the reflection of the grating is wavelength dependent, we go back to a previous derivation, Eqs. (2.25–2.29). From these equations we know that a periodic grating reflecting a plane wave produces m number of diffraction orders, where the period, p, determines how many of the orders reach the far field. In this example, we will assume that there are only three non-evanescent diffraction orders in the far field: $m = -1$, $m = 0$, and $m = 1$. Furthermore, the grating has a period allowing us to approximate the reflection from each line mirror as a cylindrical wave: We are located at a distance r from the surface of the grating, where $r \gg p$.

We can now use ray optics to find the angle, θ_m, where constructive interference occur for diffraction order m. First define two points, I_1 and I_2, that lie on the same wavefront of the incident plane wave, as shown in Fig. 4.6(b). Next, a point P is defined at a distance r from the grating surface. The length of the ray paths from points I_1 and I_2, to the mirror plane, and out to the point P, are finally defined by D_1 and D_2. Constructive interferences will then occur for angles θ_m

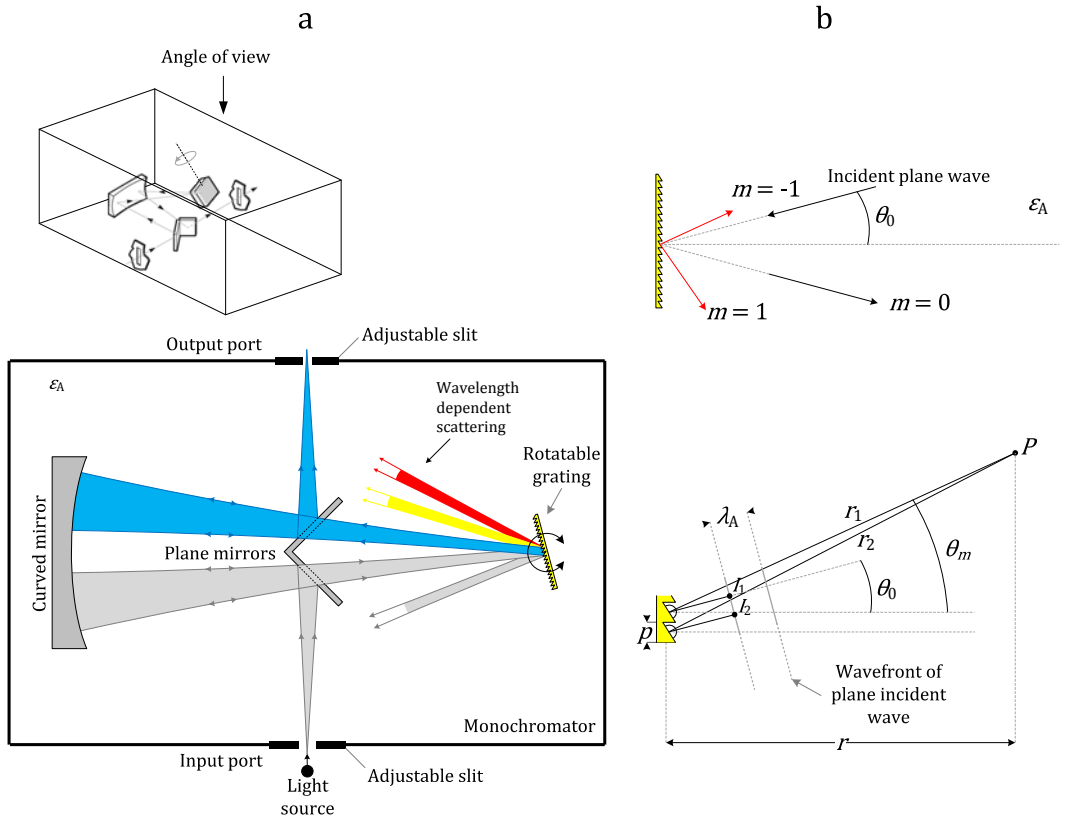

Figure 4.6: (a) Two dimensional illustration of the monochromator in Fig. 4.1, seen from the top. Broad banded light enters the input port of a box containing two plane mirrors mounted at a fixed angle, a curved mirror and a grating. Light at the input port is reflected onto the grating via one of the plane mirrors and the curved mirror. The grating is situated above the plane mirrors. The curved mirror hence focuses the light towards the grating at an angle, enabling it to pass above the plane mirrors. Only a subset of the frequencies is further reflected back towards the curved mirror, and finally exits the box out through the output port by a reflection off the second plane mirror. The slit width on the output port is tuned to adjust the band width of the output light. (b) Illustration of the grating, composed of a periodic array of line reflectors, with period p. The profile of the grating is designed to provide high diffraction efficiency for diffraction order $m = -1$, at an angle θ_m, for incident plane waves with an incident angle θ_0 and wavelength λ_A. The observation point, P, is defined such that $r \gg p$. Furthermore, we define two points, I_1 and I_2, lying on the same wavefront of the incident wave.

fulfilling the following requirement:

$$\frac{2\pi}{\lambda_A}(D_1 - D_2) = 2m\pi \Rightarrow k_A p(\sin\theta_0 + \sin\theta_m) = m\pi, \tag{4.5}$$

where $k_A = 2\pi/\lambda_A$, θ_0 is the incident angle, and λ_A is the wavelength in a medium with permittivity ϵ_A.

Equation (4.5) is called the grating equation, and shows how different wavelengths will interfere constructively at different angles, θ_m. Consequently, the grating inside our monochromator creates a fan of wavelengths, where each wavelength is entailed to an angle, θ_m. A specific band of wavelengths can hence be selected by rotating the grating and tuning the slit width on the output port. A narrow slit produces a narrow bandwidth output.

Setup B employs a Cornerstone 130 monochromator, made by Newport. It uses a 1200 lines/mm grating, and is specified to produce a minimum bandwidth of around 1 nm. Due to intensity requirements, such minimal bandwidths have not been used. In our experiments, the output slit has been tuned to produce a source bandwidth of ~ 4.5 nm.

A more detailed description of diffraction gratings can be found in a Handbook written by Erwin Loewen, available at Newport's web pages [95].

4.6 Laser

The basic components of a laser are illustrated in Fig. 4.7(a). Two mirrors, where one is partially transmitting, forms an optical cavity with length L. Using ray optics one can show that this cavity supports resonant modes with frequencies $\nu = cN/(2\sqrt{\epsilon_G}L)$, where c is the speed of light in vacuum, N is a natural number, and ϵ_G is the permittivity of the gain medium. Assume now that the cavity dimensions are designed to support a resonant mode with frequency ν_1, and that the property of the gain medium allows for stimulated emission at this frequency: A photon with frequency ν_1 propagating in the gain medium, with phase ϕ_1 and in a direction defined by $\mathbf{k}_1 = \pm k_y \mathbf{u}_y$, generates clones of itself by triggering electrons exited to higher energy levels to recombine with holes. One electron-hole recombination creates one photon.

Stimulated emission is hence only possible when the gain medium is in a state where electrons have been exited to higher energy levels. This is the function of the excitation pump. It increases the likelihood for an an electron to be available to recombine with a hole, if a photon passes by. When the excitation pump is turned on, electrons are excited to higher energy levels. Photons are initially generated from spontaneous recombination of holes and electrons. One spontaneous emitted photon results in two identical photons by stimulated emission, which further results in four identical photons by stimulated emission, and so on. Photons that fulfill the resonant condition of the cavity will eventually dominate. They all have the same phase and frequency, and are propagating along the z-axis. A coherent beam is therefore emitted through the partially reflective mirror at the right side

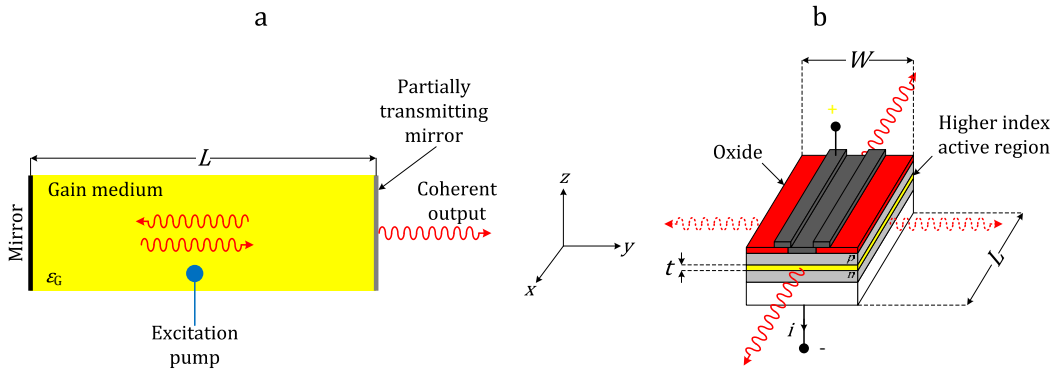

Figure 4.7: (a) Illustration of the working principle of a laser composed of one highly reflective mirror and one partially reflective mirror, forming an optical cavity in the horizontal direction. Between the two mirrors lies a gain medium, with permittivity ϵ_G, which is excited by a pump. Photons generated by spontaneous electron-hole recombination are amplified by stimulated emission, which results in coherent emission of light out through the partially reflective mirror, with a bandwidth set by the length of the cavity and the properties of the gain medium. (b) Illustration of a laser diode composed of an active region surrounded by lower index regions. The active region is both a gain medium and an optical cavity. The laser is driven by a current, i, causing emission of coherent narrowband light mainly traveling in the z-direction.

of the laser cavity. The bandwidth is set by the length of the cavity and the properties of the gain medium.

Figure 4.7(b) shows how a laser can be built in practice. A heavily doped region in a semiconductor, referred to as an active region, is formed in a pn-diode, and the sides of the diode are cleaved. The semiconductor has higher permittivity than the surrounding medium, which is typically air. The cleaved surfaces hence function as plane reflectors. Moreover, the permittivity of the active region is higher than that of all the surrounding regions. Consequently, an optical cavity is formed, with thickness t, and horizontal dimensions L and W. Since the thickness is typically small, and in the order of the wavelength of the emitted light, we can not apply ray optics to determine the frequencies of resonant modes. However, from the previous study of Maxwell's equations, we understand that resonant modes propagating in the xy-plane, bound by total internal reflection in the z-direction, will exist. In fact, the parameters, W, t and L, can be tuned to support resonant modes at frequencies where the active region works as a gain medium.

The gain is induced by forward biasing the diode. Electrons are then injected into the active region, leading to population inversion. Electron-hole pairs will

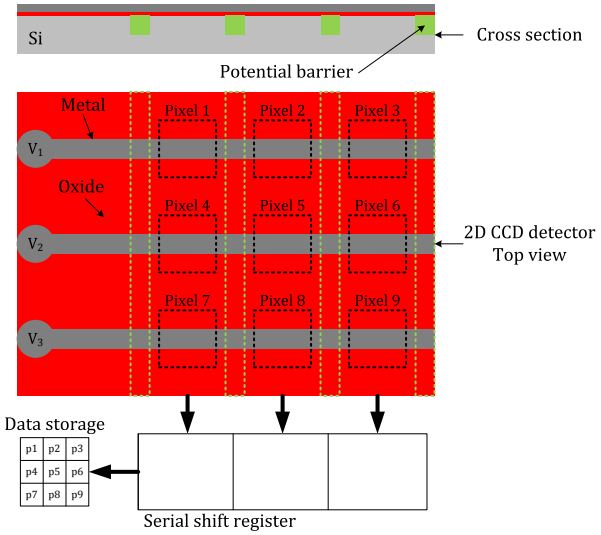

Figure 4.8: (a) Illustration of a 3×3 charge-coupled device (CCD detector), showing how the pixels are defined by a set of 1D potential barriers buried in the Si-substrate, and a perpendicular set of metallic lines. After exposure, the charge accumulated in the vicinity of each metallic line is shuffled over to the adjacent metallic line, in the direction of the serial shift register, transferring one pixel at a time into the data storage by an analog-to-digital converter.

tend to recombine, and produce light by spontaneous emission, which triggers stimulated emission. Eventually, this leads to a strong field resonating in the optical cavity, and emission of coherent light. In principle, light can be emitted out along both the x- and y-axis, as indicated by the dotted waves in Fig. 4.7(b). However, in general the geometry of the structure is designed to emit along one axis. The bandwidth is set by the dimensions of the cavity and the band structure of the gain medium. The laser used in optical setup A is a LC-LMD-635-03-01-A diode laser made by Laser Components. It has a built in collimator, and produces a 1.1 mrad divergence collimated beam with a line width of ∼4.5 nm centered at 632 nm.

For a more elaborate review on lasers and laser diodes, we refer to the following textbooks [51, 96].

4.7 Charge-coupled device (CCD)

As diodes can produce radiation by electron-hole recombination, radiation can also be absorbed by creating electron-hole pairs. By ensuring that the generated positive or negative charge is collected and detected, this process can be exploited

to make radiation detectors. For detection of visible frequencies with 2D spatial resolution, two technologies are presently well developed. These are so-called CCD and CMOS image detectors. Both technologies are built on Si-platforms, and can therefore detect wavelengths up $\sim$1.1 μm, corresponding to the band gap of Si.

CCD is an abbreviation for charge-coupled device, reflecting how the pixels are serially read out after an image has been recorded. CMOS stands for complementary metal-oxide-semiconductor, which reflects that the process used to make CMOS image detectors is the standardized CMOS process. CMOS detectors are therefore cheaper and is what you typically find in consumer products (cell phone camera, digital video cameras, etc.). CMOS detectors are generally faster than CCD detectors, while the main advantage of CCD detectors has been that they can operate with low noise. The camera chip used in setups A and B, is a F-View II Peltier cooled black and white 2D CCD made by Soft Imaging System GmbH. We will give a short introduction to how it works. A more detailed review of CCD detectors is found in the textbooks [51, 97, 98].

Figure 4.8 shows a simplified illustration of a CCD detector chip. We remark that a real CCD detector has a far more complex design, with apertures clearly defining where the substrate is exposed to light, and overlaying optics that ensure efficient collection of incident light. For color CCDs, each pixel can also comprise filters that allow the color of the light to be recorded. Options for cooling are also available in high end devices. The basic working principle can, however, still be understood from the simplified model in Fig. 4.8.

Fabrication of CCDs starts by defining a 1D grid of highly doped lines in a Si-substrate. These lines are potential barriers. Next, a thin layer of oxide is deposited, and a 1D grid of metallic lines is deposited on top of the oxide, oriented perpendicular to the highly doped lines. When the chip is illuminated, electron-hole pairs are generated in the substrate, and the number of electron-hole pairs generated is proportional to the number of photons incident on the substrate. The electron-hole pairs are further separated from each other by applying a voltage on each metallic line, creating rows of changes segmented by the vertically oriented potential barriers. This creates a 2D grid of pixels, where the intensity of the light recorded by each pixel is proportional to the charge accumulated in the vicinity of each metallic line segment.

The next step is to transfer pixel values into the data storage. How this is done is what really distinguishes CCDs from CMOS detectors. By applying a voltage algorithm on the metallic lines, the charge is shuffled from one row to the next, in the direction of a serial shift register located at one side of the CCD chip. For each row, the serial shift registered is transferred, one pixel at a time, into the data storage, via an analog-to-digital (A/D) converter. The use of only one A/D-converter is what enables CCD detectors to operate with low noise. It is, however,

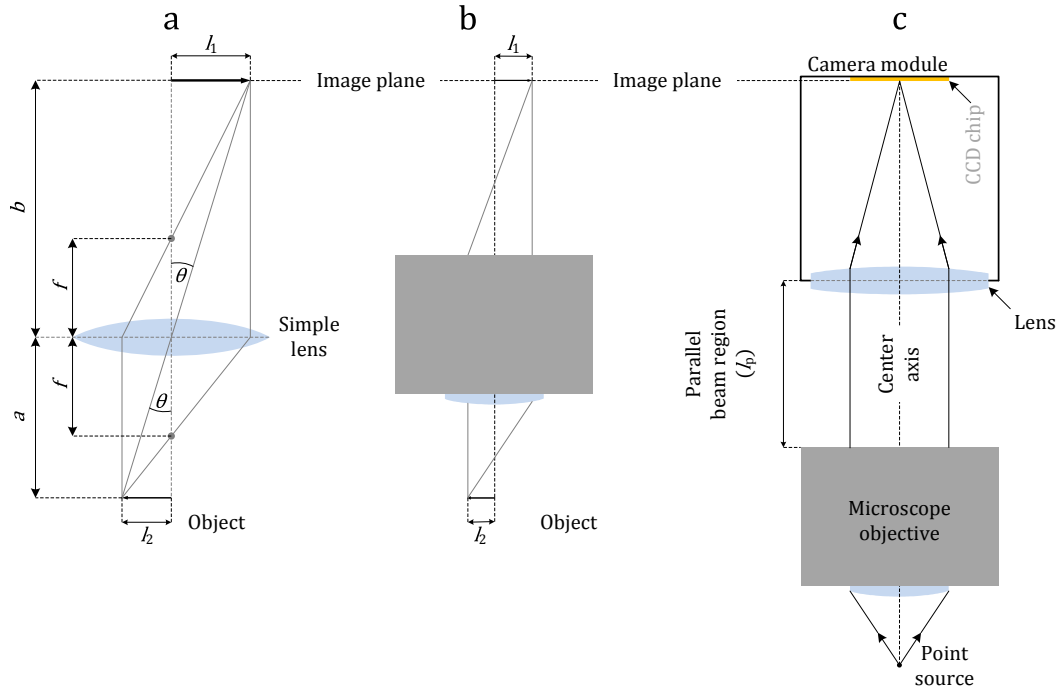

Figure 4.9: (a) Illustration of a simple biconvex lens, and (b) a micropscope objective used to create a virtual image of an object that is magnified. (c) Infinite-focus microscope setup

also what makes them slower than CMOS detectors, which typically use parallel readout schemes [98].

4.8 Optical microscopy

Optical setups A and B employs a BX51 Olympus optical microscope. We will now review aspects of optical microscopy, relevant in relation to the two setups. For a general review of optical microscopy, it is referred to the following textbooks [99, 100].

4.8.1 Basics of optical microscopy

An optical microscope is typically used for magnifying objects, or the details of an object, that are too small to be seen with the naked eye. Figure 4.9(a) shows how a lens diffracting light can give a magnified virtual image of the object in question.

Most of us have seen how this works in practice by using a simple magnifying glass, as the one illustrated in Fig. 4.9(a). The image plane, and the distance from

the lens to the object, is here described by the lens equation

$$\frac{1}{f} = \frac{1}{a} + \frac{1}{b},$$

where f is the focal length of the lens, a is the distance from the object to the center of the lens, and b is the distance from the center of the lens to where the images is in focus. From a geometric analysis of Fig. 4.9(a), we can further deduce that the magnification, M, provided by a lens with focal length f is given by

$$\tan\theta = \frac{l_1}{a} = \frac{l_2}{b} \Rightarrow \mathrm{M} = \frac{l_2}{l_1} = \frac{b}{a} = \frac{f}{a-f},$$

The magnification in a microscope is provided by a more complex objective, as illustrated in Fig. 4.9(b). The objective is typically not a simple lens, but rather a set of lenses yielding a far more complex ray path. However, the two systems basically do the same thing: Create a virtual image of the object that is magnified.

An illustration of a microscope connected to a camera is shown in Fig. 4.9(c). This specific microscope has so-called infinity-corrected optics: Imaging a point source with zero wavelength, placed at the center axis, produces a beam of parallel rays between the objective and the camera module. The rays are collected by the lens in the camera module, and are focused down to a point on the camera chip. In the case of a source with finite extent and wavelength, for example light diffracted by a small object, the objective will not produce a perfectly collimated beam of the diffracted light. However, if the source, or the diffracting object, is small and placed sufficiently close to the center axis, a perfectly collimated beam is a good approximation. This makes the setup virtually independent of the distance l_s, and allows for optical components like filters and polarizers to be inserted into the ray path as needed. Infinity-corrected optics is a practical configuration, typical for Olympus microscopes.

4.8.2 Detection of small particles and the optical diffraction limit

At this points we have explained how a microscope can magnify an object, making it appear larger than it really is. A natural question is then: How small can an object be and still be visible in an optical microscope? The answer to this question depends on what we mean by "visible".

We will first answer the question when the object is a small particle, and "visible" is defined as: The particle appears as a dot, and light diffracted by the particle can be approximated by a point source. As shown in Fig. 4.10, a point source creates spherical waves, propagating away from the particle. When ray

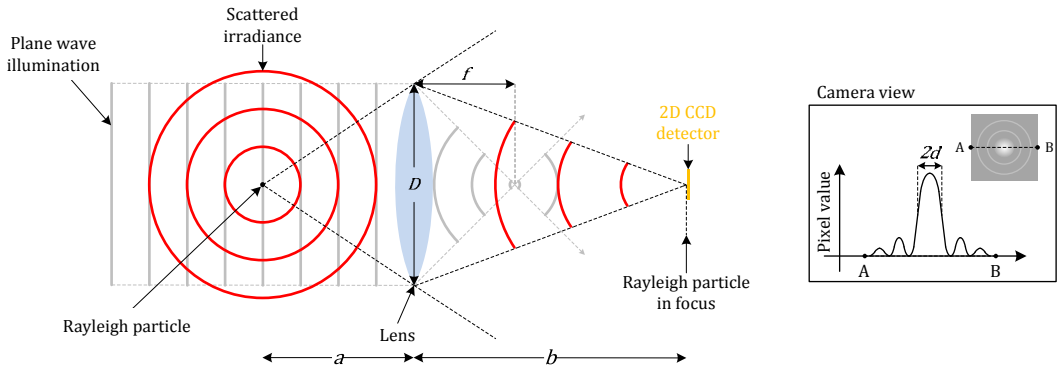

Figure 4.10: Illustration of a simple lens using plane wave illumination to image a particle.

optics applies, i.e. when the wavelength is zero, a perfect lens will focus these waves down to a point in the image plane. In theory, if the lens is infinitely large ($D \to \infty$), the point source will be perfectly reconstructed on the CCD detector. In real life, however, the lens has finite extent. This results in an imperfect reconstruction of the points source, seen as an Airy disk pattern [89, 99] on the CCD. The Airy disk pattern is composed of a bright central disk, surrounded by concentric rings of decreasing brightness, as illustrated in the box labeled *Camera View* in Fig. 4.10.

The brightness of the central disk relates to the size of the particle. At the limit where the particle can be approximated by a Rayleigh particle, the brightness is proportional to the volume of the particle squared. As described in chapter 3.2., this causes the intensity of the central disk to drown in background noise in systems where the illumination source is not inhibited from reaching the imaging plane. Excluding fluorescently labeled particles, and particles detected using dark-field techniques, single particles with a radius smaller than ∼100 nm can hence not be detected using standard optical microscopes [82].

Projecting the Airy disk pattern back to the object plane, for an object placed far away from the lens ($a \to \infty$), the radius of the central Airy disk can be expressed as

$$d = 1.22\frac{\lambda f}{D},$$

where f is the distance between the lens and the imaging plane, and D is the diameter of the lens. A corresponding equation can be developed for microscope objectives:

$$d = 1.22\frac{\lambda}{2n_{\mathrm{NA}}},$$

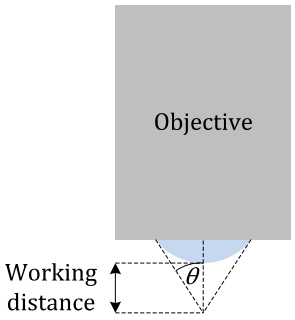

Figure 4.11: Illustration of a microscope objective, indicating the working distance of the objective. The working distance is defined by the distance between the objective and the object, when the object is in focus.

.

where d is called the diffraction limit of the microscope, and n_{NA} is the numerical aperture. The numerical aperture of an objective is defined by

$$n_{\mathrm{NA}} = \sqrt{\epsilon_0} \sin\theta,$$

where θ is the angle defining the light cone collected by the objective when the object is in focus, as illustrated in Fig. 4.11. The distance between the objective and an object in focus, is called the working distance.

Assume now that an objective has a numerical aperture of 0.6, where the maximum possible $n_{\mathrm{NA}} = 1$, and that the imaging vacuum wavelength is 600 nm. The radius of the central disk in the Airy pattern, d, is then 610 nm. We use this objective to image two adjacent particles with radii 100 nm. A comparison of the resulting image projected back to the object plane, and the actual size of the particles, is illustrated in Fig. 4.12. The figure shows how the Airy disk patterns overlap. Adjacent particles, much smaller than the diffraction limit of the microscope, can hence not be resolved and will appear as a single particle. Similarly, two adjacent bumps on top of a larger object cannot be resolved if the radius of each bump is significantly smaller than d.

In summary, since the scattered irradiance from small particles is proportional to their volume, the smallest detectable object in a standard optical microscope has size $\sim$100 nm. In order to resolve the topography of an object, meaning its shape and actual size, it must be larger than the diffraction limit of the microscope, which is essentially limited by the numerical aperture of the objective.

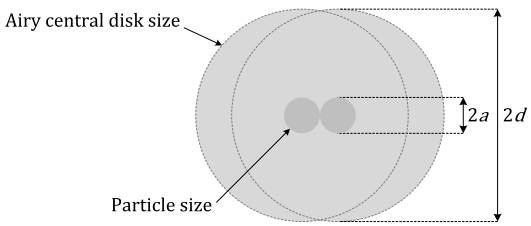

Figure 4.12: Illustration of how two small adjacent particles cannot be resolved, since the resulting Airy disk patterns overlap.

Chapter 5

Summary of work, conclusion and future work

My objective in this thesis has been to examine if photonic crystal (PC) membranes supporting guided-resonance modes can be exploited to detect single particles in the form of biomolecules such as proteins, deoxyribonucleic acid (DNA), ribonucleic acid (RNA) and viruses. I have done so by designing, and experimentally testing, a novel transducer. The thesis work includes transducer design, simulation, process development for fabrication of real devices, and building of optical setups used for characterizing fabricated devices. The scope of the thesis does not include chemical functionalization allowing biological targets to be captured. The current transducer is designed to be applied in a biosensor. It is composed in a way that facilitates chemical functionalization at locations where target capture events are optically most significant. For now, however, it should only be considered as a transducer capable of detecting and localizing small changes in permittivity.

This section describes the sensor concept and gives a summary of my work, main results, and conclusions. Finally, I give my opinion on the main strengths and weaknesses of the thesis, and propose further work.

5.1 Sensor concept

A 2D PC membrane, composed of a lattice of through holes in a thin slab, can be designed to reflect 100% of a plane normal incidence wave. This mirror property of 2D PC membranes, is a result of coupling to guided-resonance modes. Recording the transmitted light through a pristine PC, in a microscope with 2D spatial resolution, hence produces a dark image. At the same time, the field is resonantly enhanced in the vicinity of the membrane, as guided-resonance modes concentrate their power there. Introducing a local change in permittivity in this resonantly

enhanced field will lead to a change in transmittance.

The change in transmittance must, at least to some extent, be limited to the vicinity of the change in permittivity. This can be understood by considering how a guided-resonance mode is coupled to. Light incident on the PC lattice can take two paths. It can be transmitted directly through the membrane, similar to a homogeneous slab, and it can be scattered by the holes, redirected into in-plane propagating modes. The latter path is referred to as the indirect path. Light coupled to the indirect path, cannot travel indefinitely far from where it enters the PC. Since the incident field has a wave vector and frequency corresponding to a point above the light line, light coupled to the indirect path will eventually exit the membrane. Hence, for light interacting with the membrane far away from where the change in permittivity is located, the PC looks pristine.

Consequently, when observing the transmitted light through a highly reflective pristine PC, where local changes in permittivity have been introduced in the lattice, bright spots should be detected originating from the location of the permittivity change. Further, one can incorporate chemical methods that allow target molecules to be immobilized on the inside of the holes in the PC. Then, each hole will form a sensing cavity, and the PC as a whole will form an array of sensing cavities, providing a high dynamic range. High sensitivity can also be achieved, because the signal-to-noise ratio can be optimized by reducing the background signal to zero. The latter is at least possible in theory.

5.2 Summary of work

The potential of the sensor concept described above, has been explored by simulations and experiments [**24**]. I have designed a highly reflective PC that supports a guided-resonance mode, concentrating its field in the vicinity of the membrane, and peaking at the hole walls. In my research collaboration, the design has been fabricated, resulting in 2D PCs composed of a square lattice of holes, etched through a free-standing dielectric thin film stack, 50±5 nm Si_3N_4/50±5 nm SiO_2/50±5 nm Si_3N_4. Holes have a radius of 145±10 nm, and are spaced with a period of 490±5 nm. The reason for choosing a three layered stack is that this gives a cylinder surface inside each hole which is chemically different from the rest of the PC surface. In turn, this enables us to functionalize the inside of the holes to capture targeted molecules, while the rest of the PC opposes molecule capture.

In one of my fabricated PCs, a nano-particle is trapped inside one of the holes. This nano-particle causes a small local change in permittivity. The PC has been optically characterized by a custom built optical setup, revealing that the overall transmittance of the PC is low for the designed working wavelength, and that the nano-particle can indeed be observed as a bright spot originating from its location

in the lattice.

I have proposed a model for this optical effect, which describes how small particles trapped in PCs can be detected as a result of enhanced Rayleigh scattering: A guided-resonance mode provides a resonantly enhanced field in the vicinity of the membrane. If a small particle is located in this field, it will scatter similar to a Rayleigh scatterer. In effect, a small portion of the power contained in the guided-resonance mode is redirected into spherical waves traveling out from the center of the particle. The spherical waves are collected by the microscope objective, and focused down to a point in the imaging plane. Since the PC is highly reflective, these points are bright compared to the background. In this model, I assume that the guided-resonance mode field is retained, and unaffected by the presence of a particle. This is an approximation which is only valid when the particle is sufficiently small.

In order to solidify the above hypothesis, I have designed a series of simulations and experiments [**25,82,83**] examining the details of how particles in PCs behave. The results indicate that scattered irradiance from a particle trapped in a PC supporting guided-resonance modes is indeed similar to a Rayleigh scatterer. In particular, the results show that the scattered irradiance is proportional to the volume of the scattering particles squared. This enables us to estimate a detection limit of the current transducer, based on the size of the defect in our fabricated PC and the signal-to-noise ratio achieved in our optical measurements. It is also evident that the scattered irradiance is increased when the particle is located at a point where the mode field is maximized [**25**]. This agrees with Rayleigh scattering theory, and also tells us how the sensor can be optimized: The amplitude of the resonantly enhanced field should be maximized and the background signal should be minimized.

A minimized background signal should in theory be provided by the intrinsic low transmittance of the PC. However, it is difficult to achieve 100% reflection of incident light from a real PC. Consequently, the background signal cannot be tuned to zero. I therefore made a modification to the initial custom built optical setup, allowing both the incident and detected light to be linearly polarized, with arbitrary orientation [**25, 101**]. This arranges for cross-polarized excitation and detection, which is shown to produce an increased signal-to-background ratio. Using this improved optical setup, the detection limit is calculated to be particles with a radius of 26 nm.

Increasing the amplitude of the resonantly enhanced field, can in theory be achieved by decreasing the scattering strength of the PC. Weak scattering PC gratings typically support higher Q-factor guided-resonance modes. However, this is in general only true for infinite crystals and perfectly plane waves. By simulation and experimental results, I have shown how the Q-factor of guided-resonance

modes in real crystals is fundamentally limited by edge loss effects [**58**]. Guided-resonance modes, which in theory exist in an infinite lattice, may not be observable in a finite lattice if the number of periods in the lattice is insufficient. I have therefore designed a novel structure, where in-plane Bragg mirrors are used to suppress edge related losses [**58**].

5.3 Conclusion

My main achievement in this thesis has been the realization of a novel transducer for detection of nano-particles. Two possible fabrication techniques [**24, 102**] have been developed, and I have shown how guided-resonance modes, supported by fabricated PC membranes, can be exploited to detect nano-particles trapped in the lattice. My design takes into consideration that the transducer should be applicable to a point-of-care label-free biosensor. Estimations using simulations and Rayleigh scattering theory suggest that the current detector should be able to detect particles the size of a single virus.

I have also developed a model describing how small particles trapped in PCs supporting guided-resonance modes behave. Supported by simulation and experimental results, I show that these can be modeled using Rayleigh scattering theory. In conclusion, the sensitivity of the sensor scheme is proportional to the volume of particles squared, and can be improved by utilizing higher Q-factor guided-resonance modes.

In order to limit edge losses, PCs supporting high-Q guided-resonance modes must in general have a large area. Moreover, these modes are sensitive to discrepancies in the lattice, and tend to disappear if the fabrication accuracy is insufficient. Since accurate fabrication over large areas is challenging, I have developed a PC design that allows the properties of a large PC to be reproduced in smaller structures. This is done by introducing reflecting boundaries, in the form of in-plane Bragg mirrors. The novel design represents a way around the fundamental limitation on Q-factors for guided-resonances in finite photonic crystals.

5.4 Further work

Considerable development remains before the transducer can be applied in a fully functional point-of-care biosensor. In relation to the cost of a final device, I point out that both of the current fabrication processes utilize E-beam lithography. This is an expensive technique. Future process developments should consider alternative, cheaper lithography techniques, e.g. nano-imprint lithography.

An important remaining challenge is related to chemical functionalization. A

requirement set by the design, is that target particles must settle inside the holes of the PC, in order for the signal they produce to be maximized. Methods hence have to be developed, allowing the inside of holes to be chemically functionalized to capture specific target molecules, while the rest of the PC surface opposes molecule capture. It has been shown that selective functionalization of both Si_3N_4 and SiO_2 is possible on a macroscopic level [21, 38]. However, in my transducer, a SiO_2-surface inside a hole, with nanometer dimensions, needs to be functionalized. A weakness in my work is that I have not proven that this is possible. In relation to biological functionalization, I would also like to point out that relevant biological target particles are found in human samples of urine, blood and spinal fluid. These fluids mainly consist of water. Future PCs should therefore be re-designed to operate in water rather than air.

A second weakness in my work is that I have only managed to create one PC holding one ideal test particle. Since I do not know for certain what this particle is composed of, it is not clear how accurately it represents a trapped particle of interest. Future work should include an experiment where a PC holding a known particle is investigated. Ideally, the particle should be a virus, but a latex sphere is a good alternative. As mentioned above, the irradiation from particles trapped in the lattice is drawn from the power contained in the guided-resonance mode. Consequently, the mode, phase-matched to interfere destructively with directly transmitted light, loses some of its power. In addition to providing an experimental estimate of the detection limit, known particles could be used to determine if they are detected dominantly as a result of scattering, or if there is a substantial contribution from changes made to the guided-resonance mode.

Bibliography

[1] V. V. Vadakan, "The asphyxiating and exsanguinating death of president George Washington," The Permanente Journal **8**, 76–79 (2004).

[2] T. Vo-Dinh and B. Cullum, "Biosensors and biochips: Advances in biological and medical diagnostics," Fresenius J. Anal. Chem. **366**, 540–551 (1999).

[3] S. S. Saliterman, *BioMEMS and Medical Microdevices* (SPIE, 2006).

[4] A. A. Yanik, M. Huang, O. Kamohara, A. Artar, T. W. Geisbert, J. H. Connor, and H. Altug, "An optofluidic nanoplasmonic biosensor for direct detection of live viruses from biological media," Nano Lett. **10**, 4962–4969 (2010).

[5] B. Bohunicky and S. A. Mousa, "Biosensors: The new wave in cancer diagnosis," Nanotech. Sci. Appl. **4**, 1–10 (2010).

[6] P. Dario, M. Carrozza, A. Benvenuto, and A. Menciassi, "Micro-systems in biomedical applications," J. Micromech. Microeng. **10**, 235–244 (2000).

[7] I. Ahmed, M. U.and Saaem, P. C. Wu, and A. S. Brown, "Personalized diagnostics and biosensors: A review of the biology and technology needed for personalized medicine," Crit. Rev. Biotechnol. pp. 1–17 (2013).

[8] M.-C. Estevez, M. A. Otte, B. Sepulveda, and L. M. Lechuga, "Trends and challenges of refractometric nanoplasmonic biosensors: A review," Anal. Chim. Acta **806**, 55–73 (2014).

[9] M. F. Pineda, L. L. Chan, T. Kuhlenschmidt, C. J. Choi, M. Kuhlenschmidt, and B. T. Cunningham, "Rapid specific and label-free detection of porcine rotavirus using photonic crystal biosensors," IEEE Sens. J. **9**, 470–477 (2009).

[10] K. Narsaiah, S. N. Jha, R. Bhardwaj, R. Sharma, and R. Kumar, "Optical biosensors for food quality and safety assurance–a review," J. Food Sci. Technol. **49**, 383–406 (2012).

[11] M. A. Cooper, ed., *Label-Free Biosensors, Techniques and Applications* (Cambridge University Press, 2009).

[12] J. M. Jacobs, J. N. Adkins, W.-J. Qian, T. Liu, Y. Shen, D. G. Camp, and R. D. Smith, "Utilizing human blood plasma for proteomic biomarker discovery," J. Proteome Res. **4**, 1073–1085 (2005).

[13] D. Kambhampati, ed., *Protein Microarray Technology* (Wiley-Blackwell, 2004).

[14] T. A. Crowley and V. Pizziconi., "Isolation of plasma from whole blood using planar microfilters for lab-on-a-chip applications," Lab Chip **5**, 922–929 (2005).

[15] Y. Nakashima, S. Hata, and T. Yasuda, "Blood plasma separation and extraction from a minute amount of blood using dielectrophoretic and capillary forces," Sens. Actuator B-Chem. **145**, 561–569 (2010).

[16] J. L. Arlett, E. Myers, and M. Roukes, "Comparative advantages of mechanical biosensors," Nat. Nanotechnol. **6**, 203–215 (2011).

[17] X. Luo and J. J. Davis, "Electrical biosensors and the label free detection of protein disease biomarkers," Chem. Soc. Rev. **42**, 5944–5962 (2013).

[18] J. S. Daniels and N. Pourmand, "Label-free impedance biosensors: Opportunities and challenges," Electroanalysis **19**, 1239–1257 (2007).

[19] F. Vollmer and L. Yang, "Label-free detection with high-Q microcavities: A review of biosensing mechanisms for integrated devices," Nanophotonics **37**, 267–291 (2012).

[20] X. Fan, I. M. White, S. I. Shopova, H. Zhu, J. D. Suter, and Y. Sun, "Sensitive optical biosensors for unlabeled targets: A review," Anal. Chim. Acta **620**, 8–26 (2008).

[21] M.-J. Banuls, R. Puchades, and A. Maquieira, "Chemical surface modifications for the development of silicon-based label-free integrated optical (IO) biosensors: A review," Anal. Chim. Acta **777**, 1–16 (2013).

[22] M. R. Lee and P. M. Fauchet, "Nanoscale microcavity sensor for single particle detection," Opt. Lett. **32**, 3284–3286 (2007).

[23] S. Pal, E. Guillermain, R. Sriram, B. L. Miller, and P. M. Fauchet, "Silicon photonic crystal nanocavity-coupled waveguides for error-corrected optical biosensing," Biosens. Bioelectron. **26**, 4024–4031 (2011).

[24] J. O. Grepstad, P. Kaspar, O. Solgaard, I.-R. Johansen, and A. S. Sudbø, "Photonic-crystal membranes for optical detection of single nano-particles, designed for biosensor application," Opt. Express **20**, 7954–7965 (2012).

[25] J. O. Grepstad, P. Kaspar, I.-R. Johansen, O. Solgaard, and A. Sudbø, "Detection of single nano-defects in photonic crystals between crossed polarizers," Opt. Express **21**, 31375–31389 (2013).

[26] V. R. Dantham, S. Holler, C. Barbre, D. Keng, V. Kolchenko, and S. Arnold, "Label-free detection of single protein using a nanoplasmonic-photonic hybrid microcavity," Nano Lett. **13**, 3347–3351 (2013).

[27] I. Ament, J. Prasad, A. Henkel, S. Schmachtel, and C. Sonnichsen, "Single unlabeled protein detection on individual plasmonic nanoparticles," Nano Lett. **12**, 1092–1095 (2012).

[28] P. Zijlstra, P. M. R. Paulo, and M. Orrit, "Optical detection of single non-absorbing molecules using the surface plasmon resonance of a gold nanorod," Nat. Nanotechnol. **7**, 379–382 (2012).

[29] R. Bruck, E. Melnik, P. Muellner, R. Hainberger, and M. Lammerhofer, "Integrated polymer-based Mach-Zehnder interferometer label-free streptavidin biosensor compatible with injection molding," Biosens. Bioelectron. **26**, 3832–3837 (2011).

[30] D. Duval, J. Osmond, S. Dante, C. Dominguez, and L. M. Lechuga, "Grating couplers integrated on Mach-Zehnder interferometric biosensors operating in the visible range," IEEE Photonics J. **5**, 3700108–3700108 (2013).

[31] M. Mancuso, J. M. Goddard, and D. Erickson, "Nanoporous polymer ring resonators for biosensing," Opt. Express **20**, 245–255 (2012).

[32] Y. Sun and X. Fan, "Optical ring resonators for biochemical and chemical sensing," Anal. Bioanal. Chem. **399**, 205–211 (2011).

[33] S. Pal, P. M. Fauchet, and B. L. Miller, "1-D and 2-D photonic crystals as optical methods for amplifying biomolecular recognition," Anal. Chem. **84**, 8900–8908 (2012).

[34] R. Adato and H. Altug, "In-situ ultra-sensitive infrared absorption spectroscopy of biomolecule interactions in real time with plasmonic nanoantennas," Nat. Commun. **4**, 2154 (2013).

[35] A. E. Cetin and H. Altug, "Fano resonant ring/disk plasmonic nanocavities on conducting substrates for advanced biosensing," ACS Nano **6**, 9989–9995 (2012).

[36] M. E. Beheiry, V. Liu, S. Fan, and O. Levi, "Sensitivity enhancement in photonic crystal slab biosensors," Opt. Express **18**, 22702–22714 (2010).

[37] C. Ge, M. Lu, S. George, T. A. Flood, C. Wagner, J. Zheng, A. Pokhriyal, J. G. Eden, P. J. Hergenrother, and B. T. Cunningham, "External cavity laser biosensor," Lab Chip **13**, 1247–1256 (2013).

[38] M. J. Banuls, V. Gonzalez-Pedro, C. A. Barrios, R. Puchades, and A. Maquieira, "Selective chemical modification of silicon nitride/silicon oxide nanostructures to develop label-free biosensors," Biosens. Bioelectron. **25**, 1460–1466 (2010).

[39] J. D. Joannopoulos, S. Johnson, J. N. W., and R. D. Meade, *Photonic crystals, Molding the flow of light (2nd Edition)* (Princeton University Press, 2008).

[40] L. Feuz, M. P. Jonsson, and F. HÃűÃűk, "Material-selective surface chemistry for nanoplasmonic sensors: Optimizing sensitivity and controlling binding to local hot spots," Nano Lett. **12**, 873–879 (2012).

[41] C. D. Chin, V. Linder, and S. K. Sia, "Commercialization of microfluidic point-of-care diagnostic devices," Lab Chip **12**, 2118–2134 (2012).

[42] S. Kumar, M. A. Ali, P. Anand, V. V. Agrawal, R. John, S. Maji, and B. D. Malhotra, "Microfluidic-integrated biosensors: Prospects for point-of-care diagnostics," Biotechnol. J. **8**, 1267–1279 (2013).

[43] P. E. Sheehan and L. J. Whitman, "Detection limits for nanoscale biosensors," Nano Lett. **5**, 803–807 (2005).

[44] T. M. Squires, R. J. Messinger, and S. R. Manalis, "Making it stick: Convection, reaction and diffusion in surface-based biosensors," Nat. Biotechnol. **26**, 417–426 (2008).

[45] A. A. Yanik, M. Huang, A. Artar, T.-Y. Chang, and H. Altug, "Integrated nanoplasmonic-nanofluidic biosensors with targeted delivery of analytes," Appl. Phys. Lett. **96**, 021101 (2010).

[46] P. S. J. Russell, "Photonic-crystal fibers," J. Lightwave Technol. **24**, 4729–4749 (2006).

[47] J. D. Joannopoulos, P. R. Villeneuve, and S. Fan, "Photonic crystals: Putting a new twist on light," Nature **386**, 143–149 (1997).

[48] S. Fan and J. D. Joannopoulos, "Analysis of guided resonances in photonic crystal slabs," Phys. Rev. B **65**, 235112 (2002).

[49] K. B. Crozier, V. Lousse, O. Kilic, S. Kim, S. Fan, and O. Solgaard, "Air-bridged photonic crystal slabs at visible and near-infrared wavelengths," Phys. Rev. B **73**, 115126 (2006).

[50] Z. Popovic and B. D. Popovic, *Introductory Electromagnetics* (Prentice Hall, Inc., 2000).

[51] B. E. A. Saleh and M. C. Teich, *Fundamentals of Photonics* (John Wiley and Sons, Inc., 1991).

[52] O. Solgaard, *Photonic Microsystems, Micro and Nanotechnology Applied to Optical Devices and Systems* (Springer, 2009).

[53] F. Bloch, "Uber die quantenmechanik der elektronen in kristallgittern," Z. Phys. **52**, 555–600 (1929).

[54] S. S. Wang and R. Magnusson, "Theory and applications of guided-mode resonance filters," Appl. Opt. **32**, 2606–2613 (1993).

[55] W. Suh, Z. Wang, and S. Fan, "Temporal coupled-mode theory and the presence of non-orthogonal modes in lossless multimode cavities," IEEE J. Quantum Electron. **40**, 1511–1518 (2004).

[56] S. Fan, W. Suh, and J. D. Joannopoulos, "Temporal coupled-mode theory for the fano resonance in optical resonators," J. Opt. Soc. Am. A **20**, 569–572 (2003).

[57] J. Lee, B. Zhen, S.-L. Chua, W. Qiu, J. D. Joannopoulos, M. Soljacic, and O. Shapira, "Observation and differentiation of unique high-Q optical resonances near zero wave vector in macroscopic photonic crystal slabs," Phys. Rev. Lett. **109**, 067401 (2012).

[58] J. O. Grepstad, M. Greve, B. Holst, I.-R. Johansen, O. Solgaard, and A. Sudbø, "Finite-size limitations on quality factor of guided resonance modes in 2D photonic crystals," Opt. Express **21**, 23640–23654 (2013).

[59] D. K. Jacob, S. C. Dunn, and M. G. Moharam, "Design considerations for narrow-band dielectric resonant grating reflection filters of finite length," J. Opt. Soc. Am. A **17**, 1241–1249 (2000).

[60] J. M. Bendickson, E. N. Glytsis, T. K. Gaylord, and D. L. Brundrett, "Guided-mode resonant subwavelength gratings: Effects of finite beams and finite gratings," J. Opt. Soc. Am. A **18**, 1912–1928 (2001).

[61] M. G. Moharam and T. K. Gaylord, "Rigorous coupled-wave analysis of planar-grating diffraction," J. Opt. Soc. Am. **71**, 811–818 (1981).

[62] M. G. Moharam and T. K. Gaylord, "Rigorous coupled-wave analysis of grating diffraction–E-mode polarization and losses," J. Opt. Soc. Am. **73**, 451–455 (1983).

[63] M. G. Moharam and T. K. Gaylord, "Rigorous coupled-wave analysis of metallic surface-relief gratings," J. Opt. Soc. Am. A **3**, 1780–1787 (1986).

[64] L. Li, "Formulation and comparison of two recursive matrix algorithms for modeling layered diffraction gratings," J. Opt. Soc. Am. A **13**, 1024–1035 (1996).

[65] P. Lalanne and G. M. Morris, "Highly improved convergence of the coupled-wave method for TM polarization," J. Opt. Soc. Am. A **13**, 779–784 (1996).

[66] S.-D. Wu, T. K. Gaylord, E. N. Glytsis, and Y.-M. Wu, "Three-dimensional converging-diverging Gaussian beam diffraction by a volume grating," J. Opt. Soc. Am. A **22**, 1293–1303 (2005).

[67] GDcalc. Commercially available software supplied by KJ Innovation, http://software.kjinnovation.com/GD-Calc.html visited 07.01.2014.

[68] M. Neviere and E. Popov, *Light Propagation in Periodic Media, Differential Theory and Design* (Marcel Dekker Inc., 2003).

[69] A. Taflove and S. C. Hagness, *Computational Electrodynamics: The Finite-Difference Time-Domain Method* (Artech House, 2000).

[70] OptiFDTD. Commercially available software, supplied by Optiwave, http://optiwave.com, visited 07.01.2014.

[71] C. H. Edwards and D. E. Penney, *Calculus with analytic geometry (5th Edition)* (Prentice Hall, 1998).

[72] K. S. Yee, "Numerical solution of initial boundary value problems involving Maxwell's equations in isotropic media," IEEE Trans. Antennas Propag. **14**, 302–307 (1966).

[73] R. Courant, K. Friedrichs, and H. Lewy, "Uber die partiellen differenzengleichungen der mathematischen physik," Math. Ann. **100**, 32–74 (1928).

[74] R. Courant, K. Friedrichs, and H. Lewy, "On the partial difference equations of mathematical physics," IBM J. Res. Dev. **11**, 215–234 (1967).

[75] M. Stepanova and S. Dew, *Nanofabrication: Techniques and Principles* (Springer, 2012).

[76] S. A. Campbell, *Fabrication Engineering at the Micro- and Nanoscale (4th Edition)* (Oxford press, 2012).

[77] S. Franssila, *Introduction to Microfabrication* (John Wiley & Sons, 2004).

[78] C. Vieu, F. Carcenac, A. Pepin, Y. Chen, M. Mejias, A. Lebib, L. Manin-Ferlazzo, L. Couraud, and H. Launois, "Electron beam lithography: Resolution limits and applications," Appl. Surf. Sci. **164**, 111–117 (2000).

[79] A. A. Tseng, K. C., C. D. Chen, and K. J. Ma, "Electron beam lithography in nanoscale fabrication: Recent development," IEEE Trans. Electronics Packaging Manufacturing **26**, 141–149 (2003).

[80] E. L. Hu, D. M. Tennant, R. E. Howard, L. D. Jackel, and P. Grabbe, "Vertical silicon membrane arrays patterned with tri-level E-beam resist," J. Electron. Mater. **11**, 883–888 (1982).

[81] H. Akhavan, W. T. Lau, C. Nicholaou, R. Schilling, R. Gad, and O. Levi, "A new scheme for improvement of index of refraction detection limit in 2D photonic crystals," in "CLEO: 2013," (Optical Society of America, 2013), p. CTh3J.8.

[82] J. O. Grepstad, P. Kaspar, O. Solgaard, I.-R. Johansen, and A. S. Sudbø, "Optical imaging system designed for biosensing using a photonic crystal membrane to detect nanoparticles," in "Imaging and Applied Optics Technical Papers," (Optical Society of America, 2012), p. IM4C.2.

[83] J. O. Grepstad, P. Kaspar, O. Solgaard, I.-R. Johansen, and A. S. Sudbø, "Enhanced scattering from nano-particles trapped in photonic crystal membranes," in "International Conference on Optical MEMS and Nanophotonics (OMN)," (2012), pp. 21–22.

[84] C. F. Bohren and D. R. Huffman, *Absorbtion and Scattering of Light by Small Particles* (John Wiley and Sons, Inc., 1998).

[85] H. Hertz, "The forces of electric oscillations treated according to Maxwell's theory," Nature **39**, 402–404 (1889). English translation of Weidemann's Ann. 36, 1 (1889).

[86] J. D. Jackson, *Classical Electrodynamics (3rd Edition)* (Wiley, 1999).

[87] J. A. Stratton, *Electromagnetic Theory* (McGRAw-Hill book company, 1941).

[88] J. M. Senior, *Optical Fiber Communications* (Prentice Hall, 1985).

[89] M. Born and E. Wolf, *Principles of Optics: Electromagnetic Theory of Propagation, Interference and Diffraction of Light (6th Edition)* (Cambridge University Press, 1980).

[90] H. Ehrenreich, H. R. Philipp, and B. Segall, "Optical properties of aluminum," Phys. Rev. **132**, 1918–1928 (1963).

[91] S. Kim, S. Hadzialic, A. S. Sudbø, and O. Solgaard, "Reflectivity and polarization dependence of polysilicon single-film broadband photonic crystal micro-mirrors," Opt. Express **20**, 6306–6315 (2012).

[92] Thorlabs. Holographic Wire Grid Polarizers, http://www.thorlabs.com, visited 07.01.2014.

[93] Thorlabs. Economy Laminated Film Polarizers, http://www.thorlabs.com, visited 07.01.2014.

[94] BlackVelvet. http://www.edmundoptics.com/lab-production/general-tools/light-absorbing-black-out-material/1502, visited 07.01.2014.

[95] C. Palmer, "Diffraction grating handbook (5th edition)," http://www.gratinglab.com/Information/Handbook/Handbook.aspx, visited 07.01.2014 (2005). First edition by Erwin Loewen.

[96] A. L. Coldren and S. W. Corzine, *Diode Lasers and Photonic Integrated Circuits (2nd Edition)* (Wiley, 2012).

[97] R. F. Pierret, *Semiconductor Device Fundamentals* (Addison-Wesley Publishing Company, Inc., 1996).

[98] J. Nakamura, *Image Sensors and Signal Processing for Digital Still Cameras (Optical Science and Engineering)* (Taylor and Francis, 2005).

[99] D. B. Murphy, *Fundamentals of Light Microscopy and Electronic Imaging* (Wiley-Liss, Inc., 2001).

[100] J. Mertz, *Introduction to Optical Microscopy* (Roberts and Company Publishers, 2010).

[101] J. O. Grepstad, P. Kaspar, O. Solgaard, I.-R. Johansen, and A. Sudbø, "Single nano-particle sensing exploiting crossed polarizers to improve the signal-to-noise ratio," in "CLEO: 2013," (Optical Society of America, 2013), p. CM1M.2.

[102] J. O. Grepstad, M. Greve, T. Reisinger, and B. Holst, "Nano-structuring on free-standing, dielectric membranes using E-beam lithography," J. Vac. Sci. and Tech. B **31**, 06F402 (2013).

Chapter 6

List of publications

Journal papers

- **Paper A**:
  J. O. Grepstad, P. Kaspar, O. Solgaard, I.-R. Johansen, and A. S. Sudbø, "Photonic-crystal membranes for optical detection of single nano-particles, designed for biosensor application," Optics Express **20**, 7954–7965 (2012).

- **Paper B**:
  J. O. Grepstad, M. M. Greve, T. Reisinger, and B. Holst, "Nano-structuring on free-standing, dielectric membranes using electron-beam lithography," Journal of Vacuum and Science Technology B **31**, 06F402 (2013).

- **Paper C**:
  J. O. Grepstad, M. M. Greve, B. Holst, I.-R. Johansen, O. Solgaard, and A. Sudbø, "Finite-size limitations on quality factor of guided resonance modes in 2d photonic crystals," Optics Express **21**, 23640–23654 (2013).

- **Paper D**:
  J. O. Grepstad, P. Kaspar, I.-R. Johansen, O. Solgaard, and A. Sudbø, "Detection of single nano-defects in photonic crystals between crossed polarizers," Optics Express **21**, 31375–31389 (2013).

Conference papers

Presenting author in bold.

- **Paper E**:
  J. O. Grepstad, P. Kaspar, O. Solgaard, I.-R. Johansen, and A. S. Sudbø,

"Optical imaging system designed for biosensing using a photonic crystal membrane to detect nanoparticles," in *Proceedings of Imaging and Applied Optics Technical Papers 2012*, p. IM4C.2.

- **Paper F**:
  J. O. Grepstad, P. Kaspar, O. Solgaard, I.-R. Johansen, and A. S. Sudbø, "Enhanced scattering from nano-particles trapped in photonic crystal membranes," in *Proceedings of the International Conference on Optical MEMS and Nanophotonics (OMN) 2012*, pp. 21–22.

- **Paper G**:
  J. O. Grepstad, P. Kaspar, O. Solgaard, I.-R. Johansen, and A. Sudbø, "Single nano-particle sensing exploiting crossed polarizers to improve the signal-to-noise ratio," in *Proceedings of CLEO: Science & Innovations 2013*, p. CM1M.2.

Conference abstracts and poster presentations

Presenting author in bold.

- J. O. Grepstad, P. Kaspar, O. Solgaard, I.-R. Johansen, and **A. Sudbø**, "Gain in Rayleigh scattering from nanoparticles trapped in photonic crystal membranes," poster presentation at the *European Optical Society Annual Meeting 2012*

- **J. O. Grepstad**, M. M. Greve, T. Reisinger, and B. Holst, "Advances on e-beam fabrication of photonic crystal membranes," poster presentation at the *57th International Conference on Electron, Ion, and Photon Beam Technology and Nanofabrication 2013*

Patents and off topic scientific contributions

- Photonic Crystal Sensor, US2012002913 (2012).

- Photonic Crystal Sensor, NO20091226 (2009).

- Protein specific detection method, NO20120916, Patent pending.

- J. O. Grepstad and J. Skaar, "Total internal reflection and evanescent gain," Optics Express **19**, 21404–21418 (2011).

- J. O. Grepstad and J. Skaar, "Does evanescent gain exist?," in *Proceedings of XXXth URSI General Assembly and Scientific Symposium 2011*, pp. 1–4.

Chapter 7

Contributions in publications

Paper A

J. O. Grepstad, P. Kaspar, O. Solgaard, I.-R. Johansen, and A. S. Sudbø, "Photonic-crystal membranes for optical detection of single nano-particles, designed for biosensor application," Optics Express **20**, 7954–7965 (2012).

My contribution: Contributed in the developing the sensor concept. Coordinated and did parts of the fabrication, performed all simulations, built the optical setup and did the optical characterization of final devices, made all figures and wrote the paper.

Paper B

J. O. Grepstad, M. M. Greve, T. Reisinger, and B. Holst, "Nano-structuring on free-standing, dielectric membranes using electron-beam lithography," Journal of Vacuum and Science Technology B **31**, 06F402 (2013).

My contribution: Involved in developing the fabrication process and did part of the fabrication, made one figure, and contributed in writing of the paper.

Paper C

J. O. Grepstad, M. M. Greve, B. Holst, I.-R. Johansen, O. Solgaard, and A. Sudbø, "Finite-size limitations on quality factor of guided resonance modes in 2d photonic crystals," Optics Express **21**, 23640–23654 (2013).

My contribution: Conceived the idea, did all simulations, collaborated with Martin M. Greve in collecting experimental data, made all figures, and wrote the paper.

Paper D

J. O. Grepstad, P. Kaspar, I.-R. Johansen, O. Solgaard, and A. Sudbø, "Detection of single nano-defects in photonic crystals between crossed polarizers," Optics Express (2013).

My contribution: Designed and performed the simulations, built the optical setup and collected all experimental data, made all figures, and wrote the paper.

Paper E

J. O. Grepstad, P. Kaspar, O. Solgaard, I.-R. Johansen, and A. S. Sudbø, "Optical imaging system designed for biosensing using a photonic crystal membrane to detect nanoparticles," in *Proceedings of Imaging and Applied Optics Technical Papers 2012*, pp. IM4C.2.

My contribution: Designed and performed the experiment, made all figures and wrote the paper and presented (oral) the paper.

Paper F

J. O. Grepstad, P. Kaspar, O. Solgaard, I.-R. Johansen, and A. S. Sudbø, "Enhanced scattering from nano-particles trapped in photonic crystal membranes," in *Proceedings of the International Conference on Optical MEMS and Nanophotonics (OMN) 2012*, pp. 21–22.

My contribution: Contributed in developing the concept, did all simulations, collected all experimental data, made all figures, wrote and presented (oral) the paper.

Paper G

J. O. Grepstad, P. Kaspar, O. Solgaard, I.-R. Johansen, and A. Sudbø, "Single nano-particle sensing exploiting crossed polarizers to improve the signal-to-noise

ratio," in *Proceedings of CLEO: Science & Innovations 2013*, pp. CM1M.2.

My contribution: This paper is based on the preliminary results leading to Paper D. See Paper D for technical contributions. Wrote and presented (oral) the paper.

Off topic scientific contributions

J. O. Grepstad and J. Skaar, "Total internal reflection and evanescent gain," Optics Express **19**, 21404–21418 (2011).

My contribution: Contributed with analytical calculations solidifying the presented theoretical results, and wrote supplementary information.

J. O. Grepstad and J. Skaar, "Does evanescent gain exist?," in *Proceedings of XXXth URSI General Assembly and Scientific Symposium 2011*, pp. 1–4.

My contribution: Invited paper on the hypothesis presented in Paper H. See Paper H for contributions. Wrote and presented (oral) paper.

Paper A

Photonic-crystal membranes for optical detection of single nano-particles, designed for biosensor application

elink: Paper A

Photonic-crystal membranes for optical detection of single nano-particles, designed for biosensor application

Jon Olav Grepstad,[1,2,3,*] **Peter Kaspar,**[4] **Olav Solgaard,**[5] **Ib-Rune Johansen,**[2] **and Aasmund S. Sudbø**[6,3]

[1]*Department of Electronics and Telecommunications, Norwegian University of Science and Technology, NO-7491 Trondheim, Norway*
[2]*SINTEF ICT, Microsystems and Nanotechnology, NO-0373, Norway*
[3]*University Graduate Center, NO-2027 Kjeller, Norway*
[4]*Electronics Laboratory, ETH Zurich, CH-8092 Zrich, Switzerland*
[5]*E.L. Ginzton Laboratory, Stanford University, CA-94305, USA*
[6]*Department of Physics, University of Oslo, NO-0316, Norway*
[*]*jonolav.grepstad@sintef.no*

Abstract: A sensor designed to detect bio-molecules is presented. The sensor exploits a planar 2D photonic crystal (PC) membrane with sub-micron thickness and through holes, to induce high optical fields that allow detection of nano-particles smaller than the diffraction limit of an optical microscope. We report on our design and fabrication of a PC membrane with a nano-particle trapped inside. We have also designed and built an imaging system where an optical microscope and a CCD camera are used to take images of the PC membrane. Results show how the trapped nano-particle appears as a bright spot in the image. In a first experimental realization of the imaging system, single particles with a radius of 75 nm can be detected.

OCIS codes: (220.0220) Optical design and fabrication; (280.4788) Optical sensing and sensors

References and links

1. B. Bohunicky and S. A. Mousa, "Biosensors: the new wave in cancer diagnosis," Nanotech. Sci. Appl. **4**, 1–10 (2010).
2. T. Reichlin, W. Hochholzer, S. Bassetti, S. Steuer, C. Stelzig, S. Hartwiger, S. andBiedert, N. Schaub, C. Buerge, M. Potocki, M. Noveanu, T. Breidthardt, R. Twerenbold, K. Winkler, R. Bingisser, and C. Mueller, "Early diagnosis of myocardial infarction with sensitive cardiac troponinassays," N. Engl. J. Med. **361**, 858–867 (2009).
3. P. Stefaniuk, J. Cianciara, and A. Wiercinska-Drapalo, "Present and future possibilities for early diagnosis of hepatocellular carcinoma," World J. Gastroenterol. **16**, 418–424 (2010).
4. M. F. Pineda, L. L. Chan, T. Kuhlenschmidt, C. J. Choi, M. Kuhlenschmidt, and B. T. Cunningham, "Rapid specific and label-free detection of porcine rotavirus using photonic crystal biosensors," IEEE Sens. J. **9**, 470–477 (2009).
5. A. A. Yanik, M. Huang, O. Kamohara, A. Artar, T. W. Geisbert, J. H. Connor, and H. Altug, "An optofluidic nanoplasmonic biosensor for direct detection of live viruses from biological media," Nano Lett. **10**, 4962–4969 (2010).
6. Product info: http://www.axis-shield.com, visited March 15, 2012.
7. D. W. G. Morrison, M. R. Dokmeci, U. Demirci, and A. Khademhosseini, *Biomedical Nanostructures* (John Wiley & Sons, Inc., 2008). Chap. 17.
8. L. Li, "Recent development of micromachined biosensors," IEEE Sens. J. **11**, 305–311 (2011).

#161834 - $15.00 USD Received 19 Jan 2012; revised 15 Mar 2012; accepted 16 Mar 2012; published 21 Mar 2012

9. Y. Cui, Q. Wei, H. Park, and C. M. Lieber, "Nanowire nanosensors for highly sensitive and selective detection of biological and chemical species," Science **293**, 1289–1292 (2001).
10. Y. L. Bunimovich, Y. S. Shin, W. Yeo, M. Amori, G. Kwong, and J. R. Heath, "Quantitative real-time measurements of dna hybridization with alkylated nonoxidized silicon nanowires in electrolyte solution," J. Am. Chem. Soc. **128**, 16323–16331 (2006).
11. C. A. Savran, S. M. Knudsen, A. D. Ellington, and S. R. Manalis, "Micromechanical detection of proteins using aptamer-based receptor molecules," Anal. Chem. **76**, 3194–3198 (2004).
12. J. Fritz, M. K. Baller, H. P. Lang, H. Rothuizen, P. Vettiger, E. Meyer, H. J. Gntherodt, C. Gerber, and J. K. Gimzewski, "Translating biomolecular recognition into nanomechanics," Science **288**, 316–318 (2000).
13. A. K. Gupta, P. R. Nair, D. Akin, M. R. Ladisch, S. Broyles, M. A. Alam, and R. Bashir, "Anomalous resonance in a nanomechanical biosensor," Proc. Natl. Acad. Sci. U. S. A. **103**, 13362–13367 (2006).
14. E. Stern, R. Wagner, F. J. Sigworth, R. Breaker, T. M. Fahmy, and M. A. Reed, "Importance of the debye screening length on nanowire field effect transistor sensors," Nano Lett. **7**, 3405–3409 (2007).
15. J. Lee, K. Icoz, A. Roberts, A. D. Ellington, and C. A. Savran, "Diffractometric detection of proteins using microbead-based rolling circle amplification," Anal. Chem. **82**, 197–202 (2010).
16. X. Fan, I. M. White, S. I. Shopova, H. Zhu, J. D. Suter, and Y. Sun, "Sensitive optical biosensors for unlabeled targets: a review," Anal. Chim. Acta **620**, 8 – 26 (2008).
17. F. Hsiao and C. Lee, "Computational study of photonic crystals nano-ring resonator for biochemical sensing," IEEE Sens. J. **10**, 1185–1191 (2010).
18. J. G. Ruperez, V. Toccafondo, M. J. Bañuls, J. G. Castelló, A. Griol, S. Peransi-Llopis, and A. Maquieira, "Label-free antibody detection using band edge fringes in soi planar photonic crystal waveguides in the slow-light regime," Opt. Express **18**, 24276–24286 (2010).
19. M. R. Lee and P. M. Fauchet, "Nanoscale microcavity sensor for single particle detection," Opt. Lett. **32**, 3284–3286 (2007).
20. S. Zlatanovic, L. W. Mirkarimi, M. M. Sigalas, M. A. Bynum, E. Chow, K. M. Robotti, G. W. Burr, S. Esener, and A. Grot, "Photonic crystal microcavity sensor for ultracompact monitoring of reaction kinetics and protein concentration," Sens. Actuator B **141**, 13–19 (2009).
21. Q. Quan, I. B. Burgess, S. K. Y. Tang, D. L. Floyd, and M. Loncar, "High-q, low index-contrast polymeric photonic crystal nanobeam cavities," Opt. Express **19**, 22191–22197 (2011).
22. S. Lal, S. Link, and N. J. Halas, "Nano-optics from sensing to waveguiding," Nat. Photonics **1**, 641–648 (2007).
23. S. W. Bishnoi, C. J. Rozell, C. S. Levin, M. K. Gheith, B. R. Johnson, D. H. Johnson, and N. J. Halas, "All-optical nanoscale ph meter," Nano Lett. **6**, 1687–1692 (2006).
24. J. N. Anker, W. P. Hall, O. Lyandres, N. C. Shah, J. Zhao, and R. P. Duyne, "Biosensing with plasmonic nanosensors," Nat. Mater. **7**, 442–453 (2008).
25. J. C. Yang, J. Ji, J. M. Hogle, and D. N. Larson, "Multiplexed plasmonic sensing based on small-dimension nanohole arrays and intensity interrogation," Biosens. Bioelectron. **24**, 2334–2338 (2009).
26. A. Lesuffleur, H. Im, N.-C. Lindquist, and S. H. Oh, "Periodic nanohole arrays with shape-enhanced plasmon resonance as real-time biosensors," Appl. Phys. Lett. **90**, 243110 (2007).
27. M. E. Stewart, N. H. Mack, V. Malyarchuk, J. A. N. T. Soares, T. W. Lee, S. K. Gray, R. G. Nuzzo, and J. A. Rogers, "Quantitative multispectral biosensing and 1d imaging using quasi-3d plasmonic crystals," Proc. Natl. Acad. Sci. U. S. A. **103**, 17143–17148 (2006).
28. A. G. Brolo, R. Gordon, B. Leathem, and K. L. Kavanagh, "Surface plasmon sensor based on the enhanced light transmission through arrays of nanoholes in gold films," Langmuir **20**, 4813–4815 (2004).
29. M. Kanskar, P. Paddon, V. Pacradouni, R. Morin, A. Busch, J. F. Young, S. R. Johnson, J. MacKenzie, and T. Tiedje, "Observation of leaky slab modes in an air-bridged semiconductor waveguide with a two-dimensional photonic lattice," Appl. Phys. Lett. **70**, 1438–1440 (1997).
30. S. Fan and J. D. Joannopoulos, "Analysis of guided resonances in photonic crystal slabs," Phys. Rev. B **65**, 235112 (2002).
31. M. E. Beheiry, V. Liu, S. Fan, and O. Levi, "Sensitivity enhancement in photonic crystal slab biosensors," Opt. Express **18**, 22702–22714 (2010).
32. Commercially available software supplied by KJ Innovation, http://software.kjinnovation.com/GD-Calc.html visited Sept. 15, 2011.
33. Z. Popovic and B. D. Popovic, *Introductory Electromagnetics* (Prentice Hall, Inc., 2000).
34. M. J. Banuls, V. Gonzlez-Pedro, C. A. Barrios, R. Puchades, and A. Maquieira, "Selective chemical modification of silicon nitride/silicon oxide nanostructures to develop label-free biosensors," Biosens. Bioelectron. **25**, 1460–1466 (2010).
35. C. F. Bohren and D. R. Huffman, *Absorbtion and Scattering of Light by Small Particles* (John Wiley and Sons, Inc., 1998). Chap. 5.
36. J. Vrs, "The density and refractive index of adsorbing protein layers," Biophys. J. **87**, 553–561 (2004).
37. M. Huang, A. A. Yanik, T. Y. Chang, and H. Altug, "Sub-wavelength nanofluidics in photonic crystal sensors," Opt. Express **17**, 24224–24233 (2009).
38. M. G. Hale and M. R. Querry, "Optical constants of water in the 200-nm to 200-µm wavelength region," Appl.

#161834 - $15.00 USD Received 19 Jan 2012; revised 15 Mar 2012; accepted 16 Mar 2012; published 21 Mar 2012

1. Introduction

To make medical diagnosis more efficient and accurate, better instruments for specific detection of common pathogens are needed [1–3]. Accurate monitoring of contamination in sources of water- and food can prevent outbreak of disease [4]. Monitoring biological hazards has also been called for in the combat against bio-terrorism [5]. A solution to these challenges is sensors that can capture and detect very low concentrations of specific proteins, viruses, bacteria, etc., in samples where the concentration of non-targeted substances is many orders of magnitude higher. That is, biosensors with high specificity and sensitivity.

Commercially available instruments fit on a benchtop and detect a number of biological markers. Even hand-held devices are offered. Albumin, C-Reactive protein and lipid detection can be done with a stationary device the size of a shoe box [6], while hand-held glucose, fertility and pregnancy tests, can be bought in general pharmacies. By making sensors efficient, cheap and small, we provide solutions for point-of-care and in-home testing. The use of expensive and time-consuming labs run by professional personnel can hence be avoided.

Micro- and nano-fabrication techniques can in general provide devices that are small, reliable and cheap, and recent developments suggest that the next generation biosensors will be made exploiting this technology [7,8]. While platforms using electric or mechanical transducers exist [9–12], biochemical sensor platforms with optical readout seem particularly promising. Optical readout provides compatibility with the wet environment presented in a biological system [13, 14], and can also be done without physically interconnecting the light source, transducer and light detector [4, 15].

Some of the most sensitive biosensors with optical readout today are based on dielectric photonic crystals (PCs) [16–21] and nanoplasmonics [22–28]. They all rely on surface chemistry to capture specific target molecules. Specificity is hence mainly provided by chemical means. The sensitivity is limited by transducer design, where the fundamental aim is to maximize the concentration of light where captured target molecules settle.

For dielectric PC sensors, their ability to concentrate light into a very small detection volume has been exploited to demonstrate sensitivities close to a single molecule [19, 20]. However, these schemes have strict alignment requirements, because light must be coupled into single-mode waveguides in order to lead light to the detection volume . Alignment is an expensive, time-consuming process, rendering such sensors unsuitable for point-of-care applications. Sensors based on nanoplasmonics, on the other hand, are tolerant regarding alignment and still show impressive sensitivities [22–28].

In this paper we propose to combine the convenient light coupling found in nanoplasmonic sensors and the high electromagnetic field intensities obtainable in dielectric PCs, in a dielectric PC membrane. PC membranes are in general comprised of a thin slab with a periodic in-plane variation in permittivity. They can in many ways be considered as regular slab waveguides, but in addition to having a series of guided modes, they also exhibit a group of modes called guided resonances [29, 30]. Coupling to guided resonances can be done by normal incidence light, and produces high fields in the membrane [31]. A small particle placed in this field will absorb energy from the guided-resonance mode field. The particle will reradiate the absorbed energy in all directions. An adapted imaging system can then refocus the radiation on a CCD sensor, giving rise to a bright spot in the resulting image.

A novel planar 2D dielectric PC membrane has been developed to demonstrate this detection principle. We present the basic working principle, processing techniques and preliminary results from optical characterization. Detection of a single particle with $\sim$75 nm radius is demonstrated.

#161834 - $15.00 USD Received 19 Jan 2012; revised 15 Mar 2012; accepted 16 Mar 2012; published 21 Mar 2012

2. Design of photonic crystal membrane and working principle

The basic elements of the sensor are summarized in Fig. 1. At the core of the sensor there is a planar dielectric membrane with through holes. Fig. 1(A) illustrates how the membrane is free-standing, permitting gas or fluid samples to be physically pushed through the holes in the membrane. The optical effect of two nano-particles trapped inside the membrane is illustrated in Fig. 1(B). It has been simplified to illustrate the idea that nano-particles are detected by a CCD camera as bright spots on a dark background. We will further explain how this concept can be realized.

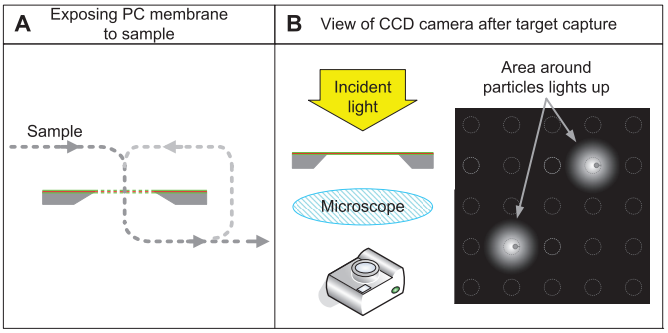

Fig. 1. A summary of how the sensor works. (A) A sample is pumped through the PC membrane and two particles are caught in the membrane holes. (B) Captured particles are detected as bright spots on a dark background by an optical microscope and a CCD-camera.

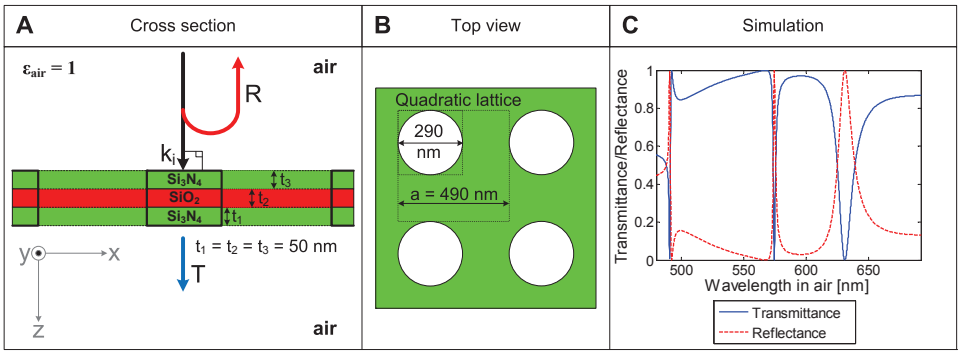

Fig. 2. (A) Cross section and (B) top view of the designed photonic crystal membrane. (C) Simulated transmittance and reflectance for a normal incidence plane wave is given as a function of wavelengths from 490 to 692 nm.

2.1. Simulations of perfectly periodic photonic crystal membranes

The current PC membrane is comprised of holes arranged in a square lattice, nominally with period $a = 490$ nm and radius $r = 145$ nm. As illustrated in Fig. 2(A) and (B), the holes are etched in a three layered thin-film stack, formed by Si_3N_4 and SiO_2 with nominal thicknesses $t_1 = t_2 = t_3 = 50$ nm.

The spectral response of the PC membrane, to linearly polarized normal incidence plane waves, has been simulated using rigorously coupled wave analysis (RCWA) in 3D, implemented in a Matlab based simulation software [32]. The spectral bandwidth of the simulation

#161834 - $15.00 USD Received 19 Jan 2012; revised 15 Mar 2012; accepted 16 Mar 2012; published 21 Mar 2012

is bound by:

$$a < \lambda < \sqrt{2}a, \tag{1}$$

where a is the lattice period and λ is the wavelength in the medium surrounding the membrane. We motivate this choice in the text below.

Plots of transmittance and reflectance as a function of wavelength are given in Fig. 2(C) for the structure in Fig. 2(A) and (B). Asymmetric resonant features, known as Fano lines, appear in the spectrum at 491, 575 and 631 nm. They can be interpreted as a slowly varying response, corresponding to what is found in homogeneous slabs, interfering with three fast varying Lorentzian shaped signals, formed as a result of incoming light coupling to guided resonance modes [30]. Consequently, we expect the electromagnetic field in the membrane to be amplified in the spectral vicinity of the three wavelengths 491, 575 and 631 nm.

Full field simulations, for normal incidence linearly polarized waves, have been performed for the guided resonance mode at 631 nm. Results show how the polarization is approximately conserved. Moreover, light couples to a "TE-like" guided resonance mode field that concentrates in the holes. This is intuitive, since the electromagnetic field is mainly polarized in the membrane plane and the normal component of the electric displacement field must be continuous at air-membrane-boundaries [33]. The field hence concentrates in the holes as a result of permittivity contrast between the membrane materials and the air in the holes. An increase in contrast between air and the membrane material, will in general induce higher electromagnetic fields in the holes. Note that, the complex geometry of three thin films is not chosen based on optical properties. Using this structure, the center layer, inside of holes, is chemically different than the membrane outer surface. In a biosensing application, surface chemistry can hence be used to functionalize the inside of holes to capture target particles, while the membrane outer surface can be passivated [34]. In this way, target particles tend to stick at positions with maximum optical field intensity, ensuring maximal sensitivity.

Requiring $\lambda > a$, the discrete translation symmetry in the PC membrane ensures that there are no diffracted waves for normal incidence waves. In that case, the optical response of the PC membrane is particularly simple. There are only two non-evanescent waves to which a normal incidence field can couple: One transmitted and one reflected wave, both with wave vectors normal to the membrane plane. The transmitted and reflected power is bound to the 0'th order of diffraction.

Placing a particle in the PC membrane breaks the discrete translation symmetry. Power is then no longer bound to the 0'th order of diffraction, but can appear also in higher diffraction orders. The details of this process are complicated, but can be greatly simplified by considering a particle of limited size. We will consider particles that are so small that the field distribution in the PC membrane is approximately unchanged by the presence of a particle in the membrane. The total optical response, as seen from a detector placed outside the membrane, is then a superposition of the scattered light from the particle on the transmitted and reflected wave.

2.2. Rayleigh scattering model for defects

The particle will scatter the field in its location, and as mentioned above, the field is approximately linearly polarized for normal incidence linearly polarized waves. To find the scattered power from the particle, we model the particle as a dielectric sphere with relative permittivity ε_p surrounded by a medium with permittivity ε_m, illuminated by a harmonic linearly polarized plane wave with amplitude E_p and vacuum wavelength λ. The sphere is assumed to be small, i.e.

$$r_p \ll \lambda/(2\pi\sqrt{\varepsilon_p}). \tag{2}$$

#161834 - $15.00 USD Received 19 Jan 2012; revised 15 Mar 2012; accepted 16 Mar 2012; published 21 Mar 2012

The sphere will scatter light, radiating a wave similar to that of an ideal dipole, a phenomenon known as Rayleigh scattering [35]. The total scattered power from one single sphere is

$$P_{\mathrm{R}} = \frac{4\pi}{3}\sqrt{\frac{\varepsilon_0}{\mu_0}}\left(\frac{2\pi}{\lambda}\right)^4 \left|\frac{\varepsilon_p - \varepsilon_m}{\varepsilon_p + 2\varepsilon_m}\right|^2 \varepsilon_m^{\frac{5}{2}} r_p^6 E_p^2. \tag{3}$$

In our context, this result is clearly an approximation. When the particle is placed inside a hole in a PC membrane, the induced electric dipole fields from the particle will induce dipoles in the hole wall. P_{R} must hence depend on the PC membrane geometry and the particle location. However, if we also impose the condition that $r_p \ll r$, where r is the radius of holes, and place the particle in the middle of a hole, the contribution from the particle dipole to the electric field inside the membrane is negligible. We can then use Eq. (3) with E_p representing the field in a membrane, at the location of the particle, with no particle present.

The scattered power, P_{R}, can then be considered as the potential change one single particle can constitute on a detector. Maximizing the sensitivity hence involves maximizing P_{R}. Investigating Eq. (3), we find that a variation in λ will maximally change P_{R} by a factor of 4 over the range of relevant values. In order to detect small particles, the parameter to maximize is hence E_p.

This involves designing a PC membrane that supports guided resonance modes that produce high electromagnetic field intensities in the PC membrane. In theory, the obtainable field intensity is limited by how small we can make the holes [30]. However, a reduction of the hole radius has two notable consequences. It is generally followed by a narrowing of the guided resonance bandwidth, and make the resonant modes sensitive to any changes from nominal design. Imperfect periodicity or general defects can cause narrow banded resonances to disappear in practice. Secondly, as the hole radius is reduced, the PC membrane will gradually become similar to a slab with waveguiding properties. Scattered light from a particle trapped in the PC membrane, will spread over a larger area as the radius of holes is reduced. The obtainable field intensity is hence set by processing accuracy, and the guided resonance field enhancement always comes with a trade-off in imaging resolution.

In conclusion, by working at wavelengths where harmonic linearly polarized normal incidence fields couple to guided resonance modes, PC membranes can be used to produce high electromagnetic field intensities. If they are small enough, particles trapped in the membrane can then be treated as dipole sources similar to ideal dipoles. Their scattered power is then described by Eq. (3).

A dipole source placed inside a PC membrane can couple light into guided modes and can be trapped in the membrane indefinitely. However, if $\lambda < \sqrt{2}a$, no guided modes can exist. Light can couple into guided resonance modes, but all the scattered power from a small particle will at some point exit the membrane and can potentially be picked up by a detector on the outside of the membrane. Moreover, if the particle can be treated as a source similar to an ideal dipole, it will radiate a spherical-like wave.

Spherical waves can be refocused to spots in an imaging plane. Picturing the membrane with a microscope with backside illumination and a CCD-camera, we hence expect pixels corresponding to the location of particles to appear as bright spots when incident light couples to guided resonance modes. The contrast will be dependent on the field amplitude and phase at the location of the particle, and the amplitude and phase of the scattered light relative to the transmitted wave.

As seen from a detector outside the membrane, it is not clear that a scattering particle trapped in a PC membrane radiates spherical-like waves. The distribution of scattered irradiation from the particle will be strongly influenced by the PC membrane dimensions and particle position. Scattered irradiation can also be partially guided by the PC membrane, to be spread over a

#161834 - $15.00 USD Received 19 Jan 2012; revised 15 Mar 2012; accepted 16 Mar 2012; published 21 Mar 2012

larger area. However, we will ignore these effects for now and see how the ideal dipole model can explain the measurement results.

3. Fabrication and experimental setup

Standard semiconductor production techniques were used to make a thin film stack of $Si_3N_4/SiO_2/Si_3N_4$ on 200 μm thick silicon wafers, with double-sided polishing. A film of Si_3N_4 was deposited using low pressure chemical vapor deposition (LPCVD). Next, the SiO_2 film was formed by poly-Si LPCVD, followed by thermal oxidation. Finally, another film of Si_3N_4 was deposited using LPCVD. Refractive index and thickness was measured with a HORIBA Jobin Yvon PZ2000 632.8 nm Laser ellipsometer and estimated by curve fitting using the least square method. Surface roughness was not measured.

A lithography step was performed to open a 700x700 μm square in the thin film stack, on the backside of the wafer. This was done with a period of 10 mm in two dimensions before the wafer was diced into 10x10 mm chips. On the front side of the chips, E-beam lithography with a 30kV Raith150 system and reactive ion etching (RIE) with a Plasmalab System80Plus from Oxford Instruments was done to produce the PCs. The nominal design was a quadratic pattern with a hole radius of $r = 145$ nm and a lattice period of $a = 490$ nm.

The PC membranes were freed by etching in tetramethylammonium hydroxide (TMAH) at a temperature of 80 ^{o}C. The etch rates of Si and Si_3N_4 were 26.6$\pm$1 μm/hour and 5$\pm$1 Å/hour, respectively. The total etching time was 490 min. A 39 min over etch was done to ensure that no Si was left on the backside (cavity side) of the membranes. The front side was not protected during etching. Referring to Fig. 2, layer 3 was hence etched for 490 min, and layer 1 nominally for 39 min. All chips were inspected by scanning electron microscopy (SEM). SEM imaging software was used to measure the period and radius of the PCs.

Finalized membranes were characterized using a custom built optical setup. The setup is illustrated in Fig. 3. It is comprised of a standard 35W halogen lamp, an Oriel Cornerstone 130 1/8 m Monochromator, an Olympus BX61 TRF microscope and an Olympus F-view II CCD camera. The light from the halogen source is guided via the monochromator by a set of lenses and optical fibers, to provide the microscope with collimated monochromatic backside illumination with normal incidence and divergence $0.01 - 0.02$ rad. The bandwidth of the monochromator is 1.5$\pm$0.5 nm. The CCD camera only sees the transmitted light, and the reflected light is discarded. The used microscope objective is an Olympus UPlanFL 40x/0.75 NA. At this magnification, one pixel on the CCD screen corresponds to 0.16x0.16 μm^2 on the membrane surface.

4. Results and discussion

Processed PC membranes were free-standing in the center of 1 cm^2 chips. Chip and PC dimensions are illustrated in Fig. 4(A). The refractive index at 638.4 nm was measured to 1.998$\pm$0.01 and 1.464$\pm$0.01 for Si_3N_4 and SiO_2, respectively. No optical quality degradation due to mechanical stresses in the thin films was observed. Stress in the Si_3N_4 is tensile and will overcompensate the compressive stress in the SiO_2, stretching the membrane and preventing deformation. An incline of the hole walls and rounded edges are pointed out in Fig. 4(A). These features have not been quantified, but are to some extent unavoidable with the current methods used to free etch the membranes.

SEM images in Fig. 4(B) show a real PC membrane and reveal two defects in the PC. In the lower right corner of the image, a lattice defect that extends 2-3 periods in the vertical direction and 1.5 in the horizontal. A nano-particle with radius 75$\pm$25 nm has settled inside a hole shown in the lower left of Fig. 4(B). These defects were introduced non-intentionally during the fabrication process, but they are well-suited objects for preliminary studies.

#161834 - $15.00 USD Received 19 Jan 2012; revised 15 Mar 2012; accepted 16 Mar 2012; published 21 Mar 2012

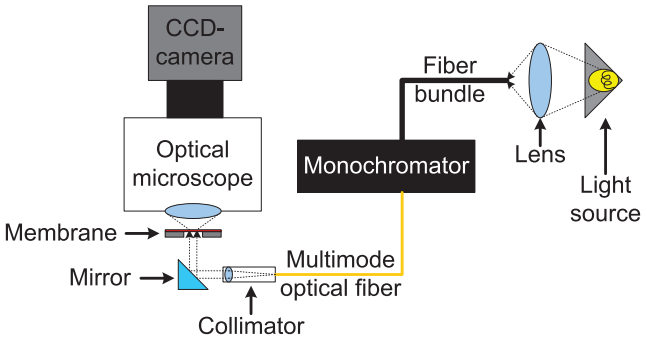

Fig. 3. A halogen light source connected to a monochromator provides the microscope with backside illumination with tunable wavelength. A photonic crystal membrane is placed in the field of view and imaged with a CCD-camera. Transmitted intensity through the membrane can hence be measured with spatial resolution, and as a function of wavelength.

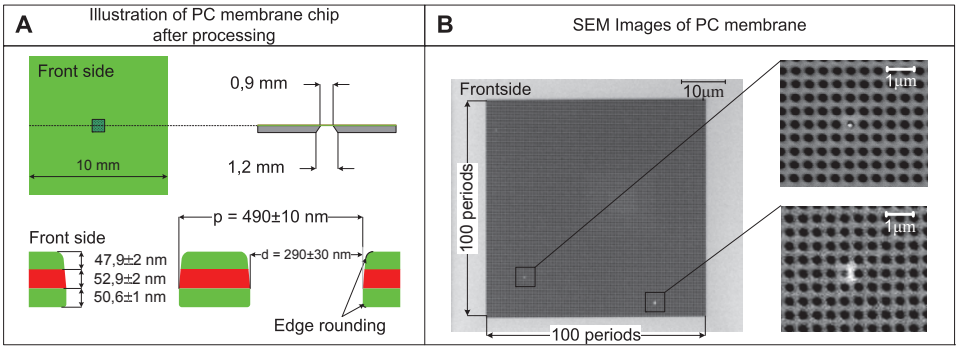

Fig. 4. (A) Illustration of photonic crystal (PC) membrane chip after processing. (B) SEM images show top views of the PC membrane. Two defects in the PC membrane have been magnified.

We have not determined the material composition of the defects, so their permittivity is not known. Based on the materials present in our fabrication facilities, it is limited to a range between 2.25 and 12.25. The lower limit is comparable to the permittivity of relevant biological target particles, which typical have a permittivity between 2 and 2.5 [36]. Using Eq. (3) and air as the surrounding media, $\varepsilon_m \approx 1$, we can then find a relative measure of the scattered intensity from the trapped nano-particle compared to a relevant biological particle of the same size. In the worst case, the biological particle has permittivity 2, while the nano-particle trapped in the PC membrane has a permittivity of 12.25. In that case, the scattering intensity will be a factor of 10 higher for the nano-particle trapped in the PC membrane.

Images were taken with the optical setup in Fig. 3 at wavelengths between 490 and 692 nm. The set of pixels M, defined in Fig. 5, was averaged to provide a measure of the average transmittance of the PC membrane. The result is given in Fig. 6(A).

Two dips in transmission can be seen around 566 and 630 nm. They correspond to the dips found in simulations represented by Fig. 2(C) around 575 and 631 nm, and imply that the fabricated structure supports guided resonance modes. We can hence expect to have an amplification of the field inside the membrane in the spectral vicinity of wavelengths 566 and 630 nm. The difference between measured and simulated results, can be attributed to the devi-

#161834 - $15.00 USD Received 19 Jan 2012; revised 15 Mar 2012; accepted 16 Mar 2012; published 21 Mar 2012

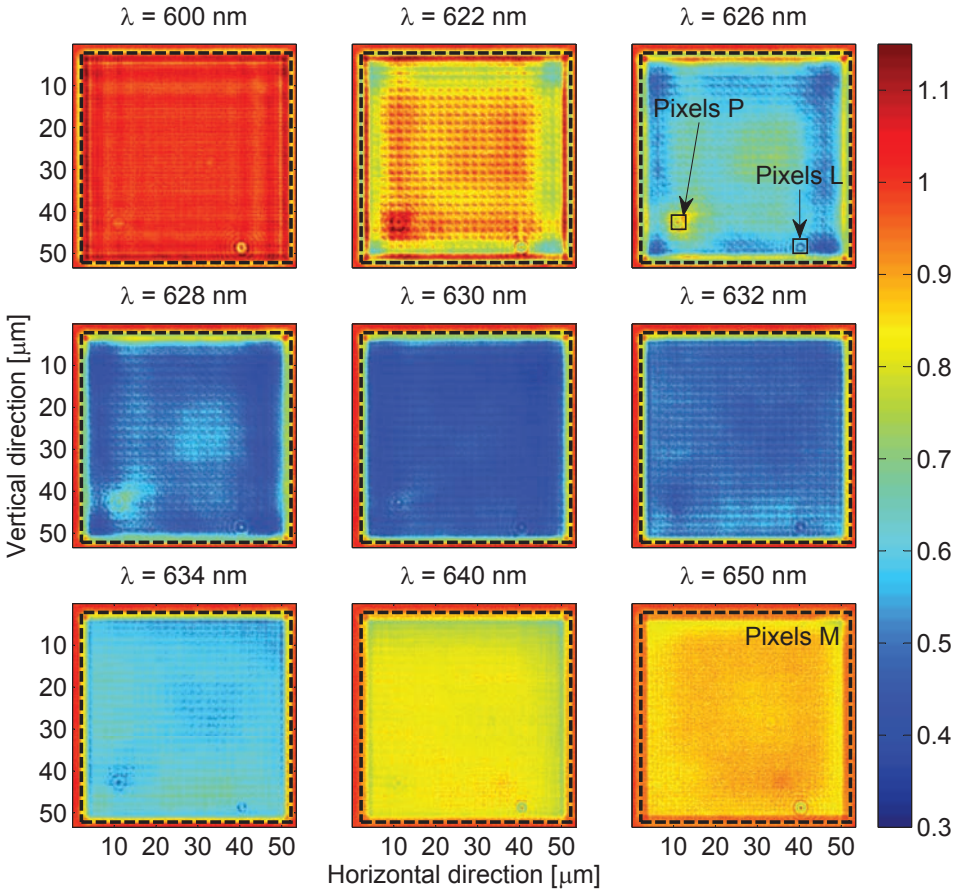

Fig. 5. Images of the PC membrane taken with the CCD camera at nine different wavelengths. The dashed black line bounds pixels M and correspond to the hole matrix. Pixels P and L are centered at pixels corresponding to the two defects in the PC membrane. The color bar shows pixel values, normalized with respect to the transmitted intensity recorded without the membrane present, at each wavelength respectively.

#161834 - $15.00 USD Received 19 Jan 2012; revised 15 Mar 2012; accepted 16 Mar 2012; published 21 Mar 2012

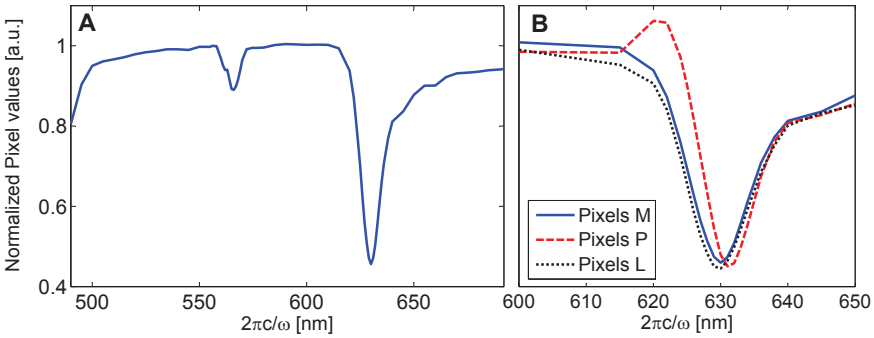

Fig. 6. (A) Average value of pixels M, defined in Fig. 5, corresponding to the transmittance of the PC membrane as a function of wavelength. (B) The average of pixels M is compared to average values of pixels P and L. Pixels P and L are also defined in Fig. 5, and correspond to the trapped nano-particle and lattice defect, respectively. Pixel values of the CCD camera have been normalized with respect to the transmitted intensity recorded without the membrane present, at each wavelength respectively.

ation from nominal thickness and inhomogeneities in hole radius and lattice period over the PC membrane, caused by limitations in fabrication accuracy. Moreover, the simulations are based on perfectly plane monochromatic incident waves. In realty, the output of monochromator has a finite bandwidth and the collimated beam a divergence. In measured transmittance, this will appear as broadening of the guided resonance bandwidths and an increase of peak values for the two dips.

From section 2.2, we then expect small particles in the membrane to show increased scattering and appear as bright spots on the CCD camera, provided that the particles are size limited by Eq. (2) and $r_p << r$, where r is the radius of holes. In this respect both the lattice defect and the nano-particle are too large, and the approximation that the field distribution in the membrane is unaffected by their presence is not necessarily correct.

Indications of the latter can be seen for the lattice defect. A selection of nine images, taken at nine different wavelengths between 600 and 650 nm, is given in Fig. 5. They show the view of the CCD camera, as the wavelength is scanned past the dip centered at $\lambda = 630$ nm. The large lattice defect is visible on all pictures, but there is no clear indication of increased scattering as a function of coupling to guided resonance modes. To the contrary, it stands out more clearly at 600 nm, where we expect the field in the membrane not to be amplified. Its effect is also not especially large compared to its size, indicating that what we see is simply the particle being imaged. In conclusion, the behavior of the large lattice defect can not be approximated by small particle scattering theory. The analysis of the lattice defect is further complicated by the fact that it is close to the edge of the PC membrane, where the field distribution of the incident field is affected by edge effects.

The nano-particle, on the other hand, behaves very differently and clearly shows increased scattering at wavelengths where we expect the field in the membrane to rise. At 600 nm the particle is barely visible. The field in the membrane is expected to be low, and so is the scattering amplitude. Moreover, the background is maximized, inducing minimal contrast. When increasing the wavelength, we expect the light to couple to the guided resonance mode at 630 nm and the field inside the membrane to increase. The particle should start to appear as a bright spot. Indeed it does, and the contrast between the background and the spot gradually increases as the average transmittance decreases and more light couples into the guided resonance mode.

Optical characterization of the membrane has also been done in the spectral region around

#161834 - $15.00 USD Received 19 Jan 2012; revised 15 Mar 2012; accepted 16 Mar 2012; published 21 Mar 2012

the dip at 566 nm. The dip in transmittance at 566 nm is not as deep as the one at 630 nm, possibly because the 566-nm resonance is more sensitive to deviations from perfect periodicity and other defects from fabrication. Furthermore, near 566 nm we find no significant difference between the spectra of pixels M (representing the nano-particle in the PC membrane) and pixels P (representing the average transmittance of the PC membrane), so we confined our attention to the spectral region around 630 nm, where such a difference is evident.

The contrast between pixels corresponding to the location of the nano-particle and the average transmittance is given in Fig. 6(B) as a function of wavelength. The average value of pixels P, defined in Fig 5, is plotted together with the average transmittance. The frame holding the set of pixels P is centered at the location of the nano-particle. It shows how maximum contrast is reached at 626 nm. As we pass 626 nm, the contrast between the particle and the background decreases. This is counter intuitive, because we expect the field intensity in the membrane to peak closer to 630 nm. However, the observation can be explained as follows: For normal incident light and $\lambda > a$, the optical response is particularly simple. The sum of sources from each unit cell of the membrane produce a transmitted field that is bound to the 0'th order of diffraction. It can be defined with an amplitude and a phase. Treating the nano-particle with small particle scattering theory, we can imagine that it radiates like a dipole. It also has an amplitude and a phase. The contrast is hence not only dependent on amplitude, but also on phase. The phase of the dipole should be the same as the guided resonance mode field at the specific location of the particle. Considering how the phase of the mode field at that location is in general different from the phase of the mode field average over the unit cell, we do not expect there to be a one-one relation between contrast and the amplitude of the guided resonance mode field.

Finally, we note that the molecules we are interested in detecting are found in liquid samples as blood, saliva, urine, etc. In biosensing it is hence most relevant to focus on detection of nano-particles in water. The current PC membrane has been design for detecting nano-particles in air, and the consequence of using the current sensor in water is considerable. The permittivity in the material surrounding the PC membrane then increases to $\sim$1.7 for visible light [38], and will in general completely change the spectral response of the PC membrane. In order to ensure field enhancement through coupling of incident light into guided resonance modes, the membrane and lattice geometries will need to be redesigned. Moreover, the scattered intensity from nano-particles in the Rayleigh regime is proportional to the permittivity contrast between the scattering particle and the surrounding material squared, $|\varepsilon_p - \varepsilon_m|^2$. Increasing ε_m will hence lead to a reduction in scattered intensity. In conclusion, adapting the sensor to detect nano-particles in water will require a change in membrane geometries, and will to some degree reduce the sensitivity.

5. Conclusion

The current system can easily detect and spatially locate single particles with radius down to 75 nm in air. Our measurements indicate that detection is a result of amplified small particle scattering, provided by coupling of the incident light to guided resonance mode fields supported by the PC membrane. This is a useful effect, because in that case, each hole in the membrane can effectively work as a sensor for single nano-particles, and the large number of holes ensures a great dynamic range. As described in the section above, we also see the potential for designing PC membranes for detection of particles in water-based solutions.

The sensor is based on small particle scattering, so the sensitivity can be increased by producing PC membranes supporting resonant modes that produce high electromagnetic field intensities in the PC membrane. This is attainable since field intensities produced by resonant modes are in theory only limited by how small we can make the holes [30], and production techniques continue to reach new levels of accuracy. That said, field enhancement through coupling to

#161834 - $15.00 USD Received 19 Jan 2012; revised 15 Mar 2012; accepted 16 Mar 2012; published 21 Mar 2012

guided resonance modes always comes with a trade-off in image resolution. The latter issue has not been investigated in detail. Is considered a topic for further research, but will effect the dynamic range of the sensor. It can also effect the contrast, since the scattering amplitude of the particle, as seen from a detector outside the membrane, will be reduced as the scattered power spreads over a larger area.

As it stands today, the sensor is not a biosensor, but the membrane is designed to be used in one. The complex geometry of the thin stack arranges for chemical passivation of the Si_3N_4 surface, while the SiO_2 inside of holes can be functionalized to capture specific bio-molecules. Target molecules will settle at positions of maximum optical field intensity, ensuring maximal sensitivity. Furthermore, the large number of holes provides a means for efficient processing of large samples. Pushing samples through the membrane instead of flushing them over, has been shown to be an efficient way of making particles in the sample interact with the membrane surface [37]. Since a target molecule has to touch a functionalized surface in order to be captured, through holes enhance the likelihood of target capture.

#161834 - $15.00 USD Received 19 Jan 2012; revised 15 Mar 2012; accepted 16 Mar 2012; published 21 Mar 2012

Paper B

Nanostructuring of free-standing, dielectric membranes using electron-beam lithography

elink: Paper B

Nanostructuring of free-standing, dielectric membranes using electron-beam lithography

Jon Olav Grepstad[a)]
Department of Electronics and Telecommunications, Norwegian University of Science and Technology, NO-7491 Trondheim, Norway

Martin M. Greve[a),b)]
Department of Physics, University of Bergen, 5007 Bergen, Norway

Thomas Reisinger
Karlsruhe Institute of Technology, 76344 Eggenstein-Leopoldshafen, Germany and University of Bergen, 5007 Bergen, Norway

Bodil Holst
Department of Physics, University of Bergen, 5007 Bergen, Norway

(Received 22 June 2013; accepted 15 August 2013; published 3 September 2013)

Nanostructured dielectric membranes are used in several applications ranging from de Broglie matter-wave optical elements to photonic crystals. Precise pattern transfer and high aspect ratio structures are crucial for many applications. The authors present an improved method for direct patterning on free-standing, dielectric membranes using electron-beam (e-beam) lithography. The method is based on an advanced etchmask that both reduces charging and allows for tuning of the etch mask thickness to support high aspect ratios even for small structures. The authors etched structures as small as 50 nm radius holes in a 150 nm thick membrane and achieved aspect ratios of up to 1.3 for this structure size range. The etch mask thickness can be tuned to achieve the required aspect ratio. The etchmask is composed of a three layer stack consisting of poly(methyl methacrylate), SiO_2 and an antireflective coating polymer. Scanning-electron micrographs of membranes produced with the fabrication method are presented. © *2013 American Vacuum Society*. [http://dx.doi.org/10.1116/1.4820019]

I. INTRODUCTION

Periodic micro- and nanostructured free-standing dielectric membranes exhibit properties useful in a range of applications. Highly sensitive and compact fiber optic pressure and temperature sensors have been demonstrated using photonic crystal silicon based membranes exploiting submicrometer structures in near infrared (IR).[1,2] Dielectric membranes with sub-500 nm periodicity have been made to demonstrate biosensors that potentially can provide sensitivities down to a single molecule.[3,4] Furthermore, dielectric membranes have been structured into free-standing optical (diffraction) elements such as gratings, zone plates, and a Poisson spot annular aperture for the manipulation of de Broglie matter-waves.[5–9]

Optical sensors based on photonic crystal dielectric membranes exploit photonic band gaps[10] and guided resonance modes[11] to achieve sensitivity. These optical properties start to appear when the pattern period is on the order of the operating wavelength. Techniques that facilitate fabrication of structures with periods and features sizes down to 500 nm are hence sufficient for sensors using IR light, i.e., they can be made using standard photolithography techniques. Moreover, IR sensors can be fabricated directly in silicon since it is virtually lossless and can be regarded as a dielectric material for wavelengths longer than 1 μm. Optical sensors operating in the visible range can usually not be made using such fabrication techniques. They typically require pattern periods smaller than 500 nm and the use of dielectric materials such as silicon nitride (Si_3N_4) and silicon dioxide (SiO_2). De Broglie matter-wave optical elements also normally require patterning on a length-scale below what is possible with standard photolithography. The smallest free-standing features made so far for such applications are around 50 nm,[7] and even less would be desirable.[12] This calls for alternative approaches, such as UV or deep UV lithography, electron-beam (e-beam) lithography, nanoimprint lithography, or scanning probe lithography.

In this paper, we will focus on fabricating photonic crystals using maskless e-beam lithography. In order to realize structures using e-beam, an electron sensitive resist is used as the pattern transferring agent. One of the most widespread resists used is the synthetic polymer poly(methyl methacrylate) (PMMA), mainly due to the high achievable patterning resolution.[13]

Using an e-beam for patterning resists on dielectric materials has the potential drawback that dielectric materials generally are insulating. This can cause charge build up, which may deflect the electron beam, resulting in patterning defects and drift in periodic patterns, limiting the minimum feature size.[14] This is especially the case when performing e-beam directly on thin, free-standing dielectric membranes. Charging effects can be reduced by performing lithography while the membrane material is still attached to a conducting or semiconducting substrate.[4] However, this leads to

[a)]J. Grepstad and M. Greve contributed equally to this work.
[b)]Electronic mail: martin.greve@ift.uib.no

complicated fabrication procedures requiring the pattern to be protected from being altered when the conducting substrate is being removed.

After patterning and developing the resist, the pattern is normally transferred to the membrane material through an etch step. This is commonly done using a dry etch, often performed with a reactive ion etcher (RIE). Chemical wet etching is also possible, but dry etch is often preferred for several reasons: With RIE, fragile membranes can be etched with reduced risk of breaking, since the sample does not have to be submerged or lifted out of a chemical etchant. Also a much higher degree of etching anisotropy is normally achieved, resulting in high aspect ratio structures and good pattern definition. Dielectric materials, used in applications for visible light, are most often Si_3N_4 and SiO_2. These two materials have been used in the semiconductor industry for decades and can now be made with an outstanding degree of purity and virtually zero optical loss. It is a problem that, however, reactive ion etching in recipes used to etch these dielectrics also etches PMMA quite aggressively.[15] Consequently, since small features require the use of a thin resist layer to minimize scattering of electrons in the resist,[16] the aspect ratio achievable in dielectrics, using e-beam and only PMMA as a mask is limited for small feature structures. The transferred pattern definition also degrades with increasing aspect ratio since the PMMA pattern tends to taper due to the etch characteristic of the PMMA.[17] Here we present an improved process for direct patterning of free-standing dielectric membranes with e-beam, which reduces charging effects (thus improving the pattern definition) and offers the possibility of high aspect ratios of the membrane structures.

II. FABRICATION TECHNIQUE

The main idea behind the new process is to use a more advanced etch mask. Instead of only transferring the pattern by a single layer of PMMA, we use a very thin layer of chrome on top of the PMMA, a SiO_2 layer, and a layer of antireflective coating (ARC) (Brewer Science XHRIC-11). The bottom layer of ARC is used since as a cross-linked polymer after baking, it has a higher dry etch resistance. That said, using other polymers as etch mask, for example, PMMA is possible, but for the relatively long dry etch times in CF_4 gas ARC has proven superior for the pattern transfer. The mask layers are deposited on the membrane, prior to e-beam exposure, and the simplicity of patterning directly onto the membrane is kept. During exposure, the chrome works as a conducting layer, reducing charge build up at the surface, while PMMA is exposed by electrons traveling through the chrome. The pattern is thus transferred to the SiO_2-layer, which works as a hard etch mask in the following ARC dry etch. We are then left with structured ARC on top of the membrane. Despite the fact that the ARC etches at approximately the same rate as the membrane material in the final step, high aspect ratio patterns can hence be transferred into the membrane in the following anisotropic dry etch. It should be noted that in spite of the name, the ARC is not used for any antireflective purposes in this application, but solely as a polymer etch mask for the pattern transfer into the membrane. The thickness of the PMMA resist can still be kept at a minimum for the patterning, while the ARC thickness can be chosen according to the required membrane etch depth. See Fig. 1 for an overview of the fabrication process. We point out that trilayer/multilayer masks have been used in different variations such as PMMA/germanium/PMMA.[18] In such a mask, the germanium layer serves as the hard etch mask and at the same time prevents charging. This is simpler than our method, which requires an extra step for the chrome. The combination chrome/SiO_2 as conductive layer and hard etch mask is however still a good choice for our application compared with a single intermediate metal layer. Chrome is a superior conductor compared to, for example, germanium, and the electron beam is nearly unaffected by the thin chrome layer. Acquiring a good contact between the sample holder and the thin sandwiched germanium layer might prove challenging. Also the SiO_2 hard etch mask reduces the amount of backscattered electrons, and hence the proximity effect, compared to a metal layer or more dense material.[19] This allows for a better pattern definition, which is an advantage, in particular for small structures.

The substrates used in the fabrication process were free-standing membranes ($900\,\mu m \times 900\,\mu m$) consisting of a $Si_3N_4/SiO_2/Si_3N_4$ thin film stack, where each layer was 50 nm, respectively. The layers were made using standard semiconductor and lithography techniques: The thin-films were deposited in consecutive steps on both sides of a double side polished 200 μm thick 4 in $\langle 100 \rangle$ silicon wafer (n-phosphorus doped with resistivity 1500 Ω cm, made by Topsil). The Si_3N_4 was made by low pressure chemical vapor deposition (LPCVD), and the SiO_2 was made by LPCVD poly-Si deposition followed by thermal oxidation (Fig. 1, step 1). A photolithography step was performed on one side of the wafer, in order to pattern membrane windows on the thin film stack. Then, a dry etch was preformed, using a Plasmatherm 790+ RIE, in order to open the dielectric stack, using 20 SCCM CF4 gas at 600 W and 10 mTorr, which leaves windows of exposed Si on one side of the Si-wafer masked by the dielectric stack (Fig. 1, step 2). Finally, a tetraethylammonium hydroxide (TMAH) wet etch of the wafer silicon was performed. This was done using a 25% TMAH solution at 80 °C, resulting in an etch rate of 22 μm/h. The sample was etched for 10 h, resulting in free-standing membranes supported by a wafer thick silicon frame (Fig. 1, step 3). (If the wafer is exposed to air for more than a couple of minutes after dry etching the mask in the dielectric thin film stack, the wafer should be left in buffer-HF for about 10 s in order to remove any native oxide before proceeding with the TMAH-etch.)

Next, the etch-mask was applied: A 150 nm spin-coated layer of ARC baked at 150 °C for 90 s, 20 nm SiO_2 deposited at a rate of 3 nm/s by electron beam evaporation (EBE), and a 150 nm spin-coated layer of PMMA baked at 175 °C for 3 min (Allresist AR-P 671). To overcome sample charging while patterning, an additional 3 nm chrome layer was deposited on top of the PMMA as a conductive layer using

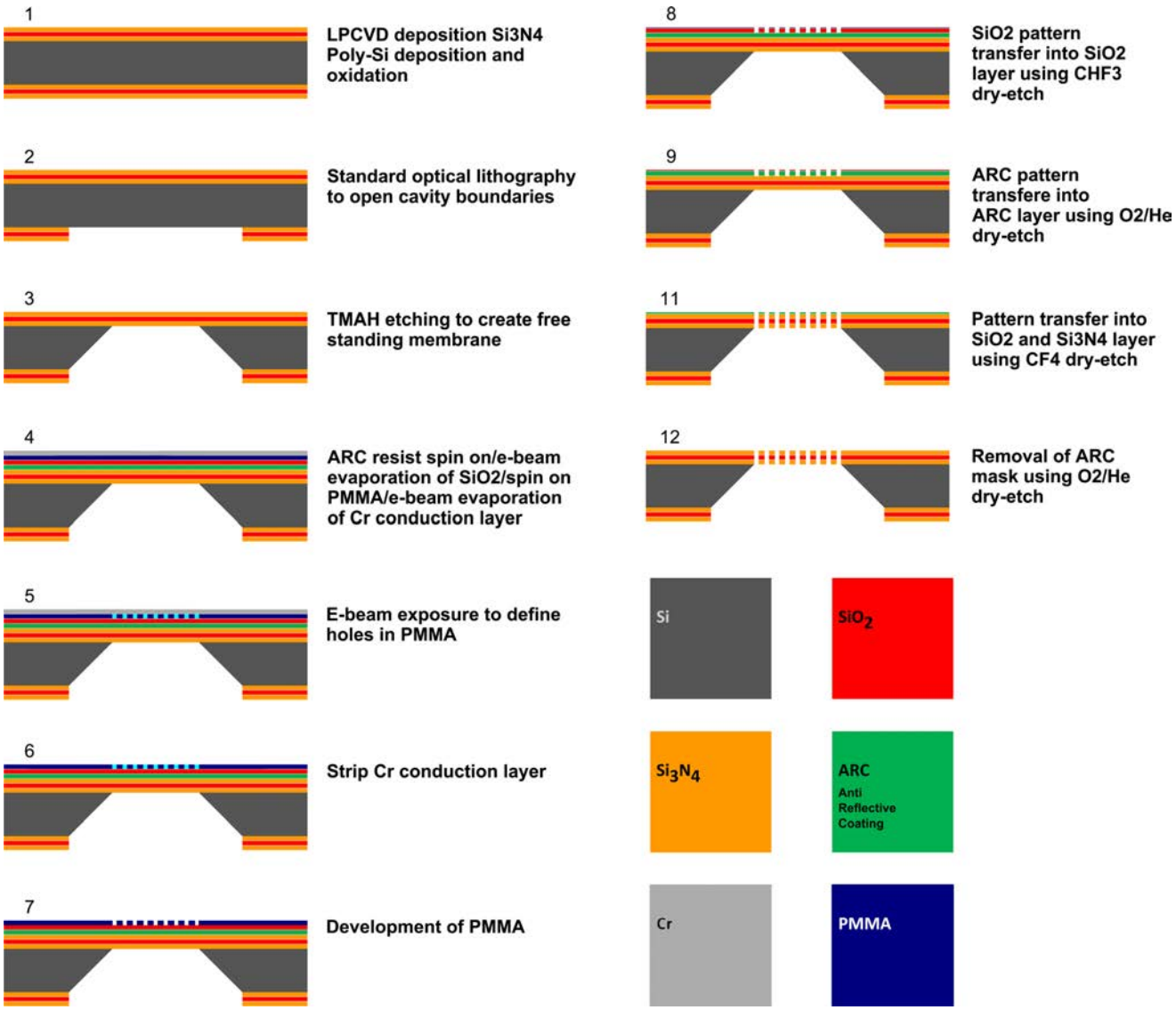

FIG. 1. (Color online) Step by step illustration of the fabrication process. Note that in step 11 the ARC layer is also partially removed, and step 12 removes the remaining ARC.

EBE (Fig. 1, step 4). It was found that chrome is a better choice than for example aluminum, since the aluminum-etchant (Transene Company INC. Aluminum Etchant Type A) was seen to etch the PMMA and consequently distort the pattern.

The pattern was exposed with an acceleration voltage of 30 kV and a beam current of 300 pA with a patterning dose of 400 μC/cm^2 (Fig. 1, step 5). These parameters were found to give the optimum shape representation of the designed pattern in the PMMA. With this dose, the resulting hole pattern had dimensions slightly larger than the digitally designed pattern. By means of "shape-biasing," the over-sizing was circumvented by measuring the hole dimensions of a test sample and decreasing the digital pattern design relative to the measured over-sizing.

After e-beam exposure, the chrome was removed using a chrome etchant (Transene Company Inc., Chromium Etchant 1020) for 8 s at 20 (C °C. The etch rate was estimated by coating a glass slide simultaneously with the membranes so both substrates would have the exact same chrome thickness. The glass slide was submerged in the chrome etchant and timed until the glass became colorless and hence the chrome fully removed. By this method, the etch rate was determined to be about 0.8 nm/s. To ensure there were no chrome residues left, we deliberately over-etched the substrates slightly. This could be done since the chrome etchant does not affect the PMMA. Then, the PMMA was developed in an e-beam developer (Allresist GMBH, AR 600-56) for 120 seconds, exposing the underlying SiO2. The SiO2 was dry etched in a 15 SCCM flow of CHF3 gas for 3 min and 30 seconds at a pressure of 7 mTorr and RF power of 100 W. This pattern transfer is needed since the PMMA cannot withstand the subsequent ARC etch. Using the SiO_2 as an etch mask, the pattern was transferred to the ARC using a 10 SCCM He and 5 SCCM O_2 gas flow mix for 10 min at 10 mTorr and 100 W. This also removed most of the PMMA (see Fig. 1 step 8).

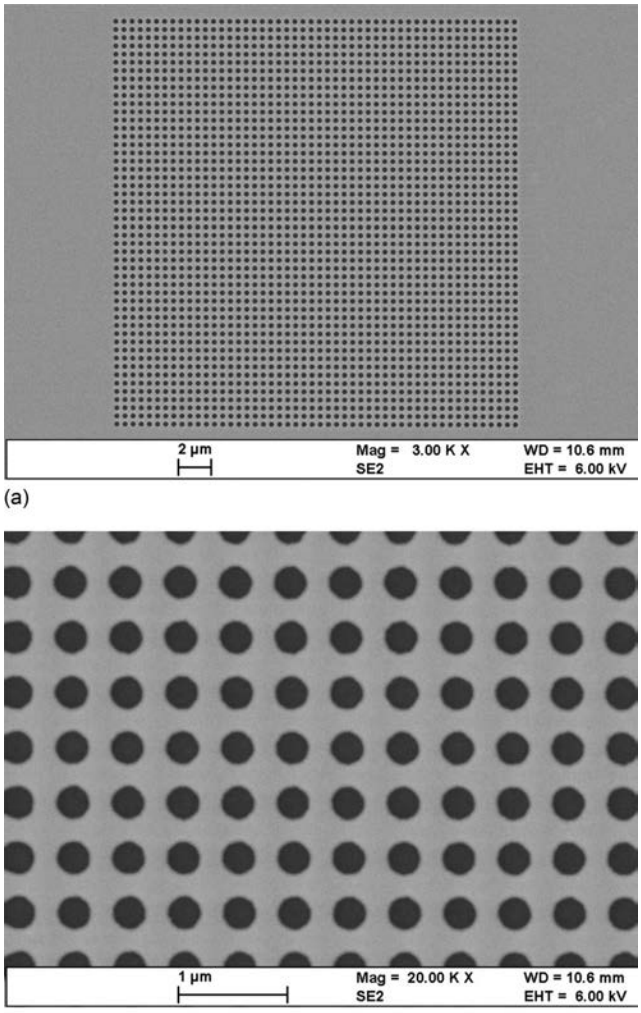

FIG. 2. SEM micrograph of (a) nanostructured dielectric membrane fabricated using the process summarized in Fig. 1, and (b) a close-up of the holes. The lattice is square with a period of 500 nm ± 3 nm. Holes have a radius of 150 nm ± 4 nm.

Finally, the pattern was transferred into the $Si_3N_4/SiO_2/Si_3N_4$ membrane, using a dry etch with 15 SCCM CF_4 gas for 14.5 min at 10 mTorr and 100 W. This etch also removed the SiO_2 mask and the ARC. We determined the etch rate to be about 9 nm/min for the membrane materials, and ~10 nm/min for the ARC, by investigation of a cleaved cross-section using a scanning electron microscope (SEM). The ARC etch rate was hard to determine solely by SEM due to low contrast between the two layers. When the membrane etch is completed, the ARC is also removed. To ensure that all ARC was removed from the membrane, a final ARC etch step was preformed using the same parameters as for the ARC etch above (see Fig. 1, steps 6–12). For stability reasons, the membranes were not etched completely through. 20 nm were left in the bottom of the holes. This is not important for the optical measurements that the membrane samples will be used for.

III. RESULTS AND DISCUSSION

Figure 2(a) shows an overview SEM micrograph of a 50 × 50 hole nanostructured dielectric membrane (photonic crystal). We fabricated photonic crystals with three different hole radii 50±6, 100±4, and 150±4 nm shown in Figs. 2(b), 3(a) and 3(b), respectively, all with a period of 500±3 nm. Closeup images can be seen in Figs. 2(b), 3(a) and 3(b). It can clearly be seen that the method works well, even down to the smallest holes with a radius of only 50 nm. The final structures reveal well shaped holes, free from defects and with borderline edge definition.

Figure 4 shows a cross-section SEM image of a sample, fabricated the same way as the photonic crystals, but not on a free-standing membrane. This allowed us to cleave the samples and verify the etch depth into the membrane material. It was measured to be, as expected, 130 nm for the specific ARC thickness used in this experiment. In case of the smallest holes, we can hence estimate that the maximum aspect ratio is as high as 1.3. In order to etch the remaining 20 nm of the membrane, which can be seen in Fig. 4, we could have used a thicker layer of ARC. This would allow even higher aspect ratios to be achieved. However, since the

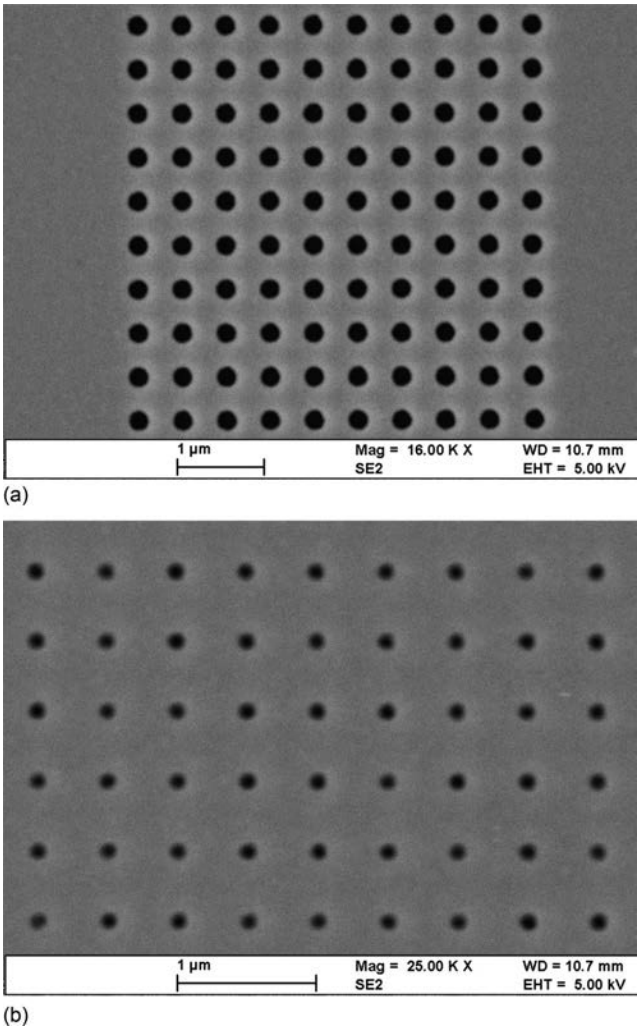

FIG. 3. SEM micrographs of holes with a radius of (a) 100 ± 4 nm and (b) 50 ± 6 nm etched in a 150 nm thick dielectric membrane. Both lattices are square with a period of 500 ± 3 nm.

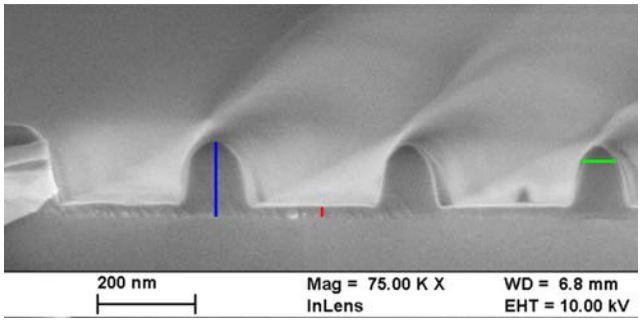

FIG. 4. (Color online) Cleaved test sample imaged at 90° to show the etch profile of the Si_3N_4/ SiO_2/ Si_3N_4 layer. The etched lines are about 250 nm wide, with walls approximately 70 nm in thickness (horizontal bar). The right most vertical bar shows the full thickness of the membrane (150 nm), and the central vertical bar shows the remaining membrane after the etch (20 nm). Calculated aspect ratio for the walls is thus (150-20)/70 ≈ 1.9.

current fabricated structures were used in an optical measurement where this was inconsequential, and a thin layer at the bottom only renders the membrane more mechanically stable, we did not try to increase the etch depth. In Fig. 4, the top of the membrane structures shows sign of rounding. This is caused due to the ARC being spent prematurely so that no mask was present in the last part of the etch. The rounding can be avoided by a thicker ARC layer or shorter etch times.

IV. CONCLUSION

We have developed a new etch mask especially useful for direct patterning, and subsequent dry-etching, of free-standing dielectric membranes using e-beam lithography. The etch mask separate the exposure and development of the resist, from the membrane dry-etch step, thus enabling higher aspect ratios and smaller feature sizes to be patterned. Also a chrome layer is deposited on top of the stack to address the issue of sample charging commonly seen when patterning dielectric membranes. The ARC thickness can be tuned to achieve the required aspect ratio in final devices. SEM micrographs of our fabricated structures shows that the process performs well, when patterning holes, with a radius of down to 50 nm and an aspect ratio of 1.3, directly on free-standing dielectric membranes.

ACKNOWLEDGMENTS

The authors thank Tim Savas for useful discussions. The authors also thank Trond Mohn with Bergens Research Foundation for generous support in setting up the UiB Nanostructures laboratory. This work was also supported by the Norwegian Research Council, through the programs Nærings-Ph.d., Norwegian PhD Network on Nanotechnology for Microsystems, Nanomat Toolplatform and Gaveforsterkning.

[1]O. C. Akkaya, O. Akkaya, M. J. F. Digonnet, G. S. Kino, and O. Solgaard, J. Microelectromech. Syst. **21**, 1347 (2012).
[2]B. Park, J. Provine, I. W. Jung, R. T. Howe, and O. Solgaard, IEEE Sens. J. **11**, 2643 (2011).
[3]A. A. Yanik, M. Huang, O. Kamohara, A. Artar, T. W. Geisbert, J. H. Connor, and H. Altug, Nano Lett. **10**, 4962 (2010).
[4]J. O. Grepstad, P. Kaspar, O. Solgaard, I.-R. Johansen, and A. S. Sudbø, Opt. Express **20**, 7954 (2012).
[5]M. Arndt, O. Nairz, J. Vos-Andreae, C. Keller, G. van der Zouw, and A. Zeilinger, Nature **401**, 680 (1999).
[6]T. Reisinger, A. A. Patel, H. Reingruber, K. Fladischer, W. E. Ernst, G. Bracco, H. I. Smith, and B. Holst, Phys. Rev. A **79**, 053823 (2009).
[7]T. Reisinger, S. Eder, M. M. Greve, H. I. Smith, and B. Holst, Microelectron. Eng. **87**, 1011 (2010).
[8]S. Rehbein, R. Doak, R. Grisenti, G. Schmahl, J. Toennies, and C. Woll, Microelectron. Eng. **53**, 685 (2000).
[9]T. Savas, M. Schattenburg, J. Carter, and H. Smith, J. Vac. Sci. Technol. B **14**, 4167 (1996).
[10]J. D. Joannopoulos and S. Johnson, *Photonic Crystals, Molding the Flow of Light*, 2nd ed. (Princeton University Press, 2008), Chaps. 5 and 10.
[11]S. Fan and J. D. Joannopoulos, Phys. Rev. B **65**, 235112 (2002).
[12]S. D. Eder, T. Reisinger, M. M. Greve, G. Bracco, and B. Holst, New J. Phys. **14**, 073014 (2012).
[13]C. Vieu, F. Carcenac, A. Pépin, Y. Chen, M. Mejias, A. Lebib, L. Manin-Ferlazzo, L. Couraud, and H. Launois, Appl. Surf. Sci. **164**, 111 (2000).
[14]K. Ohya, K. Inai, H. Kuwada, T. Hayashi, and M. Saito, Surf. Coat. Technol. **202**, 5310 (2008).
[15]J. Chinn, I. Adesida, E. Wolf, and R. Tiberio, J. Vac. Sci. Technol. **19**, 1418 (1981).
[16]A. Olkhovets and H. G. Craighead, J. Vac. Sci. Technol. B **17**, 1366 (1999).
[17]Y. Chen, Y. Zhou, L. Wang, Z. Cui, E. Huq, and G. Pan, Microelectron. Eng. **85**, 1152 (2008).
[18]E. Hu, D. Tennant, R. Howard, L. Jackel, and P. Grabbe, J. Electron. Mater. **11**, 883 (1982).
[19]C.-H. Seo and K.-Y. Suh, Korean J. Chem. Eng. **25**, 373 (2008).

Paper C

Finite-size limitations on Quality Factor of guided resonance modes in 2D Photonic Crystals

elink: Paper C

Finite-size limitations on Quality Factor of guided resonance modes in 2D Photonic Crystals

Jon Olav Grepstad,[1,*,7] **Martin M. Greve,**[2,7] **Bodil Holst,**[2] **Ib-Rune Johansen,**[3] **Olav Solgaard,**[4] **and Aasmund Sudbø,**[5,6]

[1] *Department of Electronics and Telecommunications, Norwegian University of Science and Technology, NO-7491 Trondheim, Norway*
[2] *Department of Physics, University of Bergen, 5007 Bergen, Norway*
[3] *SINTEF ICT, Microsystems and Nanotechnology, NO-0373, Norway*
[4] *E.L. Ginzton Laboratory, Stanford University, CA-94305, USA*
[5] *University Graduate Center, NO-2027 Kjeller, Norway*
[6] *Department of Physics, University of Oslo, NO-0316, Norway*
[7] *The first two authors contributed equally*
[*] *jonolav.grepstad@sintef.no*

Abstract: High-Q guided resonance modes in two-dimensional photonic crystals, enable high field intensity in small volumes that can be exploited to realize high performance sensors. We show through simulations and experiments how the Q-factor of guided resonance modes varies with the size of the photonic crystal, and that this variation is due to loss caused by scattering of in-plane propagating modes at the lattice boundary and coupling of incident light to fully guided modes that exist in the homogeneous slab outside the lattice boundary. A photonic crystal with reflecting boundaries, realized by Bragg mirrors with a band gap for in-plane propagating modes, has been designed to suppress these edge effects. The new design represents a way around the fundamental limitation on Q-factors for guided resonances in finite photonic crystals. Results are presented for both simulated and fabricated structures.

OCIS codes: (220.0220) Optical design and fabrication; (280.4788) Optical sensing and sensors; (050.5298) Photonic crystals; (140.4780) Optical resonators.

References and links

1. R. Magnusson and S. S. Wang, "New principle for optical filters," Appl. Phys. Lett. **61**, 1022–1024 (1992).
2. D. Rosenblatt, A. Sharon, and A. A. Friesem, "Resonant grating waveguide structures," IEEE J. Quantum Electron. **33**, 2038–2059 (1997).
3. S. Fan and J. D. Joannopoulos, "Analysis of guided resonances in photonic crystal slabs," Phys. Rev. B **65**, 235112 (2002).
4. K. B. Crozier, V. Lousse, O. Kilic, S. Kim, S. Fan, and O. Solgaard, "Air-bridged photonic crystal slabs at visible and near-infrared wavelengths," Phys. Rev. B **73**, 115126 (2006).
5. Y. Zhou, M. C. Y. Huang, C. Chase, V. Karagodsky, M. Moewe, B. Pesala, F. G. Sedgwick, and C. J. Chang-Hasnain, "High-index-contrast grating (hcg) and its applications in optoelectronic devices," IEEE J. Sel. Top. Quantum Electron. **15**, 1485–1499 (2009).
6. C. Chase, Y. Rao, W. Hofmann, and C.-J. Chang-Hasnain, "1550 nm high contrast grating vcsel," Opt. Express **18**, 15461–15466 (2010).
7. W. Hofmann, "Evolution of high-speed long-wavelength vertical-cavity surface-emitting lasers," Semicond. Sci. Technol. **26**, 014011 (2011).

#193105 - $15.00 USD Received 1 Jul 2013; revised 28 Aug 2013; accepted 15 Sep 2013; published 27 Sep 2013

8. B. Park, J. Provine, I. W. Jung, R. T. Howe, and O. Solgaard, "Photonic crystal fiber tip sensor for high-temperature measurement," IEEE Sens. J. **11**, 2643–2648 (2011).
9. O. C. Akkaya, O. Akkaya, M. J. F. Digonnet, G. S. Kino, and O. Solgaard, "Modeling and demonstration of thermally stable high-sensitivity reproducible acoustic sensors," J. Microelectromech. Syst. **21**, 1347–1356 (2012).
10. J. O. Grepstad, P. Kaspar, O. Solgaard, I.-R. Johansen, and A. S. Sudbø, "Photonic-crystal membranes for optical detection of single nano-particles, designed for biosensor application," Opt. Express **20**, 7954–7965 (2012).
11. B. T. Cunningham and R. C. Zangar, "Photonic crystal enhanced fluorescence for early breast cancer biomarker detection," J. Biophotonics **5**, 617–628 (2012).
12. S. Fan, W. Suh, and J. D. Joannopoulos, "Temporal coupled-mode theory for the Fano resonance in optical resonators," J. Opt. Soc. Am. A **20**, 569–572 (2003).
13. W. Suh, Z. Wang, and S. Fan, "Temporal coupled-mode theory and the presence of non-orthogonal modes in lossless multimode cavities," IEEE J. Quantum Electron. **40**, 1511–1518 (2004).
14. R. R. Boye and R. K. Kostuk, "Investigation of the effect of finite grating size on the performance of guided-mode resonance filters," Appl. Opt. **39**, 3649–3653 (2000).
15. D. K. Jacob, S. C. Dunn, and M. G. Moharam, "Design considerations for narrow-band dielectric resonant grating reflection filters of finite length," J. Opt. Soc. Am. A **17**, 1241–1249 (2000).
16. J. M. Bendickson, E. N. Glytsis, T. K. Gaylord, and D. L. Brundrett, "Guided-mode resonant subwavelength gratings: effects of finite beams and finite gratings," J. Opt. Soc. Am. A **18**, 1912–1928 (2001).
17. J. Lee, B. Zhen, S.-L. Chua, W. Qiu, J. D. Joannopoulos, M. Soljacic, and O. Shapira, "Observation and differentiation of unique high-q optical resonances near zero wave vector in macroscopic photonic crystal slabs," Phys. Rev. Lett. **109**, 067401 (2012).
18. S. Ura, S. Murata, Y. Awatsuji, and K. Kintaka, "Design of resonance grating coupler," Opt. Express **16**, 12207–12213 (2008).
19. Y. Zhou, M. Moewe, J. Kern, M. C. Huang, and C. J. Chang-Hasnain, "Surface-normal emission of a high-q resonator using a subwavelength high-contrast grating," Opt. Express **16**, 17282–17287 (2008).
20. K. Kintaka, T. Majima, J. Inoue, K. Hatanaka, J. Nishii, and S. Ura, "Cavity-resonator-integrated guided-mode resonance filter for aperture miniaturization," Opt. Express **20**, 1444–1449 (2012).
21. N. C. Lindquist, A. Lesuffleur, and S.-H. Oh, "Periodic modulation of extraordinary optical transmission through subwavelength hole arrays using surrounding bragg mirrors," Phys. Rev. B **76**, 155109 (2007).
22. S.-H. Kwon, S. Kim, S.-K. Kim, Y.-H. Lee, and S.-B. Kim, "Small, low-loss heterogeneous photonic bandedge laser," Opt. Express **12**, 5356–5361 (2004).
23. P. Nedel, X. Letartre, C. Seassal, A. Auffeves, L. Ferrier, E. Drouard, A. Rahmani, and P. Viktorovitch, "Design and investigation of surface addressable photonic crystal cavity confined band edge modes for quantum photonic devices," Opt. Express **19**, 5014–5025 (2011).
24. K. Kintaka, T. Majima, K. Hatanaka, J. Inoue, and S. Ura, "Polarization-independent guided-mode resonance filter with cross-integrated waveguide resonators," Opt. Lett. **37**, 3264–3266 (2012).
25. P. Viktorovitch, B. Ben Bakir, S. Boutami, J. L. Leclercq, X. Letartre, P. Rojo-Romeo, C. Seassal, M. Zussy, L. Di Cioccio, and J. Fedeli, "3d harnessing of light with 2.5d photonic crystals," Laser Photon. Rev. **4**, 401–413 (2010).
26. J. D. Joannopoulos and S. Johnson, *Photonic Crystals, Molding the Flow of Light Second Edition* (Princeton University Press, 2008). Chapters 5 and 10.
27. T. Ochiai and K. Sakoda, "Dispersion relation and optical transmittance of a hexagonal photonic crystal slab," Phys. Rev. B **63**, 125107 (2001).
28. X. Letartre, J. Mouette, J. L. Leclercq, P. R. Romeo, c. Seassal, and P. Viktorovitch, "Switching devices with spatial and spectral resolution combining photonic crystal and moems structures," J. Lightwave Technol. **21**, 1691 (2003).
29. J.-P. Berenger, "Numerical reflection from fdtd-pmls: a comparison of the split pml with the unsplit and cfs pmls," IEEE Trans. Antennas Propag. **50**, 258–265 (2002).
30. J. O. Grepstad, M. Greve, T. Reisinger, and B. Holst, "Nano-structuring on free-standing, dielectric membranes using e-beam lithography," J. Vac. Sci. and Tech. B **31**, 06F402 (2013).

1. Introduction

Periodic permittivity induced in a layer of high index material sandwiched between two lower index materials can support a group of optical modes called guided resonance modes [1–4]. These modes are similar to fully guided modes in terms of the distribution of the mode field inside the slab, but different in that they are not fully confined to the slab. Incoming light, with a real out-of-plane k-vector, can couple to in-plane propagating modes. This gives rise to properties that are useful in applications like vertically emitting light diodes [5–7], compact narrow fiber tip sensors [8,9] and highly sensitive optical sensors for environmental control and

#193105 - $15.00 USD Received 1 Jul 2013; revised 28 Aug 2013; accepted 15 Sep 2013; published 27 Sep 2013

medical diagnosis [10, 11].

Guided resonance modes are supported in structures with both 1D- and 2D-periodic permittivity in the plane, and are qualitatively well understood by temporal coupled mode theory [12, 13]: When incoming light hits the surface of a photonic crystal (PC), it sees a combination of a homogeneous slab and an optical resonator. Part of the light is reflected and transmitted through the slab as if it was homogeneous with some effective permittivity, and is often referred to as the direct path. Another part is coupled into in-plane propagating modes that form an optical resonator associated with a resonance frequency and spectral bandwidth. The output of the resonator is referred to as the indirect path. The two paths interfere to form the characteristic Fano-shape features in the transmitted and reflected spectrum.

We present an investigation of guided resonance modes in PCs that have a 2D-periodic permittivity imposed on a dielectric slab free-standing in air, and will focus on finite-size lattice effects. Finite-size lattice effects are seldom discussed in the literature for 2D-PCs, but based on work done on 1D-PCs [14–16], we know that they can be important. Especially narrow banded guided resonance modes, i.e. high Q-factor modes, supported by PCs made in low permittivity dielectrics like Si_3N_4 and SiO_2, may not be observable if the number of periods in the lattice is too small [17]. Although simulations on infinite 2D-PCs predict that they can be used to make outstanding optical resonators with virtually unlimited Q-factor [3], there are practical limitations: The required number of unit cells can be challenging to fabricate with high enough accuracy.

Limits on the Q-factor of guided resonance modes in finite PCs are imposed by loss. Two loss mechanisms are unavoidable, even in a perfectly fabricated crystal made in a lossless dielectric. In a finite lattice, incident light will couple into in-plane propagating modes by scattering caused by the inhomogeneous permittivity in every unit cell. If the scattered light reaches the boundary of the lattice, it will see a discontinuous transition to a homogeneous slab supporting fully guided modes. Light coupled into these fully guided modes or scattered by the discontinuity, will no longer interact with the lattice and can be regarded as lost. The band diagram of an infinite PC can in many cases be used to quantify and tailor these effects [28]. For example, the in-plane group velocity of a guided resonance mode can be designed to be close to zero within a range of in-plane k-vectors. A focused incident beam can always be represented by a superposition of plane waves with a range of in-plane k-vectors. If the group velocity is small for all the plane wave components of the beam, incident light will tend not to travel far away from where it enters the slab, but be locally confined and lead to limited edge losses. Such approaches are especially useful for high-contrast gratings, where the band diagram of the infinite lattice yields the transmission spectrum for a PC with a limited number of periods in the lattice. However, for a PC composed of very weak scatterers, an unpractically large number of unit cells can be required for the band diagram of the infinite lattice to yield the transmission spectrum. In that case, the PC should be regarded as finite, and will typically exhibit higher edge losses than predicted by calculations on infinite lattices.

In order for a finite weakly scattering 2D-PC to have properties similarly to an infinite crystal, we hence have to suppress edge-loss effects. Techniques for doing so have previously been utilized to create high-Q guided-mode resonance filters with limited aperture in 1D-PCs [18–20]. They closely resemble methods to increase the transmission through metallic hole arrays supporting surface plasmon modes [21]. By placing in-plane Bragg mirrors at two of the sides of a 1D-PC cavity, light coupled to in-plane propagating guided resonance modes, can be reflected back at the lattice boundary. Incident light cannot couple to fully guided modes outside the boundaries of the lattice, making the PC work as if it was much larger than its physical size. In this way, a fundamental problem with high-Q guided resonance modes in PCs is solved, enabling performance predicted by simulations on infinite structures to be realized in finite

#193105 - $15.00 USD Received 1 Jul 2013; revised 28 Aug 2013; accepted 15 Sep 2013; published 27 Sep 2013

structures. Furthermore, fabricating a device free of defects is easier when the structured area is small. This solution can hence increase the performance of PCs in general.

It has been reported that the same principles can be applied on 2D-PCs. Lattices composed of a cavity with larger holes surrounded by smaller, have been used for lateral confinement of guided resonance modes to increase the light extraction efficiency and tailor the geometry of the output of infrared surface emitting diodes [22, 23]. Recently also an optical filter was made by utilizing a limited aperture 2D-diffraction grating bound by four Bragg mirrors [24]. We present a 2D-PC optical filter for visible light composed of a square lattice of holes etched through a free-standing dielectric membrane bound by two in-plane Bragg mirrors. Our solution is different from the work published in [24] in that our PC is not a weak grating coupling to an underlaying homogeneous waveguide. The grating and the waveguide is one and the same in our design, and is free-standing in air. We also do not have Bragg mirrors on all four sides of the PC, and show how the orientation of the Bragg-mirrors, and the number of mirrors needed, is mode dependent. This particular design of the experiment gives a novel intuitive example of how guided resonance modes behave in real finite structures.

We start by explaining how a finite PC differs from an infinite PC. We present results from simulations on finite PC lattices, which show how Fano-lines in transmission disappear when the number of holes in the crystal is too small. Next, we present simulations of our Bragg mirror PC structure, and finally show how simulated results can be reproduced in fabricated devices.

2. Guided resonance modes in finite size photonic crystals

Temporal coupled mode theory applied to PCs usually treat the case of a lossless optical resonator [3, 13]. It can be modified to include loss [17, 25]. For a PC free-standing in air, symmetric about the center plane, the equations used to fit a Fano-line in the transmitted and reflected spectrum is then given by

$$r = r_d \pm r_g = r_d(\omega) \pm f\frac{\gamma}{i(\omega-\omega_0)+\gamma}, \text{ and} \tag{1}$$

$$t = t_d + t_g = t_d(\omega) + f\frac{\gamma}{i(\omega-\omega_0)+\gamma}, \tag{2}$$

where ω is the frequency of the incident light, and ω_0 and γ is the center frequency and bandwidth of the guided resonance mode. The direct path is represented by reflection and transmission coefficients r_d and t_d, and the indirect path is represented by coefficients r_g and t_g.

These equations have the exact same form as a lossless optical resonator, only f is no longer set by energy conservation to be $f = -(t_d \pm r_d)$ [3]. Instead

$$f = -\alpha(t_d \pm r_d), \tag{3}$$

where α is a loss dependent scalar smaller than one. The loss can be defined to include the effect of lattice discrepancies, material absorption, etc. We will limit our discussion to loss related to edge effects, which cannot be removed by improved fabrication techniques or improved intrinsic material properties. The main differences between an infinite and a finite PC can then be illustrated as shown in Fig. 1. Figure 1(a) is the lumped element model of an infinite PC, while a finite PC is modeled in Fig. 1(b). The lossy resonator model is greatly simplified, but illustrates the point we want to make: The amplitude of the resonant term is reduced when the resonator is lossy.

The difference between an infinite and a finite lattice is especially evident when it is designed to support high-Q guided resonance modes. To understand why, we start by explaining how a PC composed of a matrix of weakly scattering holes supports high-Q guided resonance modes.

#193105 - $15.00 USD Received 1 Jul 2013; revised 28 Aug 2013; accepted 15 Sep 2013; published 27 Sep 2013

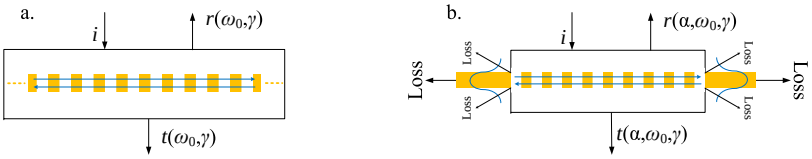

Fig. 1. (a) Lumped element model, based on temporal coupled mode theory, of an infinite photonic crystal with lattice period $p < \lambda$, where λ is the wavelength of an incoming plane wave with amplitude $i = 1$, producing a reflected and transmitted plane wave with amplitude r and t. Coupling to guided resonance modes is associated with a center frequency ω_0 and bandwidth γ. (b) Illustration of how the theory is modified to include loss related to edge effects, given by α.

Consider an infinite PC composed of unit cells with approximately homogeneous permittivity, e.g. a square lattice of holes with period p and a radius $r << p$. We also have $r << \lambda$, where λ is the wavelength of the incident field, which we choose to have normal incidence. Referring to temporal coupled mode theory, the direct response will then be approximately that of a homogeneous slab with effective permittivity slightly lower than the slab material. The resonant term is a result of incident light being scattered by the matrix of holes and coupling to a standing wave composed of waves traveling in the plane of the slab. The standing wave is similar to a sum of fully guided modes, but can scatter out of the slab by the hole matrix. This generates an out-of-plane reflected and transmitted wave. The size of the coupling coefficient, determining how much light is coupled in and out of the resonator, is hence set by the scattering strength of our hole matrix. Reducing the radius of holes, reduces the coupling coefficient. Because the Q-factor of an optical resonator is increased when the coupling coefficient is reduced, small holes or any weak scattering matrix, will generally support high-Q guided resonance modes.

The approximate band diagram of a weak scattering matrix can be found by using the dispersion relation of a homogeneous slab as a starting point. We will use a square lattice as an example. For k-vectors aligned with one of the crystals principal axes, it involves a folding of the dispersion relation of a homogeneous slab and opening of small band gaps at the edges of the Brillouin zones and at the Γ-point, as shown in Fig. 2(a) and 2(b) [4].

An incident plane wave is sent into this lattice from the side, as shown in Fig. 2(c) and 2(d). The incident wave is taken to be a fully guided mode with $k_i = 2\pi/p$ in the homogeneous slab, traveling in the positive x-direction. Its frequency, ω_m, lies between two guided resonance modes in the lattice. This means that we are in a photonic band gap [26] for in-plane propagating modes, which leads to an exponential decrease of the field amplitude as we go in the positive x-direction. Rows of holes in the y-direction function as an in-plane Bragg mirror, where the attenuation length will be increased when the radius of holes is reduced. In order to observe the effect of the in-plane band gap in a finite lattice composed of small holes, we hence need many periods. For the same reason, weakly scattering matrices supporting high-Q guided resonance modes, generally require many periods in order to be observed in finite size lattices.

We point out that it is possible to design crystals that have relatively large holes, and still support high-Q guided resonance modes that are forbidden by symmetry to couple to normally incident light [3,27]. Weak coupling to such modes can be achieved by breaking the symmetry, by changing the incident field to have an incidence angle slightly off from normal incidence [4]. However, whenever we have weak coupling between the incident light and a specific guided resonance mode of a PC, many periods of the PC are needed in order to observe the resonance in the transmission and reflection spectra [17].

In addition to the effect of lattice size on its ability to support a guided resonance mode, there is a second matter that needs to be considered. As lattices are finite in real experiments,

#193105 - $15.00 USD Received 1 Jul 2013; revised 28 Aug 2013; accepted 15 Sep 2013; published 27 Sep 2013

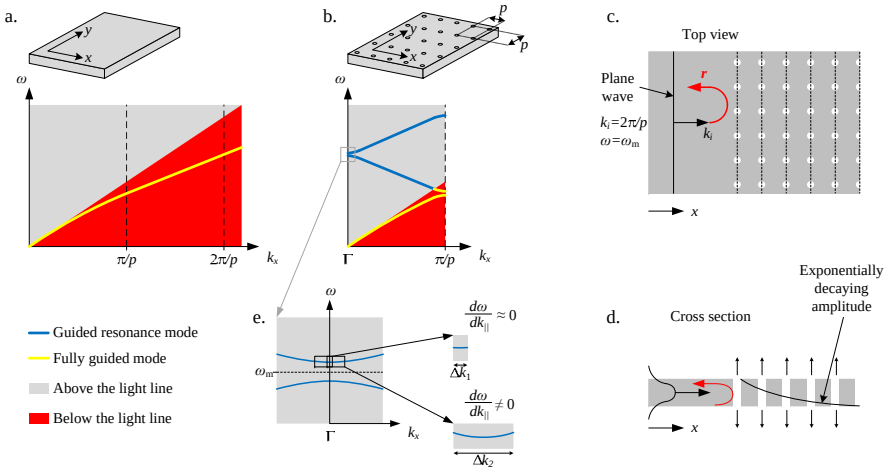

Fig. 2. (a) Dispersion relation for a homogeneous slab. (b) A square lattice of holes is introduced in the slab, which by folding about π/p introduces guided resonance modes above the light line (blue lines). A zoom-in shows the two lowest frequency guided resonance modes at the Γ-point. (c and d) We consider how a fully guided mode with frequency, ω_m, sent in from the side of this lattice, will have an exponentially decreasing amplitude as a function of distance from the lattice boundary. The decrease in amplitude is due to scattering from the holes, which creates an in-plane bad gap at this frequency. (e) Zoom in on a guided resonance mode at the Γ-point for two finite fields with different spacial extent. Going from Δk_1 to Δk_2, we go to a more localized field.

so are the incident fields. It is impossible in practice to excite a pure plane wave corresponding to a point in our band diagram. We can approximate a finite field as a sum of plane waves with different wave vectors. An incident field will hence contain a set of in-plane $k_{||}$-vectors, $\Delta k_{||}$. These sets of in-plane vectors will couple differently to a guided resonance [28]. Mathematically speaking, referring to the band diagram in Fig. 2(e) and recognizing that this plot is a projection of solutions where $k_{||} = k_x$, strong coupling requires

$$\frac{\partial \omega}{\partial k_{||}} \approx 0, \tag{4}$$

for all $k_{||}$ in $\Delta k_{||}$. If $\partial\omega/\partial k_{||} \neq 0$ for all $k_{||}$ in $\Delta k_{||}$, the transmitted and reflected spectra will be a result of coupling to a sum of guided resonance modes with different center frequency, observed as a reduction in Q-factor.

In conclusion, coupling to a guided resonance mode in finite PCs, has two main requirements. One, we have to insure that there are enough periods in our lattice for the guided resonance mode bands to form. This is closely related to the scattering strength of the lattice. Secondly, $\partial\omega/\partial k_{||}$ must be approximately zero for all in-plane k-vectors that we need in order to represent our fields.

3. Simulations on photonic crystals with finite lattices

We have designed an experiment that allows us to see how guided resonance modes disappear when the number of unit cells in a 2D-PC lattice is insufficient. We have focused on lattice size effects, since these impose fundamental limitations on the Q-factor, as oppose to finite beam size. An illustration of the simulation experiment done using FDTD is shown in Fig. 3.

#193105 - $15.00 USD Received 1 Jul 2013; revised 28 Aug 2013; accepted 15 Sep 2013; published 27 Sep 2013

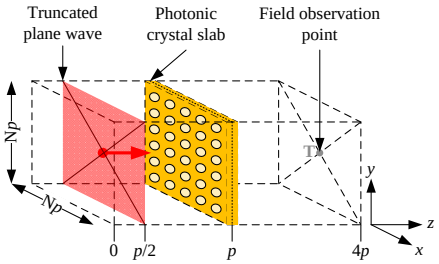

Fig. 3. Illustration of the three dimensional FDTD simulation domain. N is the number of periods in a square lattice with period p. The place of origin for the incident waves and its orientation relative to the PC, and the observation point where the field is recorded as a function time, is marked along the z-axis.

A volume, having a refractive index of air, $n_{\text{air}} = 1$, with a length corresponding to four lattice periods, $4p$, and a cross section of Np×Np, was defined. N defines the size of the lattice. The spacial resolution was set to 0.02 μm in the z-direction, and 0.01 μm in the x- and y-direction. A plane truncated wave, polarized in the y-direction, was imposed at $z = p/2$ with a Gaussian time evolution having a center frequency corresponding to $\lambda = 650$ nm in air. A slab with refractive index $n_{\text{s}} = 2$ was centered at $z = p$. The thickness of the slab was set to 160 nm and the unit cell in the lattice is composed of a hole going through the slab with a radius of 100 nm. The lattice is square with a period $p = 500$ nm.

An observation point was placed at $z = 4p$ in the center of the simulation domain on the xy-plane, allowing us to record the transmittance spectrum of the PC. Four different size lattices were simulated: N = 10, N = 20, N = 30 and an infinite lattice. N = 10, N = 20 and N = 30 were implemented by using perfectly match layers (PML) on all sides of the simulation domain. The infinite lattice was simulated by defining a domain with N = 1 and using periodic boundary conditions in both x- and y-directions.

We point out that PML does not work well for waves having k-vectors parallel to the PML [29]. Implementation of such waves is known to give rise to unphysical reflections from the boundary. This effect is present in the simulations using N = 10, N = 20 and N = 30. To reduce the required computing power and time, we simplify our model of the fabricated devices as much as possible. In spite of these simplifications and the spurious reflections from the PMLs, the simulations give us valuable insight into the physics involved.

Simulation results are presented in Fig. 4(a) and show the transmittance spectra of the four different lattice sizes. The plotted curves are the ratios between the Fourier transforms of the field recorded in point T as a function of time, and the Fourier transform of the incident Gaussian pulse. We will refer to this ratio as the transmittance. Focusing on the blue curve, two dips in transmittance can be seen. These are a result of coupling to two different guided resonance modes in the infinite lattice, and would in a simulation with higher resolution go down to zero. We will refer to the mode at 720 nm as mode A and the mode at 645 nm as mode B, as pointed out in Fig. 4(a). Note how mode A has a wider bandwidth than mode B, i.e. mode A has lower Q-factor than mode B.

In case of the finite lattice simulations, represented by the red, black and green curve, the spectrum is significantly different. We can see for both mode A and B that the resulting dips in transmission tend to disappear when the number of periods in the lattice is too small. This is clarified in Fig. 4(b), where the Q-factor of modes A and B have been calculated and plotted as a function of lattice size, represented by red and blue markers respectively. The Q-factor has been normalized as Q for the finite lattices divided by Q of the infinite lattice. The fact that

#193105 - $15.00 USD Received 1 Jul 2013; revised 28 Aug 2013; accepted 15 Sep 2013; published 27 Sep 2013

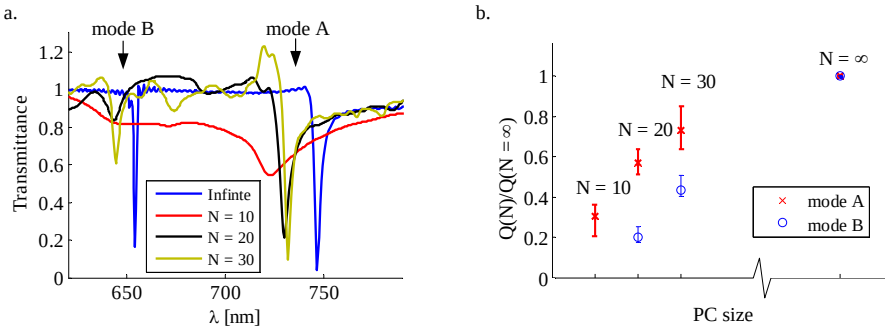

Fig. 4. (a) Simulated transmittance spectrum of a finite crystal composed of N×N holes for N = 10 (red line), N = 20 (black line), N = 30 (green line), and an infinite lattice (blue line). The transmittance is given as the ratio between the Fourier transforms of the field recorded in point T (see Fig. 3) as a function of time, and the Fourier transform of the incident pulse. Dips in transmission marked with arrows resulting from coupling to two guided resonance modes are visible, labeled mode A and B. (b) The Q-factor of mode A (red markers) and B (blue markers) has been calculated and plotted as a function of lattice size. The Q-factor has been normalized as Q for the finite lattices divided by Q of the infinite lattice.

high-Q guided resonance modes require more periods in order to be observed, can be seen by comparing the red and blue data series. Mode B is not observable for the smallest 10x10 lattice, and the Q-factor of mode A reaches its terminal value faster than mode B.

The spectra have regions in wavelength where the transmittance is above one, and there is a red shift going from small to larger lattices sizes. Values higher than one are caused by a combination of diffraction and that we are calculating the transmission based on the field amplitude at a point instead of calculating the total transmission. The red shift is caused by a reduction of $\Delta k_{||}$ as we increase the size of the lattice, in combination with band bending. As explained above, this will also limit the observable Q-factor. We will return to this matter in the discussion, to see how we can conclude that the Q-factor is mainly limited by the lattice size.

Continuous wave simulations where performed for the minima located between 700 and 750 nm in Fig. 4(a), for N = 10, N = 20 and the infinite lattice. Referring to Fig. 3, an observation plane was imposed at $z = p$, allowing us to record the field at the center of the slab. Figure 5 shows the amplitude of all three field components at this surface. The incident field is still polarized in the y-direction. From these full field images, it is evident that the sources of error mentioned earlier affect our results. Forbidden asymmetries are especially visible in the x-component of the field for the infinite lattice: The x-component of the field, shown in the bottom left in Fig. 5, does not have four folded symmetry. We can however still clearly see the underlying correct symmetric behavior of the field, and can use the results to see how the guided resonance mode is affected when making the lattice finite. Simulations with higher grid resolution were done for the 10×10 lattice. They showed that insufficient resolution is the dominant cause of these asymmetries. Effects of spurious reflections from the PML were too small to be specifically detected.

Mode A is dominated by a strong y-component, and forms as rows of holes parallel to the incident polarization oscillate in phase and couple to a guided resonance mode with in-plane k-vectors parallel to the x-axis. These are waves traveling in the positive and negative x-direction if the incident field is polarized in the y-direction. As long as the number of periods in the y-direction is large compared to the wavelength of the guided resonance mode field, it is the number of holes in the x-direction that limits the formation of the guided resonance mode.

#193105 - $15.00 USD Received 1 Jul 2013; revised 28 Aug 2013; accepted 15 Sep 2013; published 27 Sep 2013

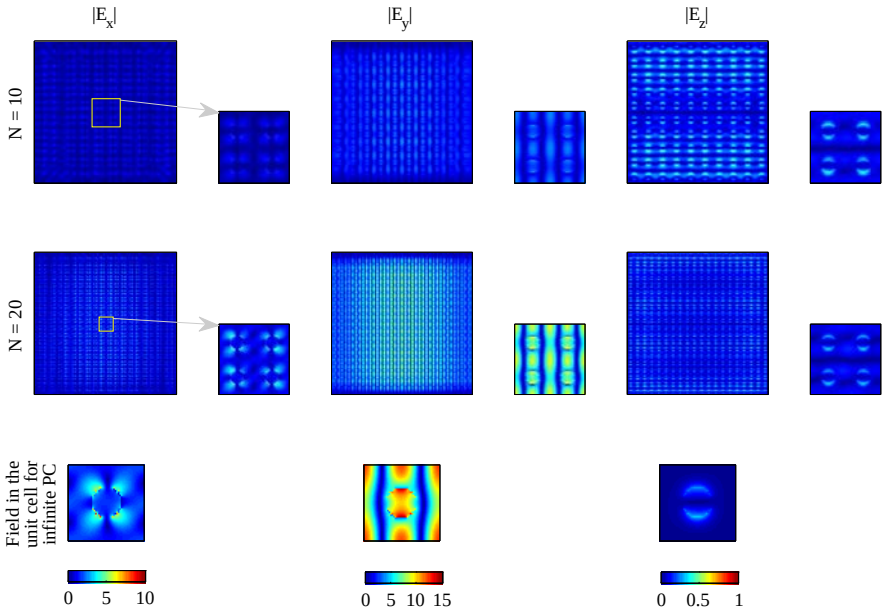

Fig. 5. Full field plots at the center plane of a finite PC consisting of 10×10 holes (N = 10) and 20×20 holes (N = 20), and the field at the center plane in a unit cell of an infinite 2D-PC, resulting from continuous wave FDTD simulations for wavelengths corresponding to the minimum values on the three plots in Fig. 4(a) above 700 nm. The center four unit cells are blown up to better see the field distribution for the two finite PCs.

Focusing on the *y*-component of the field, we can see how the field in the center of the PC converges towards the infinite case as the number of holes in the matrix increases. This is because the contribution of a specific hole to the guided resonance mode is limited in space. A unit cell at the edge, will only see the response from holes to one of its sides in the *x*-direction, while a hole in the center will see the response from neighbors on both of its sides in the *x*-direction. This causes the field in the membrane to decrease as we approach the edge of the crystal.

4. Increasing the Quality factor of finite photonic crystals

To create large Q-factors in miniaturized PC devices, we have to find a way of minimizing edge effects. A solution is to introduce reflecting boundaries. This will prevent loss induced by coupling to fully guided modes outside the lattice. For the particular mode shown in Fig. 5, this reflecting boundary condition can be imposed by placing in-plane Bragg mirrors at two of the boundaries of the lattice parallel to the incident polarization. A 3D drawing of the design is presented in Fig. 6(b). It shows a square lattice with period 500 nm, composed of holes with a radius of 100 nm imposed on a 140 nm thick membrane with refractive index $n_s = 2$. The Bragg mirrors have a period of 240 nm with open line widths of 80 nm, tuned to have an in-plane band gap for the frequency of a guided resonance mode in the hole lattice.

The transmittance spectrum of this structure is found using a setup similar to the one drawn in Fig. 3. The PC consisting only of a periodic lattice of holes, is replaced by the structure drawn in Fig. 6(b), and we simulate the response of incident fields with two orthogonal polarizations: Parallel to Bragg lines, *y*-polarized, and perpendicular to the Bragg lines, *x*-polarized. We expect

#193105 - $15.00 USD Received 1 Jul 2013; revised 28 Aug 2013; accepted 15 Sep 2013; published 27 Sep 2013

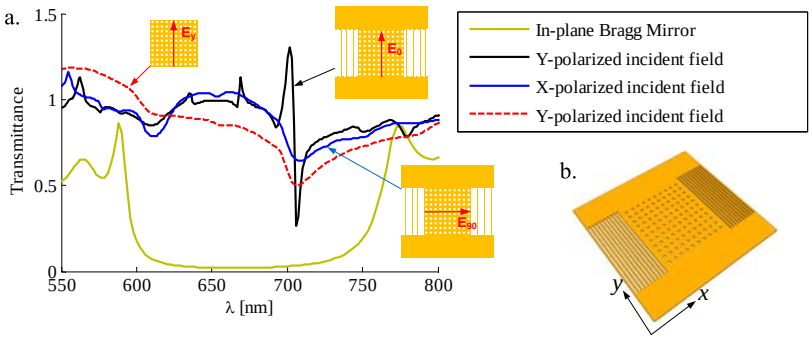

Fig. 6. (a) Simulated transmittance spectra of a PC consisting of a square lattice of 10×10 holes (red dashed), and the same hole lattice having in-plane Bragg mirrors at two of its sides. The black line results from the Bragg PC structure with incident polarization parallel to Bragg mirror lines, E_0, while the blue line results from an incident polarization perpendicular to the Bragg mirror lines, E_{90}. The transmittance is given as the ratio between the Fourier transforms of the field recorded in point T (see Fig. 3) as a function of time, and the Fourier transform of the incident pulse. The transmittance of the in-plane Bragg mirror is shown with the green line. (b) 3D illustration of the simulated PC, utilizing in-plane Bragg mirrors to trap guided resonance modes in the hole lattice with k-vectors perpendicular to the Bragg mirror lines.

that the Bragg mirrors will have little effect if the incident polarization is perpendicular to the lines in the Bragg mirror. In this case, the guided resonance mode will be waves traveling in the positive and negative y-direction. These waves do not see Bragg mirrors at the PC boundaries and can couple to fully guided modes in the homogeneous slab. For the other polarization, the guided resonance mode will be waves traveling in the positive and negative x-direction. When these waves meet the lattice boundary, they will not be allowed to propagate further and are reflected.

The results are displayed in Fig. 6(a). Four curves have been included in this plot. The in-plane Bragg mirror gives a band gap between 600 and 750 nm, as shown by the green curve. The red dashed line is the transmittance spectrum of 10×10 holes without Bragg mirrors, while the blue and black lines are the transmittance spectra of the structure in Fig. 6(b) for two different polarizations. When the polarization is perpendicular to the Bragg lines (blue line), the dip near 700 nm is clearly visible. Its minimum value is 0.65, and its width is comparable to the dip observed for the 10×10 period lattice without Bragg mirrors. Once we turn the polarization 90 degrees, a sharp dip appears that goes down to 0.13. We achieve a higher Q-factor resonance, comparable to what we see in the case of an infinite lattice. We then expect higher field amplitudes in the PC when the incident polarization is parallel to the Bragg lines. As can be seen from the continuous wave simulations presented in Fig. 7, this is the case. The figure shows the field at $z = p$ for wavelengths corresponding to the minima above 700 nm on the blue and black curves in Fig. 6(a). Referring to the center of the hole lattice, a difference in field amplitude of a factor of five can be seen when turning the incident polarization 90 degrees.

5. Fabrication and experimental setup

In order to experimentally verify the simulation results, we have fabricated PCs with dimensions similar to the ones we have simulated and characterized them optically. Due to their intended application in biosensors, the slabs are not made purely of Si_3N_4, but a more complex stack of three thin films: 50 nm Si_3N_4/50 nm SiO_2/50 nm Si_3N_4. The motive for this compo-

#193105 - $15.00 USD Received 1 Jul 2013; revised 28 Aug 2013; accepted 15 Sep 2013; published 27 Sep 2013

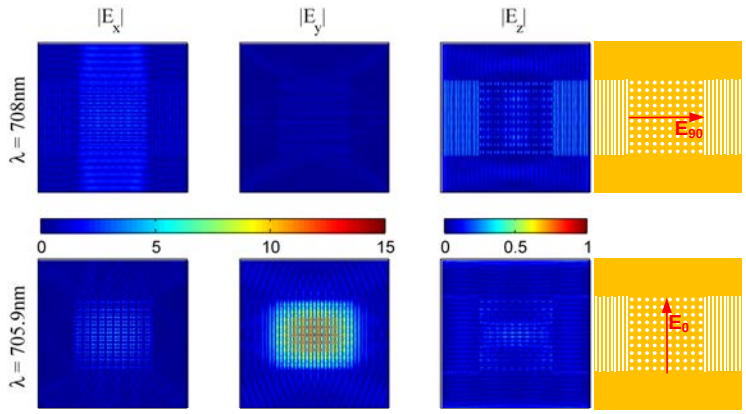

Fig. 7. Full field plots at the center plane of a PC consisting of 10×10 holes with Bragg mirrors at two of its four boundaries, for an incident field oriented perpendicular (top row) and parallel (bottom row) to the Bragg mirror lines. Plots result from continuous wave FDTD simulations for wavelengths corresponding to the minimum values of the two dips in Fig. 6(a) at 708 nm and 705.9 nm, for the incident light polarized orthogonal and parallel to the Bragg mirror lines respectively.

sition is to facilitate specific biomolecule functionalization of the PC [10]. Optically it has the effect that it lowers the effective index of the slab, because SiO_2 has lower permittivity than Si_3N_4. We expect to see similar behavior as for a pure Si_3N_4 PC, but the modes will in general be shifted towards higher frequencies. Because layers are thin compared to the operating wavelength, we do not expect to see the effect of Fabry-Perot cavities forming between boundaries of the different thin films.

First, Si_3N_4 was deposited on double side polished Si-wafers. SiO_2 was made by Poly-Si deposition followed by thermal oxidation. Standard optical lithography and a wet etch was done to form free standing membranes. Electron beam (E-beam) lithography was thereafter performed directly on the membranes to form the PC lattices. An advanced etch mask was developed to reduce charging effects and handle the fact that PMMA has poor selectivity to Si_3N_4 and SiO_2 in dry etching recipes. The mask was composed of 3 nm Cr on top of 150 nm PMMA, 20 nm SiO_2, and 150 nm polymer coating (ARC). The Cr functioned as a conductive layer during e-beam exposure of the PMMA. After e-beam exposure, the Cr was removed. The PMMA was developed, followed by a dry etch transferring the pattern into the SiO_2. Using the SiO_2 as a hard mask, the pattern was transferred to the ARC, and then into the slab. Finally, the ARC was removed. An illustration of a cross section view of a finalized chip is given in Fig. 8(f). A detailed description of the fabrication procedure can be found elsewhere [30].

Four different size PCs were made to investigate the effect of finite size lattices, composed of 10×10, 25×25, 50×50 and 100×100 periods. The final fabricated structures have a period of $p = 500 \pm 2$ nm and a hole radius of $r = 100 \pm 2$ nm. SEM images of the lattices are given in Fig. 8(a).

In the case of the PCs bound by Bragg mirrors on the sides, 2D patterns of 100 nm-radius holes with six different periods were made for a fixed set of Bragg mirror dimensions. The Bragg mirrors were made with a period of 250±2 nm and a duty cycle of 50±5 %. Four of these six designs, those with periods $p_1 = 450 \pm 2$ nm, $p_2 = 474 \pm 2$ nm, $p_3 = 500 \pm 2$ nm and $p_4 = 526 \pm 2$ nm, operated as intended. No signs of coupling to guided resonance modes was observed for periods $p_5 = 550$ nm, $p_6 = 576$ nm. The resonant modes in these structure were

#193105 - $15.00 USD Received 1 Jul 2013; revised 28 Aug 2013; accepted 15 Sep 2013; published 27 Sep 2013

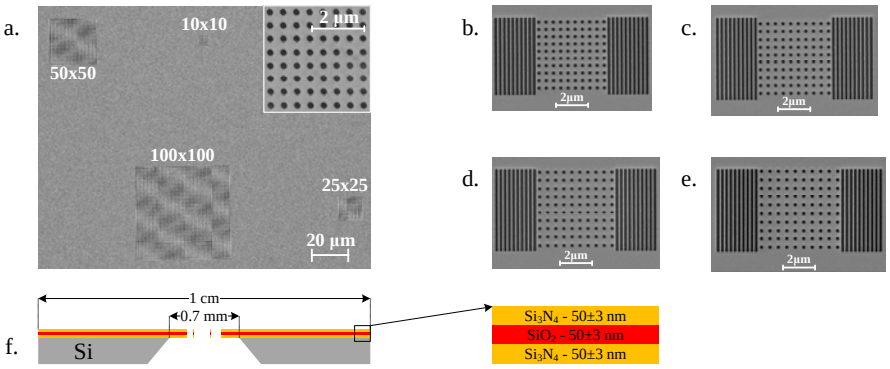

Fig. 8. Images taken with a scanning electron microscope of the fabricated structures. (a) Four square hole lattices consisting of 10×10, 25×25, 50×50 and 100×100 holes, with a period of $p = 500\pm2$ nm and a hole radius of $r = 100\pm2$ nm. (b-e) Four square hole lattices bound by in-plane Bragg mirrors. The 2D hole lattices consist of 10×10 holes, with periods (b) $p_1 = 450\pm2$ nm, (c) $p_2 = 474\pm2$ nm, (d) $p_3 = 500\pm2$ nm and (e) $p_4 = 526\pm2$ nm, from left to right. They all have a hole radius of $r = 100\pm2$ nm. The Bragg mirrors have a line spacing of 250 ± 2 nm and a duty cycle of 50 ± 5 %. All structures are etched in a 150 nm thick $Si_3N_4/SiO_2/Si_3N_4$ thin-film stack, suspended on a Si-frame. (f) Illustration of cross section view of a chip after fabrication is finalized.

outside the spectrum of our source. SEM images of the structures with p_1 to p_4 are given in Fig. 8(b)-8(e).

The optical setup measures the transmittance of the PC as a function of wavelength with spacial resolution. This is done using a 2D CCD camera connected to a Olympus BX51 Optical Microscope equipped with MPlanON 50x/0.95NA objective. A halogen lamp routed through a monochromator and a collimator provides the microscope with monochromatic backside normal incidence illumination with a bandwidth of 4.5 nm. Images were recorded with the monochromator tuned to one wavelength at a time with a spacing of 2 nm. The exposure time for each image was 5 s. The measured transmittance, presented in the results section below, is found by recording an image with and without the PC in the light path, calculating the ratio between the recorded intensities pixel by pixel.

6. Results and discussion

An image of the four different lattice sizes, as they appear in the microscope for λ=656 nm, is shown to the right in Fig. 9. Black boxes have been fitted around each lattice. The boxes are named S_{10}, S_{25}, S_{50} and S_{100}. Subscript numbers denote which lattice size each box corresponds to. A fifth box, S_0, has also been included. S_0 frames an unstructured area on the membrane. The transmittance is calculated by finding the mean value of pixels located within the boundary of each black box. The result is plotted in the graph to the left in Fig. 9.

In pixels corresponding to a solid slab, there is no sign of resonance. The 10×10 lattice, shows a broad dip around 650 nm. Looking at the plot for the 25×25 lattice, the dip close to 650 nm reaches a lower minimum value and shows a significant decrease in bandwidth. A second dip close to 570 nm also becomes visible. As we further increase the number of periods in the lattice to 50×50, these two dips continue to decrease in minimum value and bandwidth. Continuing to 100×100 periods, we do not see a decrease in minimum value, but a small increase. The bandwidth does however continue to decrease, leaving the Q-factor approximately unchanged.

#193105 - $15.00 USD Received 1 Jul 2013; revised 28 Aug 2013; accepted 15 Sep 2013; published 27 Sep 2013

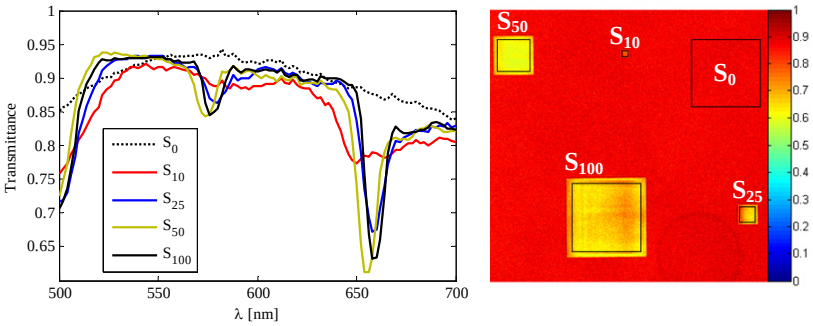

Fig. 9. (Right) Optical microscopy image of the four different lattices depicted in Fig. 8(a), recorded by a CCD camera for an incident wavelength of $\lambda = 656$ nm. Black boxes have been fitted around each lattice, named S_{10}, S_{25}, S_{50} and S_{100}. Subscripts denote the square-root of the number of holes in each lattice. A fifth box, S_0, has also been included, framing an unstructured area on the membrane. (Left) The experimentally measured transmittance, given as the mean normalized pixel value within each box, is plotted as a function of wavelength. The normalization procedure in described in section *Fabrication and experimental setup*.

The reason why we do not see a continuous increase in Q-factor and reduction of minimum dip value for larger lattice sizes than 50×50 periods, is that after 50×50 periods we start to see the effect of lattice discrepancies, such as non-symmetric holes and inhomogeneous periodicity and radius. Such defects introduce additional loss in our optical resonator model and we can hence expect a reduced Q-factor. We also note that the dip bandwidth is starting to approach the bandwidth of our scanned source for lattices larger than 50×50 periods. This limits the observable Q-factor in our optical setup. As we scan the wavelength from 500-700 nm, we do not scan a delta function over this range, but a peak with finite bandwidth of about 4.5 nm. The resulting transmittance is the convolution of the actual transmittance and source spectrum, which will also reduce the Q-factor computed directly from the transmission spectrum. In any case, the lattice size effect on guided resonance modes is clear for the three smaller lattices: As we decrease the number of holes, the effect of coupling to guided resonance modes tends to disappear.

An image of a PC with in-plane Bragg mirrors, as it appear in the microscope for $\lambda = 630$ nm (top) and 626 nm (bottom) is shown to the right in Fig. 10. SEM images have been included, showing the polarization of the incident field relative to the orientation of lines in the Bragg mirror. The period of the selected structure is $p_2 = 476$ nm, and transmittance is calculated by finding the mean value of pixels bound by each black box. The result for two orthogonal polarizations of incident light, can be seen in the graph to the left in Fig. 10.

As expected from simulations, the spectral response is highly dependent on incident polarization. When the polarization is orthogonal to lines in the Bragg mirror, a dip in reflection is visible, but the bandwidth is large and comparable to the dip seen for the 10×10 holes lattice with no Bragg mirrors in Fig. 9. Once we turn the polarization parallel to the Bragg lines, the dip bandwidth and minimum value is significantly decreased. Considering that the holes are not perfectly symmetric and the Bragg lines have a roughness in our real structures, the fabricated devices perform well and clearly show how the Q-factor of a finite PC can be increased by exploiting reflecting boundary conditions. Comparing the transmittance for different Bragg PC structures depicted in Fig. 8, dip minimum values range from 0.65 to 0.70, and the position of the dips are period dependent, but they all show the same trends.

#193105 - $15.00 USD Received 1 Jul 2013; revised 28 Aug 2013; accepted 15 Sep 2013; published 27 Sep 2013

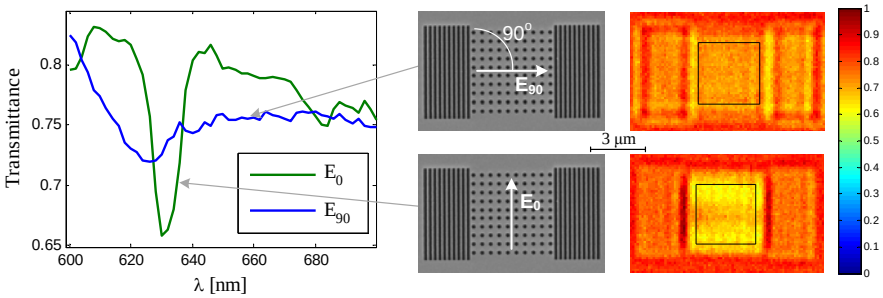

Fig. 10. (Very right) Optical microscopy images recorded with a CCD camera for two orthogonal polarizations of incident light, at wavelengths $\lambda = 630$ nm (top) and 626 nm (bottom), for the Bragg PC structure with period 476 nm (middle). (Left) The experimentally measured transmittance, given as the mean normalized pixel value within each box, is plotted as a function of wavelength. The normalization procedure in described in section *Fabrication and experimental setup*.

We note that position of the Bragg mirrors relative to the photonic crystal lattice has not been studied extensively. Light traveling in the plane, should be reflected back into the crystal as if the PC was infinite. If the phase of the reflection from the mirrors is off, we can see the opposite effect of what we are aiming for, namely weaker coupling to guided resonance modes as opposed to stronger. We also know that there will be light scattered out of the membrane at the edges, when in-plane modes meet the jump in effective index between the lattice and the homogeneous slab. Optimizing the position of the Bragg mirrors and designing a smooth transition in effective index between the lattice and the homogeneous slab, will increase the performance of our device.

We finally return to the red shift observed in Fig. 4(a) as the lattice size is increased. It is due to the fact that the bands supporting mode A and B in our structure have a positive second order derivative, $\partial^2\omega/\partial k_{||}^2 > 0$, at the Γ-point. This has been verified in simulations. Hence, as we increase the lattice size and decrease $\Delta k_{||}$, the sum of excited guided resonance modes have decreasing mean center frequency. This causes a red shift of the center wavelength of our dip in transmission, and is accompanied by an increase in observed Q-factor. The weak observable coupling to guided resonance modes in the smaller lattices, can hence be caused by excess band bending or insufficient lattice size. However, due to the strong polarization dependence evident in the Bragg PC structure, we can clearly see that the lattice size effect is dominating. This statement is further supported by inspecting the top left plot in Fig. 7. In this plot we see how there are in-plane waves propagating away from the lattice above and below the holes when the Bragg mirrors are not containing the guided resonance mode.

7. Conclusion

We have shown that guided resonance modes in 2D-PCs are not observable in the transmission spectrum of the PC if the number of periods in the lattice is insufficient. This agrees with analytic models developed for 1D-PCs [15, 16] and experimental studies of large 2D-PCs [17], and can be understood by considering a finite PC as an optical resonator with loss.

The fundamental loss mechanisms are related to coupling of incident light to fully guided modes existing outside the boundaries of the lattice and scattering of in-plane propagating waves at the lattice boundaries. We have shown how coupling to fully guided modes can be suppressed by introducing reflecting boundary conditions. This can be done using Bragg mir-

#193105 - $15.00 USD Received 1 Jul 2013; revised 28 Aug 2013; accepted 15 Sep 2013; published 27 Sep 2013

rors that have a band gap for in-plane propagating modes. Methods to reduce scattering at the lattice boundaries have not been investigated.

While our devices do not support guided resonance modes with extraordinary narrow bandwidths, the results show how lattices with limited extent can be made to work as if they are larger. Extrapolation of these results, indicate that a PC perfectly fabricated over a large number of periods can be replaced by a PC that is perfect over a small area and bound by an in-plane band gap. This is useful with respect to PCs being applied in real devices, especially in devices with high demands on miniaturization and the Q-factor of guided resonance modes.

Acknowledgment

All the photonic crystal structures used in this project were made at the University of Bergen Nanostructures Laboratory. We thank Trond Mohn, The University of Bergen and the Norwegian Research council (NFR) for funding. We also thank NFR for their support through the Norwegian PhD Network on Nanotechnology for Microsystems, IndustriPhD program and ISBILAT program.

#193105 - $15.00 USD Received 1 Jul 2013; revised 28 Aug 2013; accepted 15 Sep 2013; published 27 Sep 2013

Paper D

Detection of single nano-defects in photonic crystals between crossed polarizers

elink: Paper D

Detection of single nano-defects in photonic crystals between crossed polarizers

Jon Olav Grepstad,[1,*] Peter Kaspar,[2] Ib-Rune Johansen,[3] Olav Solgaard,[4] and Aasmund Sudbø[5,6]

[1]*Department of Electronics and Telecommunications, Norwegian University of Science and Technology, NO-7491 Trondheim, Norway*
[2]*III-V Lab, a joint lab of Alcatel-Lucent Bell Labs, Thales Research & Technology, and CEA Leti, F-91767 Palaiseau, France*
[3]*SINTEF ICT, Microsystems and Nanotechnology, NO-0373, Norway*
[4]*E.L. Ginzton Laboratory, Stanford University, CA-94305, USA*
[5]*Department of Physics, University of Oslo, NO-0316, Norway*
[6]*University Graduate Center, NO-2027 Kjeller, Norway*

[*]*jonolav.grepstad@sintef.no*

Abstract: We investigate, by simulations and experiments, the light scattering of small particles trapped in photonic crystal membranes supporting guided resonance modes. Our results show that, due to amplified Rayleigh small particle scattering, such membranes can be utilized to make a sensor that can detect single nano-particles. We have designed a biomolecule sensor that uses cross-polarized excitation and detection for increased sensitivity. Estimated using Rayleigh scattering theory and simulation results, the current fabricated sensor has a detection limit of 26 nm, corresponding to the size of a single virus. The sensor can potentially be made both cheap and compact, to facilitate use at point-of-care.

OCIS codes: (220.0220) Optical design and fabrication; (280.4788) Optical sensing and sensors; (050.5298) Photonic crystals.

References and links

1. B. Bohunicky and S. A. Mousa, "Biosensors: the new wave in cancer diagnosis," Nanotechnol. Sci. Appl. **4**, 1–10 (2010).
2. M. U. Ahmed, I. Saaem, P. C. Wu, and A. S. Brown, "Personalized diagnostics and biosensors: a review of the biology and technology needed for personalized medicine," Crit. Rev. Biotechnol. (2013).
3. M. F. Pineda, L. L. Chan, T. Kuhlenschmidt, C. J. Choi, M. Kuhlenschmidt, and B. T. Cunningham, "Rapid specific and label-free detection of porcine rotavirus using photonic crystal biosensors," IEEE Sens. J. **9**, 470–477 (2009).
4. D. Duval and L. M. Lechuga, "Breakthroughs in photonics 2012: 2012 breakthroughs in lab-on-a-chip and optical biosensors," IEEE Photonics J. **5**, 0700906 (2013).
5. F. Vollmer and L. Yang, "Label-free detection with high-q microcavities: a review of biosensing mechanisms for integrated devices," Nanophotonics **37**, 267–291 (2012).
6. R. Bruck, E. Melnik, P. Muellner, R. Hainberger, and M. Lammerhofer, "Integrated polymer-based mach-zehnder interferometer label-free streptavidin biosensor compatible with injection molding," Biosens. Bioelectron. **26**, 3832–3837 (2011).
7. D. Duval, J. Osmond, S. Dante, C. Dominguez, and L. Lechuga, "Grating couplers integrated on mach-zehnder interferometric biosensors operating in the visible range," IEEE Photonics J. **5**, 3700108 (2013).
8. M. Mancuso, J. M. Goddard, and D. Erickson, "Nanoporous polymer ring resonators for biosensing," Opt. Express **20**, 245–255 (2012).

#200180 - $15.00 USD Received 25 Oct 2013; revised 3 Dec 2013; accepted 4 Dec 2013; published 12 Dec 2013

9. V. R. Dantham, S. Holler, C. Barbre, D. Keng, V. Kolchenko, and S. Arnold, "Label-free detection of single protein using a nanoplasmonic-photonic hybrid microcavity," Nano Lett. **13**, 3347–3351 (2013).
10. S. Pal, P. M. Fauchet, and B. L. Miller, "1-d and 2-d photonic crystals as optical methods for amplifying biomolecular recognition," Anal. Chem. **84**, 8900–8908 (2012).
11. I. Ament, J. Prasad, A. Henkel, S. Schmachtel, and C. Sonnichsen, "Single unlabeled protein detection on individual plasmonic nanoparticles," Nano Lett. **12**, 1092–1095 (2012).
12. P. Zijlstra, P. M. R. Paulo, and M. Orrit, "Optical detection of single non-absorbing molecules using the surface plasmon resonance of a gold nanorod," Nat. Nanotechnol. **7**, 379-382 (2012).
13. R. Adato and H. Altug, "In-situ ultra-sensitive infrared absorption spectroscopy of biomolecule interactions in real time with plasmonic nanoantennas," Nat. Commun. **4**, 2154 (2013).
14. A. E. Cetin and H. Altug, "Fano resonant ring/disk plasmonic nanocavities on conducting substrates for advanced biosensing," ACS Nano **6**, 9989–9995 (2012).
15. A. A. Yanik, M. Huang, O. Kamohara, A. Artar, T. W. Geisbert, J. H. Connor, and H. Altug, "An optofluidic nanoplasmonic biosensor for direct detection of live viruses from biological media," Nano Lett. **10**, 4962–4969 (2010).
16. M. E. Beheiry, V. Liu, S. Fan, and O. Levi, "Sensitivity enhancement in photonic crystal slab biosensors," Opt. Express **18**, 22702–22714 (2010).
17. J. O. Grepstad, P. Kaspar, O. Solgaard, I.-R. Johansen, and A. S. Sudbø, "Photonic-crystal membranes for optical detection of single nano-particles, designed for biosensor application," Opt. Express **20**, 7954–7965 (2012).
18. C. Ge, M. Lu, S. George, T. A. Flood, C. Wagner, J. Zheng, A. Pokhriyal, J. G. Eden, P. J. Hergenrother, and B. T. Cunningham, "External cavity laser biosensor," Lab Chip **13**, 1247–1256 (2013).
19. S. Fan and J. D. Joannopoulos, "Analysis of guided resonances in photonic crystal slabs," Phys. Rev. B **65**, 235112 (2002).
20. V. Lousse, W. Suh, O. Kilic, S. Kim, O. Solgaard, and S. Fan, "Angular and polarization properties of a photonic crystal slab mirror," Opt. Express **12**, 1575–1582 (2004).
21. W. Suh, M. F. Yanik, O. Solgaard, and S. Fan, "Displacement-sensitive photonic crystal structures based on guided resonance in photonic crystal slabs," Appl. Phys. Lett. **82**, 1999–2001 (2003).
22. O. Kilic, S. Kim, W. Suh, Y.-A. Peter, A. S. Sudbø, M. F. Yanik, S. Fan, and O. Solgaard, "Photonic crystal slabs demonstrating strong broadband suppression of transmission in the presence of disorders," Opt. Lett. **29**, 2782–2784 (2004).
23. M. Huang, A. A. Yanik, T. Y. Chang, and H. Altug, "Sub-wavelength nanofluidics in photonic crystal sensors," Opt. Express **17**, 24224–24233 (2009).
24. J. O. Grepstad, P. Kaspar, O. Solgaard, I.-R. Johansen, and A. Sudbo, "Optical imaging system designed for biosensing using a photonic crystal membrane to detect nanoparticles," in *Imaging and Applied Optics Technical Papers* (Optical Society of America, 2012), pp. IM4C.2.
25. J. Voros, "The density and refractive index of adsorbing protein layers," Biophys. J. **87**, 553–561 (2004).
26. Commercially available software, OptiFDTD 9.0, supplied by Optiwave, http://optiwave.com/, visited 25 Oct. 2013.
27. Commercially available software supplied by KJ Innovation, http://software.kjinnovation.com/GD-Calc.html, visited 25 Oct. 2013.
28. J.-P. Berenger, "Numerical reflection from FDTD-PMLs: a comparison of the split PML with the unsplit and CFS PMLs," IEEE Trans. Antennas Propag. **50**, 258–265 (2002).
29. J. O. Grepstad, M. Greve, B. Holst, I.-R. Johansen, O. Solgaard, and A. Sudbo, "Finite-size limitations on quality factor of guided resonance modes in 2d photonic crystals," Opt. Express **21**, 23640–23654 (2013).
30. C. F. Bohren and D. R. Huffman, *Absorbtion and Scattering of Light by Small Particles* (John Wiley, 1998), Chap. 5.
31. J. O. Grepstad, M. Greve, T. Reisinger, and B. Holst, "Nano-structuring on free-standing, dielectric membranes using e-beam lithography," J. Vac. Sci. Technol. B **31**, 06F402 (2013).

1. Introduction

Preventive action and early detection of diseases are identified among the best and most cost efficient means of improving health care [1, 2]. This can be done by developing efficient high sensitivity biosensors that are cheap and small, allowing them to be applied by physicians at point-of-care or even as a personal appliance in the comfort of our own homes. A technology proposed to realize these next generation biosensors, is label-free optical biosensing [3, 4]. Label-free optical sensors can be made using micro- and nano-technology that generally provides devices that are cheap and small. These sensors also have some of the highest sensitivities reported today [5].

#200180 - $15.00 USD Received 25 Oct 2013; revised 3 Dec 2013; accepted 4 Dec 2013; published 12 Dec 2013

All label-free optical biosensors are based on the same two basic principles. Firstly, a surface is furnished with molecules that can capture a specific targeted molecule. The capture process is generally a time-efficient one-step reaction, in contrast to label or tag assisted detection, where a radioactive or fluorescent molecule is added to captured target molecules through a multilevel chemical reaction. Secondly, the surface is optically designed to enable concentration of light, from an excitation source, at the specific areas where captured molecules are made to settle. This induces an optical response that is sensitive to changes in permittivity in the capture zone. Capture events typically manifest themselves as a shift in resonance frequency, a dip in transmission or reflection, or as scattering. Label-free biosensors can hence be considered to be composed of two parts: A chemistry that provides selectivity and an optical transducer that provides sensitivity. The focus of this article will be the optical transducer.

A number of different transducers exist. Mach-Zehnder interferometers [6, 7], optical ring resonators [8, 9], photonic crystal cavity resonators [10], and techniques exploiting local surface-plasmon-resonance (LSPR) in metal nano-particles are promising. Some are even reported to sense changes in refractive index corresponding to a single molecule [5, 9, 11, 12]. Some of the above transducers do however call for elaborate alignment procedures in order to couple light in and out of the transducer, and they all require complex designs to achieve a high dynamic range. Consequently, these schemes seem more applicable as laboratory tools, and less suitable in cheap and compact point-of-care devices. Sensors exploiting surface-plasmon-resonance in periodic metal nano-structures [13–15], and photonic crystal sensors exploiting coupling to guided resonance modes [16–18], have so far not reached single-molecule sensitivity. These do in general have lower sensitivities, but are advantageous regarding in- and out coupling of light and can be made with a high dynamic range.

In a recent report [17], we presented a photonic crystal based biosensor that exploits coupling to guided resonance modes [19]. The transducer is composed of a membrane, where a periodic square lattice of holes has been etched through the membrane. This creates a periodic permittivity in the membrane plane that allows normal incident light to couple into in-plane propagating modes. The particular mode that we excite, concentrates its field in the vicinity of the membrane, primarily in the holes. It also produces a sharp dip in the reflected spectrum.

The center wavelength of the dip in reflectivity is highly sensitive to changes in permittivity close to the membrane, especially at the hole walls, where the field is maximized. Covering a pristine 2D PC membrane with a monolayer of biomolecules that has different permittivity than the surrounding media, will hence shift the center wavelength of the dip, allowing the monolayer to be detected. However, when aiming for sensitivities on the order of single molecules, captured molecules cannot be considered to be a monolayer. Single capture events are locally bound defects that break the symmetry of the lattice. The defects will induce local shifts in the frequency of resonant modes, but they will also provide new exit channels for light semi-bound in the guided resonance mode. It is the latter effect that we exploit in our sensor. The membrane is designed for high reflectivity in its native state [20–22], at a chosen operating wavelength. When a particle is trapped in a hole, it will be located in a strong optical field that is scattered out of the membrane. Consequently, a bright spot on a dark background, centered at the origin of the particle, can be detected in transmission. Furthermore, the choice of making an intensity based sensor, using a single operating wavelength, instead of tracking a shift in the resonance, limits the required number of optical components in the design. This is advantageous in relation to cost and compactness of a final device.

In [17], we proposed that the detection principle can be modeled as enhanced Rayleigh scattering. The current report is an extension of this work. We now present simulation and experimental results that support our hypothesis. A modified optical setup is also presented, where crossed polarizers [23] are used to suppresses the background and increases the signal-to-noise

#200180 - $15.00 USD Received 25 Oct 2013; revised 3 Dec 2013; accepted 4 Dec 2013; published 12 Dec 2013

ratio. Using the new optical setup, we calculate a detection limit corresponding to single particles the size of viruses.

2. Images obtained with unpolarized light

Figure 1(a) shows a scanning electron microscope (SEM) image of the front side of a fabricated 2D photonic crystal (PC) membrane. It is composed of a square lattice of 100×100 holes with radius 145 ± 10 nm and period 490 ± 5 nm. The holes are etched through three thin films, 50 ± 5 nm Si_3N_4/50 ± 5 nm SiO_2/50 ± 5 nm Si_3N_4, free-standing in air. This is the transducer in our sensor. The motivation for choosing a three layered stack, is that a cylinder surface is then define inside every hole, chemically different from the rest of the PC surface. In turn, this can enable us to functionalize the inside of the holes to capture targeted molecules, while the rest of the PC opposes molecule capture. A more detailed description of how molecules can be immobilized in our structure is given in previous work [17].

Figure 1(b) shows a SEM image of the membrane backside, and Fig. 1(c) is an image of the front side of the membrane recorded with an optical microscope. Two defects or contaminations are visible in all the images, SEM as well as optical. The discrepancy located at the top in Fig. 1(a), resulting in the upper bright spot in Fig. 1(c), is not visible in Fig. 1(b). It hence lies on the front side, and is known to be a contamination. It first appeared on the surface sometime after fabrication. The left defect is especially well suited for preliminary studies. It is located inside a hole, where we plan to capture biomolecules, and has a radius of 60 ± 15 nm. We will refer to it as defect A. The permittivity of the defect is unknown, but can be limited by possible contaminations in our lab, that have a permittivity between 2 and 12.25.

From Fig. 1(b), showing the backside of the PC, it appears like defect A results from a hole that has not been fully etched. This suggests that defect A is composed of a mix of Si_3N_4 and SiO_2, and has a permittivity between 2.25 and 4 for visible light. The lower limit is comparable to the permittivity of relevant biological target molecules, which typically have a permittivity between 2 and 2.5 [25].

The setup used for optical characterization, is shown in Fig. 1(d). It is composed of a narrowband light source irradiating the backside of the fabricated PC, and a microscope connected to a CCD camera recording the transmitted light with spatial resolution. Two polarizers are placed in the light path, one between the source and the PC, and a second between the PC and the CCD camera. We return to results generated with polarizers L_s and L_d employed, and a laser diode source in section 4. For now, we will focus on the image in Fig. 1(c), recorded with a light source in the form of a halogen lamp routed through a monochromator, and without the polarizers L_s and L_d in the light path [24]. The image depicts the unpolarized transmittance of the membrane, for narrowband unpolarized light, normally incident on the backside of the membrane at a center wavelength of 632 nm.

We have previously [17] proposed that the appearance of a particle trapped in a PC, as shown by the bright spot pattern in Fig. 1(c), can be understood as amplified Rayleigh small particle scattering. Provided that a particle trapped in a PC is sufficiently small, the mode field will not be affected by its presence. This results in the overall transmittance being low, and the field in the vicinity of the membrane being high. The mode field hence acts as a driving field, causing particles that are trapped in the lattice to scatter the resonantly enhanced field in the membrane. Scattered light will exit out into the surrounding medium as spherical waves with origin at the particle center, and can be refocused to form bright spots on a detector.

A closer examination of the bright spot pattern in Fig. 1(c), reveals that this description of the situation is inadequate. The pattern is composed of an ensemble of spots that follow the symmetry of the lattice.

#200180 - $15.00 USD Received 25 Oct 2013; revised 3 Dec 2013; accepted 4 Dec 2013; published 12 Dec 2013

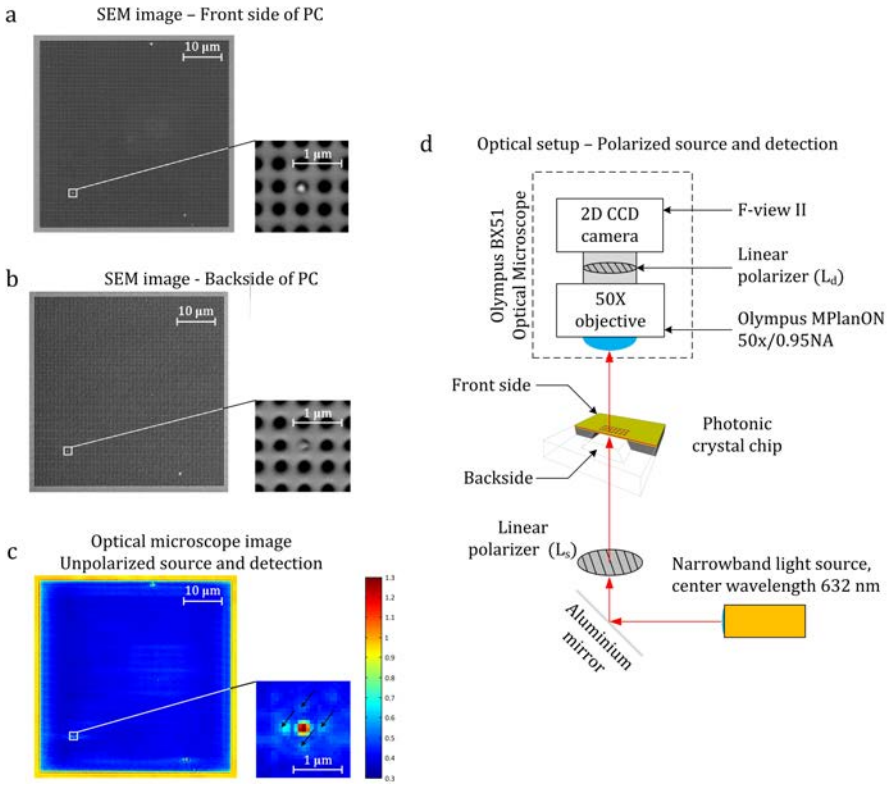

Fig. 1. Images acquired using a scanning electron microscope (SEM) of the front side (a) and backside (b) of a fabricated sample of the photonic crystal. An area of the image showing a particle with a radius of 60±15 nm has been enlarged. The particle is a defect in the lattice. (c) An image of the crystal, front side facing up, has been recorded using an optical setup [24] with monochromatic illumination at 632 nm, normally incident from the backside. The color scale gives the transmittance of the membrane. (d) Optical setup with a collimated narrowband light source centered at 632 nm, emitting a beam directed by a 45° aluminum mirror to the backside of a photonic crystal at normal incidence, via a linear polarizer, L_s. Transmitted light is collected by a 50x/0.95 NA objective lens, passes through a linear polarizer, L_d, and is recorded by a 2D CCD camera. The image displayed in (c) is recorded with the optical setup in (d), not using polarizers L_s and L_d.

3. Simulation of particles trapped in 2D photonic crystals

Finite-difference-time-domain (FDTD) simulations [26] and rigorously coupled wave analysis (RCWA) [27], have been done to further investigate the effect of placing a small particle in a 2D PC.

Results from simulation using RCWA are summarized in Fig. 2. A unit cell in the fabricated PC, with nominal dimensions, is illustrated in Fig. 2(a). Figure 2(b) shows the simulated transmittance of the perfectly periodic PC as a function of wavelength, for normal incidence light. Two dips in transmission can be seen in the plot, resulting from coupling of incident light to two guided-resonance modes. We utilize the mode causing the low-transmission dip at 631 nm. The simulated spectrum in Fig. 2(b) agrees well with the transmitted spectrum of the fabricated structure, as we have shown earlier [17], but is slightly shifted with respect to the measured

#200180 - $15.00 USD Received 25 Oct 2013; revised 3 Dec 2013; accepted 4 Dec 2013; published 12 Dec 2013

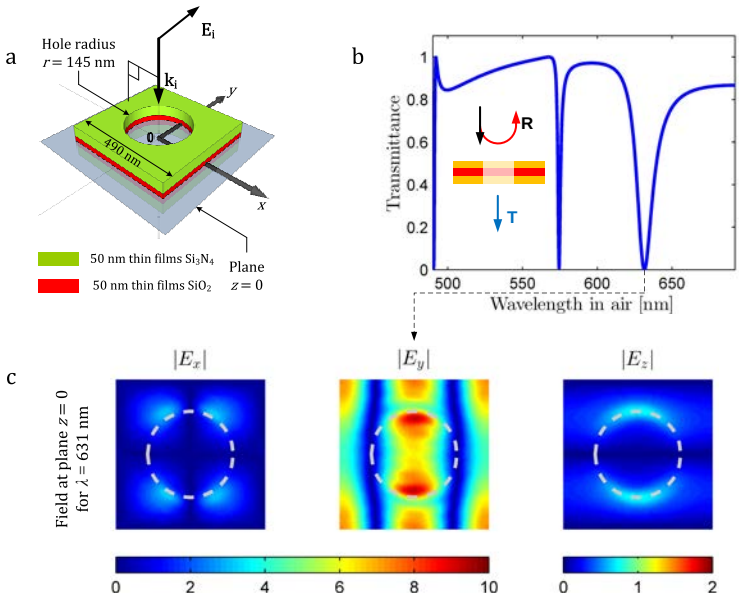

Fig. 2. Results from RCWA simulations. (a) Unit cell of a 2D photonic crystal membrane, and (b) the simulated transmittance of the crystal for normal incidence y-polarized light as a function of wavelength. (c) Color image representations of the resonantly enhanced field at the center plane, $z = 0$, is given for the dip at 631 nm. The bottom color scale gives the field amplitude, relative to the amplitude of the incident field.

dip value at 632 nm. A simulation showing the field in the center plane of a unit cell of the membrane at this wavelength, for incident light polarized in the y-direction, is given in Fig. 2(c). The y component of the mode field forms a saddle profile aligned with the y-axis, peaking at the hole walls with an amplitude 10 times the incident amplitude. Inside the holes, the x and z component are an order of magnitude or more smaller than the y component. Note that it is the absolute value of the field that is plotted in Fig. 2. Crossing zero field nodes, the phase of the fields change by a factor π.

The design of the FDTD simulation is illustrated in Fig. 3. A volume, having a refractive index of air, $n_0 = 1$, with a length corresponding to four lattice periods, $4p$, and a cross section of $15p \times 15p$, was defined. The spatial resolution was set to 20 nm in the z-direction, and 10 nm in the x- and y-direction. A slab with refractive index $n_s = 2$ was centered at $z = p$. The thickness of the slab was set to 160 nm and the unit cell in the lattice is composed of a hole going through the slab with a radius of $r = 145$ nm. The lattice is square with a period $p = 500$ nm. All simulation boundaries are terminated with absorbing layers of the perfectly matched type (PML) [28].

First, the frequency response of the PC was analyzed. This was done by imposing a planar Gaussian pulse, truncated at the simulation boundaries, with normal incidence relative to the membrane plane at $z = 0.5p$, with center frequency corresponding to a vacuum wavelength of 650 nm. The frequency response was found by calculating the Fourier transform of the amplitude of the transmitted wave, recorded at $z = 4p$ in the center of the simulation domain on the xy-plane. This allowed us to find the wavelength where the simulated PC supports the particular mode field corresponding to the one displayed in Fig. 2(c). The simulated design is not identical to the fabricated PCs, but has been modified to speed up the simulations. The

#200180 - $15.00 USD Received 25 Oct 2013; revised 3 Dec 2013; accepted 4 Dec 2013; published 12 Dec 2013

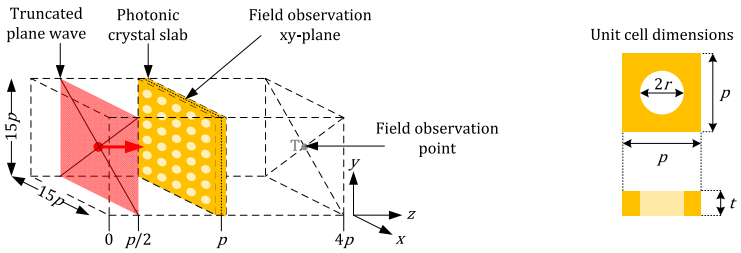

Fig. 3. (Left) Illustration of the FDTD simulation domain, composed of a volume of air, with refractive index set to $n_{\text{air}} = 1$, measuring $15\times15\times4$ periods, where the period $p =$ 500 nm. All simulation boundaries are terminated with absorbing layers of the perfectly matched type (PML). A plane incident wave, truncated at the simulation boundaries, is imposed at $z = 0.5p$, traveling in the positive z-direction, and a photonic crystal membrane with thickness $t = 160$ nm is centered at $z = p$, aligned with the xy-plane. The field is recorded as a function of time at the observation point T, and the terminal field distribution is recorded at the xy-plane at $z = p$. (Right) Drawing of the unit cell in the photonic crystal. The period is p, and the radius of the hole is $r = 145$ nm. The membrane material has a refractive index set to $n_{\text{memb}} = 2$, corresponding to Si_3N_4.

transmission spectra of the simulated and fabricated PC are therefore shifted relative to each other, due to the small differences in materials, lattice period and membrane thickness. The dip in transmission at 703.6 nm for the simulated PC, and the dip at 632 nm for the fabricated PC, are both caused by the same guided resonance mode.

Simulations using a continuous wave source tuned to 703.6 nm were thereafter performed for a pristine PC and for a PC with one particle, vertically centered, in the center hole. This was done by imposing a plane wave, truncated at the simulation boundaries, with normal incidence relative to the membrane plane at $z = 0.5p$, traveling in the positive z-direction. The fields in the center plane of the PC were observed. Three lateral positions of the particle were simulated: At the center of the hole, and off-centered in the x-direction and y-direction, touching the hole wall. The radius of the particle was set to 60 nm, similar in size to defect A. It is set to have a refractive index of 2, corresponding to Si_3N_4. Simulations with three different particle radii, centered both laterally and vertically in the center hole, were also done. Nominally, the radius of the particles were 40, 60 and 80 nm. Due to the discrete spatial resolution in the FDTD simulations, the actual simulated volumes of the particles were $2.4\cdot10^5$, $8.8\cdot10^5$, and $20.6\cdot10^5$ nm^3. We will refer to these particle sizes as V_{S}, V_{M}, V_{L}, in the following text.

The procedure of simulating a crystal of finite size is computationally intensive. Using periodic boundary conditions and a smaller simulation domain would speed up the simulations, and should be chosen if the aim is to investigate the effect of inserting a particle in every hole in a pristine PC, or every other, third, etc. In contrast to such investigations, we aim to find the effect of inserting one single particle in a pristine PC, for the case when a small fraction of the scattered light is emitted from the hole with the particle, and many holes around the particle emit scattered light. Even when terminating our 15×15 periods domain with periodic boundary conditions, and simulating the effect of inserting one particle in the center of this super cell, it is hard to extract the separate contribution from each particle. In order to see their contributions independently, we have therefore chosen to terminate the boundaries with PML, and hence been able to visualize the outward flow of optical power along the membrane from the particle.

#200180 - $15.00 USD Received 25 Oct 2013; revised 3 Dec 2013; accepted 4 Dec 2013; published 12 Dec 2013

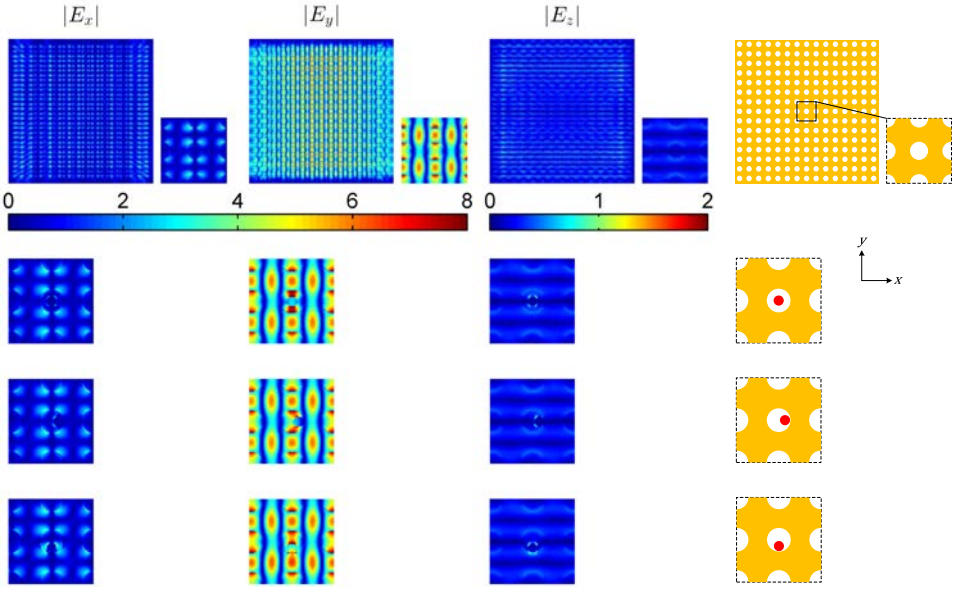

Fig. 4. Color image representations of fields resulting from continuous wave FDTD simulations of a pristine photonic crystal, illuminated with normal incidence y-polarized light at a wavelength of 703.6 nm, without a particle in the lattice (row 1), and photonic crystals with a particle inserted at three selected lateral positions in the center hole: Center (row 2), off-centered in the x-direction (row 3), and off-centered in the y-direction (row 4). The first three columns show the absolute value of the field components E_x, E_y, and E_z, respectively. Illustrations in the fourth column, corresponds to the areas in-plane over which the field has been plotted. The color scales represent the amplitude (absolute value) of each of the three components of the E-vector, divided by the amplitude of the E-vector of the incident plane wave.

3.1. Position dependence of particles trapped in photonic crystals

The FDTD simulations for a single wavelength (contiuous wave) allow us to compute an electric field vector, **E**, as a function of position. The vector **E**, has three components E_x, E_y, and E_z, each component being a complex phasor representing the amplitude and the phase relative to the incident wave. The upper row of field plots in Fig. 4, shows $|E_x|$, $|E_y|$, and $|E_z|$ in the center plane of a pristine PC. The excited guided resonance mode forms as rows of holes parallel to the incident polarization oscillate in phase and couple to a mode with in-plane k-vectors parallel to the x-axis. Since the boundaries of the simulation are terminated with absorbing walls, we are not simulating an infinite lattice, which is why the mode field declines as we approach the edge of the crystal [29]. The lower three rows in Fig. 4, show what happens when a particle is inserted in the crystal: The mode field is retained, and the effect of the particle is only visible in the immediate vicinity of the particle.

To clarify the change in fields, the absolute value of the change, $|\Delta\mathbf{E}| = |\mathbf{E}(\text{PC with particle}) - \mathbf{E}(\text{pristine PC})|$, is plotted in Fig. 5, for all three field components and particle positions. The plots show that the particle behaves similar to an ideal dipole: Inside the holes, the dominant field component of the mode field lies in-plane, pointing in the y-direction. The particle radiates spherical waves in the shape of a torus, with its axis of symmetry oriented parallel to the y-axis. It hence radiates strongly in the x-direction, and very weakly in the y-direction. The scattered light can either exit directly out into the surrounding

#200180 - $15.00 USD Received 25 Oct 2013; revised 3 Dec 2013; accepted 4 Dec 2013; published 12 Dec 2013

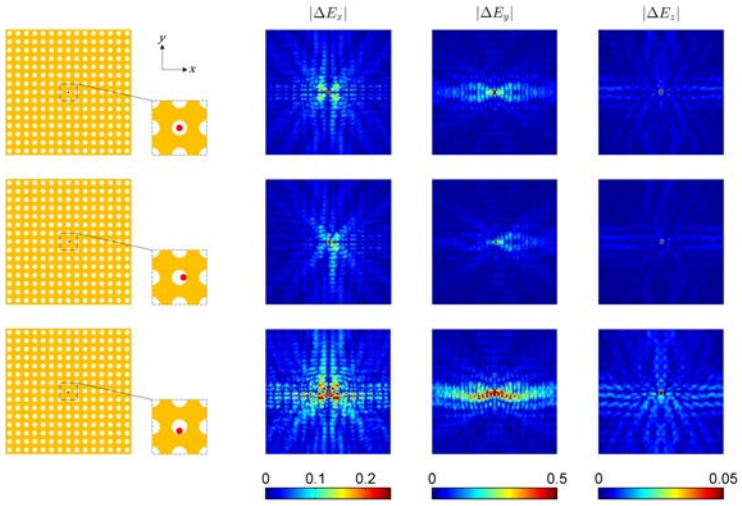

Fig. 5. Color image representations of absolute values of changes in the complex-valued field components E_x, E_y and E_z, at the center plane of a pristine photonic crystal, caused by inserting a particle in the crystal. The photonic crystal is illuminated with normally incident y-polarized light at a wavelength of 703.6 nm. Three selected lateral positions of the particle in the center hole have been investigated: Center (row 1), off-centered in the x-direction (row 2), and off-centered in the y-direction (row 3). Illustrations to the far left correspond to the areas in-plane over which the field has been plotted. The change has been calculated by subtracting the field distribution for a pristine photonic crystal shown in Fig. 4 (top row), from the field distribution in a photonic crystal with a particle trapped in the lattice, Fig. 4 (row 2-4). The plotted fields hence correspond directly to the E-field scattered by the particles. The color scales represent the absolute value of the change in of each of the three components of the E-vector, divided by the amplitude of the E-vector of the incident plane wave.

medium, or couple to guided resonance in the membrane. The torus shape of the radiation diagram of an oscillating dipole in free space, will therefore be strongly distorted, but we still expect to see high $|\Delta E|$-values perpendicular to the axis of polarization, and very low $|\Delta E|$-values parallel to the axis of polarization. This symmetry is clearly present in Fig. 5, especially in the $|\Delta E_y|$-plot.

Moreover, there is an increase in $|\Delta E|$ as the particle is moved towards the wall in the y-direction where the guided-resonance mode field is maximized, and a decrease as the particle is moved towards the wall in the x-direction where the mode field is minimized. Finally, note that scattered light from a particle close to a wall, shows stronger coupling to the side where the wall is closest to the particle.

3.2. Size dependence of particles trapped in photonic crystals

Going from left to right in Fig. 6(a), plots show the absolute value of the change in the y component of the vector $\mathbf{E}$, $|\Delta E_y| = |E_y(\text{PC with particle}) - E_y(\text{pristine PC})|$, caused by inserting particles with volumes V_S, V_M, and V_L in the center hole of a pristine PC. Qualitatively, all particle sizes induce the same change in field distribution. This is also the case for the x and z component of the field (not shown). The volume dependence is clarified in Fig. 6(b), showing a line plot of normalized field strengths from Fig. 6(a) superimposed on each other along the x-direction at $y = 0$.

#200180 - $15.00 USD Received 25 Oct 2013; revised 3 Dec 2013; accepted 4 Dec 2013; published 12 Dec 2013

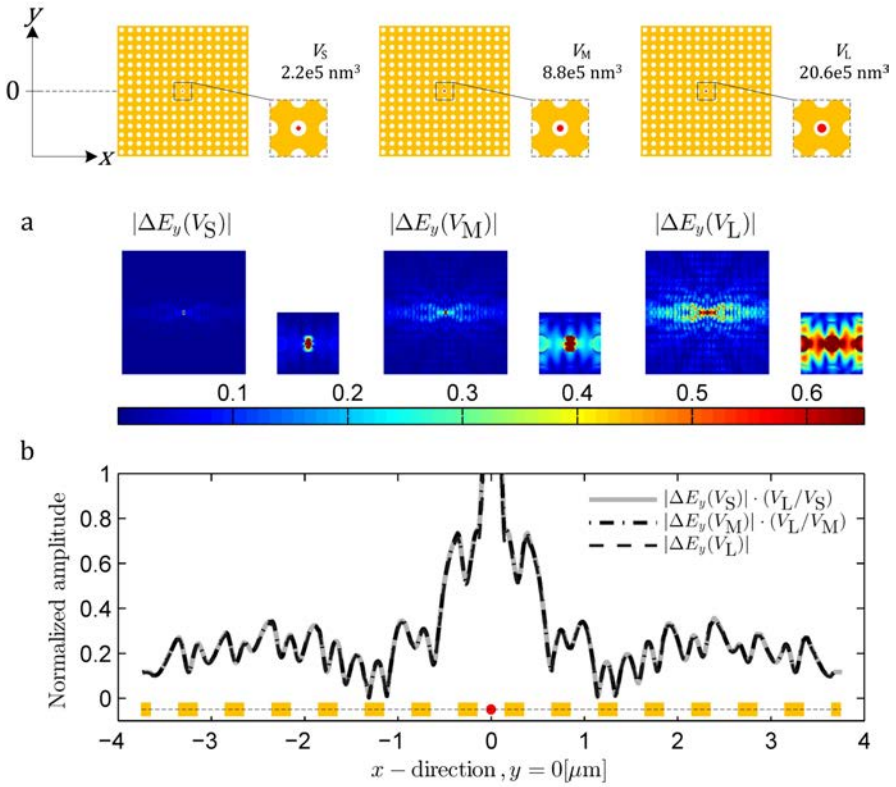

Fig. 6. (a) Color image representation of the y component of the field at the center plane of a pristine photonic crystal illuminated with normal incidence y-polarized light at a wavelength of 703.6 nm, caused by inserting a particle in the center hole of the crystal. Three different particle sizes have been simulated, as shown in the three illustrations at the top. (b) Line plot crossing the field plots in (a) in the x-direction at $y = 0$. The color scale in (a) and the abscissa in (b) both represent the absolute value of the change in E_y divided by the amplitude of the incident plane waves.

The field change resulting from the largest particle is scaled with 1, the medium particle with V_L/V_M and the smallest particle with V_L/V_S. In the holes where the particle is located, the near field dominates the field distribution, and the plots do not overlap. A period away from the center hole the line plots are virtually overlapping, meaning the amplitude of the change is proportional to the particle volume.

We point out that forbidden asymmetries are visible especially in the plots showing $|E_x|$ for the pristine PC in Fig. 4 and $|\Delta E_x|$ for the centered particle in Fig. 5. It has been verified, by increasing the grid resolution for selected structures, that these asymmetries are dominantly caused by numerical errors attributed to insufficient grid resolution. We also note that PML does not work well for waves having k-vectors parallel to the PML [28]. The presence of such waves in the simulations is known to give rise to unphysical reflections from the boundary. The effect is present in our simulations, but is too weak to be visible in Figs. 4–6.

#200180 - $15.00 USD Received 25 Oct 2013; revised 3 Dec 2013; accepted 4 Dec 2013; published 12 Dec 2013

4. Experiment

Employing the two linear polarizers, L_s and L_d, included in the optical setup illustrated in Fig. 1(d), enables polarized excitation, and cross-polarized excitation and detection. The source is in this case a diode laser producing a 1.1 mrad divergence collimated beam with a line width of $\sim$4.5 nm centered at 632 nm. The center wavelength corresponds to that of the desired guided resonance mode.

In the following results, microscope images have been recorded using two different polarizer configuration: Polarized excitation and unpolarized detection, where only polarizer L_s is applied, and cross-polarized excitation and detection, where both polarizers, L_s and L_d, are applied, and the source polarization is perpendicular to the detected polarization.

Eight recordings of the PC displayed in Fig. 2, are given in Figs. 7(a) and 7(b). One image displays the entire matrix of holes, and a smaller cut, labeled D, frames the immediate vicinity of defect A. Images in Fig. 7(a) are recorded using only polarizer L_s, and images in Fig. 7(b) are recorded with cross-polarized excitation and detection. Each row holds results for a fixed orientation of polarizer L_s, and arrows drawn on-top of a 3×3 hole matrix show the orientation of L_s and L_d relative to the lattice. The color scale shows the transmission, found by recording an image of the PC and dividing each pixel value by the mean background pixel value, found by recording an image without the PC in the light path.

A measure of the signal-to-background ratio (SBR) in each recoding is also displayed in Fig. 7. It has been calculated in the following way: Two sets of pixels with the same size were defined, corresponding to the area holding defect A [pixels D] and an area with hardly any observable defects [pixels M]. The locations of pixels D and M are the same in all recordings and have been marked with white frames labeled M and D, at the top left image in Fig. 7. The mean-, M_{mean}, and rms-value,M_{rms}, of pixels M, and the maximum value in pixels D, D_{max}, is found, and the signal-to-background ratio defined as $SBR = (D_{max} - M_{mean})/M_{rms}$.

The difference between the two polarizer configurations is clarified in Fig. 7(c), which holds line plots for both unpolarized detection and cross-polarized excitation and detection. The lines cross the recorded images in the *y*-direction, intersecting the peak in intensity in pixels D. The *x*-axis represents optical power per pixel, obtained by dividing each bit-value in the picture file by the exposure time.

4.1. Polarization dependent scattering from particles trapped in photonic crystals

The appearance of defect A for polarized excitation and unpolarized detection is shown in Fig. 7(a). As for unpolarized excitation and detection, resulting in the image in Fig. 1(c), the defect produces an ensemble of bright spots that coincide with the lattice. Light scattered by defect A is observed as a maximum, corresponding to the location of the defect, and scattered light coupled into the membrane, guided away from the defect center, is observed as re-scattering from the surrounding holes. However, in contrast to the pattern in Fig. 1(c), the symmetry of the patterns in Fig. 7(a) is not four fold symmetric. As predicted by the simulation results in Figs. 5 and 6, it is only two fold symmetric. Weaker scattering is observed from holes neighboring the defect along the line parallel to the incident polarization.

4.2. Decreasing background signal using cross-polarized excitation and detection

The signal-to-background ratio, is calculated to be 60, 80, 64 and 47 for the four different incident polarizations with unpolarized detection. Looking at the images in Fig. 7(a), the background signal is mainly limited by the non-zero and inhomogeneous transmittance of the membrane.

Using crossed polarizers, the signal-to-background ratio is changed to 91, 57, 147 and 97, respectively. The background signal is hence on average decreased relative to detected particle

#200180 - $15.00 USD Received 25 Oct 2013; revised 3 Dec 2013; accepted 4 Dec 2013; published 12 Dec 2013

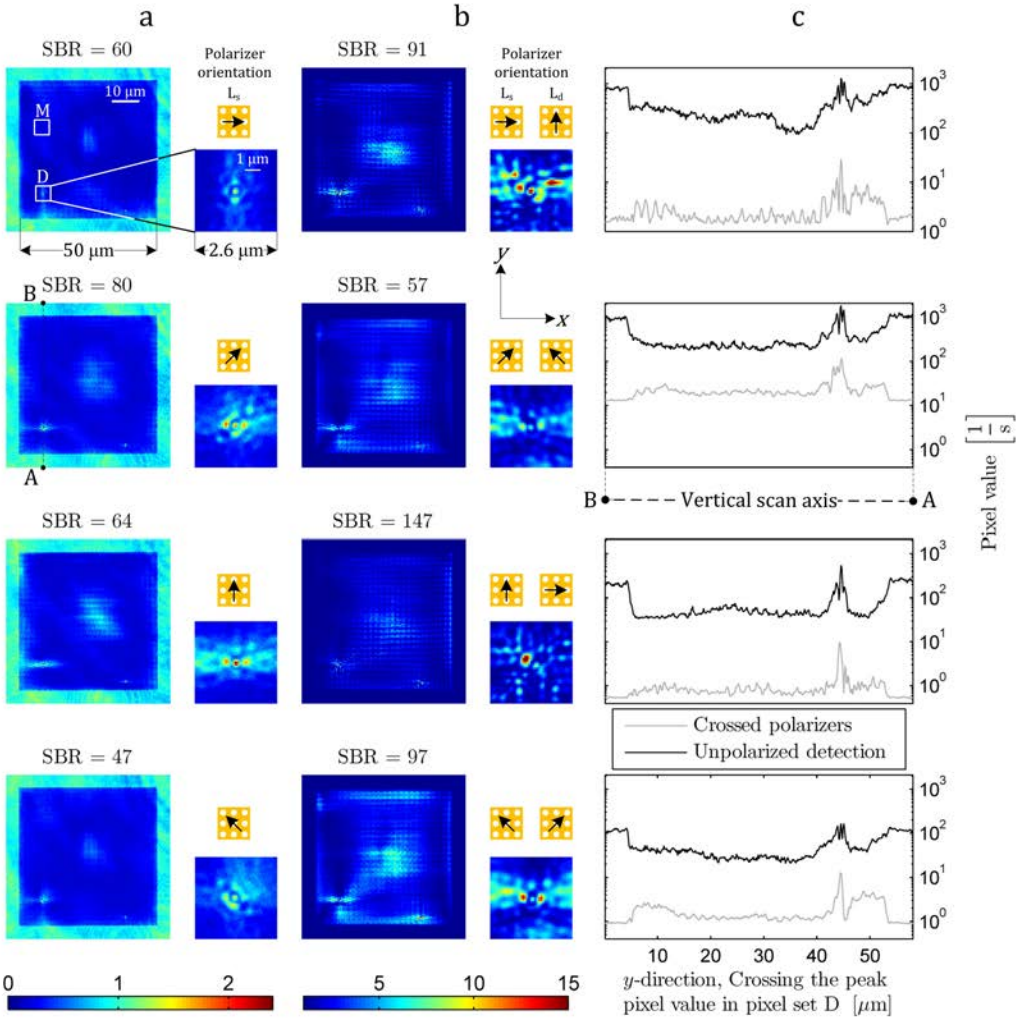

Fig. 7. Images recorded with the optical setup illustrated in Fig. 1(d). (a and b) Results are collected for four orientations of polarizer L_s, with polarizer L_d (a) not employed and (b) oriented orthogonal to L_s. Arrows drawn on-top of a 3×3 hole matrix show the orientation of L_s and L_d relative to the lattice, for each recording. A set of pixels D, corresponding to the position of defect A has been enlarged, for every recording. The color scales located at the bottom of column (a) and (b) show the transmittance of the membrane, calculated by dividing the pixel values resulting from a recording of the membrane, by the mean pixel value in a recording without the membrane in the light path. (c) Line plots of pixel values, going from point A to B, crossing the crystal in the *y*-direction, intersecting the peak in pixel value in pixels D. The ordinate in the plots in (c) represents optical power per pixel, computed by dividing each bit-value in the picture file by the exposure time.

irradiance, and mainly created by two sources of unwanted depolarization: Depolarization at the lattice boundaries and at numerous localizable points across the membrane.

#200180 - $15.00 USD Received 25 Oct 2013; revised 3 Dec 2013; accepted 4 Dec 2013; published 12 Dec 2013

5. Discussion

We have so far only focused on defect A. The two other defects or contaminations seen in the lower and upper part of of Fig. 1(a), are not reported on in this study. This is because these defects cannot be considered to resemble molecular capture events. They are both too large with respect to Rayleigh small particle scattering theory, and also lie close to the lattice boundary, where the PC performance suffers from edge effects. We also note that in biosensing it is most relevant to focus on detection of nano-particles in water. However, in this proof of principle study, we have chosen to design the PC for detecting nano-particles in air. A discussion on what needs to be done in order for the sensor to be used to detect nano-particles in water is found in previous work [17].

In our particular design, incident light couples to a guided resonance mode that supports high fields in the holes. Simulation results in Fig. 2(c), show how the mode field in the holes can be considered as a driving field that has a dominant component parallel to the incident polarization. Figures 4 and 5 show how this driving field causes particles that are trapped in the holes to scatter, but is only locally affected by the presence of the particle. In Fig. 6(c), it is evident that the field in the hole where the particle is located, is strongly perturbed due to the near-field of the scattering particle, but in the closest neighboring holes to the particle, the mode field is approximately retained. Even for the largest particle, causing the largest change in the field, the maximum amplitude of the y component of the scattered irradiation is 0.7 times the amplitude of the incident field. This is only 0.2 times the absolute value of the y component of the resonantly enhanced E-field at the center plane of the membrane, averaged over one unit cell.

The reason for the spot pattern coinciding with the lattice can be explained by two distinguishable effects. One, light scattered from defect A cannot only radiate out into the medium surrounding the membrane. Part of the scattered irradiance can couple to the membrane and be guided away from the hole where defect A is located. This light will re-scatter when it meets neighboring holes. For unpolarized normal incidence light, as is used to obtain the image in Fig. 1(c), spherical waves will hence radiate out into the surrounding media directly from defect A, and from the nearest neighboring holes. The center spot in the pattern is directly related to scattered irradiance from defect A, and has an observed intensity set by the mode field amplitude at its location. Surrounding spots are a result of scattering from holes neighboring defect A, driven by the irradiance from defect A coupling to the membrane. Two, the light that is coupled out of the membrane via scattering by defect A, is dominantly drawn from the guided resonance mode. Consequently, the mode phase-matched to interfere destructively with directly transmitted light looses some of its power. This power is also locally bound to defect A and can create a spot pattern that coincides with the symmetry of the lattice.

5.1. Dipole like behavior of particles trapped in photonic crystals

We have previously proposed that the spatial distribution of the scattered light is similar to an ideal dipole, with the zero-field axis aligned with the driving field. Field plots in Figs. 5 and 6 support that this is the case. Particles trapped in the lattice scatter dominantly perpendicularly to the polarization of the driving field. These simulation results also agree with the experimental observation in Fig. 7(a), showing the result of polarized excitation. Strong scattering is seen from the hole where the defect is located, and from the neighboring holes, going out from the defect center, in a direction perpendicular to the incident polarization. Weaker scattering is seen from the holes, going out from the defect center, in a direction parallel to the incident polarization. Consequently, all images displayed in Fig. 7(a) show spot patterns with two folded symmetry. The minor deviations from two folded symmetry, can be explained by the off-centered position of defect A in the hole. This also agrees with the simulation results

#200180 - $15.00 USD Received 25 Oct 2013; revised 3 Dec 2013; accepted 4 Dec 2013; published 12 Dec 2013

in Fig. 5, where it is evident that scattered light from the defect couples stronger to the side where it is touching the hole wall. Hence, we see stronger scattering from the lower and left neighboring holes.

Since we only have one PC holding one ideal test particle, we have not been able to verify experimentally the size dependence evident in Fig. 6. Furthermore, our simulation results show that the direction of propagation and strength of scattered light from the defect is strongly dependent on its position in the hole, and we have not been able to find a non-destructive method to determine the chemical composition of our defect. We therefore hesitate to infer anything about permittivity and size of our defect from our measurements.

The $|\Delta E|$-plots in Fig. 6(b) show that the amplitude of the scattered light is proportional to the volume of the scattering particle, and results presented in Fig. 5 show how the scattered amplitude is increased when the particle is moved into areas with a stronger driving field. This complies with Rayleigh scattering theory [30], which says that the amplitude of scattering from isolated particles is proportional to the volume of the scattering particle and the amplitude of the driving field. Since the intensity recorded by the CCD camera in our optical setup is the field amplitude squared, the sensitivity of the sensors is proportional to the volume of particles squared, and can be improved by increasing the amplitude of the driving field.

5.2. Decreased background signal by use of crossed polarizers

As shown by the zero-transmission dip at 631 nm in Fig. 2(b), an infinite pristine PC can function as a mirror. When a particle is present in the lattice, it can therefore be observed in transmission as a bright spot, or a group of spots, on a background that in theory can be made black. In practice, the reflectivity is limited by fabrication accuracy, finite extent of the lattice, non-zero divergence of the excitation source and a finite source bandwidth. The minimum transmittance in our experiments is consequently closer to 20%, as can be seen in Fig. 7(a). This relatively high background, in combination with a sensitivity that is proportional to the volume of the particles squared, is limiting. As particles are reduced in size, the scattered light they produce falls fast below the noise floor. Alternative methods for reducing the background signal are therefore needed.

Experimental results presented in Fig. 7 show how cross-polarized excitation and detection is an alternative, that increases the signal-to-background ratio by up to a factor of three. This method is especially well suited in our design. For normal incidence plane waves, incident on a square 2D PC, the symmetry of the lattice forces the reflected and transmitted fields to retain the original polarization in the far-field. If the orthogonal polarization is present in transmission, it must originate from defects in the crystal or from imperfect extinction present in the measurement setup independent of the membrane. Cross-polarized excitation and detection hence filters out all but exactly what we are looking for, namely defects in the crystal.

It is further possible to argue that our signal-to-background ratio is a modest estimate. The calculated rms-value of the background, does not only include noise related to the detector chip. Although it is found by sampling an area with little defects, there is a contribution from lattice discrepancies. The sensor is meant to capture biomolecules. Detection is done by comparing the transmittance of the membrane before and after a molecule is captured, subtracting the initial image from the image taken after capture. By this procedure, contributions to the background signal from static defects in the crystal can be removed and lead to an increased signal-to-background ratio.

As seen in Fig. 7(b), displaying results from measurements using cross-polarized excitation and detection, depolarization of the incident light is observed at numerous localizable points across the membrane. The points lie along lines parallel to the PC lattice axes, and we believe they are a result of deviations in lattice period, hole radius and hole shape. These structural

#200180 - $15.00 USD Received 25 Oct 2013; revised 3 Dec 2013; accepted 4 Dec 2013; published 12 Dec 2013

discrepancies cannot be seen using SEM. The assumption hence implies that the current background signal is mainly limited by fabrication accuracy of the PC, and the sensitivity of the sensor exceeds the resolution of our SEM, i.e. we should be able to detect 20-40 nm diameter particles. This also agrees with the calculated signal-to-background ratio, which predicts that the detection limit is close to 26.1 nm: $r_{\min} = \left(r_p^6/\mathrm{SBR}_{\max}\right)^{1/6} = \left((60 \pm 15\ \mathrm{nm})^6/147\right)^{1/6} = 26.1 \pm 6.5$ nm.

This detection limit allows us to detect particles the size of single viruses. The sensitivity of the sensor hence has to be improved in order to detect proteins, which typically have a radius of 2-10 nm. This presents a challenge, since the sensitivity is proportional to the volume of trapped particles square. The sensitivity can however be improved by increasing the amplitude of the driving field, which can be done by utilizing a guided resonance mode with a higher Q-factor. An increased Q-factor of guided resonance modes can be achieved by decreasing the scattering strength of the PC. In practice, it is a question of production accuracy, and can e.g. be done by reducing the size of the holes in the PC [19, 31].

6. Conclusion

We have designed, fabricated, and characterized a PC that can be used as a nano-particle sensor. The key component in our scheme is a photonic crystal membrane supporting guided resonance modes. Simulation and experimental results presented in this report, show how detection is a result of amplified small particle scattering. Small particles trapped in photonic crystals, excited by normal incident light coupling to a guided resonance mode, scatter similar to ideal dipoles.

Provided a chemistry that facilitates capturing of biomolecules, the current design should enable detection of single viruses. The design is simple and composed of standard optical components, allowing it to be made cheap. It can also be made compact, by replacing the microscope by a set of lenses specific to the application. Further optimization of the design is needed to reach the sensitivity level of targets like proteins.

Acknowledgments

We thank the Norwegian Research Council (NFR) for their support through the Norwegian PhD Network on Nano-technology for Microsystems and the ISBILAT program.

#200180 - $15.00 USD Received 25 Oct 2013; revised 3 Dec 2013; accepted 4 Dec 2013; published 12 Dec 2013

Paper E

Optical Imaging System Designed for Biosensing using a Photonic Crystal Membrane to Detect Nanoparticles

elink: Paper E

Optical imaging system designed for biomolecule detection using photonic crystal membranes

Jon Olav Grepstad[1,2,3,*], **Peter Kaspar**[4], **Olav Solgaard**[5], **Ib-Rune Johansen**[2] **and Aasmund S. Sudbø**[6,3]

[1] *Department of Electronics and Telecommunications, Norwegian University of Science and Technology, NO-7491 Trondheim, Norway*
[2] *SINTEF ICT, Microsystems and Nanotechnology, NO-0373, Norway*
[3] *University Graduate Center, NO-2027 Kjeller, Norway*
[4] *Electronics Laboratory, ETH Zürich, CH-8092 Zürich, Switzerland*
[5] *E.L. Ginzton Laboratory, Stanford University, CA-94305, USA*
[6] *Department of Physics, University of Oslo, NO-0316, Norway*
[*] *jonolav.grepstad@sintef.no*

Abstract: We have built an optical microscope for a new biosensor application, incorporating a 2D photonic crystal membrane enabling detection of particles with a radius less than 50 nm. The microscope has been characterized experimentally.

OCIS codes: 110.0110 Imaging systems, 180.0180 Microscopy

1. Introduction

To make medical diagnosis more efficient and accurate, better instruments for specific detection of common pathogens are needed [1]. Monitoring the level of contamination in sources of water and food can prevent outbreak of disease [2]. To prevent bio-terrorism, monitoring of biological hazards would be helpful [3]. For this purpose we need sensors that can capture and detect very low concentrations of specific proteins, viruses, bacteria, etc., that is, biosensors with high specificity and sensitivity.

As pointed out in [4], micro- and nano-fabrication techniques can in general provide devices that are small, reliable and cheap. Recent developments suggest that the next generation biosensors will be made exploiting this technology [5]. Moreover, since optical readout is compatible with the wet environment presented in a biological system, biochemical sensor platforms with optical readout seem particularly promising.

Some of the most sensitive biosensors with optical readout today are based on dielectric photonic crystals (PCs) [6,7] and nanoplasmonics [3,8]. In [4] we propose to combine the convenient light coupling found in nanoplasmonic sensors and the high Q-factors obtainable in dielectric PCs, in a dielectric PC membrane. A PC membrane is a thin slab with a periodic in-plane variation in permittivity. They have some of the same light-guiding properties as regular slab waveguides, but in addition to having a series of guided modes, they also exhibit a group of modes called guided resonances [9]. Coupling to guided resonances can be achieved by normal incidence light, and can produce a large enhancement of the optical field inside the membrane compared to the field of the incident waves. A small particle placed in a hole in the membrane will 'see' this field, absorb energy from the guided-resonance mode field, and reradiate the absorbed light in all directions. The reradiated light can be captured by a camera focused on the PC membrane, where each light-scattering particle will appear as a bright spot in the image.

In [4] we have reported on the development of a novel planar 2D dielectric PC membrane, demonstrating this particle detection principle. Furthermore, we have reported the design of a multispectral imaging system that we have built to take images of the membrane. Finally we have reported preliminary results of detection of nano-particles in holes in the membrane, with the help of our imaging system. We here present an experimental comparison of the image contrast that we have measured for nano-particles in a PC membrane compared to the image contrast that we have obtained for nano-particles placed on microscope slides.

2. Design and working principle

The elements of the sensor are summarized in Fig. 1. The transducer in the sensor, turning the presence of a particle into an optical response, is a planar dielectric membrane with through holes as shown in Fig. 1-A. Holes are arranged

in a quadratic lattice with period 490 nm and radius 290 nm. The membrane is free-standing and suspended on a silicon frame, permitting gas or fluid samples to be physically pushed through the holes in the membrane. The mi-

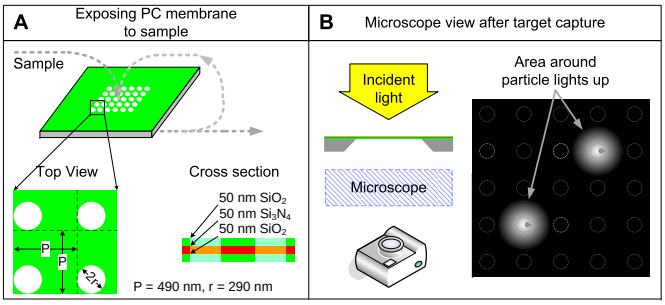

Fig. 1. Outline of the transducer and how the sensor works. (A) Samples can be pumped through the PC membrane, which is a quadratic lattice of holes with period 490 nm and radius 290 nm, etched in a stack of thin films made of Si_3N_3 and SiO_2. (B) Captured particles are detected as bright spots on a dark background by an optical microscope and a CCD-camera.

croscope setup, sketched in Fig. 1-B, is comprised of a standard 35W halogen lamp, an Oriel Cornerstone 130 1/8 m Monochromator, an Olympus BX61 TRF microscope and an Olympus F-view II CCD camera. The incident light is supplied by the halogen lamp routed through an Oriel Cornerstone 130 1/8 m Monochromator and a set of lenses and optical fibers, which provides the optical microscope with collimated backside illumination with normal incidence with respect to the PC membrane surface. A MPlanON 50x/0.95 NA objective provides magnification.

The PC membrane has been designed to allow coupling of normal-incident light into a guided resonance mode centered at 631 nm, and at the same time provide a very high reflectance. At 631 nm the PC membrane hence holds large electromagnetic fields inside the membrane and at the same time works as a mirror. Spherical particles that are small enough, will not affect the overall field distribution in the PC membrane. They will work as scattering centers producing spherical waves that appear as bright spots on the CCD screen [4], corresponding to their location on the PC membrane. Since the PC membrane works as a mirror, the contrast is maximized. The optical effect of two nano-particles trapped inside the membrane is illustrated in Fig. 1-B. It has been simplified to illustrate the idea that nano-particles are detected by the CCD camera as bright spots on a dark background. Specific capture of biological molecules can be done by chemical means.

3. Fabrication

Standard semiconductor production techniques and electron beam lithography were used to produce the membranes with a matrix of 100x100 through holes. A particle-like defect with radius ~50 nm settled inside one of the holes during production. Based on the materials present in our fabrication facilities, its permittivity is limited to a range between 2.25 and 12.25 in the spectral range of interest. This defect was introduced non-intentionally during the fabrication process, but is a well-suited object for preliminary studies. As a reference experiment, we used Latex Microspheres from Invitrogen with permittivity 2.26 and a radius of 100 nm, suspended between two microscope glass slides and dried.

4. Experiment and results

Pictures were taken at a wavelength of 631 nm of the PC membrane holding the particle-like defect and the slide holding the latex spheres. Pictures of the particle-like defect were compared with a bright spot on the microscope slide that we believe corresponds to a single latex sphere. The results are given in Fig 2.

5. Discussion and conclusion

Fig. 2 clearly shows that the 50-nm-radius particle on the PC membrane is easier to see than the 100-nm-radius particle on the glass slide. A rough estimate of the difference in contrast indicates that the contrast is twice as large for the 50 nm particle trapped in the PC membrane, as compared to the 100 nm particles on the glass slide. We would like to point out that Rayleigh scattering theory predicts that the nano-particle scattering intensity is proportional to the

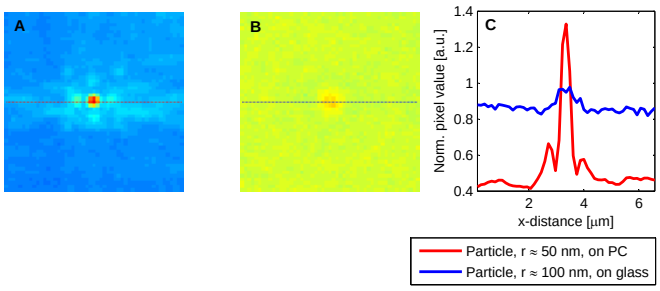

Fig. 2. (A) Particle-like defects in the PC membrane as seen from the CCD-camera, compared to (B) what we believe corresponds to a single latex sphere. (C) Normalized pixel values along a horizontal line crossing the particle locations give an impression of the difference in contrast. Pixel values of the CCD camera have been normalized with respect to the transmitted intensity recorded without the membrane present.

particle radius to the power of six. Consequently, a difference in radius of 1/2 should induce a difference in scattered intensity of 1/64.

We believe that the effect can be understood as amplified small particle scattering provided by amplification of the field inside the membrane. The amplification is induced by coupling of the incident field to guided resonance mode fields supported by the PC membrane. In combination with the PC working as a mirror, providing optimal contrast, the current sensor is estimated to detect particles down to 20 nm in radius. Further optimization of the PC membrane design is hence needed to reach the sensitivity level of targets like proteins. Proteins typically have a radius of 2-10 nm. However, if the phenomenon can be explained as amplified scattering, each hole in the membrane can effectively work as a sensor for single nano-particles. The sensitivity is virtually only limited by the field amplitude. Sufficiently high fields can be induced producing PC membranes supporting resonant modes with greater Q-factors, which in general is a question of production accuracy, since it can be done by reducing the size of holes [9]. In that case, this microscope setup can be a cheap and efficient method for nano-particle detection and can potentially provide biosensor with single molecule sensitivity.

References

1. B. Bohunicky and S. A. Mousa, "Biosensors: the new wave in cancer diagnosis," Nanotech. Sci. Appl. **4**, 1–10 (2010).
2. M. F. Pineda, L. L. Chan, T. Kuhlenschmidt, C. J. Choi, M. Kuhlenschmidt, and B. T. Cunningham, "Rapid specific and label-free detection of porcine rotavirus using photonic crystal biosensors," IEEE Sens. J. **9**, 470–477 (2009).
3. A. A. Yanik, M. Huang, O. Kamohara, A. Artar, T. W. Geisbert, J. H. Connor, and H. Altug, "An optofluidic nanoplasmonic biosensor for direct detection of live viruses from biological media," Nano Lett. **10**, 4962–4969 (2010).
4. J. O. Grepstad, P. Kaspar, O. Solgaard, I.-R. Johansen, and A. S. Sudbø, "Photonic-crystal membranes for optical detection of single nano-particles, designed for biosensor application," Opt. Express **20**, 7954 – 7965 (2012).
5. L. Li, "Recent development of micromachined biosensors," IEEE Sens. J. **11**, 305–311 (2011).
6. X. Fan, I. M. White, S. I. Shopova, H. Zhu, J. D. Suter, and Y. Sun, "Sensitive optical biosensors for unlabeled targets: A review," Anal. Chim. Acta **620**, 8 – 26 (2008).
7. F. Hsiao and C. Lee, "Computational study of photonic crystals nano-ring resonator for biochemical sensing," IEEE Sens. J. **10**, 1185–1191 (2010).
8. J. N. Anker, W. P. Hall, O. Lyandres, N. C. Shah, J. Zhao, and R. P. Duyne, "Biosensing with plasmonic nanosensors," Nat. Mater. **7**, 442–453 (2008).
9. S. Fan and J. D. Joannopoulos, "Analysis of guided resonances in photonic crystal slabs," Phys. Rev. B **65**, 235,112 (2002).

Paper F

Enhanced scattering from nano-particles trapped in photonic crystal membranes

elink: Paper F

MC3 (Contributed Oral)
2:45 PM – 3:00 PM

Enhanced scattering from nano-particles trapped in photonic crystal membranes

Jon Olav Grepstad[*,†,‡], Peter Kaspar[§], Olav Solgaard[¶], Ib-Rune Johansen[†] and Aasmund S. Sudbø[‡,‖]
[*]Department of Electronics and Telecommunications, Norwegian University of Science and Technology, NO-7491 Trondheim, Norway
Email: jonolav.grepstad@sintef.no, Telephone: +4741044764
[†]SINTEF ICT, Microsystems and Nanotechnology, NO-0373, Norway
[‡]University Graduate Center, NO-2027 Kjeller, Norway
[§]Electronics Laboratory, ETH Zürich, CH-8092 Zürich, Switzerland
[¶]E.L. Ginzton Laboratory, Stanford University, CA-94305, USA
[‖]Department of Physics, University of Oslo, NO-0316, Norway

***Abstract*—We present simulations showing how light scattered by isolated particles increases by a factor 10, when they are placed in photonic crystal membranes. Exploiting this effect, single nano-particles have been detected with an optical microscope.**

I. Introduction

Biosensors are currently used in medical diagnosis and for monitoring biological hazards in food and water to expose potentially dangerous pathogens before they reach harmful concentrations. By increasing the sensitivity of biological sensors, potential dangers can be exposed at earlier stages. Preventive action and early detection of disease are identified among the best and most cost efficient means of improving health care [1], [2]. Moreover, if the sensors can be made small and cheap, work fast and are easy to use, they can be applied at point-of-care, and even in the comfort of our own homes.

Among the many different technologies competing to become the next generation biosensors, optical label-free biosensors are promising candidates [3], [4]. Optical label-free biosensors use chemistry to immobilize specific proteins, DNA, RNA, viruses and bacteria at desired locations. In this way, chemical methods provide specificity. The sensitivity is provided by a transducer, with optical readout, that reacts to changes in permittivity, and is generally optimized by maximizing the concentration of light where the biomolecules settle.

In a recent publication [5], we propose a novel biosensor incorporating a photonic crystal (PC) membrane with a quadratic lattice of holes. Each hole in the membrane can trap a biomolecule and represents a detection volume. Concentration of light in the detection volume is achieved through coupling of normal-incidence light into so-called guided resonance modes [6]. Compared to fully guided modes, guided resonance modes are not strictly confined to the PC membrane plane. However, they still concentrate a major part of their energy here and can produce high electromagnetic fields in the vicinity of the PC membrane. A biomolecule trapped in a hole in the PC membrane will scatter these high fields. We have shown in [5] how scattered light from such particles can appear as bright spots, when the membrane is illuminated with collimated monochromatic light and imaged with a 2D CCD camera in a transmission optical microscopy setup. Contrast is optimized by operating at a wavelength where the PC membrane works as a mirror.

We have performed simulations of the light scattered from nano-particles trapped in a PC membrane like the one we have fabricated, and show how the simulation results can be modeled as enhanced Rayleigh scattering.

II. Sensor design and Optical microscopy

The transducer in the system is a free standing PC membrane, comprised of a 2D quadratic lattice of 145 nm radius holes with period 490 nm, etched in a stack of three 50 nm thin films, $Si_3N_4/SiO_2/Si_3N_4$. The PC membrane is suspended on a silicon frame. The transmittance of collimated monochromatic normal-incidence light is detected with a 2D CCD camera and magnified by an optical microscope equipped with an Olympus MPlanON 50x/0.95NA objective. The transmittance is hence measured as a function of wavelength with spatial resolution.

SEM images of the PC membrane with a trapped particle inside are given in Fig. 1(a), and an optical microscope image taken with a CCD camera, is given in Fig. 1(b). Similar images have been presented in [5]. The particle produces a pattern with a strong center spot surrounded by four weaker spots pointed out with arrows in Fig. 1(b). The symmetry of the pattern coincides with the lattice. Fig. 1(c) displays three line scans through the particle position from CCD images taken at three different illumination wavelengths. It shows how the background signal is reduced at the same time as the nano-particle stands out with increased intensity.

III. Simulation results

We have simulated the transmittance and reflectance of a normally incident wave, for the vacuum wavelength $\lambda_{vac} = 631$ nm, incident on a quadratic lattice of 145 nm radius holes with period $a = 490$ nm. The computation uses a small dielectric sphere in every 4^{th} hole, and the membrane

978-1-4577-1513-6/12/$26.00 ©2012 IEEE

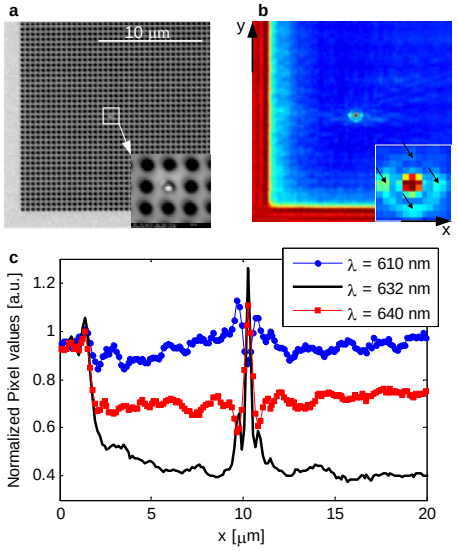

Fig. 1. (a) SEM image of the PC membrane with a trapped nano-particle, and (b) the transmittance of the corresponding area imaged by a CCD camera at a wavelength of 632 nm. (c) Line scans of images like the one in Fig. 1(b) crossing the particle in the x-direction are given at three wavelengths.

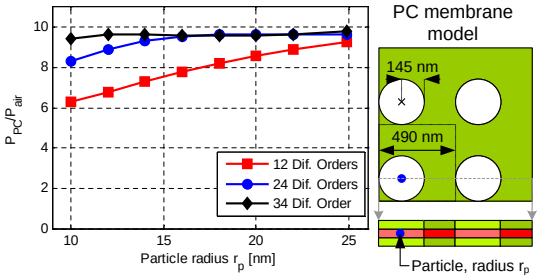

Fig. 2. Power ratio $P_{\text{PC}}/P_{\text{air}}$, simulated using 12, 24 and 34 diffraction orders. P_{PC} is the power radiated into higher diffraction orders due to particles of radius r_p lying in every 4^{th} hole in PC membrane; P_{air} is the power radiated from a Rayleigh scattering dielectric sphere in air. The membrane is illuminated with normal-incidence light at $\lambda_{vac} = 631$ nm.

is surrounded by air with permittivity $\epsilon_{air} \approx 1$. Simulations were done using rigorously coupled-wave analysis (RCWA) in 3D [7], for eight different particle radii, r_p, between 10 and 25 nm. The particle permittivity is chosen to be $\epsilon_p = 2.25$, and the incident electric field is linearly polarized along one of the crystal's principal axes and has normalized amplitude 1.

Since we restrict λ_{vac} to $a < \lambda_{vac} < \sqrt{2}a$, the PC membrane without dielectric spheres in the holes, can not scatter light into higher orders of diffraction in the air. Consequently, if power is scattered into higher orders of diffraction in air, this is due to the dielectric spheres that lie with a spacing of $a_{sup} = 2a$. We have compared the power P_{PC}, scattered into higher orders of diffraction, obtained from simulations, with the power P_{air}, scattered from a Rayleigh particle with permittivity ϵ_p in air, exited by a linearly polarized electric field with normalized amplitude 1.

We further recognize that the power scattered from Rayleigh particles scales as $r_p^6 E_p^2$ [8], where E_p is the electric field amplitude at the location of the particle. Since the ratio $P_{\text{PC}}/P_{\text{air}}$, plotted in Fig. 2, approaches a radius-independent behavior as the number of diffraction orders is increased, we can conclude that the scattered power from a particle trapped in a PC membrane also scales as r_p^6. Of particular interest is that, the ratio $P_{\text{PC}}/P_{\text{air}}$ converges towards ~ 10. This means that the power scattered by the particle is increased by a factor ~ 10 when the particle lies in the PC membrane, as compared to the same particle in free air. The imaged amplitude that a particle potentially can induce on a detector, is hence also increased by a factor 10. We believe that the enhancement is a result of increased electromagnetic fields at the location of the particle, E_p, caused by coupling of incident light into guided resonance modes of the PC membrane.

IV. Conclusion

Experimental results show how nano-particles trapped in PC membranes exhibit increased scattering when incident light couples into guided resonance modes, and can be detected as bright spots in an optical microscope. Simulation results show how the current membrane provides an enhanced scattering factor of $\sim$10 when particles lie in the center of holes. Moving the particle towards the hole wall should increase this factor, since the electric field is expected to peak at the hole wall. Moreover, further enhancement can be achieved by increasing the Q-factor of guided resonance modes, which can be done by reducing the radius of holes in the PC membrane [6].

Considering nano-particles in the form of DNA, proteins and viruses, we see a potential use of the sensor in biosensing if chemical methods are incorporated that allow capture of specific molecules in the holes.

References

[1] M. F. Pineda, L. L. Chan, T. Kuhlenschmidt, C. J. Choi, M. Kuhlenschmidt, and B. T. Cunningham, "Rapid specific and label-free detection of porcine rotavirus using photonic crystal biosensors," *IEEE Sens. J.*, vol. 9, no. 4, pp. 470–477, 2009.

[2] B. Bohunicky and S. A. Mousa, "Biosensors: the new wave in cancer diagnosis," *Nanotech. Sci. Appl.*, vol. 4, no. 12, pp. 1–10, 2010.

[3] A. A. Yanik, M. Huang, O. Kamohara, A. Artar, T. W. Geisbert, J. H. Connor, and H. Altug, "An optofluidic nanoplasmonic biosensor for direct detection of live viruses from biological media," *Nano Lett.*, vol. 10, no. 12, pp. 4962–4969, 2010.

[4] C.-S. Huang, V. Chaudhery, A. Pokhriyal, S. George, J. Polans, M. Lu, R. Tan, R. C. Zangar, and B. T. Cunningham, "Multiplexed cancer biomarker detection using quartz-based photonic crystal surfaces," *Anal. Chem.*, vol. 84, no. 2, pp. 1126–1133, 2012.

[5] J. O. Grepstad, P. Kaspar, O. Solgaard, I.-R. Johansen, and A. S. Sudbø, "Photonic-crystal membranes for optical detection of single nano-particles, designed for biosensor application," *Opt. Express*, vol. 20, pp. 7954 – 7965, 2012.

[6] S. Fan and J. D. Joannopoulos, "Analysis of guided resonances in photonic crystal slabs," *Phys. Rev. B*, vol. 65, p. 235112, 2002.

[7] Commercially available software supplied by KJ Innovation, http://software.kjinnovation.com/GD-Calc.html visited 15. Sept. 2011.

[8] C. F. Bohren and D. R. Huffman, *Absorbtion and Scattering of Light by Small Particles*. John Wiley and Sons, Inc., 1998, chapter 5.

Paper G

Single nano-particle sensing exploiting crossed polarizers to improve the signal-to-noise ratio

elink: Paper G

Single nano-particle sensing exploiting crossed polarizers to improve the signal-to-noise ratio

Jon O. Grepstad, Peter Kaspar, Olav Solgaard, Ib-Rune Johansen, Aasmund Sudbø

Norwegian University of Science and Technology, NO-7491 Trondheim, Norway, Electronics Laboratory, ETH Zurich, CH-8092 Zurich, Switzerland, E.L. Ginzton Laboratory, Stanford University, CA-94305, USA, SINTEF ICT, Microsystems and Nanotechnology, NO-0373, Norway, Department of Physics, University of Oslo, NO-0316, Norway

jonolav.grepstad@sintef.no, peter.kaspar@ife.ee.ethz.ch, solgaard@stanford.edu, ib-rune.johansen@sintef.no, aasmund.sudbo@mn.uio.no

Abstract: Crossed polarized excitation and detection has been used to improve signal-to-noise ratio in an optical nano-particle sensor exploiting guided-resonance-modes in photonic crystal membranes. The sensor can detect particles with a diameter less than 40 nm.

OCIS codes: 110.0110, 110.4235, 350.4238

Motivated by the large area of application for highly sensitive biosensors, we are aiming to develop a label-free single-molecule sensor. The sensor exploits the properties of planar 2D photonic crystal membranes (PCMs) [1]. This choice of technology is based on its potential to produce inexpensive, efficient and robust sensors that are compatible with the wet environment presented by biological systems, as well as the high sensitivities reported recently [2].

Like in most label-free optical biosensors, the specificity of our sensor is provided by chemical means. A surface on the inside of through holes in the PCM, can be furnished with capturing molecules specific to targets like proteins and viruses. The optical design of the PCM provides sensitivity. Normal incidence light can couple into guided resonance modes [3] in the PCM. The mode we use has two important properties. For a specific wavelength of the incident light, the field is concentrated in the holes and simultaneously provides very high reflectivity.

Observing the membrane in transmission with a microscope and a 2D CCD camera, a pristine PCM will look black, but when a particle is present in a hole, a bright spot will appear in the image at the location of the particle. Good signal-to-noise-ratio (SNR) is obtained, because the membrane enhances the optical field at the particle compared to the incident field and the high reflectance gives a low background signal [4]. In practice however, reflectivity is limited by production accuracy, finite lattice size and non-zero divergence of the excitation source. We have therefore implemented crossed polarizers in our setup, i.e. we are exciting with one polarization and detecting the orthogonal polarization. This reduces the background signal and improves SNR [5]: A PCM free of defects should not depolarize the light, while a nano-particle trapped in the membrane will.

Fig. 1-A shows a scanning electron microscopy (SEM) image of the fabricated PCM. It is a quadratic lattice of through holes with a spacing of 490 nm and radius 145nm, etched in a stack of three thin dielectric films, 50nm Si_3N_4/50nm SiO_2/50nm Si_3N_4. The membrane is free standing, suspended on a silicon frame. The area of the hole pattern is $50 \times 50 \mu m^2$. As shown in the inset of Fig. 1-A, a fabrication defect with a diameter of 150nm is located inside one of the holes in the membrane. It resembles a captured molecule and hence models a capture event.

The optical setup (Fig. 1-B) is designed to excite a guided resonance mode that gives minimum transmission at 631nm. A diode laser with a built-in collimator lens, produces a 1.1 mrad divergence beam with a line width of $\sim$ 1nm centered at 631nm. The beam is directed onto the backside of the PCM at normal incidence. It passes through a linear polarizer, L1, that is oriented 45 degrees relative to the lattice principal axis. The membrane is imaged in transmission using an optical microscope and a 2D CCD camera. A rotatable linear polarizer, L2, is placed in the microscope column above a 50x/0.95 NA objective that provides magnification. Images have been recorded for L2 oriented parallel and orthogonal to L1, using an exposure time of 50ms and 500ms, respectively. The results are given in Fig. 1-C and D.

For parallel polarizers, the PCM has a transmittance of 20-50% and is inhomogeneous across the membrane. Based on experiments using a different light source, we know that the inhomogeneity is largely due to the poor quality of the laser collimator lens. The nano-particle is clearly visible and the SNR is mainly limited by the non-zero and inhomogeneous transmittance of the membrane. The maximum pixel value attributed to the nano-particle divided by the standard deviation over an area holding no particles, gives an estimated SNR of 17.

Using crossed polarizers, the SNR improves to 59. As seen in Fig. 1-D, the background signal is now mainly limited by two sources of unwanted depolarization: Depolarization at the lattice boundaries and at numerous localizable points

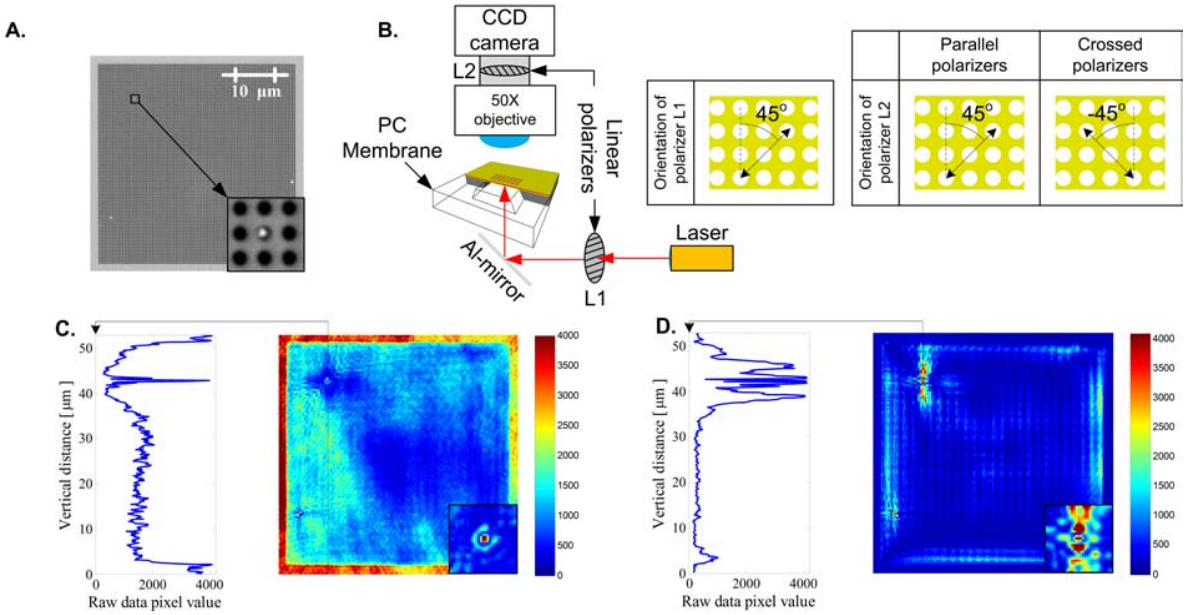

Fig. 1. (A) SEM image of fabricated photonic crystal and (B) the optical setup used for characterization. The lower left (C) and right (D) figures display images recorded with parallel and crossed polarizers, respectively. Line plots are included for a row of pixels crossing the particle location in the vertical direction.

across the membrane. The points lie along lines parallel to the PC lattice axes, and we believe they are a result of deviations in lattice period, hole radius and hole shape. These structural discrepancies can not be seen using SEM. The assumption hence implies that the current sensitivity is mainly limited by fabrication accuracy of the PCM and exceeds the resolution of our SEM, i.e. we should be able to detect 20-40nm diameter particles.

Optical sensing enabling detection of single particles of this size is highly applicable. Provided means for specific molecule capture, the sensor should be able to detect single viruses. Viruses typically have a diameter of 20-300nm. Proteins have a diameter ranging from 2-10nm. The current sensor can hence not detect proteins, but it does represent a definite step towards true single-protein sensitivity. Moreover, the simplicity of the sensor enables it to be made compact and inexpensive.

References

1. J. O. Grepstad, P. Kaspar, O. Solgaard, I.-R. Johansen, and A. S. Sudbø, "Photonic-crystal membranes for optical detection of single nano-particles, designed for biosensor application," Opt. Express **20**, 7954 – 7965 (2012).
2. M.-J. Banuls, R. Puchades, and A. Maquieira, "Chemical surface modifications for the development of silicon-based label-free integrated optical (io) biosensors. a review," Anal. Chim. Acta (2013). In Press.
3. S. Fan and J. D. Joannopoulos, "Analysis of guided resonances in photonic crystal slabs," Phys. Rev. B **65**, 235,112 (2002).
4. J. O. Grepstad, P. Kaspar, O. Solgaard, I.-R. Johansen, and A. Sudbo, "Enhanced scattering from nano-particles trapped in photonic crystal membranes," in "International Conference on Optical MEMS and Nanophotonics (OMN)," (2012), pp. 21–22.
5. M. Huang, A. A. Yanik, T. Y. Chang, and H. Altug, "Sub-wavelength nanofluidics in photonic crystal sensors," Opt. Express **17**, 24,224–24,233 (2009).